ENHANCING RATE AND RELIABILITY OF PLC IN LV/MV SMART GRID NETWORKS

by

Mahmoud Elgenedy

APPROVED BY SUPERVISORY COMMITTEE:

Naofal Al-Dhahir, Chair

Murat Torlak

John P. Fonseka

Carlos A. Busso-Recabarren

Dedicated to my parents, wife, daughter, son, sisters and brothers. I would not be anything without your support.

ENHANCING RATE AND RELIABILITY OF PLC IN LV/MV SMART GRID NETWORKS

by

MAHMOUD ELGENEDY, BS, MS

DISSERTATION

Presented to the Faculty of

The University of Texas at Dallas

in Partial Fulfillment

of the Requirements

for the Degree of

DOCTOR OF PHILOSOPHY IN

ELECTRICAL ENGINEERING

THE UNIVERSITY OF TEXAS AT DALLAS

May 2019

ACKNOWLEDGMENTS

First of all, thanks are due to the Almighty God for giving me the strength and patience to complete my studies and write this dissertation, which I sincerely hope will contribute to the welfare of people.

I would like to express my deepest gratitude to my supervisor, Dr. Naofal Al-Dhahir, for his support, guidance and trust through my candidature at UT Dallas. I was very lucky to have such a great opportunity to learn from Dr. Al-Dhahir on different levels including technical, professional, personal and ethical levels. In addition, I would like to acknowledge my PhD supervisory committee members, Dr. Murat Torlak, Dr. John P. Fonseka and Dr. Carlos Busso, for their experienced discussions and suggestions.

I would like to acknowledge my brilliant colleagues who provided invaluable feedback on my dissertation work. In particular, I would like to thank my collaborators in the different projects, Dr. Mostafa Sayed, Dr. Mohamed Awadin, Dr. Ahmed Elshafie, Dr. Ahmed Elsamadouny, Dr. Mohamed Abdallah, Dr. Rakan Chabaan, Dr. Il-han Kim, Dr. Waheed Bajwa, Dr. Ridha Hamila, Dr. Ahmed Ibrahim, Dr. Theofilos Papadopoulos, Dr. Stefano Galli, Dr. Andreas Chrysochos, Dr. Grigoris Papagiannis, Dr. Brian Evans, Dr. Junmo Sung, Sadaf Moaveninejad, Dr. Atul Kumar, Dr. Maurizio Magarini, and Dr. Andrea M. Tonello.

Special thanks to my colleagues, Hussein Saad, Dr. Ahmed Mohamed, Dr. Ahmed Ali, Dr. Ahmed Hindy, Dr. Ahmed Abotabl, Dr. Mohamed Fadel, Noha Helal, Mohamed Marzban, Sherief Helwa, Dr. Yahia Ramdan, Mahmoud Abdelgalil, Ahmed Magdy, and Rana Ahmed.

May 2019

ENHANCING RATE AND RELIABILITY OF PLC

IN LV/MV SMART GRID NETWORKS

Mahmoud Elgenedy, PhD
The University of Texas at Dallas, 2019

Supervising Professor: Naofal Al-Dhahir, Chair

Power line communications (PLC) is a promising solution for smart grid communications due to low deployment cost over the existing power line infrastructure. In this dissertation, we propose enhancing the PLC reliability and/or data rate by exploiting the noise and channel statistical properties in time, frequency and spatial domains.

For the Narrowband PLC (NB-PLC) in the 3-500 kHz frequency band, a major challenge is the presence of cyclostationary noise whose statistics vary periodically with a period of half the AC cycle. We propose two techniques to mitigate the cyclostationary noise, namely, erasure decoding and noise cancellation. For erasure decoding, we enhance the channel decoding capabilities by feeding the positions of the noise impulses to the channel decoder. Erasure decoding has been investigated for different modes including the Reed-Solomon decoder only, the Viterbi decoder only, and the concatenated decoding modes. Next, we investigate two cyclostationary noise cancellation techniques that offer better performance but at higher complexity, namely, the temporal-region-based and the frequency-shift-filtering-based (FRESH-filtering-based) techniques. The temporal-region-based technique assumes that the cyclostationary noise is stationary over each of the multiple temporal-regions, and employs a per sub-channel linear minimum mean square (LMMSE) estimator in the frequency domain. The FRESH-filtering-based technique aims to filter the cyclostationary noise in the

time domain using FRESH filters that utilize time average MMSE (TA-MMSE) estimator. Furthermore, we extend both cyclostationary noise cancellation techniques to exploit the available spatial dimensions, i.e., multiple receive powerline phases. Moreover, to ensure realistic results, we develop novel methods to generate the cyclostationary noise based on FRESH filtering where the filter coefficients are extracted based on field measurements.

For the broadband powerline communication (BB-PLC) in the 1.8-250 MHz frequency band, additional diversity can be achieved through simultaneous transmissions over powerline and unlicensed wireless frequency bands, namely, hybrid PLC-wireless system. However, a hybrid PLC-wireless system faces two main challenges. First, in-home BB-PLC systems suffer from impulsive noise (IN). Second, unlicensed wireless transmissions are subject to narrowband interference (NBI) from other in-band wireless communication systems. Therefore, we propose a new sparsity-aware framework to model and mitigate the joint effects of NBI and IN in hybrid PLC-wireless system. In addition, we explore different cases of the NBI and IN including the block sparse NBI/IN and asynchronous NBI cases. For further mitigation performance enhancements, we investigate a Bayesian LMMSE-based approach. Numerical results show superiority of our proposed joint processing of NBI and IN sparsity-based mitigation techniques versus separate processing.

Lastly, we investigate the application of multi-input multi-output (MIMO) orthogonal frequency division multiplexing (OFDM) to NB-PLC over medium-voltage (MV) underground networks. We study different MIMO transmission scenarios with different injection configurations utilizing both the cable conductor and sheath phases. Multi-conductor transmission line theory is used to characterize the underground MV NB-PLC channel transfer function. The achievable data rates are evaluated after optimizing the transmit energy allocation across different spatial information streams subject to a power constraint. The achievable data rates for MIMO configurations are shown to be significantly higher compared to single-input single-output OFDM transmission.

TABLE OF CONTENTS

LIST OF FIGURES

LIST OF TABLES

CHAPTER 1
INTRODUCTION

1.1 Smart Grid Communications

A smart grid couples a two-way communication network to the traditional power grid to enable adaptive energy management. For smart metering applications, a smart grid consists of three primary communication networks (Prakash, 2013; Gungor et al., 2011), as in Fig. 1.1[1], namely, home area network (HAN), neighborhood area network (NAN) and backhaul communications network as depicted

Power line and wireless communication technologies are two important candidates that support smart grid communications (Galli et al., 2011; Ancillotti et al., 2013). Next, we provide an overview of power line concepts to support the three types of communication links in Fig. 1.1 for sensing smart metering applications.

1.2 Powerline Communications (PLC)

Powerline communications (PLC) is an appealing solution for communications in HANs and NANs considering its low deployment cost over existing infrastructure. Based on the operating frequency bands, there are three categories of PLC systems (Nassar et al., 2012; Galli et al., 2011):

1. Ultra-Narrowband power line communications (UNB-PLC) systems that operate in the frequency band of 0.3-3 kHz to support around 100 bps data rate for distances more than 150 km. UNB-PLC used by utilities for supervisory control and data acquisition of the power generation units.

[1]Fig. 1.1 was created by Dr. Jing Lin (UT Austin) and used with permission.

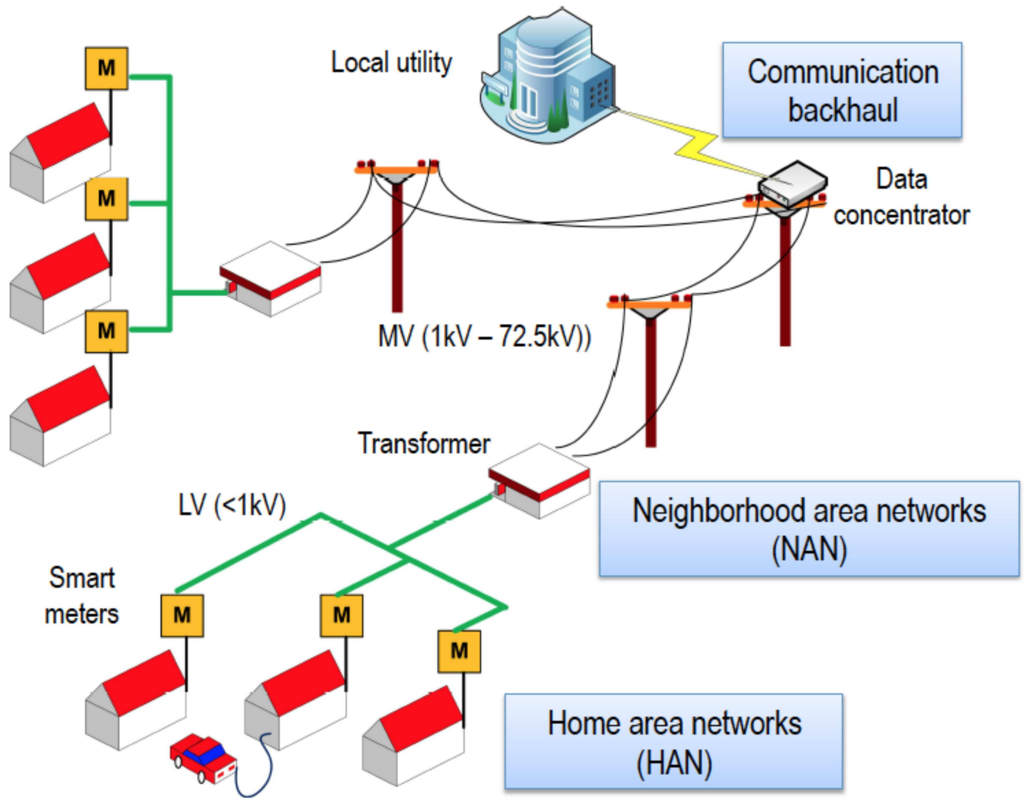

Figure 1.1: A smart grid for smart metering applications.

2. Narrowband power line communications (NB-PLC) systems in the 3 – 500 kHz frequency band for data rates up to several hundred kbps using Orthogonal Frequency Division Multiplexing (OFDM). Recently, NB-PLC gained significant interest to support NANs. Industry developed standards for NB-PLC include G3, PRIME, IEEE 1901.2 and ITU-T G.hnem.

3. Broadband power line communications (BB-PLC) systems operate in the 1.8-250 MHz frequency band providing several hundred Mbps data rates to support HANs. Standards for BB-PLC such as TIA-1113 (HomePlug 1.0), ITU-T G.hn and IEEE 1901 specifications.

In addition to the low deployment costs, an important advantage that makes PLC an appealing candidate for smart grid communications is the predictable propagation channel.

However, PLC must overcome several challenges to provide a reliable communication link. For example, the PLC channel is highly frequency selective and experiences instantaneous changes due to dynamic switching and branching in power lines (Nassar et al., 2012; Zimmermann and Dostert, 2002; Banwell and Galli, 2005; Galli and Banwell, 2005). In addition, a typical PLC system suffers from high interference and impulsive noise that dominate the background noise power and can result in severe performance degradation (Nassar et al., 2013; Katayama et al., 2006; Elgenedy et al., 2015). In PLC, interference and impulsive noise are mainly generated by electrical devices connected to2 the power line grid. An additional source of interference is caused by external signals coupled to the power lines through conduction or radiation (Galli et al., 2011).

1.3 Narrowband power line communications

Narrowband power line communications (NB-PLC) is an attractive solution for Smart Grid communications due to its low deployment cost over the existing power line infrastructure. NB-PLC is mainly used for outdoor last-mile communications between smart meters at the residential sites and data aggregators which are deployed by local utilities. The applications of NB-PLC for Smart Grid communications include automatic meter reading (AMR), device-specific billing, real-time pricing and other real-time monitoring and control tasks (Ferreira et al., 2010; Galli et al., 2011; Gungor et al., 2011; Kim et al., 2010). In addition, a reliable two-way communication link is a key enabling technology for real-time management of the vehicle-to-grid (V2G) communications services (Lopes et al., 2011; Liu et al., 2013). We assume the V2G system model shown in Fig. 1.2 where the aggregators serve as intermediate nodes between the EV supply equipment (EVSE) and the grid operator. Individual EVs connect and disconnect with an aggregator as they arrive at and leave EVSEs. The end-to-end communication link between the grid and EVs consists of two links: the grid-aggregator link and the aggregator-EV link. Both links can use wired or wireless communications for

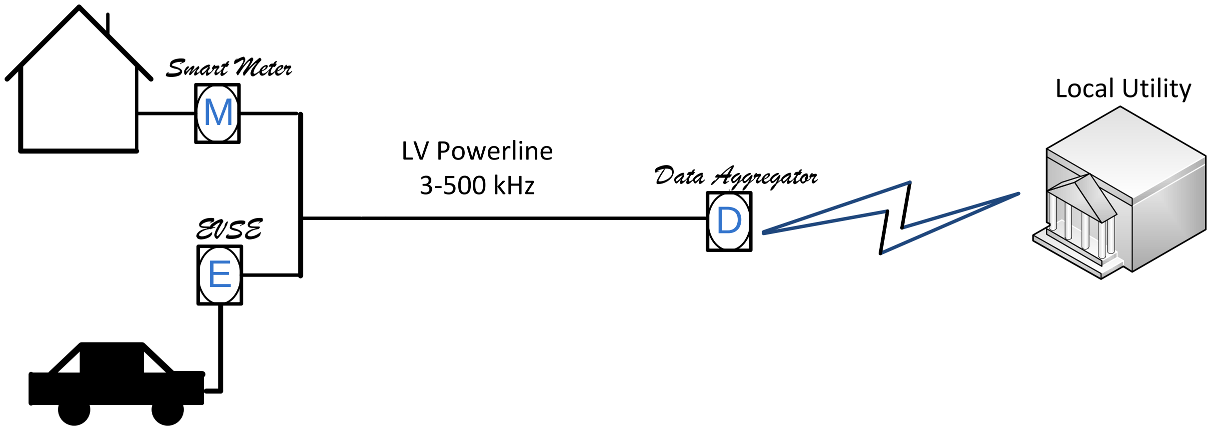

Figure 1.2: Assumed V2G communications system model.

transmission. However, they differ in terms of their operational requirements including range, power level, data rate, reliability, security, and latency. These differences must be taken into consideration when designing the overall V2G communication system (Lopes et al., 2011; Liu et al., 2013).

Several NB-PLC standards have been developed that operate in the $3 - 500$ kHz band such as the PRIME, G3, IEEE 1901.2, and ITU-T G.hnem standards. These standards adopt OFDM signaling to deliver scalable data rates up to several hundred kilo bits per second (kbps) over supported sub-bands. Supported sub-bands including a sub-band of the European CENELEC frequency band (3–95 kHz in CENELEC-A, 95–125 kHz in CENELEC-B and 125–148.5 kHz in CENELEC-CD) and a sub-band of the US FCC frequency band (34.375–487.5 kHz) (IEEE P1901.2, 2013).

1.3.1 NB-PLC Cyclostationary Noise Modeling

There has been a significant interest in characterizing NB-PLC noise due to its impact on communication performance. PLC noise deviates significantly from the additive white Gaussian noise (AWGN) assumption typically used to design and analyze communication systems. A major design challenge in Smart Grid communications over power lines is the presence of strong impulsive noise that may be tens of decibels higher than the background (thermal) noise (Nassar et al., 2012; Sayed and Al-Dhahir, 2014; Elgenedy et al., 2015; Sayed et al., 2015; Sayed et al., 2015; Lin et al., 2015; IEEE P1901.2, 2013). In general, PLC noise is known to have three main components: generalized background noise, cyclostationary periodic noise, and asynchronous impulsive noise. Cyclostationary noise is observed to be dominant in NB-PLC (Nassar et al., 2012). In particular, in NB-PLC, the dominant noise component is a periodic impulsive noise whose statistics vary periodically with a period of half the AC cycle (Nassar et al., 2012). This periodic impulsive noise is bursty in nature and typically caused by nonlinear power electronic devices such as silicon controlled rectifiers and diodes that switch on and off with the AC cycle. Hence, the periodic impulsive noise in NB-PLC exhibits cyclostationarity in both the time and frequency domains (Lin et al., 2015; Katayama et al., 2006; Nassar et al., 2012).

For instance, the NB-PLC noise model proposed in (Katayama et al., 2006) represents the noise as a colored cyclostationary Gaussian process with power spectral density (PSD) fitted to the measured noise. However, this model ignores the time-varying spectral behavior of the noise which limits its applicability to NB single-carrier systems, making it inappropriate for orthogonal frequency division multiplexing (OFDM) systems. This spectral variation results from the noise being the superposition of various noise processes with different generation mechanisms (Nassar et al., 2012).

To address the problems of the model in (Katayama et al., 2006), the authors of (Nassar et al., 2012) proposed a cyclostationary noise model for the NB-PLC that accounts for both the time and frequency properties of the measured noise. In particular, (Nassar et al., 2012) partitions the cyclostationarity period of the NB-PLC noise into multiple temporal regions and generates the noise within each region as a stationary colored Gaussian process. Each noise temporal region is characterized by a particular PSD, which is fitted to actual noise measurements. Although the model presented in (Nassar et al., 2012) is computationally tractable and provides a good fitting for the measured NB-PLC noise, it suffers from two drawbacks. First, the number of stationary temporal regions and the region boundaries are inferred by visually inspecting the measured noise spectrogram and do not rely on a mathematical model. Second, the noise process within each region is generated independently of the other regions which ignores any possible cross-correlation between the different noise processes across the regions.

1.3.2 NB-PLC Cyclostationary Noise Mitigation

Several techniques have been proposed to mitigate the impulsive noise in PLC. They can be divided into two main categories: (1) Impulsive noise estimation and compensation. (2) Channel coding enhancement in the presence of impulsive noise, e.g. using erasure decoding. Estimation of impulsive noise in OFDM systems based on compressed sensing techniques has been proposed in (Lampe, 2011a; Caire et al., 2008b), where the authors exploit the sparsity of noise in the time domain using null/pilot tones in the frequency domain. The authors of (Lin et al., 2013) extended the work of (Lampe, 2011a; Caire et al., 2008b) by developing a higher computationally-intensive estimation technique based on sparse Bayesian learning theory. When prior knowledge about the noise's statistical model is available at the receiver, efficient parametric estimators can be used. After noise estimation, direct cancellation (subtraction) is the most widely-used compensation technique (Lin et al., 2013; Caire et al., 2008b). The author in (Lampe, 2011a) compared noise suppression (i.e., nulling the time domain samples) to noise cancellation. Cancellation requires instantaneous estimation of the noise samples and achieves better performance when these estimates are reliable. However, cancellation may lead to bad performance for unreliable noise estimates due to increased noise variance. On the other hand, noise suppression does not require instantaneous noise samples estimates since only the locations of the high-noise samples are needed. The benefit of suppression is the robustness in case of an unreliable impulsive noise estimate.

The second category of impulsive noise mitigation techniques is channel coding performance enhancements mainly through erasure decoding. Erasure decoding was used with the Reed-Solomon (RS) decoder to mitigate burst noise for deep space communications in (Pollara, 1987; Pitt III and Swanson, 1985) and later to mitigate impulsive noise for digital subscriber lines (DSL) in (Toumpakaris et al., 2004; Mahadevan et al., 2008). The authors in (Toumpakaris et al., 2004) used erasure decoding to reduce the interleaver latency. Joint erasure marking and Viterbi decoding was proposed in (Li et al., 2008). As in the signal suppression scenario, a key advantage of erasure decoding is that it does not require estimation of the instantaneous noise samples. It is sufficient to determine the locations of the high noise samples (which are also likely to be the error sample locations). Different methods were proposed in the literature to mark erasures to the decoder. Reliability metrics for the received bits can be used to locate the error samples as proposed in (Viterbi, 1982) and used with some variations in (Pollara, 1987; Pitt III and Swanson, 1985; Toumpakaris et al., 2004; Mahadevan et al., 2008). Using the RS output errors (syndrome checking) and marking the adjacent symbols in the interleaver (looping) as erasures was also proposed by (Pitt III and Swanson, 1985) for deep space communications and later proposed by (Toumpakaris et al., 2004) for DSL.

Prior work on mitigating SISO cyclostationary impulsive noise in OFDM systems includes (Lin et al., 2013), (Lin et al., 2015) and (Shlezinger and Dabora, 2014). In (Lin et al., 2013), time-domain block interleaving/de-interleaving is proposed to spread the noise bursts into short impulses, over multiple OFDM symbols, that can be estimated using sparse recovery techniques. In particular, the authors in (Lin et al., 2013) propose a sparse Bayesian learning algorithm to estimate the instantaneous noise samples. However, such sample-level time-domain interleaving involves storing the continuous-valued time-domain signal which requires considerably larger memory than the bit-level frequency-domain interleaving (Lin et al., 2015). In (Lin et al., 2015), the authors proposed a time-frequency modulation diversity scheme that exploits the diversity provided by the periodically-varying and spectrally-shaped cyclostationary noise in NB-PLC. In particular, the modulation diversity scheme jointly modulates multiple symbols using higher-dimensional signal constellations, and transmits components of each signal point over different sub-channels. In (Shlezinger and Dabora, 2014), the authors proposed a FRESH filtering based SISO receiver to exploit the cyclostationary properties of both the NB-PLC noise and the OFDM signal. Specifically, the receiver architecture in (Shlezinger and Dabora, 2014) consists of two FRESH filtering stages in series. The first FRESH filtering stage is utilized for extracting the cyclostationary NB-PLC noise, which is followed by noise subtraction from the received signal. The second FRESH filtering stage is used to recover the OFDM signal by exploiting its cyclostationary properties due to the redundancy in the cyclic prefix (CP) of the OFDM blocks. However, the proposed two-stage FRESH filtering in (Shlezinger and Dabora, 2014) is suboptimal in the sense that it separates cyclostationary noise estimation and cancellation from OFDM signal estimation.

1.4 Broadband Powerline Communications

Indoor BB-PLC is mainly used for home area networks that interconnect smart appliances with smart meters for energy consumption profiling and control. Broadband PLC standards such as IEEE P1901.1 (IEEE P1901.2, 2013) and ITU-T G.hn (Oksman and Zhang, 2011) adopt orthogonal frequency division multiplexing (OFDM) in the 1.8–250 MHz frequency band. In-home PLC systems suffer from impulsive noise because of sudden voltage changes caused by on-off switching of in-home appliances and power electronics devices such as silicon-controlled rectifiers, switching regulators, and brush motors (Ferreira et al., 2010). In addition, uncoordinated interference from noninteroperable neighboring PLC modems is shown to be asynchronous impulsive noise in nature (Galli et al., 2011). Different statistical models have been proposed to fit the impulsive noise data in the BB-PLC such as Middleton's

Class A, Nakagami-m, and Rayleigh, Gaussian mixture and Middleton distributions (Chan and Donaldson, 1989; Meng et al., 2005; Bert et al., 2011; Nassar et al., 2011).

Similar to NB-PLC, to mitigate the impulsive noise in the BB-PLC, both suppression and cancellation techniques can be used. Specific work studies for noise analysis and mitigation in BB-PLC including (Lampe, 2011b; Ma et al., 2005).

1.5 Multi-Input Multi-Output (MIMO) Powerline Communications

To achieve higher data rates without the need to increase the transmit power or bandwidth, MIMO schemes have been thoroughly investigated for wireless (Diggavi et al., 2004) and digital subscriber line (DSL) (Ginis and Cioffi, 2002) communications.

MIMO PLC is a promising technology to increase the data rate and/or provide robustness against impulsive noise encountered in PLC environments (Lampe, 2016; Berger et al., 2014; Hashmat et al., 2010). Unlike wireless transmission, possible MIMO configurations in PLC systems are limited by the maximum number of physically available ports. MIMO schemes have been efficiently integrated with OFDM for PLC using space-time/frequency codes (Hao and Guo, 2007) or spatial multiplexing (Schwager et al., 2011), but focusing mainly on in-home and BB-PLC applications (ITU-T G.9963, 2015). Moreover, impulsive noise mitigation for MIMO broadband PLC was studied in (Liu et al., 2016).

In NB-PLC, the data rate enhancement achieved by MIMO over medium voltage powerlines is investigated in (Papadopoulos et al., 2017; Chrysochos et al., 2016a). The MIMO channel of overhead and underground (UG) low voltage (LV) and MV broadband powerline networks are investigated in (Lazaropoulos, 2013) based on modal analysis. For UG LV powerline networks, the main focus has been on the performance of SISO NB-PLC channel characteristics (Cataliotti et al., 2008) or SISO OFDM designs for BB-PLC as in (Anatory et al., 2009). The application of MIMO to MV NB-PLC overhead networks is investigated in (Chrysochos et al., 2016b) where the transmit energy budget and bit loading across the

OFDM sub-channels are optimized to maximize MIMO-OFDM achievable data rates. The work in (Chrysochos et al., 2016b) is extended in (Chrysochos et al., 2015) to investigate MIMO-OFDM transmission through distribution transformers. To the best of the author's knowledge, MIMO-OFDM transmission has not been investigated for NB-PLC MV UG networks.

1.5.1 Unlicensed Wireless Communication System for Smart Grid Applications

Initially, cellular communications was the main wireless communication system used for smart meters communications application. The main drawback of cellular technologies is the high running cost of leasing networks/services from the carriers. Later, wireless mesh networks gained much attention as a low-power/low-priced solution for the application of smart metering communications. International standards for mesh networks include IEEE 802.15.4 O-QPSK (used by Zigbee, Z-wave, Thread, etc.), IEEE 802.11ah (IEEE 802.11ah, 2016) and IEEE 802.15.4g (IEEE 802.15.4g, 2012). Specifically, to connect smart meters to data concentrators, ZigBee technology was used to deliver $20-250$ kbps in the frequency bands around 868 MHz, 915 MHz or 2.4 GHz over a distance of $10-200$ m. Moreover, wireless smart utility networks (Wi-SUN) in the frequency band of 450 MHz-2.4 GHz, based on the IEEE 802.15.4g standard, provide different data rates to support low-power indoor communications between smart meters and smart appliances. Furthermore, the IEEE 802.11ah standard supports a few hundred kbps data rates over 200 meters in the sub-1 GHz unlicensed frequency bands targeting smart metering applications. Broadband wireless local area network (WLAN) standards such as IEEE 802.11n also adopt OFDM in the 2.4 GHz and/or 5 GHz unlicensed frequency bands.

The main challenge for wireless communications over unlicensed frequency bands is the existence of strong interference caused by uncoordinated transmissions. Specifically, neighboring devices based on different standards running in the same frequency band cause interference to each other. Different models have been proposed to capture the interference statistics due to the uncoordinated wireless transmissions in the unlicensed frequency bands including the Gaussian mixture (GM), Middleton Class-A (MCA), symmetric alpha stable ($S\alpha$S), and Partitioned Markov Chain (PMC) models (Nassar et al., 2008; Saaifan and Henkel, 2017; Blackard et al., 1993; Sacuto et al., 2014). We refer to the interference in the unlicensed wireless system as narrow-band interference (NBI).

1.6 Hybrid PLC/Wireless Systems

To enhance communication reliability, a hybrid PLC-wireless communication system simultaneously transmits OFDM symbols over the PLC and WLAN channels followed by joint processing of both received signals to exploit the independence of the interference and channels characteristics of the two physical media. Unlike channel fading and interference in receive-diversity-based wireless communication systems which typically follow the same statistical distributions on all receive branches, channel fading and interference distributions are different for the PLC and wireless receive branches.

Hybrid wireless and PLC systems are studied in (Guzelgoz et al., 2010; Lai and Messier, 2012; Lai et al., 2014; Lee and Kim, 2014) for broadband communications and in (Sebaali and Evans, 2015; Sayed and Al-Dhahir, 2014; Sayed et al., 2015; Sayed et al., 2017; Sayed et al., 2017; Sayed and Al-Dhahir, 2016) for narrowband communications. In (Guzelgoz et al., 2010; Lai and Messier, 2012; Lai et al., 2014), the performance of maximum ratio combining, selection combining and other receiver combining schemes are analyzed. Both (Lai and Messier, 2012) and (Lai et al., 2014) assume that the noise in the PLC link follows a Middleton Class-A model and the noise in the wireless link is additive white Gaussian noise (AWGN), while the authors of (Guzelgoz et al., 2010) assume that the noise in both the PLC and wireless links is AWGN. Using relaying in wireless and PLC networks is investigated in (Lee and Kim, 2014) under the AWGN model for the wireless link.

1.7 Contributions

The key contributions of this dissertation can be summarized as follows,

1. We propose a cyclostationary noise model for SISO narrowband power line communication (NB-PLC) based on frequency-shift (FRESH) filtering.

    - The FRESH filters are designed to shape an input white noise spectrum to a cyclic spectrum extracted from experimental noise measurements.
    - The noise modeling problem is formulated as a system identification problem that minimizes the time-averaged mean square error (TA-MSE) between a reference measured noise and the model generated noise.
    - We propose the normalized mean square error (NMSE) in the cyclic auto-correlation between the measured and the generated noise as a performance measure.

2. We propose a cyclostationary noise model for multi-input multi-output (MIMO) narrowband power line communication (NB-PLC) based on frequency-shift (FRESH) filtering.

    - The MIMO FRESH filters are designed to shape a multi-input white noise spectrum to a muti-output cyclic spectrum extracted from experimental noise measurements of three-phase low-voltage power lines.
    - The noise modeling problem is formulated as a system identification problem that minimizes the time-averaged mean square error (TA-MSE) between a reference measured noise waveform and the model-generated noise waveform.
    - We propose the normalized mean-square-error (NMSE) for both the cyclic auto-correlation and cyclic cross-correlation between the measured and the generated noise waveforms as a performance measure.

3. We exploit the cyclostationarity of the NB-PLC to accurately estimate the cyclostationary noise's power spectral density in each of its temporal regions and use it to enhance the Viterbi and/or Reed-Solomon decoder performance by employing erasure decoding. In addition, the high spatial correlation is exploited to mitigate cyclostationary noise effects through erasure decoding.

4. We propose a temporal-region-based LMMSE signal estimation technique that operates in the frequency domain (FD) and exploits the noise PSD and spatial correlation per OFDM subchannel across the different receive phases.

   - We propose simple and efficient estimation techniques for both the noise PSD and the FD per-subchannel noise cross-correlation across the different receive phases.
   - We develop a novel practical temporal noise region boundary detection algorithm.

5. We propose two SIMO FRESH-filtering-based LMMSE cyclostationary signal detection techniques that operate in the time domain (TD), namely, time domain noise filtering (TD-NF) and time domain equalization and noise filtering (TD-ENF). The two techniques have different performance/complexity tradeoffs and achieve considerable performance gains over a SISO receiver.

   - We utilize a single-stage FRESH filter that includes the cyclic frequencies of both the NB-PLC noise and the OFDM information signal.
   - The proposed SIMO FRESH-filtering approach exploits the joint cyclostationarity of the received signals across the receive phases by considering their cyclic auto-correlations and cyclic cross-correlations. To the best of our knowledge, neither SIMO cyclostationary noise mitigation nor SIMO FRESH filtering were studied before in the literature.

- We derive the optimal SIMO LMMSE FRESH filter-based estimator for the two TD-based techniques and their associated mean square errors (MSEs). Based on the optimal estimators, we propose suboptimal practical implementations for the two techniques that minimize the time-averaged MSE (TAMSE). Furthermore, we study the applicability of both techniques to coherent and differential modulation schemes and their channel state information (CSI) knowledge requirements.
- In the proposed TD-ENF technique, we introduce the SIMO FRESH TD equalization, which jointly equalizes the channel and filters out the noise. It is worth mentioning that SIMO FRESH TD equalization has not been studied in the literature.
- For the proposed TD-based techniques, we compare multiple approaches for the design of the FRESH filter including the selection of the number of branches as well as the number of taps per branch.

6. We study the performance/complexity tradeoffs for the noise mitigation techniques in terms of the achieved MSE, the average bit-error rate (BER) performance and the implementation complexity.

7. We test our proposed techniques based on data collected from actual field noise and channel measurements for SIMO NB-PLC.

8. We investigate novel approaches for joint NBI and IN mitigation in OFDM-based hybrid PLC-wireless transmissions by exploiting the inherent sparsity of the NBI and IN signals in the frequency and time domains, respectively.

    - We develop a novel sparsity-based framework to jointly mitigate non-contiguous and contiguous NBI and IN in hybrid PLC-wireless communication systems by exploiting the NBI and IN inherent sparsity in the time and frequency domains.

- We utilize prior knowledge of the sparsity level across different receive ports and propose a multi-level orthogonal matching pursuit (OMP) algorithm for non-contiguous NBI and IN signals.
- To improve the estimation accuracy of asynchronous NBI, we apply a time-domain windowing to the received signal to enhance the asynchronous NBI's sparsity.
- We investigate sparsity-based mitigation algorithms under different assumptions that exploit the bursty structure of contiguous NBI and IN for NBI and IN estimation. Assuming known bursts' boundaries (block sparse case[2]), we investigate the use of the block orthogonal matching pursuit (BOMP) algorithm (Eldar et al., 2010). Without this knowledge, we study another sparsity-based mitigation algorithm which was proposed in (Cevher et al., 2009).
- We exploit prior knowledge of NBI and IN second-order statistics and quantify the performance gains of a Bayesian linear minimum mean square error estimator (LMMSE) over the conventional least-squares estimator for contiguous and non-contiguous NBI and IN.
- We exploit the spatial correlation across the receive ports (either antennas or wires) for the wireless or PLC links to convert the non-contiguous NBI and IN recovery problem to a block sparse signal recovery problem. Then, we propose a multi-level BOMP recovery algorithm for the case of different NBI and IN burst sizes. The proposed multi-level BOMP algorithm is less complex and enjoys a performance advantage over the OMP algorithm.
- We compare the NBI and IN mitigation performance in the case of joint and separate processing of PLC and wireless received signals and demonstrate the

[2]The term *bursts* is used in this dissertation when the bursts' boundaries are unknown, while the term *block* is used for the case of known bursts' boundaries.

superiority of the former over the latter for a wide span of NBI and IN power levels.

9. We investigate the applicability of MIMO NB-PLC designs to MV UG cable networks. To the best of the author's knowledge, MIMO-OFDM transmission has not been investigated for NB-PLC MV UG networks.

   - Different SISO/MIMO configurations incorporating both cable conductors and sheaths are presented. Specifically, for the SISO case, we evaluate the conductor-sheath, conductor-conductor and sheath-sheath signal injections. For the MIMO case, the applicability of 2x3, 3x3, 4x6 and 5x6 configurations are systematically examined.
   - The achievable data rates are evaluated for all configurations, while the bit loading is optimized across the spatial information streams for all frequency sub-channels subject to the standard-defined transmit power spectral density (PSD) constraint. In addition, the desired target error rate and performance margin are guaranteed in all cases. The optimization of bit-loading and transmit energy allocation are done jointly based on the concept of incremental energy (Cioffi, b) that yields an integer number of bits so that the data rate projections are more realistic.
   - Our evaluation of the performance of MIMO NB-PLC is based on transmission PSD levels and frequency bands as specified in the international standards such as the recently revised ITU-T recommendation G.9901 (ITU-T G.9901, 2017).
   - The impact of the MV line length and coupler loss on the MV channel spatial-spectral characteristics is analyzed.
   - We evaluate the channel impulse response (CIR) based on the channel transfer functions. Moreover, we calculate the channel root mean square delay spread

(RMS-DS) and analyze the cyclic prefix (CP) design trade-offs for the different signal injections configurations.

- The data rate gain of MIMO over SISO systems comes at the price of increased implementation complexity and cost of couplers. Therefore, we compare the implementation complexity of the different proposed MIMO configurations in terms of the required number of multiplications. In addition, we show how to reduce the transceiver processing complexity while minimizing the data rate loss from the full-complexity scenario. Moreover, for complexity-constrained NB-PLC systems, we quantify the effect of the bit cap on the achievable data rate.

1.8 Organization

This dissertation is organized as follows,

In Chapter 2, the system model assumptions for the NB-PLC including the channel and noise models are described. In addition, the system simulation parameters are specified.

In Chapter 3, we present and discuss our proposed FRESH-filtering-based noise modeling for SISO and MIMO NB-PLC.

In Chapter 4, we investigate the erasure decoding techniques to mitigate the cyclostationary noise effect in NB-PLC. Since the NB-PLC standard offers a concatenated convolutional and Reed-Solomon channel coding mode, we test the erasure decoding for both the Viterbi and Reed-Solomon decoders and propose different ways to mark the erasures.

In Chapter 5, the temporal-region-based cyclostationary noise mitigation is introduced for both SISO and SIMO schemes. Based on a prior estimation for per sub-channel noise statistics, the proposed technique employs a per sub-channel LMMSE estimator in the frequency domain to estimate the information signal. We exploit the noise cyclostationarity to estimate the per sub-channel noise statistics assuming noise stationarity per temporal region.

In Chapter 6, FRESH-filtering-based cyclostationary noise mitigation is proposed for both SISO and SIMO schemes. A single stage FRESH filter is used to exploit the cyclostationarity of the OFDM signal as well as the cyclostationary noise. We show that this single stage is the optimal solution for this estimation problem. Moreover, the FRESH filter structure is extended in the spatial domain to support the SIMO case. In addition, we propose a simpler FRESH filtering technique that implements a joint noise cancelation and channel equalization. Finally, the performance and complexity for all proposed techniques, including the temporal-region-based technique (proposed in Chapter 5), are analyzed and compared to existing techniques in the literature.

In Chapter 7, we investigate how to achieve additional diversity dimensions by simultaneously transmitting over PLC and wireless links. In addition, we propose using compressed sensing techniques to jointly mitigate the PLC's impulse noise and the wireless link's narrowband interference.

In Chapter 8, we investigate how to increase the data rate by employing MIMO transmission over medium voltage narrowband underground network. We analyze different input-output injection configurations and calculate the achievable data rates for every configuration. Moreover, we discuss different practical implementation issues and complexity reduction methods.

In Chapter 9, we conclude our contributions and propose future research extensions.

Notation: Unless otherwise stated, lower and upper case bold letters denote vectors and matrices, respectively. $\mathbb{R}$ denotes the set of real numbers, $\mathbb{Z}$ denotes the set of integer numbers and $\mathbb{Z}^+$ denotes the set of non-negative integer numbers. $\mathbb{E}\{\cdot\}$ denotes statistical expectation. $\langle\cdot\rangle_n$ denotes the discrete time-average operator with respect to n. $\langle\cdot\rangle_{n,P}$ denotes the discrete time-average operator over P samples. diag$\{.\}$ forms a diagonal matrix with the input vector on the main diagonal. $(\cdot)^*$ denotes the complex-conjugate operation. $(\cdot)^\top$ denotes the transpose operation. $(\cdot)^H$ denotes transpose, and complex-conjugate operations.

$[\cdot]_{k,l}$ denotes the (k,l)-th entry of a matrix, $[\cdot]_k$ denotes the k-th entry of a vector. $(\cdot)^{-1}$ is the inverse of the matrix between the brackets. $\mathbf{1}_{\mathcal{A}}$ is an indicator function where $\mathbf{1}_{\mathcal{A}} = 1$ if the event $\mathcal{A}$ is true and 0 otherwise. The l_0 norm of a vector $\mathbf{a}$ is denoted by $\|\mathbf{a}\|_0$ which counts the number of non-zero elements of the vector $\mathbf{a}$. Finally, $\|\mathbf{a}\|_1$ and $\|\mathbf{a}\|_2$ denote the l_1 norm and l_2 norm of the vector $\mathbf{a}$, respectively, while $\|\mathbf{A}\|$ denotes the spectral norm of the matrix $\mathbf{A}$ and is given by $\max_{\mathbf{x}:\mathbf{x}\neq 0} \|\mathbf{A}\mathbf{x}\|_2 / \|\mathbf{x}\|_2$.

CHAPTER 2

PLC SYSTEM MODEL AND BACKGROUND

2.1 Noise and Channel Models for LV NB-PLC

The key variables used in this chapter are summarized in Table 2.1.

As shown in Fig. 2.1, for low-voltage (LV) power lines, the transmit/receive links can in general be: phase A to the neutral, phase B to the neutral and phase C to the neutral. At the receiver side, the receive phases are subject to interference from the other phases. In this dissertation, we consider a SIMO communication scenario where only a single phase is utilized for transmission (phase A) while two or three phases ($N_p = 2, 3$) can be utilized for reception. Hence, our goal is to enhance the communication reliability by exploiting the high spatial correlation of the noise across the receive phases to mitigate their effects. Moreover, adopting the SIMO scenario does not require any standard changes since all modifications are at the receiver side only. Considering OFDM transmission, the TD SIMO received signals over the receive power line phases can be written as follows

$$y_i(n) = x_i(n) + \zeta_i(n),\ i \in \{0,\, 1,\, \cdots,\, N_p - 1\},\ \forall n \in \mathbb{Z}, \tag{2.1a}$$

$$x_i(n) = \sum_{m\in\mathbb{Z}} h_i(n-m)d(m). \tag{2.1b}$$

It is worth mentioning that all the TD signals in (2.1a) and (2.1b) are real signals since the NB-PLC signal transmission is in the baseband. The i-th phase of the FD SIMO received signals at the k-th sub-channel of the l-th OFDM symbol can be expressed as follows

$$\begin{aligned}\bar{y}_{i,l}(k) = \bar{h}_{i,l}(k)\bar{d}_l(k) + \bar{\zeta}_{i,l}(k),\ i \in \{0,\, \cdots,\, N_p - 1\}& \\ ,\ k \in \{0,\, \cdots,\, N_{sc} - 1\},\ \forall l \in \mathbb{Z}^+.&\end{aligned} \tag{2.2}$$

Next, we describe the NB-PLC noise and channel models assumed in this dissertation.

Table 2.1: Key variables used throughout the chapter

Variable	Definition	Variable	Definition
N_p	The number of receive phases	$h_i(n)$	The CIR corresponding to the i-th receive phase
$y_i(n)$	The TD received signal over the i-th phase	$\bar{y}_{i,l}(k)$	The i-th branch FD received data symbol over the k-th OFDM subchannel at the l-th OFDM block
$x_i(n)$	The TD transmitted signal convolved with the CIR corresponding to the i-th receive phase	$\bar{d}_l(k)$	The FD transmitted data symbol over the k-th OFDM subchannel at the l-th OFDM block
$d(n)$	The TD transmitted signal	$\bar{\zeta}_{i,l}(k)$	The i-th branch FD noise over the k-th OFDM subchannel at the l-th OFDM block
$\zeta_i(n)$	The TD noise observed at the i-th receive phase	$\bar{h}_{i,l}(k)$	The i-th branch FD channel over the k-th OFDM subchannel at the l-th OFDM block
N_{SC}	The number of FD OFDM subchannels	N_B	The number of samples per TD OFDM block including the cyclic prefix
N_{CP}	The OFDM cyclic prefix length	P_ζ	The cyclostationarity period of the NB-PLC noise

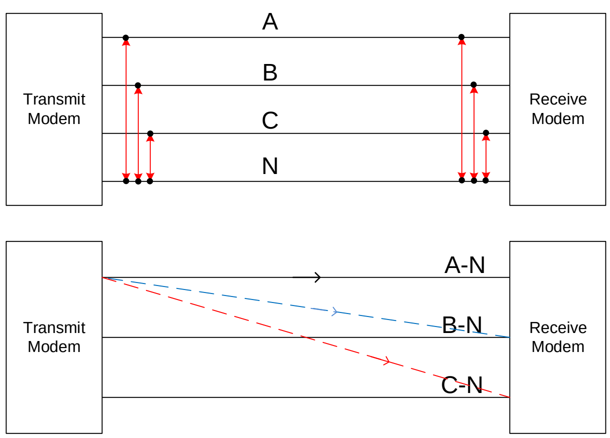

Figure 2.1: SIMO PLC configuration.

2.1.1 Cyclostationary NB-PLC Noise Models

In this section, we discuss the different approaches for cyclostationary noise modeling in NB-PLC that we use in to test our proposed mitigation techniques.

In particular, we simulate our proposed cyclostationary noise mitigation techniques mainly using the SISO/SIMO models proposed in (Elgenedy et al., 2016; Elgenedy et al., 2016). In addition, we use the SISO temporal-region-based model in (Nassar et al., 2012) to test our erasure decoding techniques. Moreover, we generalize the SISO temporal-region-based model in (Nassar et al., 2012) to the SIMO case. The generalized SIMO temporal-region-based noise model is mainly used in testing the cyclostationary noise spatial correlation effect on the receiver performance. In the following, we briefly describe the FRESH-filter-based noise modeling approach proposed in (Elgenedy et al., 2016; Elgenedy et al., 2016) for both SISO and SIMO cases. In addition, we describe the temporal-region-based SISO noise modeling in (Nassar et al., 2012) together with our SIMO generalization for it.

FRESH-Filtering-Based (FFB) NB-PLC Noise Model

In (Elgenedy et al., 2016), the cyclostationary noise modeling problem is formulated as a linear periodic time variant (LPTV) system identification problem. The LPTV is designed such that minimizes the TAMSE between a reference measured noise signal d and the model-generated noise signal ζ. The SISO LPTV filter is implemented using FRESH filter $\boldsymbol{h}$ which is given by

$$\boldsymbol{h} = \overline{\mathbf{R}}_{\mathbf{zz}}^{-1}\overline{\mathbf{r}}_{\mathbf{z}d}, \tag{2.3}$$

where $\overline{\mathbf{r}}_{\mathbf{z}d}$ denotes the time-averaged cross-correlation vector between the desired signal and the frequency-shifted input vector, and $\overline{\mathbf{R}}_{\mathbf{zz}}$ denotes the time-averaged auto-correlation matrix of the frequency-shifted input vector. The input excitation n is a zero-mean white Gaussian signal. However, in computing both $\overline{\mathbf{r}}_{\mathbf{z}d}$ and $\overline{\mathbf{R}}_{\mathbf{zz}}$, the input is assumed to be a noisy version of the desired signal under a very low SNR assumption.

In (Elgenedy et al., 2016), a generalization of the SISO FRESH-filtering-based noise model in (Elgenedy et al., 2016) to the SIMO case is proposed. To generate N_p different noise streams and adjust both the cyclic auto and cross-correlation functions, N_p^2 different FRESH filters are needed. The filter structure for $N_p = 2$ is shown in Fig. 2.2 where

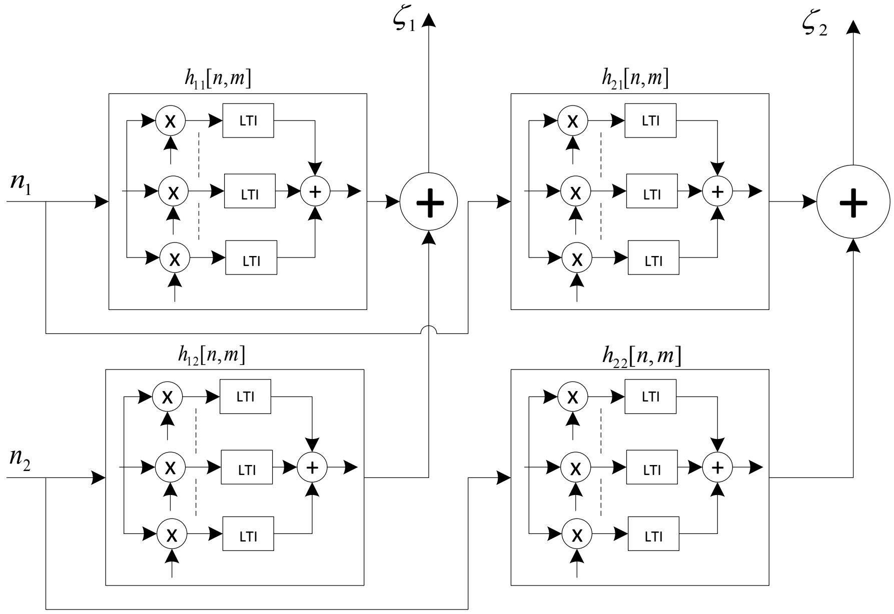

Figure 2.2: FRESH filter based (FFB) multiple-phases cyclostationary noise modeling structure, $N_p = 2$ (Elgenedy et al., 2016).

filter coefficients can be generated using Equation (2.3). In this case, $\boldsymbol{h}$ represents the filter coefficients matrix in which the first column is a concatenation of $\boldsymbol{h}_{11}$ and $\boldsymbol{h}_{12}$ while the second column is a concatenation of $\boldsymbol{h}_{21}$ and $\boldsymbol{h}_{22}$. The input excitation signal consists of two independent white Gaussian signals $n_1$and n_2. In computing $\overline{\mathbf{r}}_{\mathbf{z}d}$ and $\overline{\mathbf{R}}_{\mathbf{zz}}$, the input signal is assumed to be a noisy version of a concatenated vector of the two desired streams under a very-low-SNR assumption. The time-averaged cross-correlation $\overline{\mathbf{r}}_{\mathbf{z}d}$ is a matrix in which the first column represents the cross-correlation vector between the input and the first desired stream $\overline{\mathbf{r}}_{\mathbf{z}d_1}$, while the second column is the cross-correlation between the input and the second desired stream $\overline{\mathbf{r}}_{\mathbf{z}d_2}$.

Temporal-region-based (RB) NB-PLC Noise Model

We start by briefly describing the noise model presented in (Nassar et al., 2012). In that model, the cyclostationarity period of the NB-PLC noise is divided into N_R temporal regions

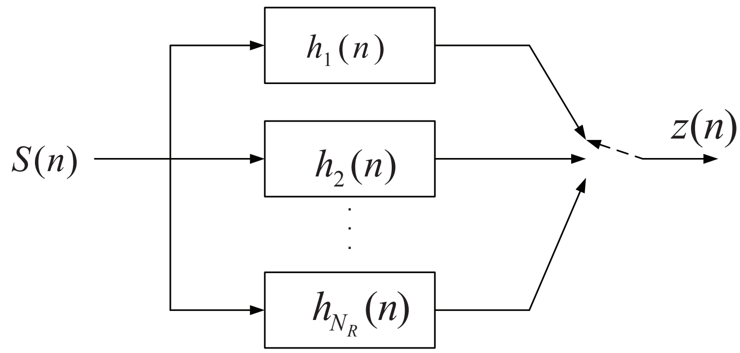

Figure 2.3: NB-PLC cyclostationary noise model

where the noise is assumed stationary within each temporal region. Hence, each temporal region is characterized by a certain PSD and a corresponding shaping filter. The noise PSD over each temporal region is estimated from the noise data collected from field measurements. The noise generation can be implemented by feeding a white Gaussian input signal n to an LPTV filter that is realized using a bank of N_R LTI filters followed by multiplexing over their outputs. A block diagram for the cyclostationary noise generation over one period is depicted in Fig. 2.3, where the noise is assumed to be partitioned into three temporal regions within each the noise is a stationary Gaussian random process characterized by a particular PSD.

The PSDs for the filters used in the simulations are shown in Fig. 2.4 where the ratio of the average noise powers over the three regions are $-6.59 : 1.93 : 5.15$ dB, respectively. The time spans of the three regions are around 5, 2 and 1.3 ms, respectively as shown in Fig. 2.5.

To generalize an RB single-stream noise model to a multiple-stream noise generator, additional filters are needed to adjust the cross-correlation functions between the different noise streams. According to the basic assumption of the RB model, namely the stationarity assumption per temporal region, the cross-correlation function should be constant in each region. If the temporal regions of the different noise streams are aligned, the number of cross-correlation functions needed is equal to N_R. However, if the temporal regions of the different noise streams are not aligned, the number of needed cross-correlation functions may

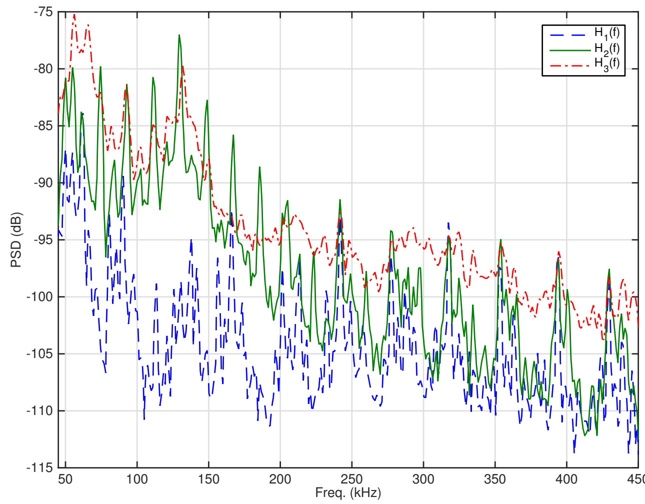

Figure 2.4: Noise region's PSD

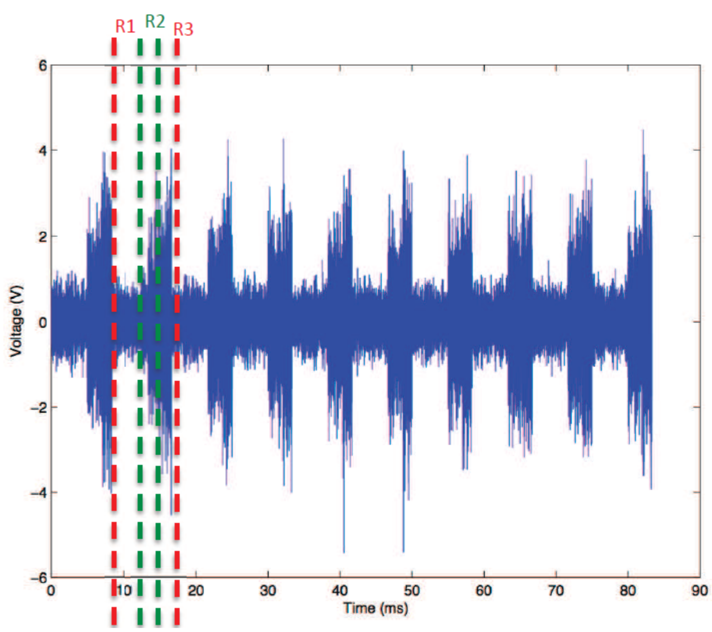

Figure 2.5: NB-PLC noise in time domain

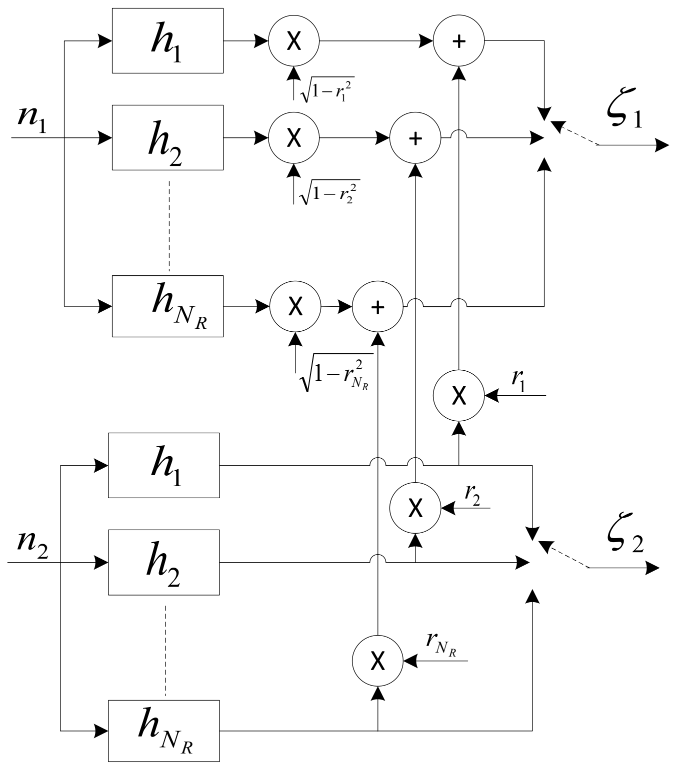

Figure 2.6: NB-PLC region-based (RB) multiple-phases noise model, $N_p = 2$.

increase up to $N_p \times N_R$. Fig. 2.6 shows a generalized structure for the RB noise modeling for the SIMO cyclostationary noise modeling in the case of $N_p = 2$.

For simplicity, we introduce a constant cross-correlation factor between the different spatial noise streams, i.e., $r_1 = r_2 = ... = r_{N_R}$. As it will be shown in the numerical results section, the region-based noise model is used mainly to illustrate the effect of the cross-correlation between the different noise streams on the receiver performance. The constant cross-correlation factor for the case of two noise streams is given by

$$\zeta_1 = r.\bar{\zeta}_2 + \sqrt{1-r^2}\bar{\zeta}_1, \ \zeta_2 = \bar{\zeta}_2 \tag{2.4}$$

where ζ_1 and ζ_2 are the generated correlated noise streams with constant cross-correlation factor r, and $\bar{\zeta}_1$ and $\bar{\zeta}_2$ are two independent region-based-generated noise streams.

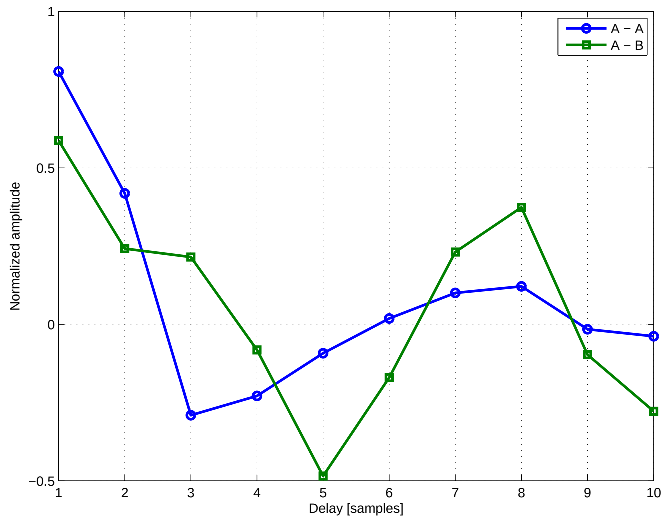

Figure 2.7: Measured CIR for A-A and A-B links.

2.1.2 NB-PLC Channel Model

The NB-PLC channel modeling follows the transmission line modeling approach (Nassar et al., 2012) where the channel is viewed as a deterministic quantity that depends primarily on the network topology and the electrical components connected to it. In this dissertation, we adopt a channel model based on our field measurements for low-voltage (LV) powerlines. In particular, we measured the channel impulse response (CIR) by sending a known periodic training sequence from one end of the powerline and then estimating the CIR from the received signal at the other end.

The CIR was measured by sending a known periodic training sequence (chirp sequence) from phase A and then estimating the CIR from the received signal at phases A and B. The normalized CIRs for the A-A and A-B links are shown in Fig. 2.7. The channel measurements in Fig. 2.7 show that the received signal at phase B is attenuated by 4 dB compared to the received signal at phase A.

2.1.3 NB-PLC System Simulation Parameters

The end-to-end system simulation including the cyclostationary noise modeling and mitigation techniques have been conducted using the **MATLAB® and SIMULINK®** tools. We assumed BPSK transmission in the CENELEC-A frequency band (35.9375 – 90.6250 kHz). The sampling rate is set to 400 kHz. We assume OFDM transmission with FFT size of 256 subchannels and a cyclic prefix of 22 samples. These parameters are chosen to be compliant with the IEEE 1901.2 NB-PLC standard, which also adopts concatenated coding with an inner rate-1/2 convolutional code with constraint length 7 and an outer Reed-Solomon (RS) code of rate 239/255. At the receiver side, a Viterbi decoder with soft decision decoding is implemented. For simplicity, the number of receive phases in the following simulation results is $N_P = 2$.

For the region-based noise model, the number of stationary noise temporal regions is $N_R = 3$ as in (Nassar et al., 2012). Also, we consider two different noise parameter sets that correspond to noise measurements carried out on different PLC network topologies. The first noise parameter set is obtained from the IEEE 1901.2 NB-PLC standard and corresponds to the low-voltage site 14 (LV14); referred to as RB-LV14 in the numerical results section. The second noise parameter set is obtained from the field measurements provided to us by TI; referred to as RB-TI. For the RB-TI noise parameters, the ratios of the average noise powers over the three noise temporal regions are $-6.59 : 1.93 : 5.15$ dB and the ratios of the time spans are $\mathcal{R}_1 = 8/13$, $\mathcal{R}_2 = 3/13$ and $\mathcal{R}_3 = 2/13$. Figs. 2.8 and 2.9 show the noise PSD for the three temporal regions for the RB-LV 14 and RB-TI noise parametersets, respectively. For the FRESH-filter-based noise model, the FRESH filter coefficients were generated as in (Elgenedy et al., 2016) using our SIMO/MIMO field noise measurements; referred to as FFB-TI. The number of branches for the FFB-TI model was set to 19 branches while the number of coefficients per each branch was set to 50. Fig. 2.10 shows the FRESH filter coefficients we used to generate the cyclostationary noise waveform for the FFB-TI model.

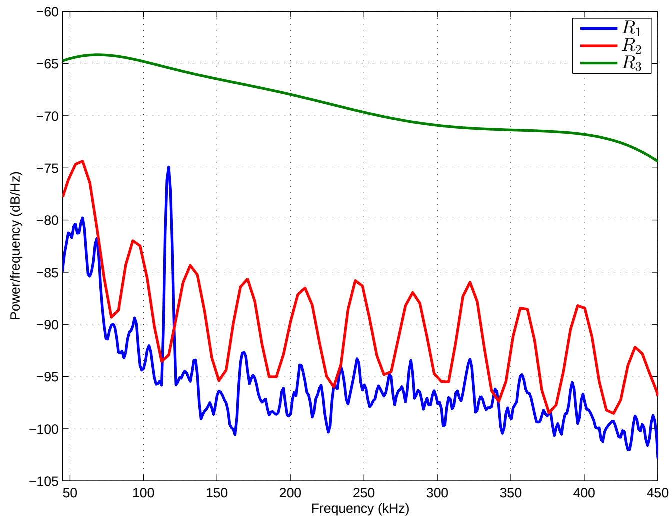

Figure 2.8: RB-LV14 PSD for the three noise temporal regions.

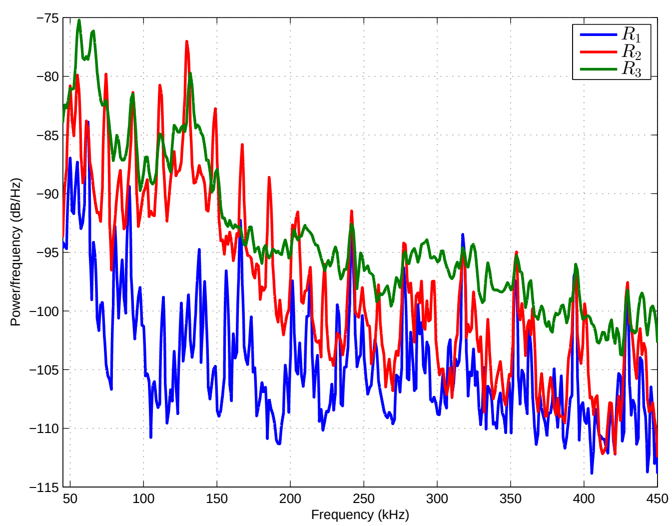

Figure 2.9: RB-TI PSD for the three noise temporal regions.

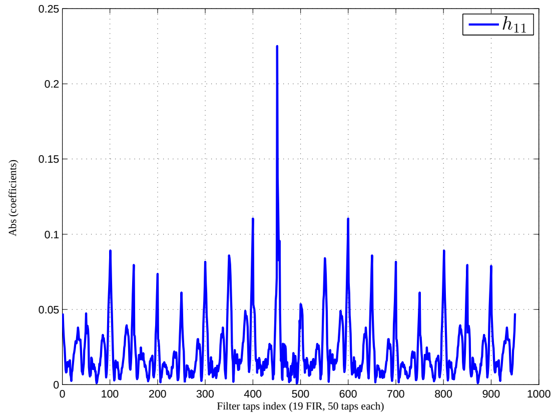

(a) h_{11}

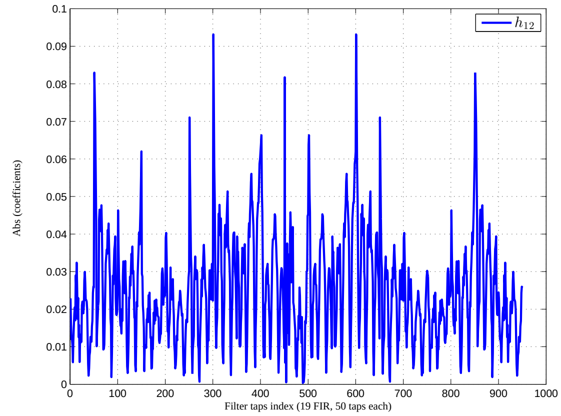

(b) h_{12}

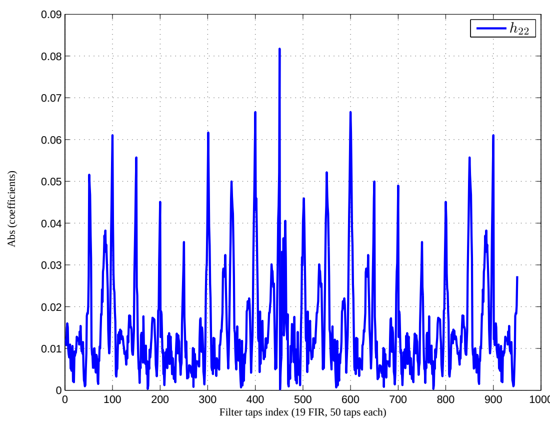

(c) h_{21}

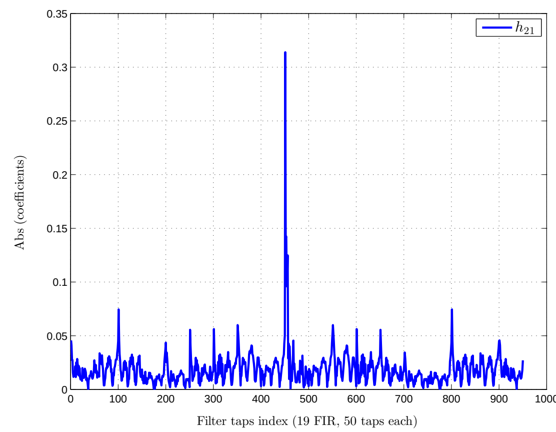

(d) h_{22}

Figure 2.10: FFB-TI noise model FRESH filters coefficients.

CHAPTER 3

CYCLOSTATIONARY NOISE MODELING BASED ON FREQUENCY-SHIFT FILTERING IN NB-PLC [1] [2]

Although the model presented in (Nassar et al., 2012) is computationally tractable and provides a good fitting for the measured NB-PLC noise, it suffers from two main drawbacks. First, the number of stationary temporal regions and the region boundaries are inferred by visually inspecting the measured noise spectrogram and do not rely on a mathematical model. Second, the noise process within each temporal region is generated independently of the other regions which ignores any possible cross-correlation between the different noise processes across the regions. To address the drawbacks in (Nassar et al., 2012), we proposed in (Elgenedy et al., 2016) to synthesize the NB-PLC noise samples using FRESH filtering that is designed to shape an input white noise spectrum to a cyclic spectrum extracted from experimental noise measurements. The model we proposed in (Elgenedy et al., 2016) is expected to be the best fitting model since the filters are shaped based on the cyclic auto-correlation which completely characterizes the cyclostationary signals (Gardner, 1986). The periodicity of the auto-correlation function of a second-order cyclostationary process is completely characterized by its cyclic auto-correlations, and equivalently their frequency-transform counterparts, the cyclic PSDs (Gardner, 1986). Hence, we adopt the cyclic auto-correlation of the generated noise and compare it to that of the measured noise as a metric to evaluate the accuracy of the noise generation model. To the best of our knowledge, a FRESH-

[1]© 2016 IEEE M. Elgenedy, M. Sayed, A. El Shafie, I. H. Kim and N. Al-Dhahir, "Cyclostationary Noise Modeling Based on Frequency-Shift Filtering in NB-PLC," 2016 IEEE Global Communications Conference (GLOBECOM), Washington, DC, 2016, pp. 1-6.

[2]© 2016 IEEE M. Elgenedy, M. Sayed and N. Al-Dhahir, "A frequency-shift-filtering approach to cyclostationary noise modeling in MIMO NB-PLC," 2016 IEEE Global Conference on Signal and Information Processing (GlobalSIP), Washington, DC, 2016, pp. 881-885.

filter-based approach to SISO NB-PLC noise modeling based on actual measurement has not been investigated in the literature.

Moreover, impulsive Noise modeling for MIMO broadband PLC was proposed in (Hashmat et al., 2012a,b). However, to the best of our knowledge, cyclostationary noise modeling for MIMO NB-PLC has not been investigated in the literature. The basic challenge for MIMO cyclostationary noise modeling is to include the cross-correlation between the different phases which is cyclostaionary also.

The periodicity of the auto/cross-correlation function of a second-order cyclostationary process is completely characterized by its cyclic auto/cross-correlations, or equivalently their frequency-transform counterparts know as the cyclic power spectral densities (PSDs) (Gardner, 1986). Therefore, we propose first cyclostationary noise modeling for MIMO NB-PLC in (Elgenedy et al., 2016) based on FRESH filtering. In particular, we adopt the cyclic auto/cross-correlation of the model-generated noise and compare it to that of the measured noise as a metric to evaluate the accuracy of a noise generation model. In this chapter, we synthesize the NB-PLC noise samples using a MIMO frequency-shift (FRESH) filter that is designed to shape a multi-input white noise spectrum to a multi-output cyclic spectrum extracted from experimental noise measurements. For simplicity and without loss of generality, we consider a two-phase MIMO configuration.

3.1 Preliminaries

3.1.1 Cyclostationary Signals Representation

Consider a complex-valued discrete-time process $x[n]$. If both the expected value $\mathbb{E}\left\{x[n]\right\}$ and the auto-correlation function $r_{xx}[n;l]$ of $x[n]$ are periodic with some integer period P such that $\mathbb{E}\left\{x[n]\right\} = \mathbb{E}\left\{x[n+P]\right\}$ and $r_{xx}[n;\ell] = \mathbb{E}\{x[n+\ell]x^*[n]\} = r_{xx}[n+P;\ell]$, the process $x[n]$ is said to be a wide-sense cyclostationary process. Since $r_{xx}[n;\ell]$ is periodic in n, it

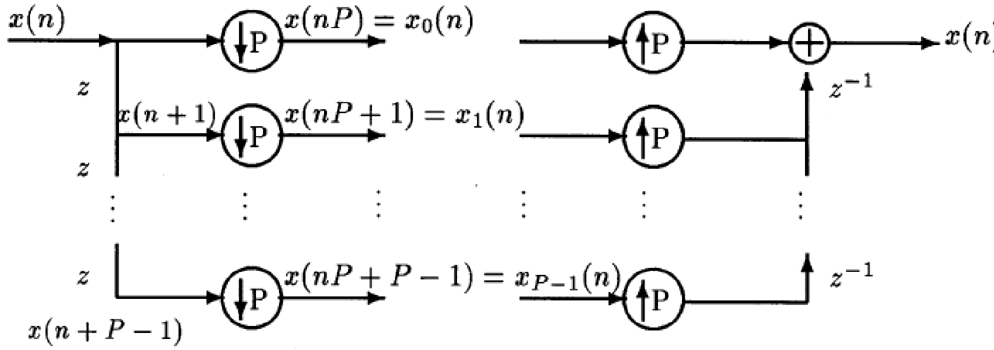

Figure 3.1: Decimated Representation

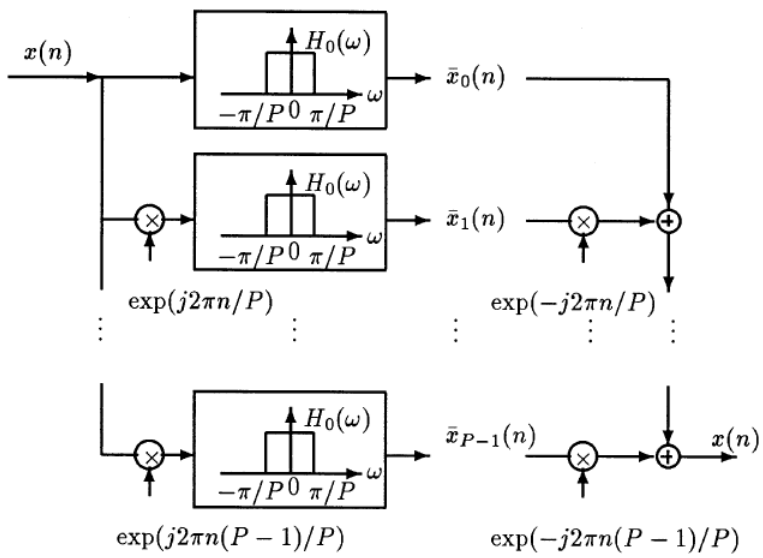

Figure 3.2: Subband Representation

has a Fourier series expansion, whose coefficients, referred to as the cyclic auto-correlation function, are given by

$$r_{xx}^{\alpha_k}\left[\ell\right] = \frac{1}{P}\sum_{n=0}^{P-1} r_{xx}\left[n;\ell\right] e^{-j2\pi\alpha_k n} \tag{3.1}$$

where $\alpha_k = \frac{k}{P}$, $k = 0, 1, \ldots, P-1$ are referred to as the cyclic frequencies.

Two main representations are used to analyze the cyclostationary signals as described in (Gardner, 1986) and (Giannakis, 1998): Decimated Components and Subband Components. In the Decimated Components representation, the cyclostationary process $x[n]$ with a period

P is represented as P different stationary processes $x_i[n] = x[nP + i],\ i = 0, \ldots, P - 1$. In other words, for each time sample, we have a different stationary process. Auto- and cross-correlations for the $x_i[n]$ processes can be computed through the cyclic auto-correlation of $x[n]$. In the Subband Components representation, the cyclostationary process $x[n]$ with a period P is represented as a superposition of P stationary NB subprocesses, where $x[n] = \sum_{m=0}^{P-1} \bar{x}_m[n]\, \mathrm{e}^{-j2\pi mn/P}$. Similarly, the auto- and cross-correlation for $\bar{x}_m[n]$ can be computed from the cyclic auto-correlation of $x[n]$. Note that both methods can be also used for synthesis as shown in Figs. 3.1 and 3.2. Thus, cyclostationary noise modeling can be realized using either one of those two representations but that would entail a high-complexity since we have to implement P stationary processes and set the auto- and cross-correlations for all of them.

The model presented in (Nassar et al., 2012) can be viewed as an approximation for the Decimated Components representation with the assumption that all samples that lie in the same region have the same auto- and cross-correlation properties. Our proposed model does not follow either of the basic two representations although its structure may look similar to the Subband Components representation. However, our proposed model depends mainly on constructing the cyclic frequency components of the cyclic auto-correlation using FRESH filters (Gardner, 1986). As we will show in Section 3.4, this approach will greatly simplify the cyclostationary noise model since in most cases, only few cyclic frequency components, namely the low-frequency components, contain most of the energy.

3.1.2 Frequency-Shift (FRESH) Filtering

The cyclostationary counterpart of linear time-invariant (LTI) filtering is the FRESH filtering. For instance, linear periodic time variant (LPTV) filtering is implemented equivalently in the form of FRESH filtering(Gardner, 1993). Let $h[n, m]$ denote the impulse response of

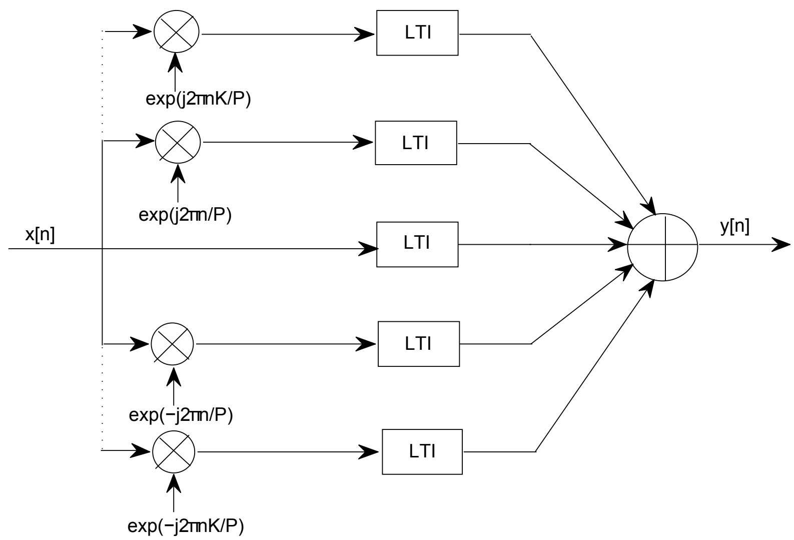

Figure 3.3: FRESH Filtering.

an LPTV filter. The output signal $y[n]$ for input $x[n]$ is given by

$$y[n] = \sum_{m=-\infty}^{\infty} h[n,m]x[m] \tag{3.2}$$

The impulse response $h[n,m]$ is defined as $h[n,m] = \sum_{k=0}^{P-1} \tilde{h}_k[n-m]\mathrm{e}^{-j2\pi\alpha_k m}$, where P is the cyclic period of the LPTV filter $h[n,m]$, $\tilde{h}_k[n]$ is the k-th Fourier series coefficient of $h[n,m]$, and $\alpha_k = \frac{k}{P}$ is the k-th cyclic frequency. The relationship between the input $x[n]$ and the output $y[n]$ of the filter can be therefore written as

$$y[n] = \sum_{k=0}^{P-1} \sum_{m=-\infty}^{\infty} \tilde{h}_k[n-m]x_k[m] \tag{3.3}$$

where $x_k[n] = x[n]\mathrm{e}^{-j2\pi\alpha_k n}$. We observe that the system performs LTI filtering of frequency shifted versions of $x[n]$. Therefore, the FRESH filters can be modeled as an LTI filter-bank applied to the frequency shifted versions of the input signal (Ojeda and Grajal, 2011). Fig. A.1 shows a block diagram for the FRESH filtering.

3.2 Experimental Noise Measurement

Extensive field noise measurements for SISO NB-PLC were conducted in (Nassar et al., 2012; Nassar et al., 2012) by Texas Instruments (TI) and presented in the Appendix of the IEEE

P1901.2 standard (IEEE P1901.2, 2013). Since there is no available field noise measurements for the SIMO case, we conducted experimental noise measurements for the 3-phase SIMO case. The noise measurement setup is shown in Fig. 3.4 for an LV power line cable connected with various loads. The conditions of our SIMO experiment is similar to the substaion-1 conditions in the IEEE P1901.2 standard (IEEE P1901.2, 2013). More details about the map of the sites where the measurements were collected are presented in the IEEE P1901.2 standard (IEEE P1901.2, 2013). Without information signal transmission, we captured the noise over the 3-phase power line cables using an oscilloscope at $F_s = 2.5$ MHz sampling rate. Then, we performed the statistical analysis on a down-sampled version of the measured noise waveform that is sampled at 400 kHz which is one of the sampling rates adopted in the IEEE 1901.2 NB-PLC standard. For this down-sampled version, the noise's cyclostationarity period for a 60 Hz AC cycle is around 3333 samples.

The first step in our statistical analysis was to check the spatial correlation properties between the noise samples over the three phases. The noise spatial cross-correlation is estimated using (39) assuming that the number of noise temporal regions is equal to the number of OFDM symbols per cyclostationary period P_ζ (i.e., assuming that the noise is stationary per OFDM symbol). Fig. 3.5 depicts the absolute value of the noise's spatial cross-correlation in the frequency-domain over the active frequency subchannels across multiple OFDM symbols. It is worth noting that the noise spatial correlation is a periodic function of time with the noise cyclostationary period P_ζ. As evident from Fig. 3.5, the absolute value of the spatial cross-correlation of the multi-stream cyclostationary noise in the SIMO NB-PLC system is generally high (higher than 0.5 for more than 60% of the time and higher than 0.9 for more than 30% of the time). Moreover, Fig. 3.6 shows that the high correlation regions correspond to the high PSD regions which contain most of the noise power. This high spatial correlation for the cyclostationary noise across different phases is expected since the source of the cyclostationary noise is the network-based switched power supplies.

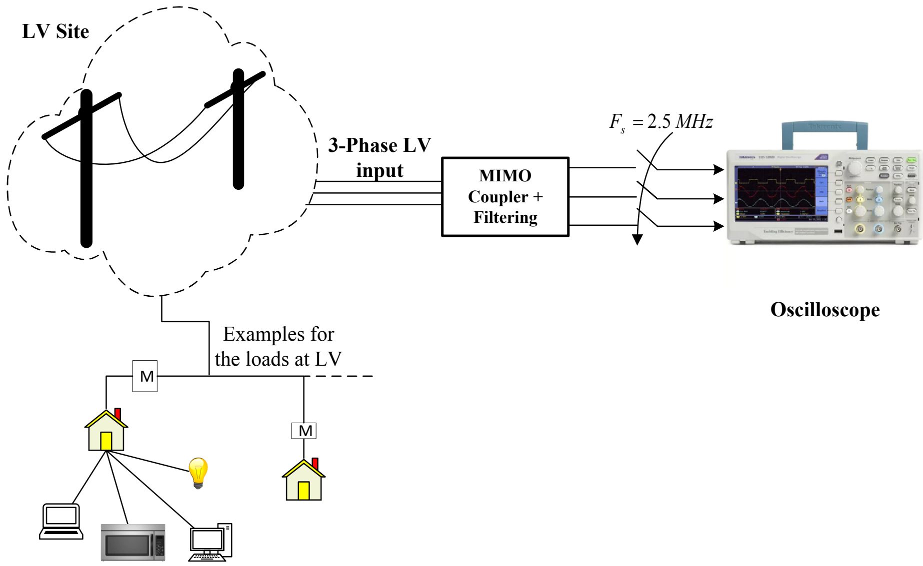

Figure 3.4: Noise and Channel measurements setup.

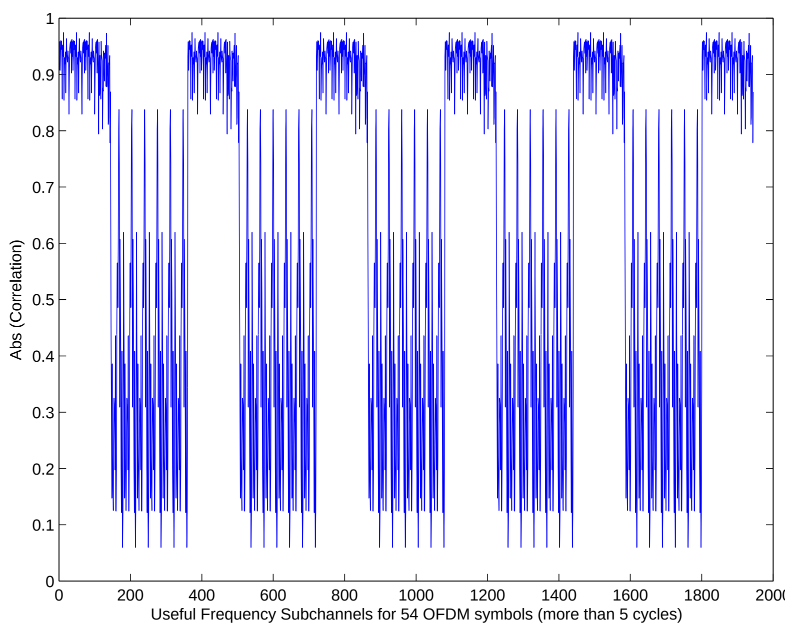

Figure 3.5: Absolute values of the spatial cross-correlation for the cyclostationary noise between phases A and B measured in the frequency domain.

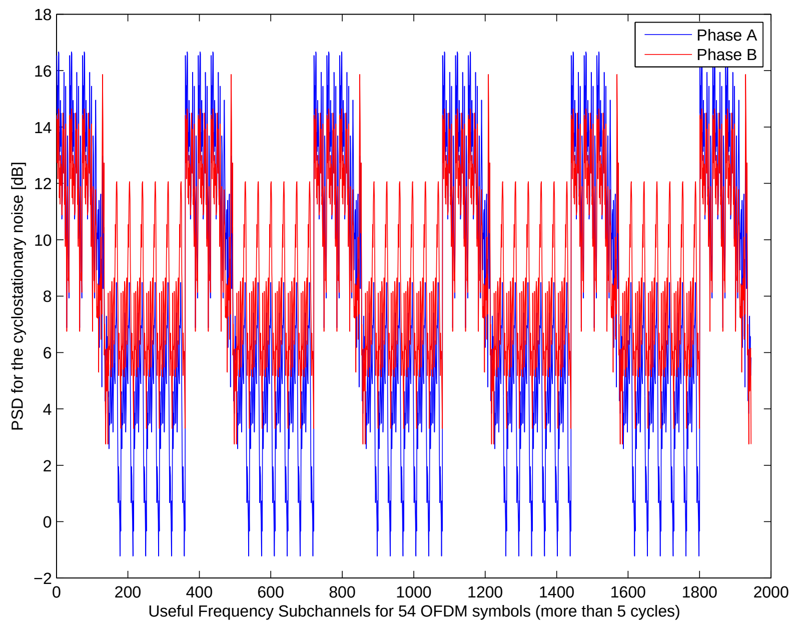

Figure 3.6: PSD for the cyclostationary noise for phases A and B measured in the frequency domain.

3.3 FRESH Filtering-Based Noise Model for SISO NB-PLC

3.3.1 LPTV SISO System Identification

The system identification problem of an LPTV system using measurements of its cyclostationary response to a known input excitation is discussed in (Gardner, 1986). To fit a model for an LPTV system, we solve for the model's time-variant impulse response that minimizes the time-averaged mean-square-error (TA-MSE) between measurements of the actual system response and the response of the model. It is worth noting that the MSE here is a periodic function of time and so we adopt the time-averaged value of the MSE to obtain a single number as a performance measure.

The optimal LPTV filter, implemented through FRESH filtering, in the sense of TA-MSE minimization is developed in (Gardner, 1993). Let $x[n]$ represent the excitation, $d[n]$ represent the desired cyclostationary signal, and $\hat{d}[n]$ represent the filter output. Let each

LTI filter in the implementation of the FRESH filter consist of a finite-impulse-response (FIR) filter of L_{FIR} taps.

Following (Tian et al., 2011) and (Shlezinger and Dabora, 2014), let K denote the total number of cyclic frequencies used by the FRESH filter, α_k denote the k-th cyclic frequency, $h_k[i] = \tilde{h}_k^*[i]$ denote the conjugate of the i-th coefficient of the k-th FIR filter, and $\mathbf{z}[n] = [\mathbf{x}_0[n], \mathbf{x}_1[n], \cdots, \mathbf{x}_{K-1}[n]]^\top$ denote the frequency-shifted input vector at time n, where $(\mathbf{x}_k[n])_i = x[n-i]e^{-j2\pi\alpha_k(n-i)}$, $i \in \mathcal{L} = \{0, 1, \ldots, L_{\text{FIR}} - 1\}$. Finally, let $\mathbf{h}$ denote the concatenated conjugate of the FIR filter coefficients vector given by $\mathbf{h} = [\mathbf{h}_0, \mathbf{h}_1, \cdots, \mathbf{h}_{K-1}]^\top$, where $(\mathbf{h}_k)_i = h_k[i]$, $i \in \mathcal{L}$. The input-output relationship of the FIR FRESH filter can now be written as

$$\hat{d}[n] = \sum_{k=0}^{K-1} \sum_{i=0}^{L_{\text{FIR}}-1} h_k^*[i] x_k[n-i] e^{-j2\pi\alpha_k(n-i)} = \mathbf{h}^H \mathbf{z}[n] \tag{3.4}$$

As shown in (Tian et al., 2011) and (Shlezinger and Dabora, 2014), the optimal FRESH filter is obtained as

$$\mathbf{h} \;=\; \bar{\mathbf{R}}_{zz}^{-1} \bar{\mathbf{r}}_{\mathbf{zd}} \tag{3.5}$$

where $\bar{\mathbf{r}}_{\mathbf{zd}} = \langle \mathbf{r}_{\mathbf{zd}}[n] \rangle = \langle \mathbb{E}\{\mathbf{z}[n] d^*[n]\} \rangle$ denotes the time-averaged cross-correlation vector between the desired signal and the frequency-shifted received vector, and $\bar{\mathbf{R}}_{zz} = \langle \mathbf{R}_{\mathbf{zz}}[n] \rangle = \langle \mathbb{E}\left\{\mathbf{z}[n]\mathbf{z}^H[n]\right\} \rangle$ denotes the time-averaged auto-correlation matrix of the frequency-shifted received vector.

3.3.2 Proposed SISO Noise Model

The NB-PLC noise modeling can be viewed as an LPTV system identification problem. However, in the noise modeling problem, the input excitation corresponding to the measured noise is unknown, which renders the computation of $\bar{\mathbf{r}}_{\mathbf{zd}}$ not possible. To resolve this problem, we assume the input excitation to be $x[n] = d[n] + \zeta[n]$, where $d[n]$ represents the measured noise and $\zeta[n]$ is assumed to be a zero-mean AWGN process. In this case, given the independence of $d[n]$ and $\zeta[n]$, $\mathbf{r_{zd}}[n]$ and $\mathbf{R_{zz}}[n]$ can be expressed as

$$(\mathbf{r_{zd}}[n])_i = r_{dd}(n; -q_i)e^{-j2\pi\alpha_{p_i}(n-q_i)}, \tag{3.6}$$

$$\begin{aligned}[\mathbf{R_{zz}}[n]]_{u,v} &= [r_{dd}[n-q_v;\, q_v-q_u] + r_{\zeta\zeta}[n-q_v; q_v-q_u]] \\ &\times \;\; \mathrm{e}^{j2\pi(\alpha_{p_v}(n-q_v)-\alpha_{p_u}(n-q_u))},\end{aligned} \tag{3.7}$$

where

$$i = p_i L_{\text{FIR}} + q_i,\; q_i \in \mathcal{L},\; p_i \in \mathcal{K} = \{0, 1, \ldots,\, K-1\},$$

and

$$u = p_u L_{\text{FIR}} + q_u,\, v = p_v L_{\text{FIR}} + q_v p_u,\, p_v \in \mathcal{K},\, q_u, q_v \in \mathcal{L}.$$

However, using the input excitation as $x[n] = d[n] + \zeta[n]$, which includes $d[n]$, results in a correlation between $\hat{d}[n]$ and $d[n]$ which is proportional to the signal-to-noise-ratio (SNR), $\mathbb{E}\left[d^2[n]\right]/\mathbb{E}\left[\zeta^2[n]\right]$. Such correlation is not desirable since our goal is to generate $\hat{d}[n]$ completely independent from $d[n]$. To alleviate such a problem, we assume a very low SNR. In such case, we can ignore the effect of $d[n]$ in the input $x[n]$, i.e., $x[n] \approx \zeta[n]$. Furthermore, although we approximated $x[n]$ to be $\zeta[n]$, we keep the filter design equation in (3.10) unchanged as if $x[n] = d[n] + \zeta[n]$.

In summary, as shown in Fig. 3.7, the proposed noise modeling approach uses Equation (3.10) to generate the FIR FRESH filter coefficients under the assumption of very low SNR with AWGN input excitation, $\zeta[n]$. The SNR value is optimized through simulation based on the NMSE of the time averaged auto-correlation (the cyclic auto-correlation at α_0).

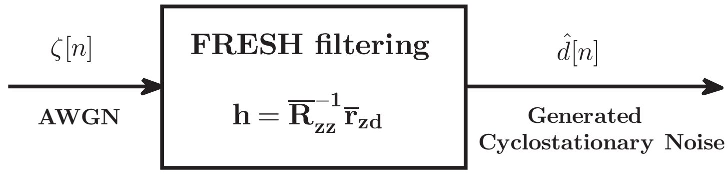

Figure 3.7: Proposed FRESH filtering noise model.

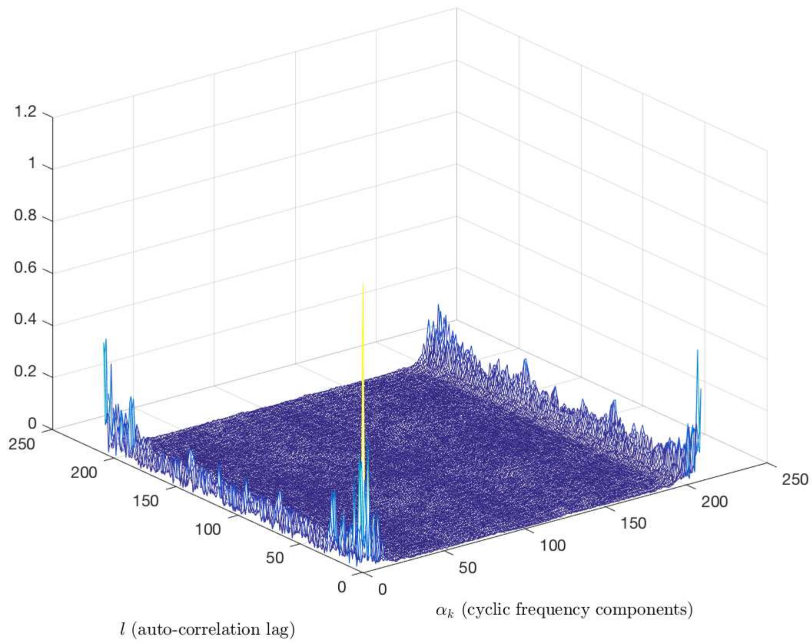

Figure 3.8: Cyclic Auto-correlation for the down-sampled measured noise.

3.4 FRESH-Filtering-Based Noise Model for MIMO NB-PLC

3.4.1 LPTV MIMO System Identification

Next, we generalize the SISO LPTV filter to the correponding MIMO 2X2. Let $x_1[n]$ and $x_2[n]$ represent the excitation signals, $d_1[n]$ and $d_2[n]$ represent the desired cyclostationary signals and $\hat{d}_1[n]$ and $\hat{d}_2[n]$ represent the filter outputs. Let each LTI filter in the FRESH implementation consist of a finite-impulse-response (FIR) filter of L_{FIR}taps. Let K denote the total number of cyclic frequencies used by the FRESH filter, α_k denote the k-th cyclic frequency, $h_k[i] = \tilde{h}_k^*[i]$ denote the conjugate of the i-th coefficient of the k-th FIR filter.

The MIMO LPTV filter structure is shown in Fig. 3.9, where for each branck k there are four FIR filters, denoted by $\hat{\mathbf{h}}_k = [\mathbf{h}_{11,k}, \mathbf{h}_{12,k}, \mathbf{h}_{21,k}, \mathbf{h}_{22,k}]^T$. Now, let $\mathbf{h}$ denotes the concatenated FIR filter coefficients vector given by $\mathbf{h} = [\hat{\mathbf{h}}_{\frac{-(K-1)}{2}}, \cdots, \hat{\mathbf{h}}_{-1}, \hat{\mathbf{h}}_0, \hat{\mathbf{h}}_1, \cdots, \hat{\mathbf{h}}_{\frac{(K-1)}{2}}]^T$. Our goal is to estimate (generate) the vector $\hat{\mathbf{d}}[n] = [\hat{d}_1[n], \hat{d}_2[n]]^T$ which corresponds to the desired signal vector $\mathbf{d}[n] = [d_1[n], d_2[n]]^T$. Following (Tian et al., 2011) and (Shlezinger and Dabora, 2014), let $\mathbf{z}[n] = [\mathbf{x}_{\frac{-(K-1)}{2}}[n], \cdots, \mathbf{x}_{-1}[n], \mathbf{x}_0[n], \mathbf{x}_1[n], \cdots, \mathbf{x}_{\frac{(K-1)}{2}}[n]]^T$ denote the frequency-shifted input vector at time n, where

$$(\mathbf{x}_k[n])_i \quad = \quad \begin{cases} x_1[n-i]e^{-j2\pi\alpha_k(n-i)} \\ \quad , i \in \mathcal{L} = \{0, 1, \ldots, \frac{L_{\text{FIR}}}{2} - 1\} \\ \\ x_2[n-i-\frac{L_{\text{FIR}}}{2}]e^{-j2\pi\alpha_k(n-i-\frac{L_{\text{FIR}}}{2})} \\ \quad , i \in \mathcal{L} = \{\frac{L_{\text{FIR}}}{2}, 1, \ldots, L_{\text{FIR}} - 1\} \end{cases} . \tag{3.8}$$

The input-output relationship of the FIR FRESH filter can now be written as

$$\hat{\mathbf{d}}[n] = \mathbf{h}^H \mathbf{z}[n] \tag{3.9}$$

As shown in (Tian et al., 2011) and (Shlezinger and Dabora, 2014), the optimal FRESH filter is obtained as

$$\mathbf{h} \;=\; \bar{\mathbf{R}}_{zz}^{-1} \bar{\mathbf{r}}_{\mathbf{zd}} \tag{3.10}$$

where $\bar{\mathbf{r}}_{\mathbf{zd}} = \langle \mathbf{r}_{\mathbf{zd}}[n] \rangle = \langle \mathbb{E}\{\mathbf{z}[n]\mathbf{d}^*[n]\} \rangle$ denotes the time-averaged cross-correlation vector between the desired signal and the frequency-shifted received vector, $\bar{\mathbf{R}}_{zz} = \langle \mathbf{R}_{\mathbf{zz}}[n] \rangle = \langle \mathbb{E}\{\mathbf{z}[n]\mathbf{z}^H[n]\} \rangle$ denotes the time-averaged auto-correlation matrix of the frequency-shifted received vector.

3.4.2 Proposed MIMO Noise Model

The MIMO NB-PLC noise modeling can be viewed as an LPTV system identification problem. However, in the noise modeling problem, the input excitation corresponding to the measured noise is unknown, which renders the computation of $\bar{\mathbf{r}}_{\mathbf{zd}}$ not possible. To resolve this problem, we assume the input excitation to be a noisy version of the desired signal (measured noise), i.e., $x_1[n] = d_1[n] + \zeta_1[n]$ and $x_2[n] = d_2[n] + \zeta_2[n]$, where $d_m[n]$ represents the measured noise for the phase m and $\zeta_m[n]$ is assumed to be a zero-mean AWGN process. In this case, given the independence of $d_m[n]$ and $\zeta_m[n]$, $\mathbf{r}_{\mathbf{zd}}[n]$ and $\mathbf{R}_{\mathbf{zz}}[n]$ can be expressed as

$$\mathbf{r}_{\mathbf{zd}}[n] = \begin{bmatrix} \mathbf{r}_{\mathbf{zd}}^{11}[n] & \mathbf{r}_{\mathbf{zd}}^{12}[n] \\ \mathbf{r}_{\mathbf{zd}}^{21}[n] & \mathbf{r}_{\mathbf{zd}}^{22}[n] \end{bmatrix}, \tag{3.11}$$

where

$$\begin{aligned} (\mathbf{r}_{\mathbf{zd}}^{\mathbf{sm}}[n])_i &= r_{d_s d_m}(n; -q_i) e^{-j2\pi\alpha_{p_i}(n-q_i)}, \\ i &= p_i L_{\text{FIR}} + q_i, \\ q_i &\in \mathcal{L},\ p_i \in \mathcal{K} = \{0, \ldots, K-1\}. \end{aligned}$$

$$\mathbf{R}_{\mathbf{zz}}[n] = \begin{bmatrix} \mathbf{R}_{\mathbf{zz}}^{11}[n] & \mathbf{R}_{\mathbf{zz}}^{12}[n] \\ \mathbf{R}_{\mathbf{zz}}^{21}[n] & \mathbf{R}_{\mathbf{zz}}^{22}[n] \end{bmatrix}, \tag{3.12}$$

where

$$(\mathbf{R}_{\mathbf{zz}}^{\mathbf{sm}}[n])_{u,v} = \Big[r_{d_s d_m}[n - q_v;\ q_v - q_u] + r_{\zeta_s \zeta_m}[n - q_v; q_v - q_u] \Big] \mathrm{e}^{j2\pi(\alpha_{p_v}(n-q_v) - \alpha_{p_u}(n-q_u))},$$

$$\begin{aligned} u &= p_u L_{\text{FIR}} + q_u, \\ v &= p_v L_{\text{FIR}} + q_v, \end{aligned}$$

$$p_u,\, p_v \quad \in \quad \mathcal{K}, q_u, q_v \in \mathcal{L}.$$

However, using the input excitation as $x_m[n] = d_m[n] + \zeta_m[n]$, which includes the desired signal $d_m[n]$, results in a correlation between $\hat{d}_m[n]$ and $d_m[n]$ which is proportional to the signal-to-noise-ratio SNR $=\mathbb{E}\,[d_m^2[n]]/\mathbb{E}\,[\zeta_m^2[n]]$. Such correlation is not desirable since our goal is to generate $\hat{d_m}[n]$ completely independent from $d_m[n]$. To alleviate such a problem, we assume a very low SNR. In such case, we can ignore the effect of $d_m[n]$ in the input $x_m[n]$, i.e., $x_m[n] \approx \zeta_m[n]$. Furthermore, although we approximated $x_m[n]$ to be $\zeta_m[n]$, we keep the filter design equation in (3.10) unchanged as if $x_m[n] = d_m[n] + \zeta_m[n]$. The SNR value is optimized by simulations based on the NMSE of the time averaged auto-correlation (i.e., the cyclic auto-correlation at α_0).

3.5 Numerical Results

3.5.1 SISO Noise Model Numerical Results

In this subsection, we evaluate the performance of our proposed cyclostationary noise modeling approach versus the model complexity, which is measured by the number of branches and the number of FIR filter taps in each branch. In addition, we compare the performance with the time-region-based model proposed in (Nassar et al., 2012). We chose the performance metric to be the normalized MSE (NMSE) in the cyclic auto-correlation function between the measured noise and the generated noise. Using the NMSE of the cyclic auto-correlation instead of the NMSE of the filter output samples (usually used in minimum MSE (MMSE) approach) is more suitable for our modeling problem. Since, in our case, the generated noise and the measured noise are required to be totally uncorrelated (so we can generate more independent noise samples from the model), yet having the same statistical properties, namely the cyclic auto-correlation. The NMSE over the k-th cyclic frequency component can be

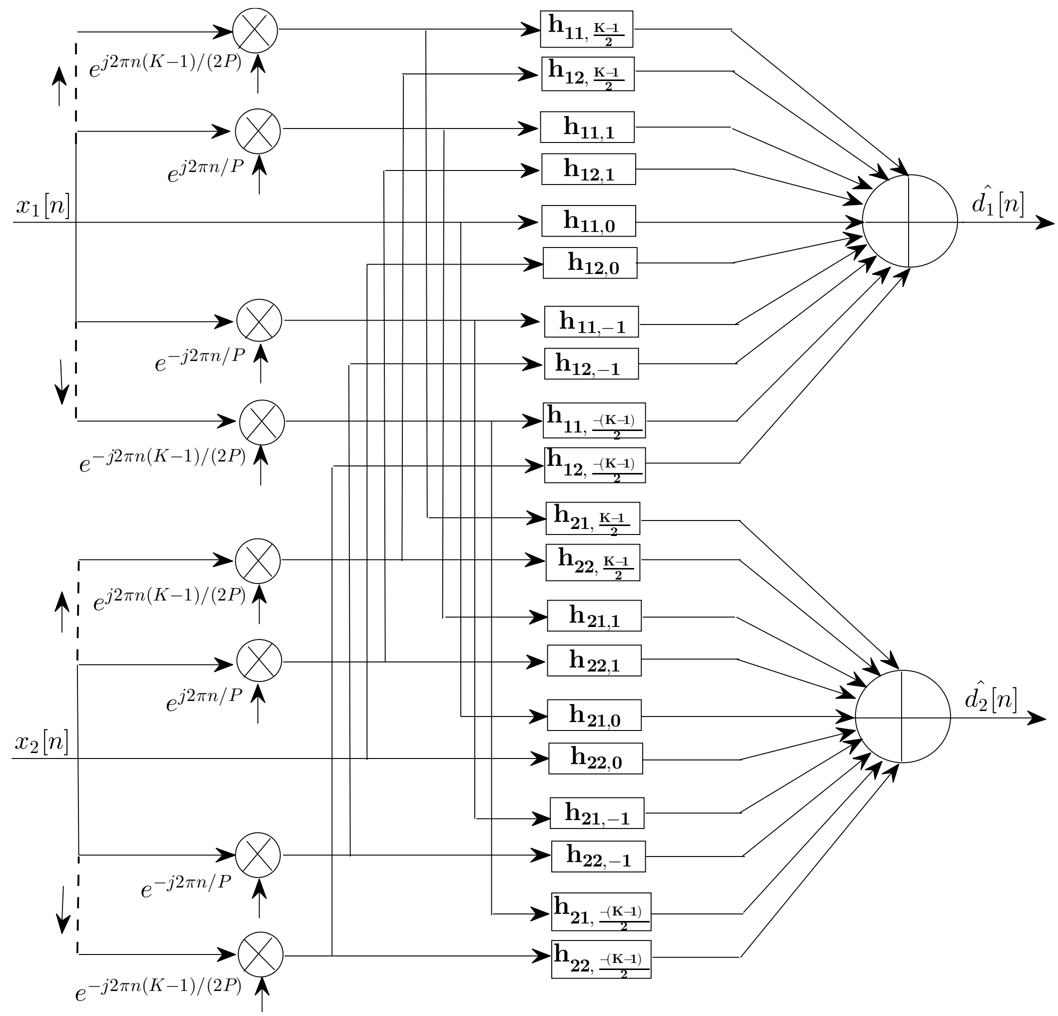

Figure 3.9: 2x2 MIMO FRESH filter

written as follows

$$\mathrm{NMSE}_{\alpha_k} = \frac{\sum_l |r_{dd}^{\alpha_k}[\ell] - r_{\hat{d}\hat{d}}^{\alpha_k}[\ell]|^2}{\sum_l |r_{dd}^{\alpha_k}[\ell]|^2} \tag{3.13}$$

In addition, the cumulative NMSE till the k-th cyclic frequency component is given by

$$\mathrm{NMSE}_{\mathrm{C},\alpha_j} = \frac{\sum_{k=0}^{j}\sum_l |r_{dd}^{\alpha_k}[\ell] - r_{\hat{d}\hat{d}}^{\alpha_k}[\ell]|^2}{\sum_{k=0}^{j}\sum_l |r_{dd}^{\alpha_k}[\ell]|^2} \tag{3.14}$$

To compute the total NMSE, we sum over all components $\{\alpha_k : k = 0, \dots, P-1\}$, then normalize by the total energy of the noise measured cyclic auto-correlation function.

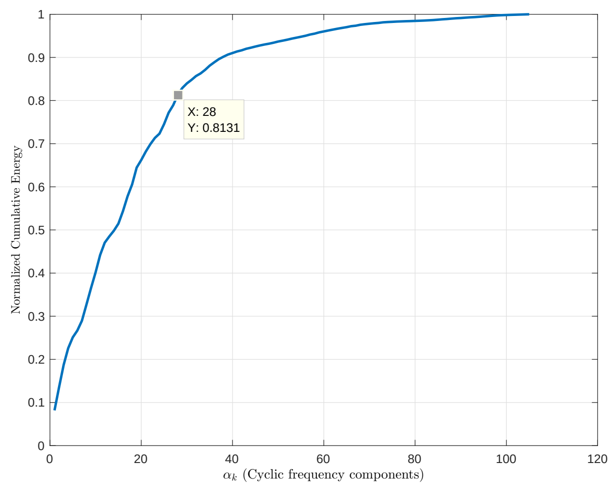

Figure 3.10: Normalized cumulative energy versus the cyclic frequency components for the partial-band noise case.

The main parameters that control the performance/complexity tradeoff are the number of branches and the FIR FRESH filter length in each branch. The number of branches corresponds to the number of the significant components in the cyclic auto-correlation. Fortunately, for the NB-PLC noise cyclic auto-correlation, only few components contain most of the energy where the lower the component frequency is, the higher is its energy. Fig. 3.8 shows the cyclic auto-correlation for the partial-band version of the measured noise.

To better illustrate the energy contained in each cyclic frequency component, we compute the normalized cumulative energy for the j-th cyclic frequency component as

$$\overline{E}_{\mathrm{C},\alpha_j} = \frac{\sum_{k=0}^{j} \sum_l |r_{dd}^{\alpha_k}[\ell]|^2}{\sum_{k=0}^{P-1} \sum_l |r_{dd}^{\alpha_k}[\ell]|^2} \tag{3.15}$$

Fig. 3.10 depicts the normalized cumulative energy over different cyclic frequency components for the partial-band noise case. It shows that 80% of the energy is contained in the first 28 components in each side (i.e., total of 56 out of 210 components which is 27% of the total number of cyclic frequency components). Note that we plot over one-sided cyclic frequency components due to symmetry. However, as shown in Fig. 3.11 for the full-band

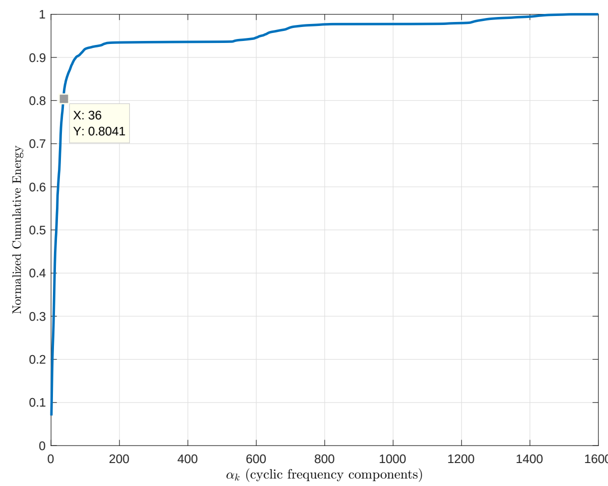

Figure 3.11: Normalized cumulative energy versus the cyclic frequency components for the full-band noise case.

noise measured, 80% of energy is contained in the first 36 components in each side (total of 72 out of 3200 which is only 2% of the total number of cyclic frequency components). This demonstrates the significant noise modeling complexity reduction for the full-band measured noise.

In general, the FIR filter length is dictated by the maximum lag, ℓ, for which the cyclic auto-correlation is non-zero over all cyclic frequencies. The larger the FIR filter length is, the more accurate the modeled auto-correlation per component will be. In Fig. 3.12, we show the NMSE reduction for the time-averaged cyclic auto-correlation (the dominant component) versus the FIR FRESH filter length.

To check the overall performance and compare with the time-region-based model represented in (Nassar et al., 2012), we set the FIR filter length to 210 taps and evaluate the cumulative NMSE using different number of branches. Fig. 3.13 shows the NMSE computed cumulatively over different cyclic frequency components for our proposed model compared to the model in (Nassar et al., 2012). In generating the noise according to the model presented in (Nassar et al., 2012), we used 4 temporal regions while the FIR filter for each temporal region is fitted to the measured PSD.

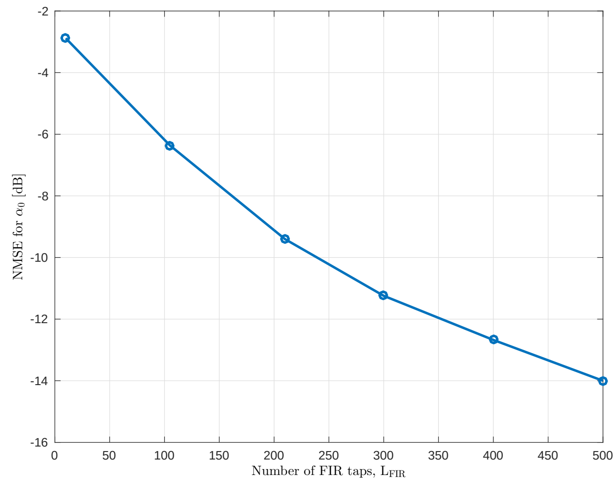

Figure 3.12: NMSE versus the FIR FRESH filter length for $K = 5$.

Fig. 3.13 shows that our proposed model provides more accurate cyclic auto-correlation than the model in (Nassar et al., 2012) for almost the same complexity (5 branches). In particular, the proposed model provides about 6 dB gain in the NMSE of the time-averaged cyclic auto-correlation (at cyclic frequency α_0) as shown in Fig. 3.13. Furthermore, in the proposed model, enhancing the performance is easily done by increasing the number of FRESH filter branches. Moreover, Fig. 3.13 shows that the cumulative NMSE is mainly affected by the first few cyclic frequency components and then the error tends to be almost constant. In Fig. 3.13, we also note that the initial cumulative NMSE at α_o depends on the FIR filter length while the slope of the linear segment of the curve depends on the number of branches. Hence, in order to decrease the total error for the FRESH filter-based noise modeling method, we can decrease the initial error by increasing the FIR filter length and/or decreasing the slope of the linear segment of the error curve by increasing the number of branches.

3.5.2 MIMO Noise Model Numerical Results

We evaluate the performance of our proposed cyclostationary MIMO noise modeling approach versus the model complexity. The model complexity is measured by the number of

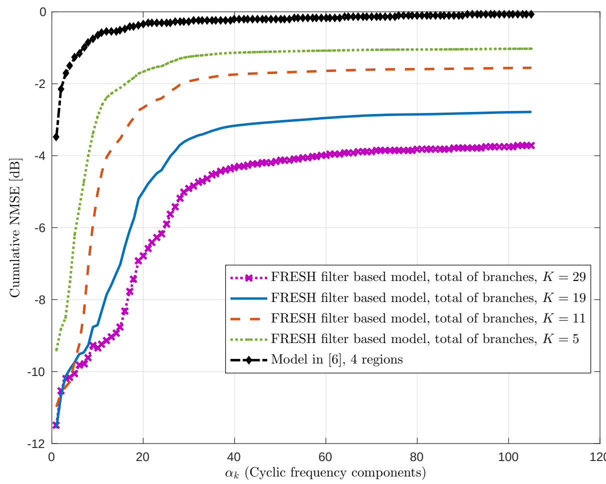

Figure 3.13: Cumulative NMSE over cyclic frequencies for $L_{\text{FIR}} = 210$.

branches and the number of FIR filter taps in each branch. We chose the performance metric to be the normalized MSE (NMSE) in the cyclic auto-correlation and cyclic cross-correlation functions between the measured noise and the generated noise. Using the NMSE of the cyclic auto/cross-correlation instead of the NMSE of the filter output samples (usually used in the minimum MSE (MMSE) approach) is more suitable for our modeling problem. The reason is that in our case the generated noise and the measured noise are required to be totally uncorrelated (so we can generate more independent noise samples from the model), yet having the same statistical properties, namely the cyclic auto/cross-correlation. The NMSE over the k-th cyclic frequency component can be written as follows

$$\text{NMSE}^{sm}_{\alpha_k} = \frac{\sum_l |r^{\alpha_k}_{d_s d_m}[l] - r^{\alpha_k}_{\hat{d_s}\hat{d_m}}[l]|^2}{\sum_l |r^{\alpha_k}_{d_s d_m}[l]|^2} \tag{3.16}$$

where $\text{NMSE}^{11}_{\alpha_k}$ represents the normalized mean sequare error in the cyclic auto-correlation of phase 1 and similarly $\text{NMSE}^{22}_{\alpha_k}$ for phase 2, while $\text{NMSE}^{12}_{\alpha_k} = \text{NMSE}^{21}_{\alpha_k}$ represents the normalized mean square error in the cyclic cross-correlation between phsae 1 and phase 2.

In addition, the cumulative NMSE till the k-th cyclic frequency component is given by

$$\text{NMSE}^{sm}_{\text{C},\alpha_r} = \frac{\sum_{k=0}^{r} \sum_l |r^{\alpha_k}_{d_S d_m}[l] - r^{\alpha_k}_{\hat{d_s}\hat{d_m}}[l]|^2}{\sum_{k=0}^{r} \sum_l |r^{\alpha_k}_{d_s d_m}[l]|^2} \tag{3.17}$$

To compute the total NMSE, we sum over all components $\{\alpha_k : k = 0, \ldots, P-1\}$, then normalize by the total energy of the noise measured cyclic auto-correlation function. The main parameters that control the performance/complexity tradeoff are the number of branches and the FIR FRESH filter length in each branch. The number of branches corresponds to the number of the significant components in the cyclic auto-correlation. Fortunately, for the NB-PLC noise cyclic auto/cross-correlation, only few components contain most of the energy where the lower the component's frequency is, the higher is its energy.

In general, the FIR filter length is dictated by the maximum lag, i, for which the cyclic auto-correlation is non-zero over all cyclic frequencies. The larger the FIR filter length is, the more accurate the modeled auto-correlation per component will be.

In the following simulation results, we set the FIR filter length to 420 taps (equivalently 210 for each phase) and evaluate the cumulative NMSE using different number of branches. Fig. 3.14 shows the NMSE computed cumulatively over different cyclic frequency components. Note that we plot over one-sided cyclic frequency components due to symmetry. In the proposed model, enhancing the performance is easily done by increasing the number of FRESH filter branches. Fig. 3.14 also shows that the cumulative NMSE is mainly affected by the first few cyclic frequency components and then the error tends to be almost constant. We also note that the initial cumulative NMSE at α_o depends on the FIR filter length while the slope of the linear segment of the curve depends on the number of branches. Hence, in order to decrease the total error for the FRESH filter-based noise modeling method, we can decrease the initial error by increasing the FIR filter length and/or decreasing the slope of the linear segment of the error curve by increasing the number of branches.

3.6 Summary of Cyclostationary Noise Modeling

We proposed a new cyclostationary model for the NB-PLC noise based on FRESH filtering. The input to the FRESH filters is an AWGN process. In particular, the FRESH filters

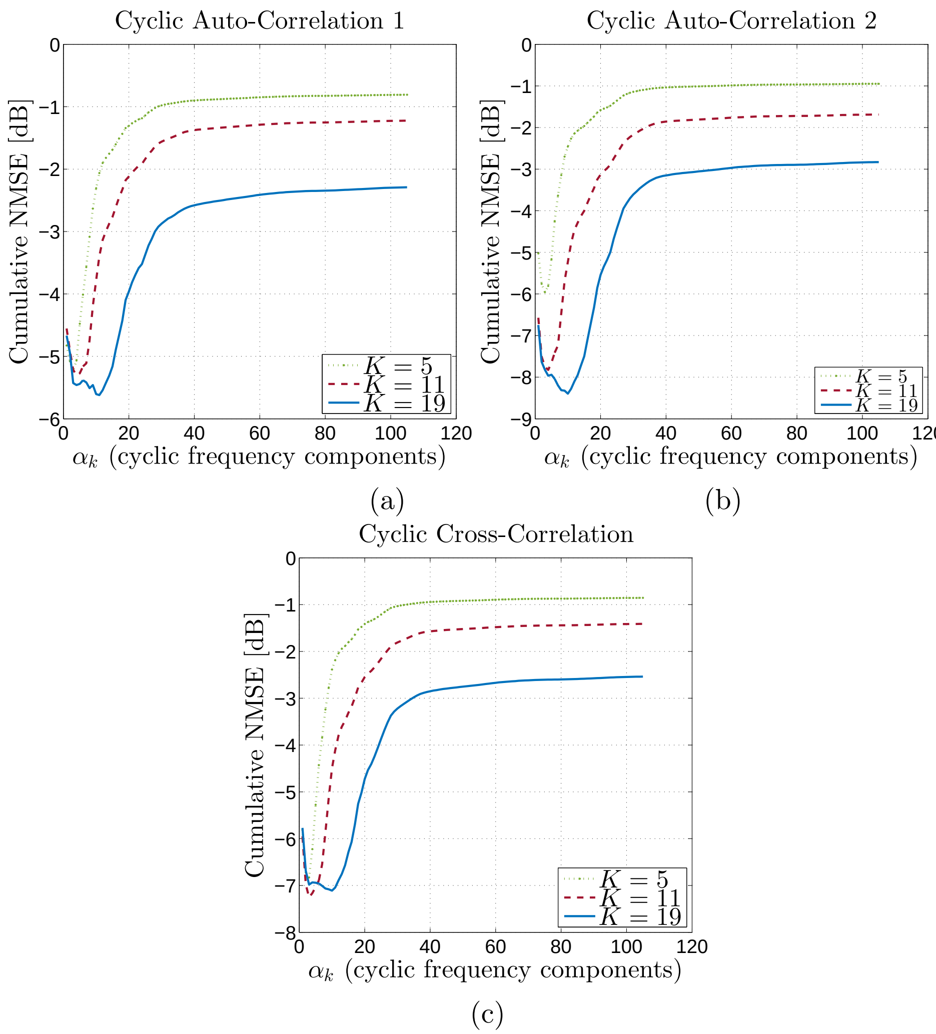

Figure 3.14: Cumulative NMSE over cyclic frequencies for $L_{\text{FIR}} = 420$. (a) Cumulative NMSE for the cyclic auto-correlation of phase 1. (b) Cumulative NMSE for the cyclic auto-correlation of phase 2. (c) Cumulative NMSE for the cyclic cross-correlation between phase 1 and phase 2.

coefficients are generated to minimize the TA-MSE between the generated and measured noise. The proposed model shows a clear performance gain over the time-region-based model presented in (Nassar et al., 2012), in terms of the NMSE in the cyclic auto-correlation, at the same complexity. Numerical results show about 6 dB gain in the NMSE of the time-averaged cyclic auto-correlation (at cyclic frequency α_0). Moreover, an important advantage for the proposed model over the previous models is the scalability in the performance/complexity, i.e., the performance can be enhanced by increasing the number of branches and/or the number of filter taps with a higher complexity.

In addition, we proposed a cyclostationary model for the MIMO NB-PLC noise based on FRESH filtering. The input to the FRESH filters is an AWGN process. In particular, the FRESH filters coefficients are generated to minimize the TA-MSE between the generated and measured noise. As shown in the simulation results, the proposed model is able to track the original measurements statistics (cyclic auto/cross-correlation). Moreover, an important advantage for the proposed model is the scalability in the performance/complexity, i.e., the performance can be enhanced by increasing the number of branches and/or the number of filter taps with a higher complexity. Moreover, the proposed model can be easily upgraded to any number of phases.

Finally, it is worth mentioning that the model complexity can be further reduced by implementing the FRESH filters using adaptive filtering techniques to avoid matrix inversion. However, the complexity should not be an issue in modeling since the filter coefficients are generated once then stored.

CHAPTER 4

CYCLOSTATIONARY NOISE MITIGATION BASED ON ERASURE DECODING [1]

The main motivation of this chapter is the nature of the cyclostationary noise in the narrowband PLC link; namely, the lack of time-domain or frequency-domain noise sparsity within each OFDM symbol. Even if we assumed longer OFDM symbols which span more than one complete period of the noise, the noise sparsity level will not be enough to allow sparse estimation algorithms (e.g. as in (Lampe, 2011a; Caire et al., 2008b)) to work well. The use of a time-domain interleaver to enhance the sparsity of the noise was proposed in (Lin et al., 2013). However, this solution is not practical not only because of its high complexity at the receiver side but also because it violates the transmission specifications in the IEEE 1901.2 NB-PLC standard since the frequency subchannels will spread over the whole bandwidth (i.e., null subchannels will be totally occupied with data).

Therefore, instead of enhancing the sparsity of the NB-PLC noise, we propose to enhance the system performance by employing erasure decoding which requires information about the positions of the noise impulses (Elgenedy et al., 2015). To decide on the positions of the noise impulses, we exploit key features of the NB-PLC noise in time and spatial domains. We exploit the temporal feature of the NB-PLC noise, namely, considering the noise's cyclostationarity in the time domain to estimate the power spectral density (PSD) of the cyclostationary noise over its different temporal regions. The estimated PSD can be used either individually or together with log likelihood ratios (LLRs) to mark erasures for the Reed-Solomon decoder. The other feature we use is the noise's spatial correlation across the three power line phases. In particular, we noticed that the received signal on the other

[1] © 2015 IEEE M. Elgenedy, M. Sayed, M. Mokhtar, M. Abdallah and N. Al-Dhahir, "Interference mitigation techniques for narrowband powerline smart grid communications," 2015 IEEE International Conference on Smart Grid Communications (SmartGridComm), Miami, FL, 2015, pp. 368-373.

phases are weak compared to the main phase. Hence, we proposed to use the received signal samples on the other phases to mark erasures for the main phase signal.

4.1 LLR based Erasure Decoding

The IEEE 1901.2 NB-PLC standard uses concatenated coding with an inner convolutional code and an outer Reed-Solomon (RS) code which was proposed by Irving Reed and Gus Solomon in (Reed and Solomon, 1960). RS codes are non-binary cyclic codes with symbols of m-bits, where m is a positive integer greater than 2. For RS code (n, k), $n = 2^m - 1$ and $k = 2^m - 1 - 2t$, where k is the number of data symbols to be encoded, n is the encoder output codeword length in symbols, t is the coding error correcting capability in symbols and $n - k = 2t$ is number of parity symbols. Correcting t symbols through the RS decoder requires $2t$ parity symbols (t symbols to detect the error locations and another t symbols to correct them). When the exact location of the erroneous symbols is known. The decoder can perform erasure decoding and can successfully correct up to $2t$ symbol errors. In general, for a number of errors e with unknown locations and u with known locations, the RS decoder can successfully decode the received codeword as long as $2e + u <= 2t$.

In the concatenated mode, a common approach is to calculate the erasure decisions from the convolutional decoder output metrics (LLRs) as in (Pitt III and Swanson, 1985; Pollara, 1987; Toumpakaris et al., 2004). Fig. 4.1 shows approximately 0.5 dB SNR gain at BER $= 10^{-5}$. Although this SNR gain is not large, yet it is beneficial and in line with the results in (Pitt III and Swanson, 1985).

It is also worth mentioning here that the iterative method proposed in (Pitt III and Swanson, 1985; Toumpakaris et al., 2004) that uses the RS output syndrome check assumes an interleaver between the two decoders which is not compliant with the IEEE 1901.2 NB-PLC standard.

Using RS encoding only is not standardized. However, it could be an additional useful mode for higher rate requirements at high SNR (in order to eliminate the high overhead of the rate 1/2 convolutional code) as proposed by (Kim et al., 2010). When the RS code is used without inner coding, the erasure positions can be determined from the LLR output of the demapper, PSD or LLR scaled with the PSD. Note that for the case of very large noise impulses with opposite polarity to the transmitted BPSK symbol, the LLR value may be large but that does not mean it is reliable since it is already wrong. An attractive approach in case of RS-only mode is to scale the LLRs by the noise's PSD (to decrease LLR values at the locations of very high noise impulses) before taking the erasure decisions. Fig. 4.2 shows about = 1 dB SNR gain at BER = 10^{-6} for the RS-only mode when using erasure decoding based on LLRs scaled with PSD. Results also show the benefits of using the RS code only since the SNR gain is about 6 dB when compared to the uncoded case with a very small rate loss.

In the following, we propose a simple technique to estimate the PSD of the cyclostationary noise. The received signal power over the l-th OFDM symbol and the k-th subchannel index can be written as

$$|Y_k^l|^2 = |H_k^l X_k^l|^2 + |Z_k^l|^2 + 2\mathfrak{Re}\left[H_k^l X_k^l Z_k^{l*}\right]$$

Averaging over $|Y_k^l|^2$, we get

$$\begin{aligned} \mathrm{E}|Y_k^l|^2 &= \mathrm{E}|H_k^l|^2 \mathrm{E}|X_k^l|^2 \\ &+ \mathrm{E}|Z_k^l|^2 + 2\mathfrak{Re}\left[\mathrm{E}\left(H_k^l X_k^l\right)\mathrm{E}\left(Z_k^{l*}\right)\right] \end{aligned}$$

where E(.) denotes the expectation operator. Since $\mathrm{E}\left(Z_k^{l*}\right) = 0$, then $\mathrm{E}|Y_k^l|^2$ reduces to

$$\mathrm{E}|Y_k^l|^2 = \mathrm{E}|H_k^l|^2 \mathrm{E}|X_k^l|^2 + \mathrm{E}|Z_k^l|^2$$

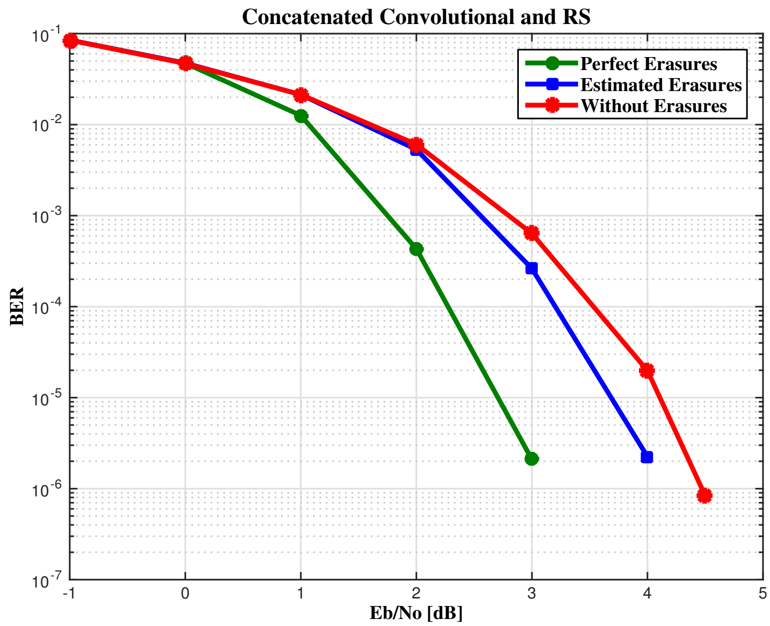

Figure 4.1: Average BER versus E_b/N_o in dB, under AWGN only, for concatenated convolutional and Reed-Solomon codes with erasure decoding. BPSK, RS code $(239, 255)$, Convolutional code rate $= 1/2$.

Setting $\mathrm{E}|X_k^l|^2 = 1$, we get

$$\begin{aligned} \mathrm{E}|Y_k^l|^2 &= \mathrm{E}|H_k^l|^2 + \mathrm{E}|Z_k^l|^2 \\ \bar{\sigma}_k^2 &= \mathrm{E}|Z_k^l|^2 = \mathrm{E}|Y_k^l|^2 - \mathrm{E}|\hat{H}_k^l|^2 \end{aligned}$$

where $\bar{\sigma}_k^2$ is the estimated noise PSD and $\hat{H}_k^l$ is the estimated channel at OFDM symbol l and subchannel k.

As in the case of the Viterbi decoder, the results for RS-only mode are generated without the frequency-domain interleaver. However, the important point to make in the RS-only case is that the frequency-domain interleaver will not enhance the results since the RS block spans several noise cycles which means that the bursts are repeated inside each RS block with almost constant cycle and, hence, there is no gain from spreading them within the same RS block.

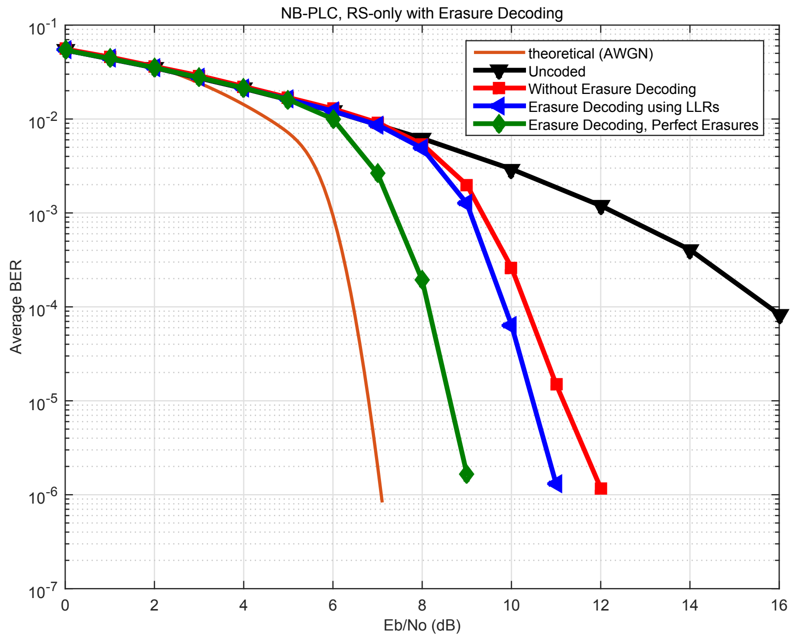

Figure 4.2: Average BER versus E_b/N_o in dB, under AWGN only, for Reed-Solomon code only with erasure decoding. BPSK, RS code $(239, 255)$.

4.2 Spatial Correlation based Erasure Decoding

We exploit knowledge of the instantaneous noise at the other phases where there is no differential input excitation to mitigate the noise on the active A-N phase. We investigate erasure decoding for both RS and convolutional codes.

For simplicity, we only consider the frequency-domain received signals, at a given OFDM subchannel[2] and within a coherence time where the channels can be assumed constant, over two phases[3] which are given by

$$Y_1 = H_1 X + Z_1,$$

[2]We omit the subchannel index to simplify notation

[3]Extending the analysis for the case of three phases combining is an interesting topic for future research

$$Y_2 = H_2X + Z_2$$

where H_1 and H_2 are the frequency-domain channel coefficients for phases A-N and B-N, respectively. Measurements show that the phase difference between H_1 and H_1 is very small ($\angle H_1 - \angle H_2 = \theta_1 - \theta_2 << 1$ radians) while the magnitude of H_2 is less than H_1. Hence, we can assume $|H_2| = \delta|H_1|$ where $0 < \delta < 1$.

Z_1 and Z_2 are the correlated narrow-band noise samples at the considered OFDM sub-channel which are assumed to have a variance σ^2 and spatial correlation factor r. Furthermore, define $\tilde{Z}_1$ and $\tilde{Z}_2$ to be two i.i.d narrow-band noise samples with variance σ^2, then Z_1 and Z_2 can be modeled as defined in Chapter 2 as follows

$$\begin{aligned} Z_1 &= r\tilde{Z}_1 + \sqrt{1-r^2}\tilde{Z}_2 \\ Z_2 &= \tilde{Z}_1 \end{aligned}$$

In the following analysis, we compare the performance of two simple receiver structures **which do not require knowledge of the spatial correlation factor** r: a maximum-ratio-combiner (MRC) receiver which is equivalent to a spatial matched filter and a simple noise canceller.

4.2.1 MRC Receiver

The output signal after MRC is given by

$$\begin{aligned} \tilde{Y}_{MRC} &= {H_1}^*Y_1 + {H_2}^*Y_2 \\ &= (|H_1|^2 + |H_2|^2)X + {H_1}^*Z_1 + {H_2}^*Z_2 \\ &= (1+\delta^2)|H_1|^2X + {H_1}^*(r + \delta e^{-j\tilde{\theta}})\tilde{Z}_1 \end{aligned}$$

$$+ \quad {H_1}^* \sqrt{1-r^2} \tilde{Z}_2$$

where $\tilde{\theta} = (\theta_2 - \theta_1) << 1$.

Therefore, under the assumption of $e^{-j\tilde{\theta}} \approx 1 - j\tilde{\theta} \approx 1$, the MRC output SNR is given by

$$SNR_{MRC} = \frac{(1+\delta^2)^2 |H_1|^2}{[(1+\delta^2) + 2r\delta]\sigma^2}$$

Now, we notice that the signal power is enhanced by a factor of $(1+\delta^2)^2$ due to the coherent combining and the assumed perfect knowledge of H_1 and H_2 at the receiver. However, the noise power is also enhanced by a factor $(1+\delta^2) + 2r\delta$ due to the positive spatial correlation (i.e., $0 < r < 1$) between the narrow-band noise across the 2 output phases.

Note that when $r = 0$ (i.e., no spatial correlation), SNR_{MRC} will be the matched-filter bound $SNR_{MFB} = \frac{(1+\delta^2)|H_1|^2}{\sigma^2}$.

SNR_{MRC} becomes less than the SNR_{MFB} as the spatial correlation factor increases r until there is no enhancement compared to the input SNR (i.e., until $SNR_{MRC} = SNR_{input} = \frac{|H_1|^2}{\sigma^2}$) which occurs at $r = r_1$ where

$$r_1 = \frac{\delta(1+\delta^2)}{2}$$

When the correlation factor $r > r_1$, MRC degrades the output SNR since the SNR gain from coherent signal power combining will be lower than the SNR loss from coherent noise combining because the noise spatial covariance matrix is assumed unknown at the receiver. Hence, we can not perform spatial noise whitening before MRC.

4.2.2 Noise Canceller

A second technique which does not require knowledge of the noise spatial covariance matrix, is a simple noise canceller which subtracts the second-phase received signal Y_2 from the first-phase received signal Y_1 to get

$$
\begin{aligned}
\tilde{Y}_C &= Y_1 - Y_2 = (H_1 - H_2)X + (Z_1 - Z_2) \\
&= H_1(1 - \delta e^{j\tilde{\theta}})X + (r-1)\tilde{Z}_1 + \sqrt{1-r^2}\tilde{Z}_2
\end{aligned}
$$

Hence, under the assumption of $e^{+j\tilde{\theta}} \approx 1 + j\tilde{\theta} \approx 1$, the output SNR after cancellation is

$$
SNR_{Canceller} = \frac{|H_1|^2(1-\delta)^2}{2(1-r)\sigma^2}
$$

We notice here that the signal power is decreased by a factor $(1-\delta)^2 < 1$. However, the noise power is also decreased by a factor $2(1-r)$ for $0.5 < r < 1$.

The case of no SNR gain from cancellation, i.e., when $SNR_{MRC} = SNR_{input} = \frac{|H_1|^2}{\sigma^2}$, happens at $r = r_2$ where

$$
r_2 = 1 - \frac{1}{2}(1-\delta)^2
$$

Hence, if the spatial correlation factor $r < r_2$, subtracting the outputs of the 2 phases degrades the SNR since the SNR loss due to signal power subtraction will be larger than the SNR gain from noise cancellation.

To conclude, the choice of whether to perform MRC or cancellation depends on the correlation factor r and on the ratio between $|H_1|$ and $|H_2|$. As a practical example, assume that the ratio between $|H_1|$ and $|H_2|$ at a certain OFDM subchannel (within a coherence time) is 6 dB, i.e., $\delta \approx \frac{1}{2}$. In this case, $r_1 = 0.3125$ and $r_2 = 0.88$ which means that there is no benefit from using MRC when the correlation factor $r > 0.3125$. Typical values for the spatial correlation factor r in PLC are much larger than $r > 0.3125$, hence, MRC is not beneficial in our application. Noise cancellation (subtraction) enhances the performance for the values of correlation factor $r > 0.88$. However, care should be taken when using cancellation since if the correlation factor r decreases below 0.88, performance degradation will occur.

Alternatively, since $|H_2|$ is much smaller than $|H_1|$, we propose to use Y_2 to represent the instantaneous noise samples Z_1 and use it to mark the erasure locations by comparing the signs of Y_1 and $\tilde{Y}_C$ and if they are different, mark an erasure. Comparing the signs of Y_1 and $\tilde{Y}_C$ could be seen as a two-step erasure detection technique. First, we compare the noise power to the received data power. Then, if the noise power is larger than the data power, we compare the signs for both the noise and data samples since if they have the same sign, there is no error. This enhanced erasure detection technique comes as a benefit of using the instantaneous noise samples to mark the erasures rather than just using the average noise power (i.e., noise PSD) to scale the LLR values.

Simulation results in Figs. 4.3 and 4.4 show a clear performance enhancement for cancellation (up to 3 dB at BER $= 10^{-5}$) at high correlation factor $r \approx 0.94$. The performance gain from using erasure decoding is clear when the correlation factor r is less than or equal $r_2 = 0.88$. For example, at $r \approx 0.88$, there is no performance enhancement when using cancellation but about 1 dB gain when using erasure decoding at BER $= 10^{-5}$ for the RS decoder as in Fig. 4.3 and BER $= 10^{-4}$ for the Viterbi decoder as in Fig. 4.4. Moreover, erasure decoding shows robustness when the correlation factor decreases since for $r = 0.8$ there is no degradation when using erasure decoding while cancellation suffers about 2 dB SNR loss at BER $= 10^{-3}$ as in Figs. 4.3 and 4.4.

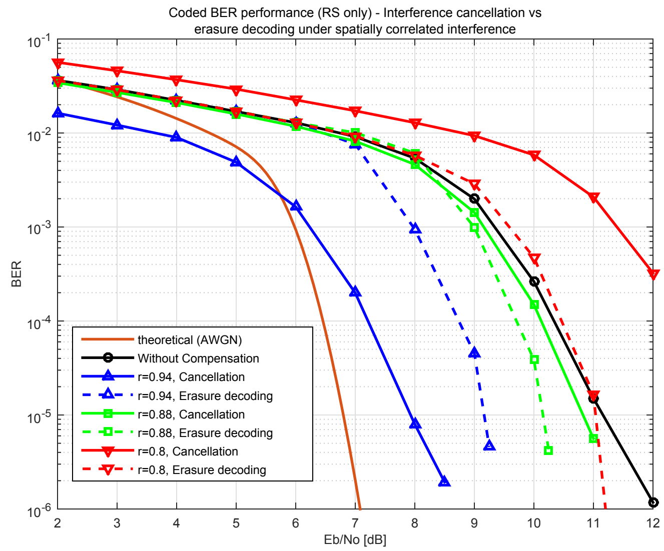

Figure 4.3: Coded BER performance for RS only mode, under AWGN only - Noise cancellation vs erasure decoding under spatially correlated Noise. BPSK, RS code $(239, 255)$.

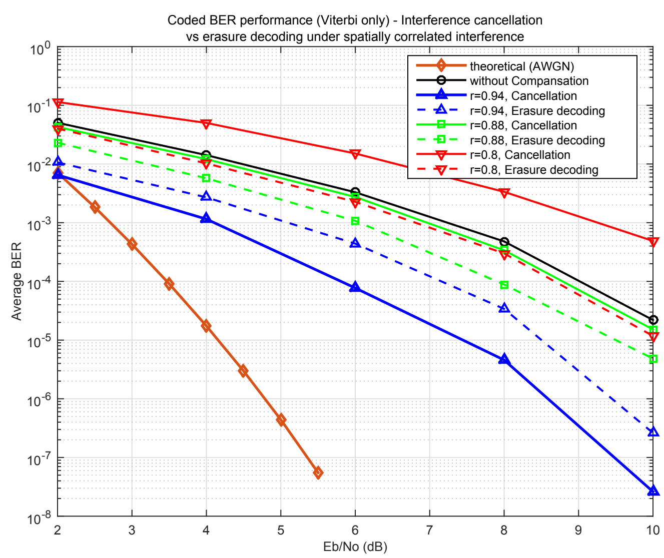

Figure 4.4: Coded BER performance for Viterbi only mode, under AWGN only - Noise cancellation vs erasure decoding under spatially correlated Noise. BPSK, Convolutional code rate $= 1/2$.

CHAPTER 5

TEMPORAL-REGION-BASED CYCLOSTATIONARY NOISE MITIGATION FOR SIMO POWERLINE COMMUNICATIONS [1] [2]

Single-Input Multi-Output (SIMO) communications can be employed to enhance the robustness against the impulsive noise (Tse and Viswanath, 2005). SIMO communications systems achieve diversity gain through transmission over different channels in addition to a power gain since more power is collected at the receiver side using more than one receive antenna (phase). Moreover, in NB-PLC, an additional advantage for SIMO communications is the high spatial correlation between the cyclostationary noise signals on the different phases. This high correlation is expected since the source of the cyclostationary noise is the network-based switched power supplies (IEEE P1901.2, 2013). This fact was also observed through our measurements and verified through simulations as discussed in Chapter 2. Therefore, this chapter presents the first study of SIMO communications for NB-PLC. As shown in Fig. 2.1, multiple power line receive phases can be jointly processed for signal recovery by exploiting the cross coupling between them while transmitting the OFDM information signal over a single power line phase. However, to the best of our knowledge, cyclostationary noise mitigation for SIMO communications was not proposed before in the literature.

We propose an FD SIMO noise mitigation technique that operates on a per-OFDM-subchannel basis to estimate the FD data symbols using an LMMSE estimator (Elgenedy et al., 2018b). Furthermore, we present simple and efficient estimation techniques for both the noise PSD and the FD noise cross-correlation per-subchannel over the different receive phases. Moreover, the proposed FD noise mitigation technique leverages the estimates of the noise PSD and cross-correlation in the design of the LMMSE estimator.

As explained in the Appendix, a cyclostationary process $x[n]$ with period P can, in general, be decomposed into P different stationary processes $x_i[n] = x[nP+i],\ i = 0, \ldots, P-1$. Hence, each time sample in a cyclostationary process is drawn from a stationary random process with a certain PSD. As an approximation, the cyclostationarity period can be divided into multiple temporal regions over which the process is assumed stationary and, thus, has a time-invariant PSD. The NB-PLC noise model presented in (Elgenedy et al., 2016) follows the general cyclostationary process definition while the model presented in (Nassar et al., 2012) adopts the temporal-region-based approximation of the NB-PLC noise as a cyclostationary process.

In this section, adopting the stationary temporal-region-based approximation for the NB-PLC noise, we propose a FD noise mitigation technique that operates on a per-subchannel basis. In particular, we derive an LMMSE estimator for the FD data symbols that exploits the spatial correlation of the FD noise per subchannel across the different receive phases. In addition, we present simple and efficient estimation techniques for both the noise PSD and the FD per-subchannel noise cross-correlation across the different receive phases.

Let $\bar{\mathbf{x}}_l(k) = [\bar{x}_{0,l}(k), \cdots, \bar{x}_{N_p-1,l}(k)]^\top$, $\bar{\zeta}_l(k) = [\bar{\zeta}_{0,l}(k), \cdots, \bar{\zeta}_{N_p-1,l}(k)]^\top$ and $\bar{\mathbf{h}}_l(k) = [\bar{h}_{0,l}(k), \cdots, \bar{h}_{N_p-1,l}(k)]^\top$. Hence, $\bar{\bar{\mathbf{x}}}_l(k)$ can be written as

$$\bar{\mathbf{y}}_l(k) = \bar{\mathbf{h}}_l(k)\bar{d}_l(k) + \bar{\zeta}_l(k). \tag{5.1}$$

The LMMSE estimate for $\bar{d}_l(k)$ is given by

$$\hat{\bar{d}}_l(k) = \left[1 + \bar{\mathbf{h}}_l^H(k)\mathbf{R}_{\bar{\zeta}\bar{\zeta},l}^{-1}(k)\bar{\mathbf{h}}_l^H(k)\right]^{-1} \bar{\mathbf{h}}_l^H(k)\mathbf{R}_{\bar{\zeta}\bar{\zeta},l}^{-1}(k)\bar{\mathbf{y}}_l(k), \tag{5.2}$$

where $\mathbf{R}_{\bar{\zeta}\bar{\zeta},l}(k) = \mathbb{E}\{\bar{\zeta}_l(k)\bar{\zeta}_l(k)^\top\}$. Alternatively, for a coded system, we can directly compute the LLR for the received FD data symbols to be used as an input to the decoder. In particular, assuming BPSK modulation, an expression for the LLR to detect $\bar{d}_l(k)$ from the FD received vector $\bar{\mathbf{y}}_l(k)$ can be derived as follows

$$\begin{aligned}\mathrm{LLR}_{l,k} &= \log \frac{f(\bar{\mathbf{y}}_l(k)|\bar{d}_l(k)=1, \bar{\mathbf{h}}_l(k))}{f(\bar{\mathbf{y}}_l(k)|\bar{d}_l(k)=-1, \bar{\mathbf{h}}_l(k))} \\ &= \left(\bar{\mathbf{y}}_l(k)+\bar{\mathbf{h}}_l(k)\right)^H \mathbf{R}^{-1}_{\bar{\zeta}\bar{\zeta},l}(k) \left(\bar{\mathbf{y}}_l(k)+\bar{\mathbf{h}}_l(k)\right)^H \\ &- \left(\bar{\mathbf{y}}_l(k)-\bar{\mathbf{h}}_l(k)\right)^H \mathbf{R}^{-1}_{\bar{\zeta}\bar{\zeta},l}(k) \left(\bar{\mathbf{y}}_l(k)-\bar{\mathbf{h}}_l(k)\right)^H .\end{aligned} \tag{5.3}$$

The calculation of (5.2) and (5.3) requires knowledge of the noise temporal regions boundaries as well as the noise PSDs and spatial correlation functions. Thus, in the following, we present simple and practical techniques to estimate these required parameters.

5.1 Noise Temporal Regions Boundaries Estimation

Here, we describe a simple technique for estimating the temporal regions boundaries of the NB-PLC noise.

For the cyclostationary NB-PLC noise, each noise temporal region has a different noise variance. Hence, as shown in Fig. 5.1, to detect the transition from one noise region to the next noise region, we use two consecutive sliding inner windows W_0 and W_1 that slide over the received signal on a sample-by-sample basis. For each window placement, we calculate the signal energy within each of the two inner windows W_0 and W_1. Let E_0 and E_1 denote the signal energies within the two windows, W_0 and W_1, respectively. To detect the transition from a region with a lower noise power to a region with a higher noise power, we use the ratio E_1/E_0, and we refer to this case as an upward transition. On the other hand, to detect the transition from a region with a higher noise power to a region with a lower noise power, we use the ratio E_0/E_1, and we refer to this case as a downward transition. As shown in Fig. 5.1, for both cases, the peak of the energy ratio in case of threshold crossing is detected to be

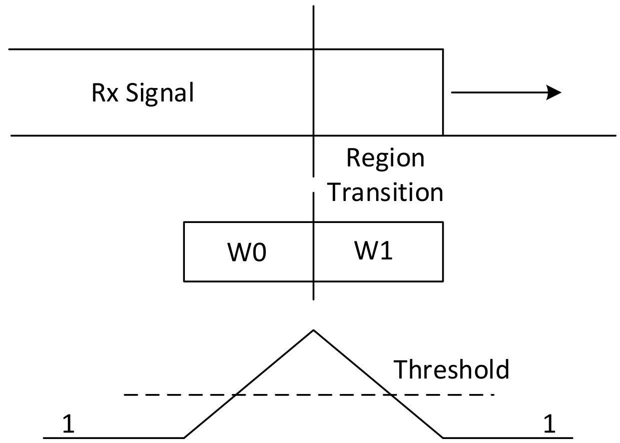

Figure 5.1: Region boundary estimation using double-sliding energy window.

corresponding to the region transition. Since the noise power is periodic, with a period of half the AC cycle, we average the noise power profile over multiple periods to obtain an accurate estimate and then we apply the double-sliding window transition detection technique as described in Fig. 5.1.

Figs. 5.2 and 5.3 show two examples for the noise power profile over one period for the upward and the downward transition cases, respectively. The noise power profile in Fig. 5.2 and 5.3 are averaged over 100 AC cycles. Moreover, Fig. 5.2 shows the ratio E_1/E_0 while Fig. 5.3 shows the ratio E_0/E_1, where both ratios are averaged over 100 AC cycles.

As shown in Fig. 5.4 and 5.5, we divide the energy ratio profile into smaller segments to detect the transitions since multiple transitions are likely to occur within one period. For instance, in Fig. 5.4 and 5.5, the sliding window length is set to 128 samples and the detection segment length is set to 256. We determine the maximum over each segment that has a threshold crossing and then the index corresponding to the maximum value over all of theses maxima is selected to be the starting index of the new region. In this technique, we assume that the separation between two transitions is larger than the segment length and this should be the design criterion for selecting the segment length.

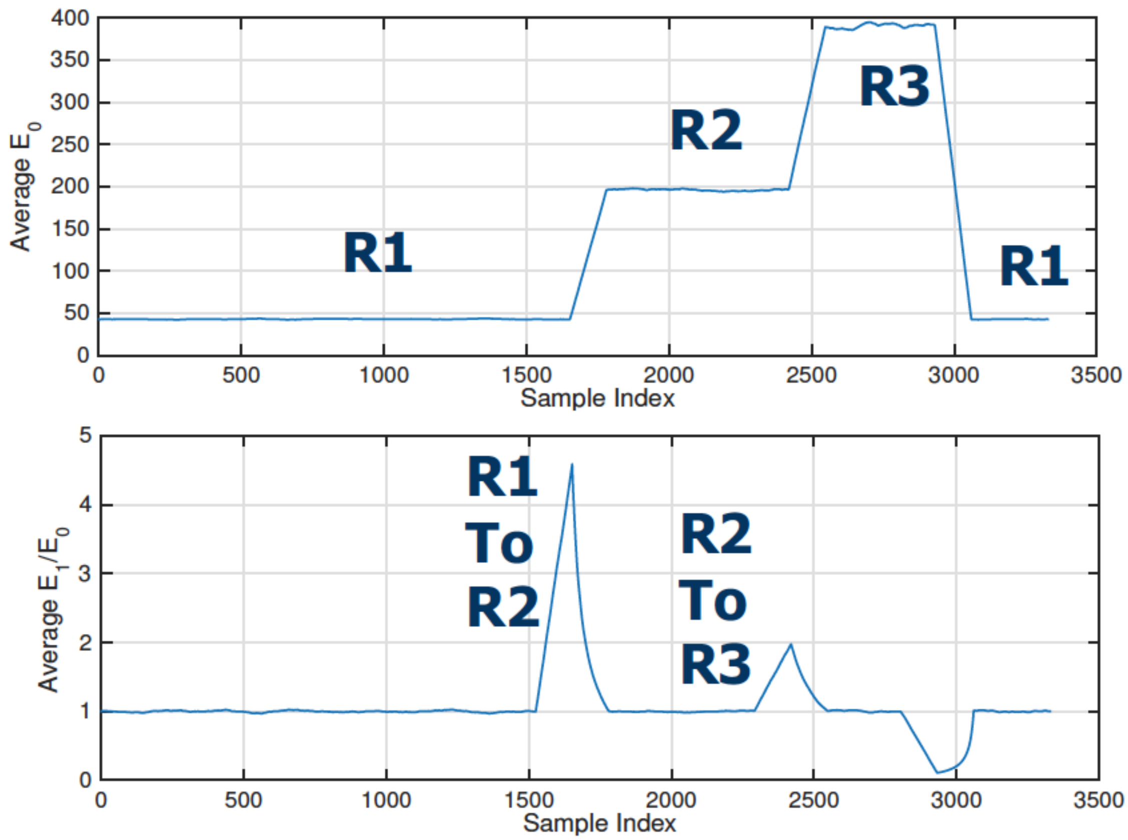

Figure 5.2: The ratio E_1/E_0 over one AC cycle period averaged over 100 cycles (an upward transition example).

To assess the performance of this technique, in Fig. 5.6, we plot the missed detection rate (MDR) versus the number of AC cycles used in averaging the noise energy profile for SNR values of 0 dB and 5 dB. In particular, in calculating the MDR, we consider it a miss if the detected region boundary is off from the correct boundary by more than 32 samples. As shown in Fig. 5.6, the MDR is less than 10^{-2} if the number of AC cycles used for the noise energy profile averaging is greater than 30 cycles. It is worth noting that the MDR is less in the case of 0 dB SNR than in the case of 5 dB SNR as the noise power is higher in the 0 dB SNR case.

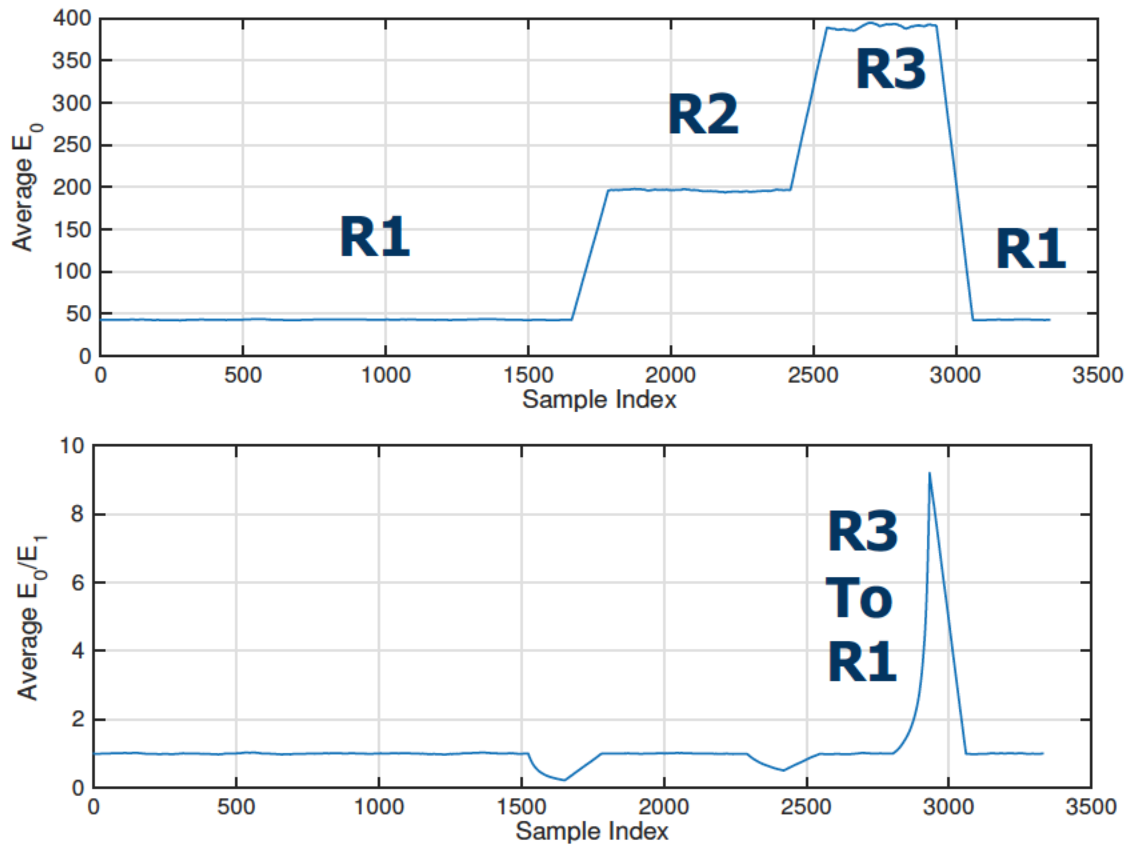

Figure 5.3: The ratio E_0/E_1 over one AC cycle period averaged over 100 cycles (a downward transition example).

5.2 Noise PSD and Spatial Correlation Estimation

Assuming knowledge of the noise temporal region boundaries, the noise PSD over each stationary temporal region is estimated only from the OFDM blocks that belong to this region. Without loss of generality, $\bar{d}_l(k)$ is assumed to have a unity variance. Thus, the noise PSD can be estimated as

$$
\begin{aligned}
\bar{\sigma}^2_{i,l,k} &= \mathbb{E}\left(|\bar{\zeta}_{i,l}(k)|^2\right) = \mathbb{E}\left(|\bar{y}_{i,l}(k)|^2\right) - \mathbb{E}\left(|\bar{h}_{i,l}(k)|^2\right) \\
&- 2\mathfrak{Re}\left[\mathbb{E}\left(\bar{h}_{i,l}(k)\right)\mathbb{E}\left(\bar{\zeta}^*_{i,l}(k)\right)\right], \\
&= \mathbb{E}\left(|\bar{y}_{i,l}(k)|^2\right) - \mathbb{E}\left(|\bar{h}_{i,l}(k)|^2\right). \qquad (5.4)
\end{aligned}
$$

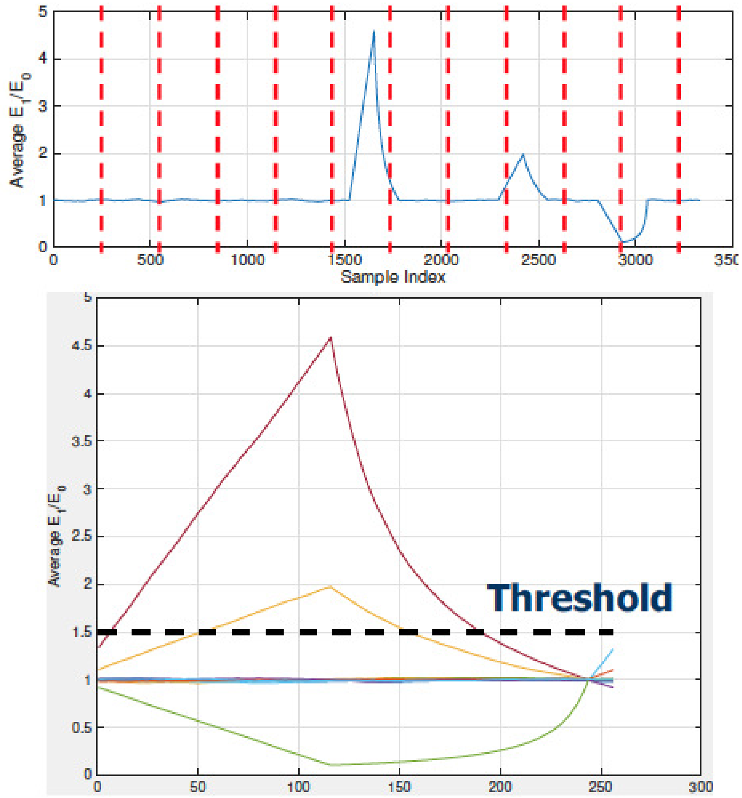

Figure 5.4: Dividing the average energy ratio into segments to perform the region boundary detection (upward transition detection example).

The expectation in (5.4) is implemented in the form of time averaging. In particular, the time averaging is performed per frequency subchannel and per noise stationary temporal region over the OFDM blocks that belong to that region. The averaging time duration has to be long enough to suppress the term $\mathbb{E}\left(\bar{\zeta}^*_{i,l}(k)\right)$ and obtain an accurate noise PSD estimate. The NB-PLC channel is a deterministic channel that is either fixed over all OFDM blocks or periodic over one (or half) AC cycle (Nassar et al., 2012). Hence, the channel averaging over one AC cycle is sufficient to obtain the average power of the channel gain per subchannel.

Similar to PSD estimation, the noise spatial cross-correlation can be estimated as follows

$$\begin{aligned} \bar{\rho}^2_{ij,l,k} &= \frac{\mathbb{E}\left(\bar{\zeta}_{i,l}(k)\bar{\zeta}^*_{j,l}(k)\right)}{\bar{\sigma}_{i,l,k}\bar{\sigma}_{j,l,k}} = \frac{1}{\bar{\sigma}_{i,l,k}\bar{\sigma}_{j,l,k}} \\ &\times \left[\mathbb{E}\left(\bar{y}_{i,l}(k)\bar{y}^*_{j,l}(k)\right) - \mathbb{E}\left(\bar{h}_{i,l}(k)\right)\mathbb{E}\left(\bar{h}^*_{j,l}(k)\right)\right]. \end{aligned} \tag{5.5}$$

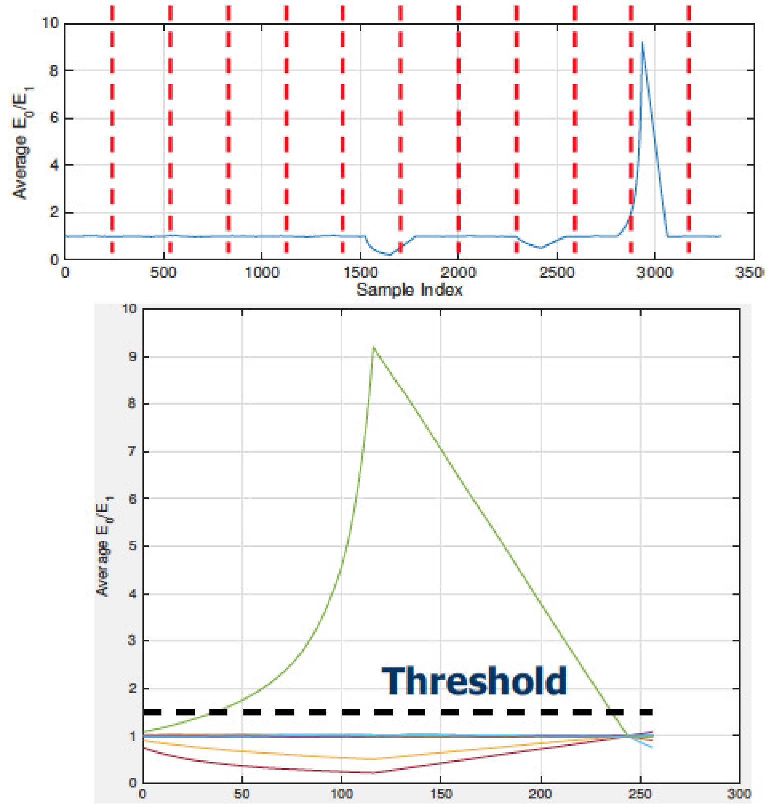

Figure 5.5: Dividing the average energy ratio into segments to perform the region boundary detection (downward transition detection example).

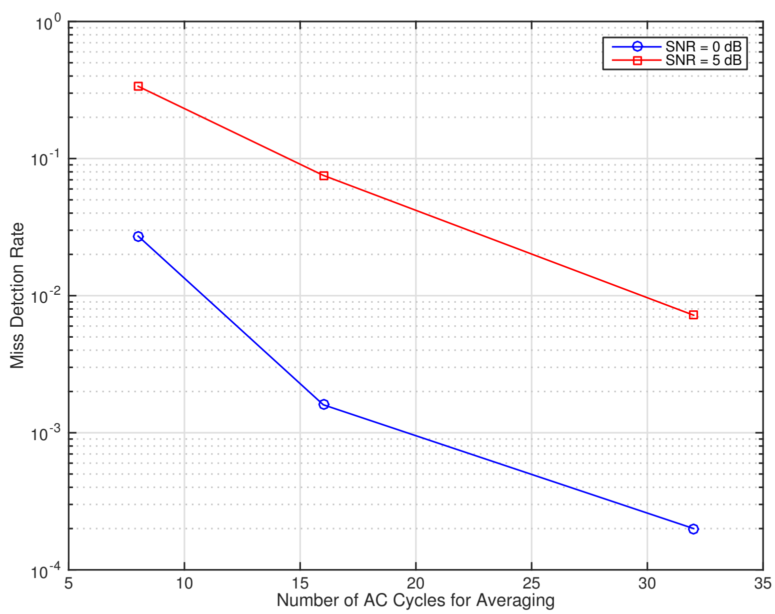

Figure 5.6: MDR versus the number of AC cycles used in the averaging.

5.3 Simulation Results

In the following simulation, the MSE is calculated as $\mathbb{E}\{(\hat{\bar{d}}_l(k) - \bar{d}_l(k))^2\}$ and plotted versus the SNR of the direct link (from transmit phase A to receive phase A) measured on the active OFDM subchannels (72 total active subchannels out of 256 subchannels symmetric around the DC) so that the results can be compared to a SISO system utilizing the same link. Furthermore, the BER performance is plotted versus $\frac{E_b}{N_o}$ of the direct link, where E_b is the average energy per information bit in both the uncoded and coded cases and $\frac{N_o}{2}$ is the noise variance.

5.3.1 MSE Performance

Fig. 5.7 depicts the MSE achieved by the proposed noise mitigation technique. It is evident from Fig. 5.7 that the simulated MSE almost matches the analytical expression. A small mismatch in the MSE can be observed and the reason is that the stationarity assumption per temporal noise region, which is adopted in deriving the MSE expression, is not very accurate for the FFB noise model.

5.3.2 Average BER Performance

The coded average BER performance for the proposed receiver is shown in Fig. 5.8. The gain for the SIMO temporal-region-based mitigation technique over the SISO receiver without noise mitigation is close to 7 dB at a coded BER of 10^{-4}. For the SISO case, the estimated noise PSD per temporal region is used in the LLR calculations and it shows more than 3 dB gain at coded BER of 10^{-4} over the SISO receiver without mitigation. Since there is no previous work in the literature on the SIMO receivers under the cyclostationary noise, we show the performance of the following two cases as benchmarks:

1. The performance of the conventional SIMO MRC combiner without noise filtering, i.e., assuming stationary noise. As shown in Fig. 5.8, the coded BER performance of our

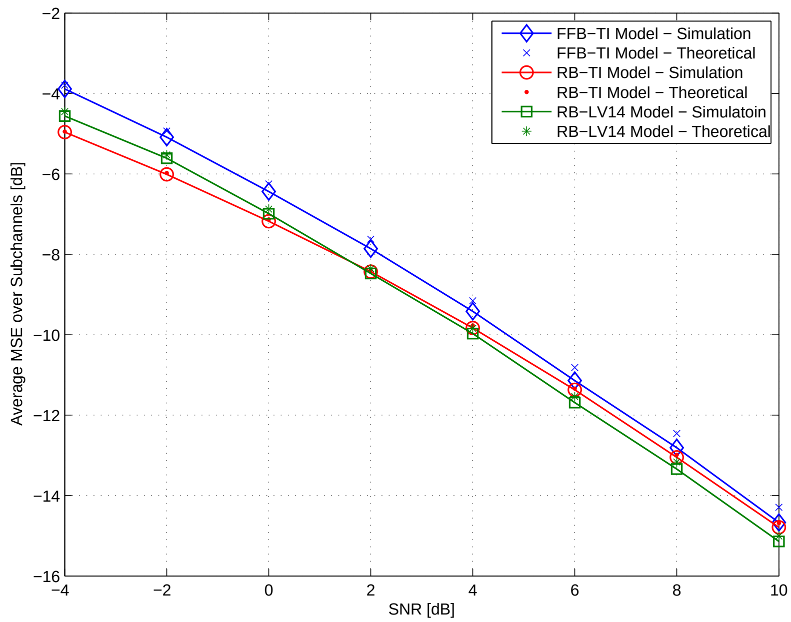

Figure 5.7: MSE of the proposed SIMO FD technique for different noise models.

proposed SIMO mitigation technique outperforms the conventional MRC by more than 5 dB at a coded BER of 10^{-3}.

2. We include the SISO coded BER performance of the technique in (Shlezinger and Dabora, 2014) which is based on the cascaded FRESH filtering design. As shown in Fig. 5.8, our proposed SISO temporal-region-based mitigation technique achieves little better performance than the SISO mitigation technique developed in (Shlezinger and Dabora, 2014) at a much lower complexity. The complexity of the FRESH filter developed in (Shlezinger and Dabora, 2014) is $1600 \times 5 + 128 \times 5 = 8640$ taps while the complexity of our proposed SISO temporal-region-based mitigation technique is only 36 multiplications each OFDM symbol. Moreover, our proposed SIMO temporal-region-based mitigation technique outperforms the SISO mitigation technique developed in (Shlezinger and Dabora, 2014) by 4 dB at a coded BER of 10^{-4} while the complexity of our proposed SIMO receiver is only 36×4 multiplications per OFDM symbol.

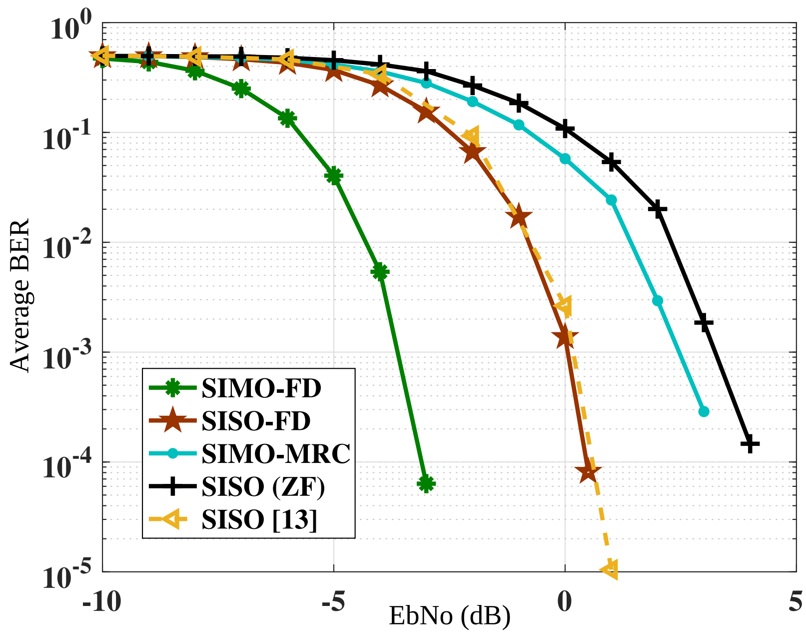

Figure 5.8: Coded average BER for the proposed temporal-region-based cyclostationary noise mitigation technique.

CHAPTER 6

FREQUENCY-SHIFT-BASED CYCLOSTATIONARY NOISE MITIGATION FOR SIMO POWERLINE COMMUNICATIONS [1]

In this chapter, for SIMO NB-PLC, we propose two TD LMMSE-estimation-based cyclostationary noise mitigation techniques using FRESH filtering, namely the joint TD equalization and noise FRESH filtering (TD-ENF) technique and the TD noise FRESH filtering (TD-NF) technique (Elgenedy et al., 2018a). The proposed TD SIMO noise mitigation techniques exploit the joint cyclostationarity of both the NB-PLC noise samples and the OFDM signal samples over the different receive power line phases by considering their cyclic auto and cross-correlations. Both the TD-ENF and the TD-NF techniques filter out the cyclostationary NB-PLC noise using only a single FRESH filtering stage that includes the cyclic frequencies of both the NB-PLC noise and the OFDM signal. The TD-ENF technique estimates the TD OFDM information signal by designing the FRESH filters to jointly equalize the channel and filter out the noise. On the other hand, the TD-NF technique estimates the TD OFDM signal, which is the signal at the channel output, without equalizing the channel. Then, in the FD, an LMMSE-based channel equalization and signal combining technique is integrated into the log-likelihood ratios (LLRs) computation for the information bits.

It is worth noting that our proposed noise mitigation techniques can be also classified into FRESH filtering based techniques and region based techniques similar to the noise modeling classification. Figs. 6.1 and 6.2 show the classification of the noise modeling approaches as well as the proposed noise mitigation techniques.

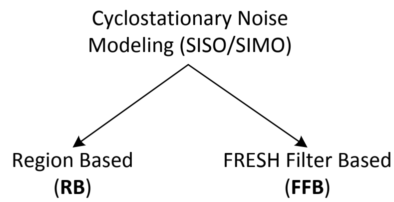

Figure 6.1: NB-PLC cyclostationary noise modeling classification.

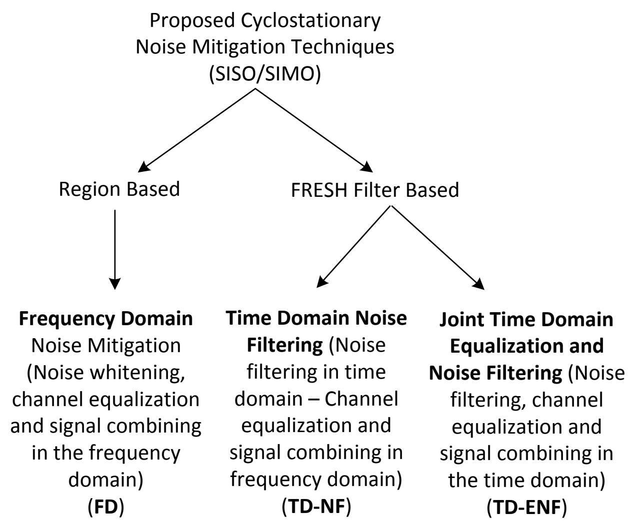

Figure 6.2: NB-PLC cyclostationary noise proposed mitigation techniques classification.

6.1 Proposed SIMO TD Noise FRESH Filtering (TD-NF) Technique

In this technique, we process the TD SIMO received signal to estimate the TD OFDM signal, which is the noise-free signal at the channel output, on each receive powerline phase. After that, we perform the channel equalization and combining in the FD as part of the LLRs computation for the information bits. Thus, we refer to this technique as the *TD noise FRESH filtering technique* (TD-NF).

In this section, first we start by establishing the optimality of the SIMO linear almost periodic time-varying filters (LAPTV) for LMMSE estimation of the *almost cyclostationary* signals (ACS). We show that the optimal set of the filter's cyclic frequencies is the set of all the cyclic frequencies of both the information and the noise signals. Then, we present our proposed SIMO TD-NF technique as a suboptimal LAPTV filtering technique using only a

Table 6.1: The key variables used in Sections 6.1 and 6.2.

Definition	Dimension
$\mathbf{x}(n) = [x_0(n),\, x_1(n),\, \cdots,\, x_{N_p-1}(n)]^\top$	N_p-vector
$\zeta(n) = [\zeta_0(n),\, \zeta_1(n),\, \cdots,\, \zeta_{N_p-1}(n)]^\top$	N_p-vector
$\mathbf{y}(n) = [y_0(n),\, y_1(n),\, \cdots,\, y_{N_p-1}(n)]^\top$	N_p-vector
$\mathcal{A}_{xx} = \mathcal{A}_{dd} = \{m/N_B : m \in \mathbb{Z}\},\ \mathcal{A}_{\zeta\zeta} = \{m/P_\zeta : m \in \mathbb{Z}\}$	
$\mathbf{R}_{\mathbf{xx}}(k,n) = \mathbb{E}\left\{\mathbf{x}(k)\mathbf{x}^\top(n)\right\} \xrightarrow{FS} \{\mathbf{R}^\alpha_{\mathbf{xx}}(l) : \alpha \in \mathcal{A}_{xx}\}$ $[\mathbf{R}_{\mathbf{xx}}(k,n)]_{i,j} = r_{x_ix_j}(k,n),\ [\mathbf{R}^\alpha_{\mathbf{xx}}(l)]_{i,j} = r^\alpha_{x_ix_j}(l)$	$N_p \times N_p-$ Matrix
$\mathbf{R}_{\zeta\zeta}(k,n) = \mathbb{E}\left\{\zeta(k)\zeta^\top(n)\right\} \xrightarrow{FS} \{\mathbf{R}^\alpha_{\zeta\zeta}(l) : \alpha \in \mathcal{A}_{\zeta\zeta}\}$ $[\mathbf{R}_{\zeta\zeta}(k,n)]_{i,j} = r_{\zeta_i\zeta_j}(k,n),\ \left[\mathbf{R}^\alpha_{\zeta\zeta}(l)\right]_{i,j} = r^\alpha_{\zeta_i\zeta_j}(l)$	$N_p \times N_p-$ Matrix
$\mathbf{R}_{\mathbf{yy}}(k,n) = \mathbb{E}\left\{\mathbf{y}(k)\mathbf{y}^\top(n)\right\} \xrightarrow{FS} \{\mathbf{R}^\alpha_{\mathbf{yy}}(l) : \alpha \in \mathcal{A}_{yy}\}$ $[\mathbf{R}_{\mathbf{yy}}(k,n)]_{i,j} = r_{y_iy_j}(k,n),\ \left[\mathbf{R}^\alpha_{\mathbf{yy}}(l)\right]_{i,j} = r^\alpha_{y_iy_j}(l)$	$N_p \times N_p-$ Matrix
$\mathbf{r}_{x_i\mathbf{y}}(k,n) = \mathbb{E}\left\{x_i(k)\mathbf{y}^\top(n)\right\} \xrightarrow{FS} \{\mathbf{r}^\alpha_{x_i\mathbf{y}}(l) : \alpha \in \mathcal{A}_{xy}\}$ $[\mathbf{r}_{x_i\mathbf{y}}(k,n)]_j = r_{x_iy_j}(k,n),\ \left[\mathbf{r}^\alpha_{x_i\mathbf{y}}(l)\right]_j = r^\alpha_{x_iy_j}(l)$	N_p-vector
$\mathbf{r}_{x_i\mathbf{x}}(k,n) = \mathbb{E}\left\{x_i(k)\mathbf{x}(n)\right\} = \mathbf{e}_i^\top\mathbf{R}_{\mathbf{xx}}(k,n) \xrightarrow{FS} \{\mathbf{r}^\alpha_{x_i\mathbf{x}}(l) = \mathbf{e}_i^\top\mathbf{R}^\alpha_{\mathbf{xx}}(l) : \alpha \in \mathcal{A}_{xx}\}$ $[\mathbf{r}_{x_i\mathbf{x}}(k,n)]_j = r_{x_ix_j}(k,n),\ \left[\mathbf{r}^\alpha_{x_i\mathbf{x}}(l)\right]_j = r^\alpha_{x_ix_j}(l)$	N_p-vector
$r_{dd}(k,n) = \mathbb{E}\left\{d(k)d(n)\right\} \xrightarrow{FS} \{r^\alpha_{dd}(l) : \alpha \in \mathcal{A}_{dd}\}$	Scalar
$\mathbf{r}_{d\mathbf{y}}(k,n) = \mathbb{E}\left\{d(k)\mathbf{y}^\top(n)\right\} \xrightarrow{FS} \{\mathbf{r}^\alpha_{d\mathbf{y}}(l) : \alpha \in \mathcal{A}_{dy}\}$ $[\mathbf{r}_{d\mathbf{y}}(k,n)]_j = r_{dy_j}(k,n),\ \left[\mathbf{r}^\alpha_{d\mathbf{y}}(l)\right]_j = r^\alpha_{dy_j}(l)$	N_p-vector
$\mathbf{r}_{d\mathbf{x}}(k,n) = \mathbb{E}\left\{d(k)\mathbf{x}(n)\right\} \xrightarrow{FS} \{\mathbf{r}^\alpha_{d\mathbf{x}}(l) : \alpha \in \mathcal{A}_{dd}\}$ $[\mathbf{r}_{d\mathbf{x}}(k,n)]_j = r_{dx_j}(k,n),\ [\mathbf{r}^\alpha_{d\mathbf{x}}(l)]_j = r^\alpha_{dx_j}(l)$	N_p-vector
$\mathbf{g}_i(k,n) \xrightarrow{FS} \{\mathbf{g}^\alpha_i(l) : \alpha \in \mathcal{A}_g\}$ $\mathbf{g}_i(k,n) =$ $[g_{i,0}(k,\, n),\, g_{i,1}(k,\, n),\, \cdots,\, g_{i,N_p-1}(k,\, n)]^\top$ $\mathbf{g}^\alpha_i(l) = [g^\alpha_{i,0}(l),\, g^\alpha_{i,1}(l),\, \cdots,\, g^\alpha_{i,N_p-1}(l)]^\top$	N_p-vector
$\mathbf{g}(k,n) \xrightarrow{FS} \{\mathbf{g}^\alpha(l) : \alpha \in \mathcal{A}_g\}$ $\mathbf{g}(k,n) = [g_0(k,\, n),\, g_1(k,\, n),\, \cdots,\, g_{N_p-1}(k,\, n)]^\top$ $\mathbf{g}^\alpha(l) = [g^\alpha_0(l),\, g^\alpha_1(l), \cdots,\, g^\alpha_{N_p-1}(l)]^\top$	N_p-vector

limited subset of cyclic frequencies from the optimal cyclic frequencies set. The mathematical variables used in this section and the next section are listed in Table 6.1.

6.1.1 TD-NF Optimal SIMO LAPTV Filtering

Considering the TD SIMO received signal expression in (2.1a), we formulate an LMMSE minimization problem to estimate the TD OFDM signals, $\{x_i(n) : i \in \{0, 1, \cdots, N_p\}\}$, over the N_p receive phases as follows

$$\min_{\mathbf{g}_i(n,.)\in\mathbb{R}^{N_p}} \mathrm{MSE}_{x_i(n)} = \mathbb{E}\left\{[x_i(n) - \hat{x}_i(n)]^2\right\}$$

$$, \ i \in \{0, 1, \cdots, N_p\}, \ \forall n \in \mathbb{Z}, \tag{6.1a}$$

$$\hat{x}_i(n) = \sum_{m\in\mathbb{Z}} \mathbf{g}_i^\top(n, m)\mathbf{y}(m), \tag{6.1b}$$

where $\mathbf{g}_i(k, n)$ is an N_p-vector that contains the impulse responses of the set of filters designed to estimate $x_i(n)$. It is worth noting that $y_i(n)$ is an ACS process since it is the sum of the two ACS processes $x_i(n)$ and $\zeta_i(n)$. Furthermore, the signals $\{x_i(n), y_i(n) : i \in \{0, 1, \cdots, N_p\}\}$ are pairwise jointly ACS since each signal is an ACS process and they are all pairwise mutually dependent. In addition, since $x_i(n)$ and $\{y_j(n) : j \in \{0, 1, \cdots, N_p\}\}$ are jointly ACS and not jointly stationary, using a set of LTI filters is no longer optimal in the sense of minimizing the MSE, and the optimal LMMSE estimation filters are LAPTV filters (Gardner, 1986). Thus, $\mathbf{g}_i(k, n)$ is almost periodic in both k and n with some integer period P_g for each $l = k - n$, i.e., $\mathbf{g}_i(k, n) \approx \mathbf{g}_i(k + P_g, n + P_g)$, $\forall l = k - n \in \mathbb{Z}$, where P_g is the least common multiple of all the discrete-time periodicities of the functions involved in the design formula for $\mathbf{g}_i(k, n)$. Therefore, $\mathbf{g}_i(k, n)$ can be represented by the Fourier series

$$\mathbf{g}_i(k, n) = \sum_{\alpha\in\mathcal{A}_g} \mathbf{g}_i^\alpha(k - n)\, \mathrm{e}^{j2\pi\alpha n}, \tag{6.2a}$$

$$\mathbf{g}_i^\alpha(l) = \langle \mathbf{g}_i(n + l, n)\mathrm{e}^{-j2\pi\alpha n}\rangle_n, \tag{6.2b}$$

where $\mathbf{g}_i^\alpha(k - n)$ is an N_p-vector that contains the Fourier series coefficients of $\mathbf{g}_i(k, n)$. In addition, $\mathcal{A}_g$ is a countable set that contains all the integer multiples of the fundamental frequencies of the functions involved in the design formula for $\mathbf{g}_i(k,n)$. Since $\{x_i(n) : i \in \{0, 1, \cdots, N_p-1\}\}$ and $\{\zeta_i(n) : i \in \{0, 1, \cdots, N_p-1\}\}$ are uncorrelated, then $\mathbf{R}_{\mathbf{yy}}(k,n) = \mathbf{R}_{\mathbf{xx}}(k,n) + \mathbf{R}_{\zeta\zeta}(k,n)$ and $\mathbf{r}_{x_i\mathbf{y}}(k,n) = \mathbf{r}_{x_i\mathbf{x}}(k,n)$. Hence, we note that $\mathcal{A}_{yy} = \mathcal{A}_{xx} \cup \mathcal{A}_{\zeta\zeta}$ and $\mathcal{A}_{xy} = \mathcal{A}_{xx}$.

To obtain the optimal vector $\mathbf{g}_i(k,n)$ that minimizes $\mathrm{MSE}_{x_i(n)}$ in (6.1a), we set $\partial\mathrm{MSE}_{x_i(n)} / \partial\mathbf{g}_i^\top(n,k) = \mathbf{0}_{1\times N_p}$, which yields

$$\sum_{m\in\mathbb{Z}} \mathbf{g}_i^\top(n,m)\mathbf{R}_{\mathbf{yy}}(m,k) = \mathbf{r}_{x_i\mathbf{y}}(n,k)$$
$$, \; i \in \{0, \cdots, N_p-1\}, \; \forall n, \; k \in \mathbb{Z}. \tag{6.3}$$

Using the expressions of the Fourier series pairs for $\mathbf{g}_i(k,n)$, $\mathbf{R}_{\mathbf{yy}}(k,n)$ and $\mathbf{r}_{x_i\mathbf{y}}(k,n)$, we derived the following design formula for the optimal LAPTV filter. In particular, consider that $\mathbf{R}_{\mathbf{yy}}(k,n)$ and $\mathbf{r}_{x_i\mathbf{y}}(k,n)$ have the following generalized Fourier series pairs (assuming convergence)

$$\mathbf{R}_{\mathbf{yy}}(k,n) = \sum_{\beta\in\mathcal{A}_{yy}} \mathbf{R}_{\mathbf{yy}}^{\beta}(k-n)\mathrm{e}^{j2\pi\beta n}, \tag{6.4a}$$

$$\mathbf{R}_{\mathbf{yy}}^{\beta}(l) = \langle \mathbf{R}_{\mathbf{yy}}(n+l,n)\mathrm{e}^{-j2\pi\beta n}\rangle_n, \tag{6.4b}$$

$$\mathbf{r}_{x_i\mathbf{y}}(k,n) = \sum_{\gamma\in\mathcal{A}_{xy}} \mathbf{r}_{x_i\mathbf{y}}^{\gamma}(k-n)\mathrm{e}^{j2\pi\gamma n}, \tag{6.4c}$$

$$\mathbf{r}_{x_i\mathbf{y}}^{\gamma}(l) = \langle \mathbf{r}_{x_i\mathbf{y}}(n+l,n)\mathrm{e}^{-j2\pi\gamma n}\rangle_n. \tag{6.4d}$$

Substituting (6.2a) and (6.4a) in (6.3) yields

$$\sum_{m\in\mathbb{Z}} \sum_{\alpha\in\mathcal{A}_g} \sum_{\beta\in\mathcal{A}_{xx}\cup\mathcal{A}_{\zeta\zeta}} \left[\mathbf{g}_i^{\alpha}(n-m)\right]^\top \mathbf{R}_{\mathbf{yy}}^{\beta}(m-k)$$
$$\times\, \mathrm{e}^{j2\pi(\alpha m+\beta k)} = \mathbf{r}_{x_i\mathbf{y}}(n,k), \forall n, \; k \in \mathbb{Z}. \tag{6.5}$$

Setting $l = n - k$ in (6.5) and then inserting (6.5) into (6.4d), we get

$$\begin{aligned}\langle\sum_{m\in\mathbb{Z}}\sum_{\alpha\in\mathcal{A}_g}\sum_{\beta\in\mathcal{A}_{xx}\cup\mathcal{A}_{\zeta\zeta}} \left[\mathbf{g}_i^{\alpha}(k+l-m)\right]^{\top}\mathbf{R}_{\mathbf{yy}}^{\beta}(m-k) \\ \times \mathrm{e}^{j2\pi\alpha m}\mathrm{e}^{j2\pi(\beta-\gamma)k}\rangle_k = \mathbf{r}_{x_i\mathbf{y}}^{\gamma}(l), \forall l\in\mathbb{Z}.\end{aligned} \tag{6.6}$$

Setting $q = m - k$ yields

$$\begin{aligned}\sum_{q\in\mathbb{Z}}\sum_{\alpha\in\mathcal{A}_g}\sum_{\beta\in\mathcal{A}_{xx}\cup\mathcal{A}_{\zeta\zeta}} \left[\mathbf{g}_i^{\alpha}(l-q)\right]^{\top}\mathbf{R}_{\mathbf{yy}}^{\beta}(q)\mathrm{e}^{j2\pi\alpha q} \\ \times \langle\mathrm{e}^{j2\pi(\beta-\gamma+\alpha)k}\rangle_k = \mathbf{r}_{x_i\mathbf{y}}^{\gamma}(l), \forall l\in\mathbb{Z}.\end{aligned} \tag{6.7}$$

Using the identity

$$\langle\mathrm{e}^{j2\pi(\beta-\gamma+\alpha)k}\rangle_k = \begin{cases}1, & \beta=\gamma-\alpha \\ 0, & \text{otherwise}\end{cases}.$$

Hence, we arrive at the following design formula for the optimal LAPTV filter

$$\begin{aligned}\sum_{\alpha\in\mathcal{A}_g}\sum_{q\in\mathbb{Z}}\left[\mathbf{g}_i^{\alpha}(l-q)\right]^{\top}\mathbf{R}_{\mathbf{yy}}^{\gamma-\alpha}(q)\mathrm{e}^{j2\pi\alpha q} &= \mathbf{r}_{x_i\mathbf{y}}^{\gamma}(l), \forall l\in\mathbb{Z} \\ ,\gamma,\alpha\in\mathcal{A}_{xx}\cup\mathcal{A}_{\zeta\zeta}.\end{aligned} \tag{6.8}$$

The formula in (6.8) simplifies the design of the optimal LAPTV filter set $\{\mathrm{g}_{i,j}(k,n) : i,j \in \{0, 1, \cdots, N_p-1\}\}$ into designing the set of LTI filters $\{\mathrm{g}_{i,j}^{\alpha}(l = k-n) : \alpha \in \mathcal{A}_g, i,j \in \{0, 1, \cdots, N_p-1\}\}$, which correspond to their Fourier series coefficients. It is worth mentioning that the design formula in (6.8) is a vector generalization of the optimal MMSE filter design derived in (Gardner, 1986, Eq. 12.284) where both formulas are equivalent when setting $N_p = 1$ in (6.8).

Let $\grave{\mathcal{A}}_{xx} = \mathcal{A}_{xx}\backslash\{0\}$ and $\grave{\mathcal{A}}_{\zeta\zeta} = \mathcal{A}_{\zeta\zeta}\backslash\{0\}$. Thus, if $\alpha,\gamma\in\mathcal{A}_{xx}$, then $\gamma-\alpha\in\mathcal{A}_{xx}\cup\mathcal{A}_{\zeta\zeta}$ and $\mathbf{R}_{\mathbf{yy}}^{\gamma-\alpha}(l)\neq 0$, $\mathbf{r}_{x_i\mathbf{y}}^{\gamma}(l)\neq 0$. On the other hand, if $\alpha,\gamma\in\mathcal{A}_{\zeta\zeta}$, then $\gamma-\alpha\in\mathcal{A}_{xx}\cup\mathcal{A}_{\zeta\zeta}$ and $\mathbf{R}_{\mathbf{yy}}^{\gamma-\alpha}(l)\neq 0$, $\mathbf{r}_{x_i\mathbf{y}}^{\gamma}(l) = 0$. Otherwise, if $\alpha\in\grave{\mathcal{A}}_{xx}$ while $\gamma\in\grave{\mathcal{A}}_{\zeta\zeta}$, or vice versa, then

$\gamma - \alpha \notin \mathcal{A}_{xx} \cup \mathcal{A}_{\zeta\zeta}$ and $\mathbf{R}_{\mathbf{yy}}^{\gamma-\alpha}(l) = 0$. Hence, $\alpha, \gamma \in \mathcal{A}_{xx}$ or $\alpha, \gamma \in \mathcal{A}_{\zeta\zeta}$ is required such that $\mathbf{R}_{\mathbf{yy}}^{\gamma-\alpha}(l) \neq 0$ and the left-hand side of the system of equations in (6.8) is non-zero. Therefore, we conclude that the optimal selection of the cyclic frequencies for $\mathrm{g}_{i,j}(k,n)$ is to range over all the cyclic frequencies of *both* the information and the noise signals, or equivalently $\mathcal{A}_g = \mathcal{A}_{xx} \cup \mathcal{A}_{\zeta\zeta}$. Therefore, P_g is the least common multiple of N_B and P_ζ.

It is worth mentioning that the two-stage SISO FRESH filtering technique presented in (Shlezinger and Dabora, 2014) is suboptimal in the sense that it separates the cyclostationary noise estimation/cancellation and the OFDM signal estimation over the two stages. Furthermore, the cyclic frequencies of both the noise and the OFDM signal are not jointly included in the design of the first stage, which is employed for the cyclostationary noise estimation. However, an optimal design has to include all the cyclic frequencies of both the noise and the OFDM signal in a single FRESH filtering stage. In Section 6.3, for the SISO case, we present a performance comparison between a single-stage FRESH filtering and the two-stage FRESH filtering proposed in (Shlezinger and Dabora, 2014).

The MSE associated with the optimal filter $\mathbf{g}_i(k,n)$ can be obtained by simplifying $\mathrm{MSE}_{x_i(n)}$ in (6.1a) as follows

$$\mathrm{MSE}_{x_i(n)} = r_{x_i x_i}(n,n) - \sum_{m\in\mathbb{Z}} \mathbf{g}_i^\top(n,m)\mathbf{r}_{\mathbf{x}x_i}(m,n). \tag{6.9}$$

Therefore, from (6.9), we note that the MSE is an almost periodic function since it depends on the auto-correlation of the TD OFDM signal as well as the LMMSE filter. Hence, to measure the performance by a single number, we adopt the TAMSE given by $\mathrm{TAMSE}_{x_i(n)} = \langle \mathrm{MSE}_{x_i(n)} \rangle_n$ (Gardner, 1986). Inserting (6.2a) into (6.1b) yields

$$\hat{x}_i(n) = \sum_{\alpha\in\mathcal{A}_g} \sum_{m\in\mathbb{Z}} \left[\mathbf{g}_i^\alpha(n-m)\right]^\top \left[\mathbf{y}(m)\mathrm{e}^{j2\pi\alpha m}\right], \tag{6.10}$$

which represents the optimal FRESH-filtering-equivalent form of the estimator for $x_i(n)$. In practice, suboptimal performance is achieved when constraining α to range over only a limited set of cyclic frequencies within $\mathcal{A}_g = \mathcal{A}_{xx} \cup \mathcal{A}_{\zeta\zeta}$, which is the main takeaway from the previous analysis.

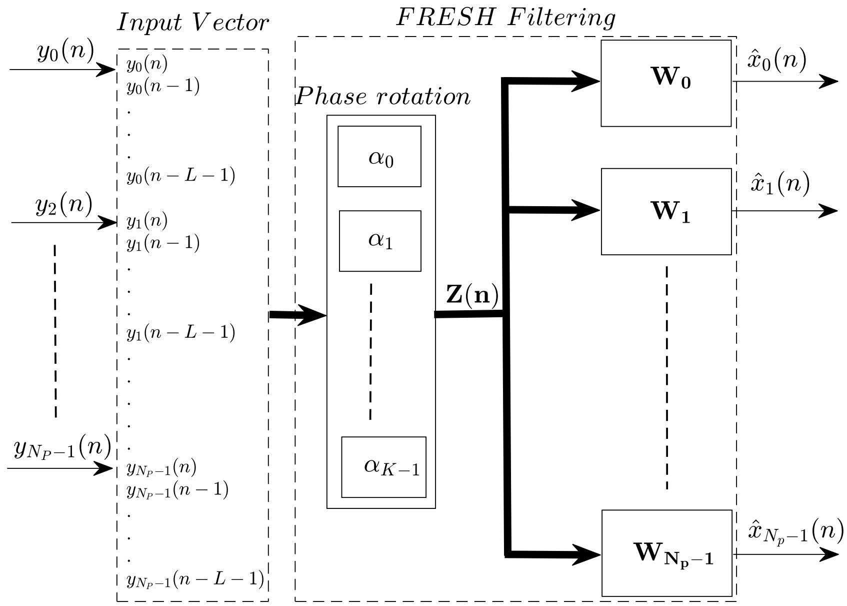

Figure 6.3: System block diagram illustrating the proposed SIMO TD-NF technique.

6.1.2 TD-NF Suboptimal SIMO FRESH Filtering Design

The optimal LMMSE estimation formula in (6.10) assumes infinite-length filters as well as an infinite set of cyclic frequencies. From (6.8), we have shown that the cyclic frequencies of the LMMSE filter must belong to the set $\mathcal{A}_{xx} \cup \mathcal{A}_{\zeta\zeta}$. However, for the suboptimal SIMO FRESH filter design, determining the best subset of cyclic frequencies, $\mathcal{A}_g^s \subset \mathcal{A}_{xx} \cup \mathcal{A}_{\zeta\zeta}$, under some design constraints is quite challenging. For instance, under a maximum number of cyclic frequencies constraint, the best $\mathcal{A}_g^s$ is highly dependent on the cyclic correlation functions $\mathbf{R}_{\mathbf{yy}}^{\gamma-\alpha}(l)$ and $\mathbf{r}_{x_i\mathbf{y}}^{\gamma}(l)$, which are dependent on the lag parameter l. To simplify the FRESH filter design, $\mathcal{A}_g^s$ is typically fixed beforehand and the common approach is to select the cyclic frequencies that correspond to the largest values of the functions $\mathbf{R}_{\mathbf{yy}}^{\gamma-\alpha}(l)$ and $\mathbf{r}_{x_i\mathbf{y}}^{\gamma}(l)$ (Ojeda and Grajal, 2011; Gardner, 1993). Hence, for a fixed $\mathcal{A}_g^s = \{\alpha_k : k \in \{0, \cdots, K-1\}\}$ of cardinality K, and assuming a finite length L for $\mathbf{g}_i^{\alpha}(n-m)$, (6.10) can be rewritten as follows

$$\hat{x}_i(n) \;\; = \;\; \sum_{\alpha \in \mathcal{A}_g^s} \sum_{m=n-L+1}^{n} \left[\mathbf{g}_i^{\alpha}(n-m)\right]^{\top} \left[\mathbf{y}(m) e^{j2\pi\alpha m}\right]$$

$$= \mathbf{w}_i^H \mathbf{z}(n), \tag{6.11}$$

where $\mathbf{w}_i = [\mathbf{w}_i^{\alpha_0 \top}, \cdots, \mathbf{w}_i^{\alpha_{K-1} \top}]^\top$, and $\mathbf{w}_i^{\alpha_k}$ is an N_pL-vector such that $[\mathbf{w}_i^{\alpha_k}]_{jL+l} = \left(\mathrm{g}_{i,j}^{\alpha_k}(l)\right)^*$, where $j \in \{0, \cdots, N_p-1\}$ and $l \in \{0, \cdots, L-1\}$. In addition, $\mathbf{z}(n) = [\mathbf{z}^{\alpha_0 \top}(n), \cdots, \mathbf{z}^{\alpha_{K-1} \top}(n)]^\top$, and $\mathbf{z}^{\alpha_k}(n)$ is an N_pL-vector such that

$$[\mathbf{z}^{\alpha_k}(n)]_{jL+l} = y_j(n-l)\mathrm{e}^{j2\pi\alpha_k(n-l)}. \tag{6.12}$$

Furthermore, $\mathbf{z}(n) = \mathbf{\Sigma}(n)\mathbf{y}(n)$, where $\mathbf{\Sigma}(n)$ is a $KN_pL \times KN_pL$ diagonal matrix where $[\mathbf{\Sigma}(n)]_{kN_pL+jL+l} = \mathrm{e}^{j2\pi\alpha_k(n-l)}$ and $\mathbf{y}(n) = [\mathbf{y}^{\alpha\top}(n), \cdots, \mathbf{y}^{\alpha\top}(n)]^\top$, which is the vector $\mathbf{y}^{\alpha}(n)$ repeated K times, where $\mathbf{y}^{\alpha}(n)$ is an N_pL-vector such that $[\mathbf{y}^{\alpha}(n)]_{jL+l} = y_j(n-l)$.

A block diagram for the SIMO TD-NF technique as described by (6.11) for the case of two receive phases is shown in Fig. 6.3. It is worth noting that $\mathcal{A}_g^s$ is assumed to contain $\alpha_k = 0$ which corresponds to the stationary component of the correlation function. Hence, according to (6.11), $\hat{x}_i(n)$ is estimated by applying a bank of N_pK filters, which are represented by the concatenated filter $\mathbf{w}_i$, to the frequency-shifted versions of the SIMO received signals $\{y_j(n) : j \in \{0, \cdots, N_p-1\}\}$. The suboptimal filter $\hat{\mathbf{w}}_i$ is obtained by solving the linear system of equations in (6.8) after constraining $\mathcal{A}_g$ to $\mathcal{A}_g^s$ and setting $\mathrm{g}_{i,j}^{\alpha_k}(l) = 0$, $\forall l \notin \{0, \cdots, L-1\}$. In this case, $\hat{\mathbf{w}}_i$ is optimal only when compared to all other FRESH filters that use the cyclic frequency set $\mathcal{A}_g^s$ and are limited to L filter coefficients. On the other hand, the optimal FRESH filter given by (6.8) is optimal within the class of linear estimators. An equivalent, yet more compact, expression for $\hat{\mathbf{w}}_i$ can be obtained from minimizing the TAMSE with respect to $\mathbf{w}_i$ as follows

$$\begin{aligned}\min_{\mathbf{w}_i \in \mathbb{R}^{KN_pL}} \mathrm{TAMSE}_{x_i(n)} &= \langle \mathbb{E}\left\{|x_i(n) - \mathbf{w}_i^H \mathbf{z}(n)|^2\right\}\rangle_n \\ &, \ i \in \{0,\ 1,\ \cdots,\ N_p\},\ \forall n \in \mathbb{Z}.\end{aligned} \tag{6.13}$$

Setting the derivative of $\mathrm{TAMSE}_{x_i(n)}$ with respect to $\mathbf{w}_i^*$ to zero yields

$$\hat{\mathbf{w}}_i = \overline{\mathbf{R}}_{\mathbf{zz}}^{-1} \overline{\mathbf{r}}_{\mathbf{z}x_i}, \tag{6.14}$$

where $\overline{\mathbf{R}}_{\mathbf{zz}} = \langle \mathbb{E}\left\{\mathbf{z}(n)\mathbf{z}^H(n)\right\}\rangle_n$ is a $KN_pL \times KN_pL$ matrix and $\overline{\mathbf{r}}_{\mathbf{z}x_i} = \langle \mathbb{E}\left\{\mathbf{z}(n)x_i(n)\right\}\rangle_n$ is a KN_pL-vector. From (6.11) and the solution for $\hat{\mathbf{w}}_i$ obtained from (6.8), we learned that $\hat{\mathbf{w}}_i$ is an LTI filter. Thus, in obtaining $\hat{\mathbf{w}}_i$ from (6.13), the time-averaging operation is applied to $\mathbf{R}_{\mathbf{zz}}(n) = \mathbb{E}\left\{\mathbf{z}(n)\mathbf{z}^H(n)\right\}$ and $\mathbf{r}_{\mathbf{z}x_i}(n) = \mathbb{E}\left\{\mathbf{z}(n)x_i(n)\right\}$ to extract their stationary components so that the resulting $\hat{\mathbf{w}}_i$ is time-invariant. Moreover, since the expressions obtained for $\hat{\mathbf{w}}_i$ using (6.8) and (6.14) are equivalent, we conclude that $\hat{\mathbf{w}}_i$ is only optimal in the sense of minimizing the TAMSE rather than the MSE at all time instants. In other words, another FRESH filter, even with the same length and using the same cyclic frequency set, might exhibit a lower MSE at certain time instants(Ojeda and Grajal, 2011). On the other hand, the optimal SIMO FRESH filter given by (6.8) minimizes the MSE at all time instants. In the following, we show how $\overline{\mathbf{R}}_{\mathbf{zz}}$ and $\overline{\mathbf{r}}_{\mathbf{z}x_i}$, which are required to compute $\hat{\mathbf{w}}_i$ using (6.14), can be estimated in practice.

Let $u = kN_pL + jL + l$ and $v = \tilde{k}N_pL + \tilde{j}L + \tilde{l}$, where $k, \tilde{k} \in \{0, \cdots, K-1\}$, $j, \tilde{j} \in \{0, \cdots, N_p - 1\}$ and $l, \tilde{l} \in \{0, \cdots, L-1\}$, then using (6.12) and exploiting the fact that $x_i(n)$ and $\zeta_j(n)$ are independent, $\left[\overline{\mathbf{R}}_{\mathbf{zz}}\right]_{u,v}$ can be expressed as

$$\begin{aligned}
\left[\overline{\mathbf{R}}_{\mathbf{zz}}\right]_{u,v} &= \langle \mathbb{E}\left\{y_j(n-l)y_{\tilde{j}}(n-\tilde{l})\right\} \\
&\times \; \mathrm{e}^{-j2\pi[\alpha_{\tilde{k}}(n-\tilde{l})-\alpha_k(n-l)]}\rangle_n \\
&= r_{y_j y_{\tilde{j}}}^{\alpha_{\tilde{k}}-\alpha_k}(\tilde{l}-l)\mathrm{e}^{j2\pi\alpha_k(\tilde{l}-l)} \\
&= \left[r_{x_j x_{\tilde{j}}}^{\alpha_{\tilde{k}}-\alpha_k}(\tilde{l}-l) + r_{\zeta_j \zeta_{\tilde{j}}}^{\alpha_{\tilde{k}}-\alpha_k}(\tilde{l}-l)\right]\mathrm{e}^{j2\pi\alpha_k(\tilde{l}-l)}.
\end{aligned} \tag{6.15}$$

It is important to note that $\left[\overline{\mathbf{R}}_{\mathbf{zz}}\right]_{u,v} = 0$ when $\alpha_k \in \grave{\mathcal{A}}_{xx}$ and $\alpha_{\tilde{k}} \in \grave{\mathcal{A}}_{\zeta\zeta}$, or vice versa. Otherwise, $\left[\overline{\mathbf{R}}_{\mathbf{zz}}\right]_{u,v}$ can be evaluated by estimating $r_{y_j y_{\tilde{j}}}^{\alpha_{\tilde{k}}-\alpha_k}(\tilde{l}-l)$ in (6.15) directly from the SIMO received signals $\{y_j(n) : j \in \{0, \cdots, N_p - 1\}\}$ using the cyclic correlation estimation approach explained in the Appendix. We note that (6.15) provides an element-wise expression for the matrix $\overline{\mathbf{R}}_{\mathbf{zz}}$, which is useful in computing $\overline{\mathbf{R}}_{\mathbf{zz}}$ in practice. However, for compactness, $\overline{\mathbf{R}}_{\mathbf{zz}}$ can be expressed in a matrix form as follows

$$\overline{\mathbf{R}}_{\mathbf{zz}} = \langle \mathbf{\Sigma}(n) \mathbf{R}_{\mathbf{yy}}(n) \mathbf{\Sigma}^*(n) \rangle_n,$$

where $\mathbf{R}_{\mathbf{yy}}(n) = \mathbb{E}\left\{\mathbf{y}(n)\mathbf{y}^\top(n)\right\}$. Similar to $\left[\overline{\mathbf{R}}_{\mathbf{zz}}\right]_{u,v}$, $\left[\overline{\mathbf{r}}_{\mathbf{z}x_i}\right]_u$ can be computed as

$$\begin{aligned}\left[\overline{\mathbf{r}}_{\mathbf{z}x_i}\right]_u &= \langle \mathbb{E}\left\{y_j(n-l)x_i(n)\mathrm{e}^{j2\pi\alpha_k(n-l)}\right\}\rangle_n \\ &= \left(r^{\alpha_k}_{x_i y_j}(l)\right)^* = \left(r^{\alpha_k}_{x_i x_j}(l)\right)^*. \end{aligned} \tag{6.16}$$

In addition, $\overline{\mathbf{r}}_{\mathbf{z}x_i}$ can be written in a compact matrix form as follows

$$\overline{\mathbf{r}}_{\mathbf{z}x_i} = \langle \mathbf{\Sigma}(n) \mathbf{R}_{\mathbf{xx}}(n) \mathbf{e}_{iL} \rangle_n,$$

where $\mathbf{R}_{\mathbf{xx}}(n) = \mathbb{E}\left\{\mathbf{x}(n)\mathbf{x}^\top(n)\right\}$ given that $\mathbf{x}(n) = [\mathbf{x}^{\alpha\top}(n), \cdots, \mathbf{x}^{\alpha\top}(n)]^\top$, which is the vector $\mathbf{x}^\alpha(n)$ repeated K times, and $[\mathbf{x}^\alpha(n)]_{jL+l} = x_j(n-l)$; $\mathbf{e}_{iL}$ is an KN_pL-vector with unity at the iL-th index and zeros at all other entries.

Since $r^{\alpha_k}_{x_i x_j}(l)$ is required in the computation of $\left[\overline{\mathbf{r}}_{\mathbf{z}x_i}\right]_u$, it is important to show how $r^{\alpha_k}_{x_i x_j}(l)$ can be computed in practice. Hence, using (2.1a), $r^{\alpha_k}_{x_i x_j}(l)$ can be simplified to

$$r^{\alpha_k}_{x_i x_j}(l) = \sum_{m=0}^{\nu} \sum_{\tilde{m}=0}^{\nu} h_i(m) h_j(\tilde{m}) r^{\alpha}_{dd}\left(l + \tilde{m} - m\right) \mathrm{e}^{-j2\pi\alpha_k \tilde{m}}. \tag{6.17}$$

Therefore, $r^{\alpha_k}_{x_i x_j}(l)$ can be estimated using (6.17) in terms of the cyclic auto-correlation function of the TD OFDM signal $d(n)$ given the CIR knowledge. However, exploiting the independence between the noise and the information signals, $r^{\alpha_k}_{x_i x_j}(l)$ can be estimated without the CIR knowledge as

$$r^{\alpha_k}_{x_i x_j}(l) = r^{\alpha_k}_{y_i y_j}(l) - r^{\alpha_k}_{\zeta_i \zeta_j}(l). \tag{6.18}$$

The cyclic correlation function of the noise, denoted by $r^{\alpha_k}_{\zeta_i \zeta_j}(l)$, can be estimated during the silent intervals between consecutive NB-PLC transmission bursts which typically last for several minutes (Nassar et al., 2012). The estimation of both $r^{\alpha_k}_{y_i y_j}(l)$ and $r^{\alpha_k}_{\zeta_i \zeta_j}(l)$ follows the cyclic correlation estimation approach explained in the Appendix. It is worth noting that the estimation of $r^{\alpha_k}_{y_i y_j}(l)$ can reuse the same computations used to estimate the terms $r^{\alpha_{\tilde{k}}-\alpha_k}_{y_j y_{\tilde{j}}}(\tilde{l}-l)$ in (6.15) when setting $\alpha_k = 0$ and $l = 0$, which are also computed as part of the $\overline{\mathbf{R}}_{\mathbf{zz}}$ estimation process. Furthermore, the implementation of the SIMO TD-NF technique without the need for channel knowledge makes this technique attractive for the case of differential modulation where channel knowledge is not available at the receiver. It is worth mentioning that differential modulation schemes are adopted in the NB-PLC standards, e.g. IEEE 1901.2, as mandatory transmission schemes. In addition, for coherent modulation, performing the noise filtering in TD prior to channel estimation using the SIMO TD-NF technique leads to a more robust channel estimation performance since the residual noise after filtering becomes less severe.

Let $\mathcal{A}^s_g = \mathcal{A}^s_{xx} \cup \mathcal{A}^s_{\zeta\zeta} \cup \{0\}$, where $\mathcal{A}^s_{xx} = \{\alpha_k : k \in \{0, \cdots, K_x - 1\}\}$, $\mathcal{A}^s_{\zeta\zeta} = \{\alpha_{k+K_x+1} : k \in \{0, \cdots, K_\zeta - 1\}\}$ and $K_x + K_\zeta + 1 = K$. It is assumed that $\alpha_{K_x} = 0$, and hence it is not included in either $\mathcal{A}^s_{xx}$ or $\mathcal{A}^s_{\zeta\zeta}$. In addition, let $\mathbf{z}(n) = [\mathbf{z}_0^\top(n), \mathbf{z}_1^\top(n), \mathbf{z}_2^\top(n)]^\top$, where $\mathbf{z}_0(n) = [\mathbf{z}^{\alpha_0\top}(n), \cdots, \mathbf{z}^{\alpha_{K_x-1}\top}(n)]^\top$, $\mathbf{z}_1(n) = \mathbf{z}^{\alpha_{K_x}}(n)$ and $\mathbf{z}_2(n) = [\mathbf{z}^{\alpha_{K_x+1}\top}(n), \cdots, \mathbf{z}^{\alpha_{K-1}\top}(n)]^\top$. Therefore, $\overline{\mathbf{R}}_{\mathbf{zz}}$ can be written as follows

$$\begin{aligned}
\overline{\mathbf{R}}_{\mathbf{zz}} &= \begin{bmatrix} \overline{\mathbf{R}}_{\mathbf{z}_0\mathbf{z}_0} & \overline{\mathbf{R}}_{\mathbf{z}_0\mathbf{z}_1} & \overline{\mathbf{R}}_{\mathbf{z}_0\mathbf{z}_2} \\ \overline{\mathbf{R}}_{\mathbf{z}_1\mathbf{z}_0} & \overline{\mathbf{R}}_{\mathbf{z}_1\mathbf{z}_1} & \overline{\mathbf{R}}_{\mathbf{z}_1\mathbf{z}_2} \\ \overline{\mathbf{R}}_{\mathbf{z}_2\mathbf{z}_0} & \overline{\mathbf{R}}_{\mathbf{z}_2\mathbf{z}_1} & \overline{\mathbf{R}}_{\mathbf{z}_2\mathbf{z}_2} \end{bmatrix} \\
&= \begin{bmatrix} \overline{\mathbf{R}}_{\mathbf{z}_0\mathbf{z}_0} & \overline{\mathbf{R}}_{\mathbf{z}_0\mathbf{z}_1} & \mathbf{0}_{K_x N_p L \times K_\zeta N_p L} \\ \overline{\mathbf{R}}_{\mathbf{z}_1\mathbf{z}_0} & \overline{\mathbf{R}}_{\mathbf{z}_1\mathbf{z}_1} & \overline{\mathbf{R}}_{\mathbf{z}_1\mathbf{z}_2} \\ \mathbf{0}_{K_\zeta N_p L \times K_x N_p L} & \overline{\mathbf{R}}_{\mathbf{z}_2\mathbf{z}_1} & \overline{\mathbf{R}}_{\mathbf{z}_2\mathbf{z}_2} \end{bmatrix},
\end{aligned} \tag{6.19}$$

where $\overline{\mathbf{R}}_{\mathbf{z}_q\mathbf{z}_{\tilde{q}}} = \langle \mathbb{E}\left\{\mathbf{z}_q(n)\mathbf{z}^H_{\tilde{q}}(n)\right\}\rangle_n$, $q, \tilde{q} \in \{0, 1, 2\}$. Hence, from (6.19), we conclude that the system of equations in (6.14) cannot be decoupled into two separate systems of equations.

Inserting (6.14) into the TAMSE expression in (6.13), the minimum $\text{TAMSE}_{x_i(n)}$, denoted by $\hat{\sigma}_i^2$, is given by

$$\hat{\sigma}_i^2 = r^0_{x_i x_i}(0) - \bar{\mathbf{r}}_{x_i \mathbf{z}} \overline{\mathbf{R}}_{\mathbf{zz}}^{-1} \bar{\mathbf{r}}_{\mathbf{z} x_i}, \ i \in \{0,\, 1,\, \cdots,\, N_p\}. \tag{6.20}$$

6.1.3 FD Signal Combining

The estimated TD signals across the N_p receive phases, $\{\hat{x}_i(n) : i \in \{0, \cdots, N_p - 1\}\}$, are transformed to the FD after removing the cyclic prefix. Let $\hat{x}_i(n)$ be expressed as

$$\hat{x}_i(n) = x_i(n) + \hat{\zeta}_i(n). \tag{6.21}$$

where $\hat{\zeta}_i(n)$ denotes the n-th residual noise sample after applying the SIMO TD-NF technique and $\hat{\zeta}_i(n)$ is assumed be a white Gaussian stationary process whose variance is constant over n and equal to $\hat{\sigma}_i^2$. Furthermore, we assume that $\hat{\zeta}_i(n)$ is spatially uncorrelated over the receive phases. Hence, let $\hat{\zeta}(n) = [\hat{\zeta}_0(n), \cdots, \hat{\zeta}_{N_p-1}(n)]^\top$, then $\mathbf{R}_{\hat{\zeta}\hat{\zeta}} = \mathbb{E}\{\hat{\zeta}^\top \hat{\zeta}\} = \text{diag}\{\hat{\sigma}_i^2 : i \in \{0, \cdots, N_p - 1\}\}$. Moreover, let $\bar{\hat{x}}_{i,l}(k)$ and $\bar{\hat{\zeta}}_{i,l}(k)$ denote the i-th phase FD estimated symbol and the residual noise over the k-th frequency subchannel, respectively, over the k-th OFDM subchannel at the l-th OFDM block. Hence, $\bar{\hat{x}}_{i,l}(k)$ can be expressed as follows

$$\bar{\hat{x}}_{i,l}(k) = \bar{h}_{i,l}(k)\bar{d}_l(k) + \bar{\hat{\zeta}}_{i,l}(k). \tag{6.22}$$

Therefore, an expression for the LLR of $\bar{\hat{x}}_{i,l}(k)$ assuming BPSK modulation can be derived as follows

$$\begin{aligned}
\text{LLR}_{l,k} \ &= \ \sum_{i=0}^{N_p-1} \text{LLR}_{i,l,k} \\
&= \ \sum_{i=0}^{N_p-1} \log \frac{f(\bar{\hat{x}}_{i,l}(k) | \bar{d}_l(k) = 1, \bar{h}_{i,l}(k))}{f(\bar{\hat{x}}_{i,l}(k) | \bar{d}_l(k) = -1, \bar{h}_{i,l}(k))} \\
&= \ \sum_{i=0}^{N_p-1} \frac{1}{\hat{\sigma}_i^2} \Big[|\bar{\hat{x}}_{i,l}(k) + \bar{h}_{i,l}(k)|^2 \\
&- \ |\bar{\hat{x}}_{i,l}(k) - \bar{h}_{i,l}(k)|^2 \Big]
\end{aligned} \tag{6.23}$$

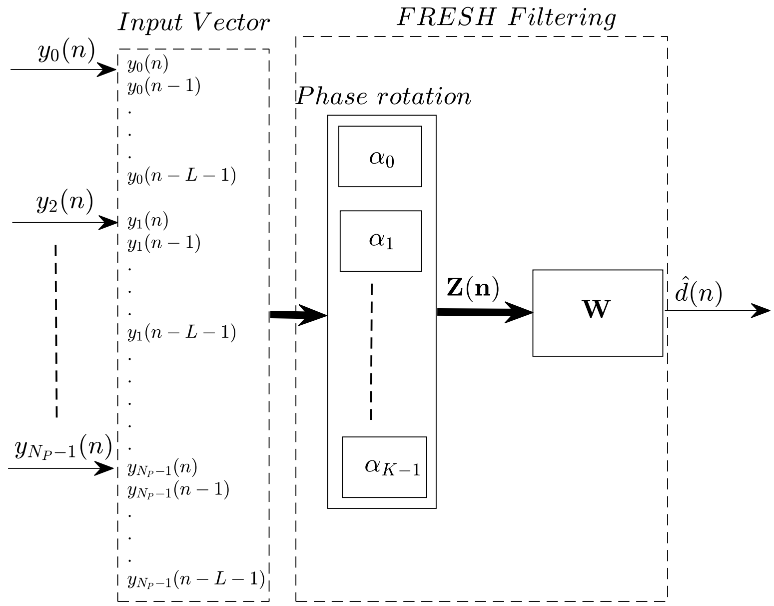

Figure 6.4: System block diagram illustrating the proposed SIMO TD-ENF technique.

6.2 Proposed SIMO Joint TD Equalization and Noise Filtering (TD-ENF) Technique

In this technique, we estimate the TD OFDM information signal by processing the TD SIMO received signal to jointly equalize the channel and filter out the cyclostationary noise. Thus, we refer to this technique as the *joint TD equalization and noise filtering technique* (TD-ENF).

6.2.1 TD-ENF Optimal SIMO LAPTV Filtering

Considering the TD SIMO received signal expression in (2.1a), we formulate an LMMSE minimization problem to directly estimate the TD transmitted signal, $d(n)$, from the TD SIMO received signals $\{y_j(n) : j \in \{0, \cdots, N_p - 1\}\}$ as

$$\min_{\mathbf{g}(n,.)\in\mathbb{R}^{N_p}} \text{MSE}_{d(n)} = \mathbb{E}\left\{\left[d(n) - \hat{d}(n)\right]^2\right\},\ \forall n \in \mathbb{Z}, \tag{6.24a}$$

$$\hat{d}(n) = \sum_{m\in\mathbb{Z}} \mathbf{g}^\top(n,m)\mathbf{y}(m) \tag{6.24b}$$

where $\mathbf{g}(k,n)$ is an N_p-vector contains the impulse responses of the set of filters designed to estimate $d(n)$. Note that $y_i(n)$ is an ACS process since it is the sum of the two ACS processes $x_i(n)$ and $\zeta_i(n)$. Furthermore, the signals $\{x_i(n), y_i(n) : i \in \{0, \cdots, N_p\}\}$ are pairwise jointly ACS since each signal is an ACS process and they are all pairwise mutually dependent. In addition, since $x_i(n)$ and $\{y_j(n) : j \in \{0, \cdots, N_p\}\}$ are jointly ACS and not jointly stationary, using a set of LTI filters is no longer optimal in the sense of minimizing the MSE, and the optimal LMMSE estimation filters are LAPTV filters (Gardner, 1986). Thus, $\mathbf{g}(k,n)$ is almost periodic in both k and n with some integer period P_g for each $l = k - n$, i.e., $\mathbf{g}(k,n) \approx \mathbf{g}(k+P_g, n+P_g)$, $\forall l = k-n \in \mathbb{Z}$, where P_g is the least common multiple of all the discrete-time periodicities of the functions involved in the design formula for $\mathbf{g}(k,n)$. Therefore, $\mathbf{g}(k,n)$ can be represented by Fourier series

$$\mathbf{g}(k,n) \;=\; \sum_{\alpha \in \mathcal{A}_g} \mathbf{g}^{\alpha}(k-n)\, \mathrm{e}^{j2\pi\alpha n}, \tag{6.25a}$$

$$\mathbf{g}^{\alpha}(l) = \langle \mathbf{g}(n+l,n) \mathrm{e}^{-j2\pi\alpha n} \rangle_n, \tag{6.25b}$$

where $\mathbf{g}^{\alpha}(k-n)$ is an N_p-vector that contains the Fourier series coefficients of $\mathbf{g}(k,n)$. In addition, $\mathcal{A}_g$ is a countable set that contains all the integer multiples of the fundamental frequencies of the functions involved in the design formula for $\mathbf{g}(k,n)$. Since $\{x_i(n) : i \in \{0,\, 1,\, \cdots,\, N_p - 1\}\}$ and $\{\zeta_i(n) : i \in \{0,\, 1,\, \cdots,\, N_p - 1\}\}$ are uncorrelated, then $\mathbf{R}_{\mathbf{yy}}(k,n) = \mathbf{R}_{\mathbf{xx}}(k,n) + \mathbf{R}_{\zeta\zeta}(k,n)$ and $\mathbf{r}_{d\mathbf{y}}(k,n) = \mathbf{r}_{d\mathbf{x}}(k,n)$. Hence, we note that $\mathcal{A}_{yy} = \mathcal{A}_{xx} \cup \mathcal{A}_{\zeta\zeta} = \mathcal{A}_{dd} \cup \mathcal{A}_{\zeta\zeta}$ and $\mathcal{A}_{xy} = \mathcal{A}_{xx} = \mathcal{A}_{dd}$. To obtain the optimal vector $\mathbf{g}(k,n)$ that minimizes $\mathrm{MSE}_{d(n)}$ in (6.24a), we set $\partial \mathrm{MSE}_{d(n)} / \partial \mathbf{g}^{\top}(n,k) = \mathbf{0}_{1\times N_p}$, which yields

$$\sum_{m\in\mathbb{Z}} \mathbf{g}^{\top}(n,m) \mathbf{R}_{\mathbf{yy}}(m,k) = \mathbf{r}_{d\mathbf{y}}(n,k),\ \forall n,\ k \in \mathbb{Z}. \tag{6.26}$$

Using the expressions of the Fourier series pairs for $\mathbf{g}(k,n)$, $\mathbf{R}_{\mathbf{yy}}(k,n)$ and $\mathbf{r}_{d\mathbf{y}}(k,n)$, we derived the following design formula for the optimal LAPTV filter. In particular, consider that $\mathbf{R}_{\mathbf{yy}}(k,n)$ and $\mathbf{r}_{d\mathbf{y}}(k,n)$ have the following generalized Fourier series pairs (assuming convergence)

$$\mathbf{R}_{\mathbf{yy}}(k,n) = \sum_{\beta\in\mathcal{A}_{yy}} \mathbf{R}^{\beta}_{\mathbf{yy}}(k-n)\mathrm{e}^{j2\pi\beta n}, \tag{6.27a}$$

$$\mathbf{R}^{\beta}_{\mathbf{yy}}(l) = \langle \mathbf{R}_{\mathbf{yy}}(n+l,n)\mathrm{e}^{-j2\pi\beta n}\rangle_n, \tag{6.27b}$$

$$\mathbf{r}_{d\mathbf{y}}(k,n) = \sum_{\gamma\in\mathcal{A}_{dy}} \mathbf{r}^{\gamma}_{d\mathbf{y}}(k-n)\mathrm{e}^{j2\pi\gamma n}, \tag{6.27c}$$

$$\mathbf{r}^{\gamma}_{d\mathbf{y}}(l) = \langle \mathbf{r}_{d\mathbf{y}}(n+l,n)\mathrm{e}^{-j2\pi\gamma n}\rangle_n. \tag{6.27d}$$

Substituting (6.25a) and (6.27a) in (6.26) yields

$$\begin{aligned}\sum_{m\in\mathbb{Z}}\sum_{\alpha\in\mathcal{A}_g}\sum_{\beta\in\mathcal{A}_{dd}\cup\mathcal{A}_{\zeta\zeta}} &\left[\mathbf{g}^{\alpha}(n-m)\right]^{\top}\mathbf{R}^{\beta}_{\mathbf{yy}}(m-k)\\ &\times \mathrm{e}^{j2\pi(\alpha m+\beta k)} = \mathbf{r}_{d\mathbf{y}}(n,k), \forall n,\, k\in\mathbb{Z}.\end{aligned} \tag{6.28}$$

Setting $l = n-k$ in (6.28) then inserting (6.28) into (6.27d), we get

$$\begin{aligned}\langle\sum_{m\in\mathbb{Z}}\sum_{\alpha\in\mathcal{A}_g}\sum_{\beta\in\mathcal{A}_{dd}\cup\mathcal{A}_{\zeta\zeta}} &\left[\mathbf{g}^{\alpha}(k+l-m)\right]^{\top}\mathbf{R}^{\beta}_{\mathbf{yy}}(m-k)\\ &\times\mathrm{e}^{j2\pi\alpha m}\mathrm{e}^{j2\pi(\beta-\gamma)k}\rangle_k = \mathbf{r}^{\gamma}_{d\mathbf{y}}(l), \forall l\in\mathbb{Z}.\end{aligned} \tag{6.29}$$

Setting $q = m-k$ yields

$$\begin{aligned}\sum_{q\in\mathbb{Z}}\sum_{\alpha\in\mathcal{A}_g}\sum_{\beta\in\mathcal{A}_{dd}\cup\mathcal{A}_{\zeta\zeta}} &\left[\mathbf{g}^{\alpha}(l-q)\right]^{\top}\mathbf{R}^{\beta}_{\mathbf{yy}}(q)\mathrm{e}^{j2\pi\alpha q}\\ &\times\langle\mathrm{e}^{j2\pi(\beta-\gamma+\alpha)k}\rangle_k = \mathbf{r}^{\gamma}_{d\mathbf{y}}(l), \forall l\in\mathbb{Z}.\end{aligned} \tag{6.30}$$

Using the identity

$$\langle\mathrm{e}^{j2\pi(\beta-\gamma+\alpha)k}\rangle_k = \begin{cases}1, & \beta=\gamma-\alpha\\ 0, & \text{otherwise}\end{cases}.$$

Hence, we arrive at the following design formula for the optimal LAPTV filter

$$\sum_{\alpha \in \mathcal{A}_g} \sum_{q \in \mathbb{Z}} \left[\mathbf{g}^{\alpha}(l-q)\right]^{\top} \mathbf{R}_{\mathbf{yy}}^{\gamma-\alpha}(q) \mathrm{e}^{j2\pi\alpha q} = \mathbf{r}_{d\mathbf{y}}^{\gamma}(l), \forall l \in \mathbb{Z}$$
$$, \gamma, \alpha \in \mathcal{A}_{dd} \cup \mathcal{A}_{\zeta\zeta}. \tag{6.31}$$

The formula in (6.31) simplifies the design of the optimal LAPTV filter set $\{\mathrm{g}_j(k,n) : j \in \{0, 1, \cdots, N_p-1\}\}$ into designing the set of LTI filters $\{\mathrm{g}_j^{\alpha}(l=k-n) : \alpha \in \mathcal{A}_g, j \in \{0, 1, \cdots, N_p-1\}\}$, which correspond to their Fourier series coefficients. It is worth mentioning that the design formula in (6.31) is a vector generalization of the optimal MMSE filter design derived in (Gardner, 1986, Eq. 12.284) where both formulas are equivalent when setting $N_p = 1$ in (6.31). Let $\grave{\mathcal{A}}_{dd} = \mathcal{A}_{dd} \backslash \{0\}$ and $\grave{\mathcal{A}}_{\zeta\zeta} = \mathcal{A}_{\zeta\zeta} \backslash \{0\}$. Thus, if $\alpha, \gamma \in \mathcal{A}_{dd}$, then $\gamma - \alpha \in \mathcal{A}_{dd} \cup \mathcal{A}_{\zeta\zeta}$ and $\mathbf{R}_{\mathbf{yy}}^{\gamma-\alpha}(l) \neq 0$, $\mathbf{r}_{d\mathbf{y}}^{\gamma}(l) \neq 0$. On the other hand, if $\alpha, \gamma \in \mathcal{A}_{\zeta\zeta}$, then $\gamma - \alpha \in \mathcal{A}_{dd} \cup \mathcal{A}_{\zeta\zeta}$ and $\mathbf{R}_{\mathbf{yy}}^{\gamma-\alpha}(l) \neq 0$, $\mathbf{r}_{d\mathbf{y}}^{\gamma}(l) = 0$. Otherwise, if $\alpha \in \grave{\mathcal{A}}_{dd}$ while $\gamma \in \grave{\mathcal{A}}_{\zeta\zeta}$, or vice versa, then $\gamma - \alpha \notin \mathcal{A}_{dd} \cup \mathcal{A}_{\zeta\zeta}$ and $\mathbf{R}_{\mathbf{yy}}^{\gamma-\alpha}(l) = 0$. Hence, $\alpha, \gamma \in \mathcal{A}_{dd}$ or $\alpha, \gamma \in \mathcal{A}_{\zeta\zeta}$ is required such that $\mathbf{R}_{\mathbf{yy}}^{\gamma-\alpha}(l) \neq 0$ and the left-hand side of the system of equations in (6.31) is nonzero. Therefore, we conclude that the optimal selection of the cyclic frequencies for $\mathrm{g}_j(k,n)$ is to range over all the cyclic frequencies of *both* the information and the noise signals, or equivalently $\mathcal{A}_g = \mathcal{A}_{dd} \cup \mathcal{A}_{\zeta\zeta}$. Therefore, P_g is the least common multiple of N_B and P_ζ.

The MSE associated with the optimal filter $\mathbf{g}(k,n)$ can be obtained by simplifying $\mathrm{MSE}_{d(n)}$ in (6.24a) as follows

$$\mathrm{MSE}_{d(n)} = r_{dd}(n,n) - \sum_{m \in \mathbb{Z}} \mathbf{g}^{\top}(n,m) \mathbf{r}_{\mathbf{x}d}(m,n). \tag{6.32}$$

Therefore, from (6.32), we note that the MSE is an almost periodic function since it depends on the auto-correlation of the TD OFDM signal as well as the LMMSE filter. Hence, to measure the performance by a single number, we adopt the TAMSE given by $\mathrm{TAMSE}_{d(n)} =$

$\langle \text{MSE}_{d(n)} \rangle_n$ (Gardner, 1986). Inserting (6.25a) into (6.24b) yields

$$\hat{d}(n) = \sum_{\alpha \in \mathcal{A}_g} \sum_{m \in \mathbb{Z}} \left[\mathbf{g}^{\alpha}(n-m)\right]^{\top} \left[\mathbf{y}(m) \mathrm{e}^{j2\pi\alpha m}\right], \tag{6.33}$$

which represents the optimal FRESH-filtering-equivalent form of the estimator for $d(n)$. In practice, suboptimal performance is achieved when constraining α to range over only a limited set of cyclic frequencies within $\mathcal{A}_g = \mathcal{A}_{dd} \cup \mathcal{A}_{\zeta\zeta}$, which is the main takeaway from the previous analysis.

6.2.2 TD-ENF Suboptimal SIMO LAPTV Filtering

Furthermore, for a fixed $\mathcal{A}_g^s = \{\alpha_k : k \in \{0, \cdots, K-1\}\}$ of cardinality K, and assuming a finite length L for $\mathbf{g}^{\alpha}(n-m)$, a suboptimal SIMO FRESH-filtering estimator for $d(n)$ can be expressed as follows

$$\begin{aligned} \hat{d}(n) &= \sum_{\alpha \in \mathcal{A}_g^s} \sum_{m=n-L+1}^{n} \left[\mathbf{g}^{\alpha}(n-m)\right]^{\top} \left[\mathbf{y}(m) \mathrm{e}^{j2\pi\alpha m}\right] \\ &= \mathbf{w}^H \mathbf{z}(n), \end{aligned} \tag{6.34}$$

where $\mathbf{w} = [\mathbf{w}^{\alpha_0 \top}, \cdots, \mathbf{w}^{\alpha_{K-1} \top}]^{\top}$, and $\mathbf{w}^{\alpha_k}$ is an $N_p L$-vector such that $\left[\mathbf{w}^{\alpha_k}\right]_{jL+l} = \left(\mathrm{g}_j^{\alpha_k}(l)\right)^*$, where $j \in \{0, \cdots, N_p - 1\}$ and $l \in \{0, \cdots, L-1\}$. It is worth noting that $\mathbf{z}(n) = \mathbf{\Sigma}(n)\mathbf{y}(n) = \mathbf{\Sigma}(n)\mathbf{H}\mathbf{d}(n)$, where $\mathbf{H}$ is a $KN_pL \times (L+\nu)$ matrix such that $\mathbf{H} = [\mathbf{H}^{\alpha \top}, \cdots, \mathbf{H}^{\alpha \top}]^{\top}$, which is the matrix $\mathbf{H}^{\alpha}$ repeated K times, and $\mathbf{H}^{\alpha}$ is the channel convolution matrix with dimensions $N_pL \times (L+\nu)$. Furthermore, $\mathbf{d}(n)$ is an $(L+\nu)-$vector such that $\left[\mathbf{d}(n)\right]_l = d(n-l)$.

A block diagram for the SIMO TD-ENF technique as described by (6.34) for the case of two receive phases is shown in Fig. 6.4. As shown in Section (6.1), the suboptimal SIMO FRESH filter $\hat{\mathbf{w}}$ can be obtained by solving the linear system of equations in (6.31) after constraining $\mathcal{A}_g$ to $\mathcal{A}_g^s$ and setting $\mathrm{g}_j^{\alpha_k}(l) = 0$, $\forall l \notin \{0, \cdots, L-1\}$. However, $\hat{\mathbf{w}}_i$ can alternatively be obtained from minimizing the TAMSE in estimating $d(n)$ with respect to $\mathbf{w}$ as follows

$$\min_{\mathbf{w}_i \in \mathbb{R}^{KN_pL}} \text{TAMSE}_{d(n)} = \langle \mathbb{E}\left\{|d(n) - \mathbf{w}^H \mathbf{z}(n)|^2\right\} \rangle_n, \forall n \in \mathbb{Z}. \tag{6.35}$$

Setting the derivative of $\text{TAMSE}_{d(n)}$ with respect to $\mathbf{w}_i^*$ to zero yields

$$\hat{\mathbf{w}} \;=\; \overline{\mathbf{R}}_{\mathbf{zz}}^{-1}\overline{\mathbf{r}}_{\mathbf{z}d}, \tag{6.36}$$

where $\overline{\mathbf{r}}_{\mathbf{z}d} = \langle \mathbb{E}\left\{\mathbf{z}(n)d(n)\right\}\rangle_n$. It follows from the discussion in Section 6.1 that $\hat{\mathbf{w}}$, like $\hat{\mathbf{w}}_i$ in Section 6.1, is only optimal in the sense of minimizing $\text{TAMSE}_{d(n)}$ and does not necessarily minimize the MSE at all time instants. To compute $\hat{\mathbf{w}}$, $\overline{\mathbf{R}}_{\mathbf{zz}}$ can be obtained using (6.15) as explained in Section 6.1. In addition, $\left[\overline{\mathbf{r}}_{\mathbf{z}d}\right]_u$ can be expressed as follows

$$\begin{aligned}\left[\overline{\mathbf{r}}_{\mathbf{z}d}\right]_u &= \langle \mathbb{E}\left\{y_j(n-l)d(n)\mathrm{e}^{j2\pi\alpha_k(n-l)}\right\}\rangle_n \\ &= \left(r_{dy_j}^{\alpha_k}(l)\right)^* = \left(r_{dx_j}^{\alpha_k}(l)\right)^*,\end{aligned} \tag{6.37a}$$

In addition, $\overline{\mathbf{r}}_{\mathbf{z}d}$ can be written in the following compact matrix form

$$\overline{\mathbf{r}}_{\mathbf{z}d} = \langle \mathbf{\Sigma}(n)\mathbf{H}\mathbf{R}_{\mathbf{dd}}(n)\mathbf{e}_0\rangle_n,$$

where $\mathbf{R}_{\mathbf{dd}}(n) = \mathbb{E}\left\{\mathbf{d}(n)\mathbf{d}^\top(n)\right\}$.

The computation of $r_{dx_j}^{\alpha_k}(l)$, which is required in computing $\left[\overline{\mathbf{r}}_{\mathbf{z}d}\right]_u$, can be performed using

$$r_{dx_j}^{\alpha_k}(l) = \sum_{m=0}^{\nu} h_j(m) r_{dd}^{\alpha_k}\left(l+m\right)\mathrm{e}^{-j2\pi\alpha_k m}. \tag{6.37b}$$

Thus, $r_{dx_j}^{\alpha_k}(l)$ can be estimated using (6.37b) in terms of the cyclic auto-correlation function of the TD OFDM signal $d(n)$ given the CIR knowledge.

6.2.3 FD Signal Combining

After obtaining $\hat{d}(n)$, it is transformed to the FD after removing the cyclic prefix. Let $\bar{\hat{d}}_l(k)$ denote the FD estimated data symbol over the k-th OFDM subchannel at the l-th OFDM block. Thus, an expression for the LLR of $\bar{\hat{d}}_l(k)$ assuming BPSK modulation can be derived as

$$\text{LLR}_{l,k} \;=\; \log\frac{f(\bar{\hat{d}}_l(k)|\bar{d}_l(k)=1)}{f(\bar{\hat{d}}_l(k)|\bar{d}_l(k)=-1)}$$

$$= \quad |\bar{\hat{d}}_l(k) + 1|^2 - |\bar{\hat{d}}_l(k) - 1|^2. \tag{6.38}$$

One advantage of the TD-ENF technique over the TD-NF technique is that it does not require estimating the noise cyclic correlation function, denoted by $r_{\zeta_i\zeta_j}^{\alpha_k}(l)$. In addition, the TD-ENF technique requires only one estimation filter while the TD-NF technique requires N_p estimation filters. However, the TD-ENF technique requires the CIR estimation to be performed prior to the noise filtering resulting in a reduced CIR estimation accuracy compared to the CIR estimation accuracy obtained when using the TD-NF technique. Moreover, the CIR knowledge requirement in the TD-ENF technique renders it inapplicable to differential modulation schemes.

6.3 Numerical Results

In this section, we evaluate the performance and the implementation complexity of the proposed noise mitigation techniques. The performance results are presented in terms of the MSE and the average BER. The implementation complexity is analyzed in terms of the number of multiplications required for each of the proposed techniques.

6.3.1 Simulation Parameters

The simulated system block diagram including the proposed noise mitigation techniques is shown in Fig. 6.5.

For the TD-NF and the TD-ENF techniques, we set $K = 29$ and $L = 20$. As it will be discussed in the complexity analysis section, all of the proposed cyclostationary noise mitigation techniques are implemented in two stages to speed up the simulation. The first stage is to estimate the noise statistical properties, namely the cyclic auto/cross-correlations matrices for the time-domain techniques and spatial-correlation matrices for the frequency-domain technique. In particular, the cyclic auto/cross-correlation is computed using (A.4a)

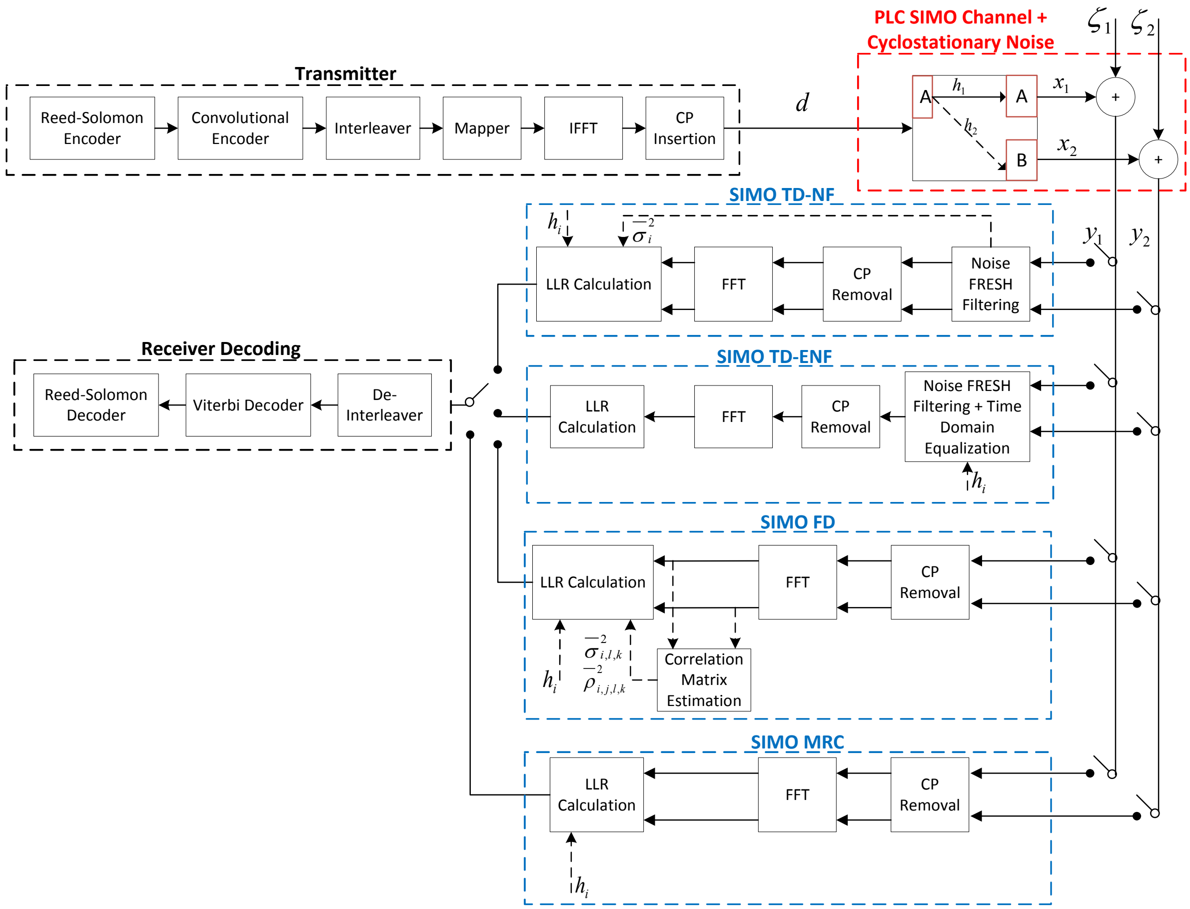

Figure 6.5: End-to-end simulated system block diagram illustrating the proposed SIMO noise mitigation techniques.

while the spatial-correlation per OFDM frequency sub-channel is computed using (5.4) and (5.5). In the second stage, we run the Monte Carlo simulation for the end-to-end NB-PLC system for different SNR values. At each SNR value, we generate the mitigation filters coefficients using the stored noise statistical matrices calculated in the first stage. In particular, we compute the time-domain FRESH filters using (6.14) and (6.36) while computing the frequency-domain filter coefficients using (5.2). The MSE results presented in this section are plotted versus the SNR of the direct link (from transmit phase A to receive phase A) measured on the active OFDM subchannels (72 total active subchannels out of 256 subchannels symmetric around the DC). Thus, all MSE results can be compared to a SISO

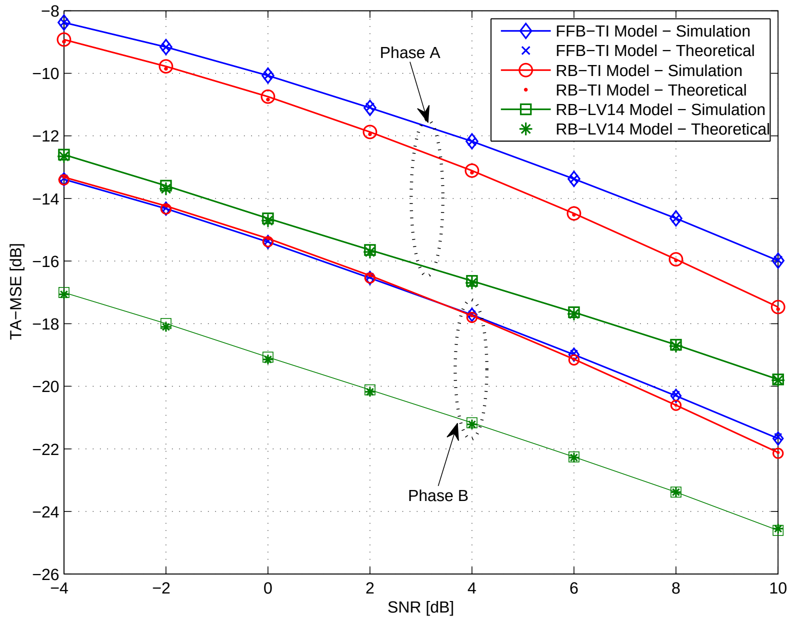

Figure 6.6: TAMSE of the proposed SIMO TD-NF technique for Phase A assuming different noise models.

system utilizing the same link. Furthermore, the BER performance is plotted versus $\frac{E_b}{N_o}$ of the direct link, where E_b is the average energy per information bit in both the uncoded and coded cases and $\frac{N_o}{2}$ is the noise variance.

6.3.2 MSE Performance

Fig. 6.6 shows the TAMSE achieved by the SIMO TD-NF technique in extracting the TD OFDM signal over receive phases A and B. Furthermore, the TAMSE results in Fig. 6.6 are presented for both the FFB and the RB noise models. We note from Fig. 6.6 that the achieved TAMSE is dependent on the assumed noise model and its parameters. It is worth mentioning that the achieved TAMSE in phase B is less than that achieved in phase A since the signal attenuation in phase B is around 4 dB higher than that in phase A.

Note that the TAMSE represents the absolute square of the estimation error (i.e., it is not normalized to the signal power), hence, the TAMSE decreases as the signal power goes

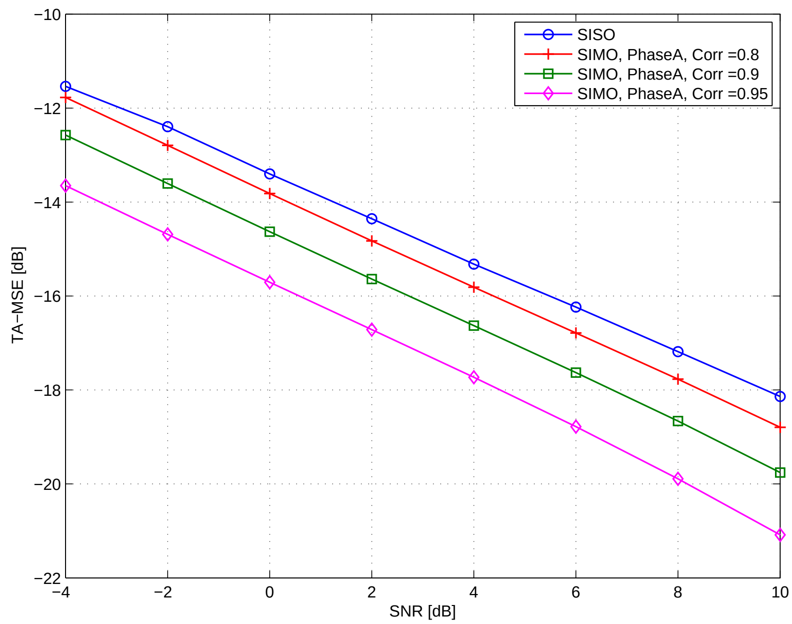

Figure 6.7: TAMSE of the proposed SIMO TD-NF technique for Phase A assuming RB-LV14 with different correlation values r.

down. In addition, Fig. 5.7 depicts the MSE achieved by the proposed FD noise mitigation technique for both the FFB and the RB noise models. We note from Fig. 5.7 that the achieved MSE under the RB noise model is less than that achieved under the FFB noise model since the stationarity assumption per noise region is satisfied in the RB noise model. It is evident from Figs. 6.6 and 5.7 that the simulation results for the TAMSE and the MSE, respectively, match their analytical expressions. However, in Fig. 5.7, a small mismatch in MSE can be observed between the simulation result and the theoretical expression for the FD noise mitigation technique under the FFB noise model. The reason is that the stationarity assumption per temporal noise region, which is adopted in deriving the MSE expression, is not very accurate for the FFB noise model.

Figs. 6.7 and 6.8 show the TAMSE of the proposed TD-NF technique applied to a SIMO receiver jointly processing both phase A and phase B in comparison with a SISO receiver that processes only phase A. The SISO receiver also applies the TD-NF technique by setting

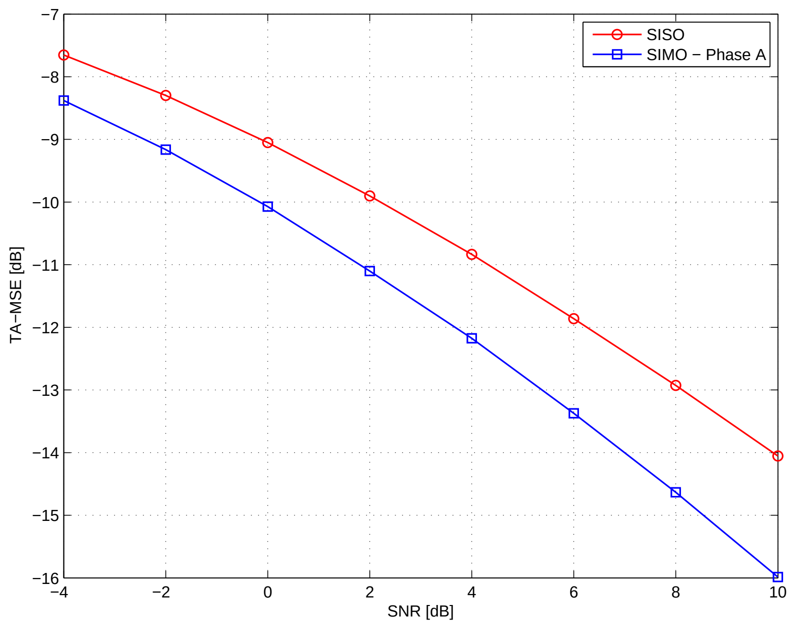

Figure 6.8: TAMSE of the proposed SIMO TD-NF technique for Phase A assuming FFB-TI noise model compared to SISO case.

Table 6.2: The TAMSE reduction for the SIMO receiver over the SISO receiver using the TD-NF technique.

Fig.	Fig. 6.7, 0.8-correlation, −18 dB TAMSE	Fig. 6.7, 0.9-correlation, −18 dB TAMSE	Fig. 6.7, 0.95-correlation, −18 dB TAMSE	Fig. 6.8, −14 dB TAMSE
Reduction (dB)	1 dB	3 dB	5 dB	3dB

$N_p = 1$. The results are presented for the RB noise model in Figs. 6.7 and for the FFB noise model in Fig. 6.8. Furthermore, in Fig. 6.7, we present the TAMSE results for different levels of the noise spatial correlation factor for the RB noise model. In Table 6.2, we quantify the performance gains achieved by the joint processing of the received signal over the two phases in the SIMO receiver compared to the SISO receiver performance. The high correlation between the different phases observed by field measurements and shown in Fig. 3.5 (which is implemented in the FFB noise model) explains the clear performance gain shown in Fig. 6.8 for the proposed SIMO TD-NF estimator.

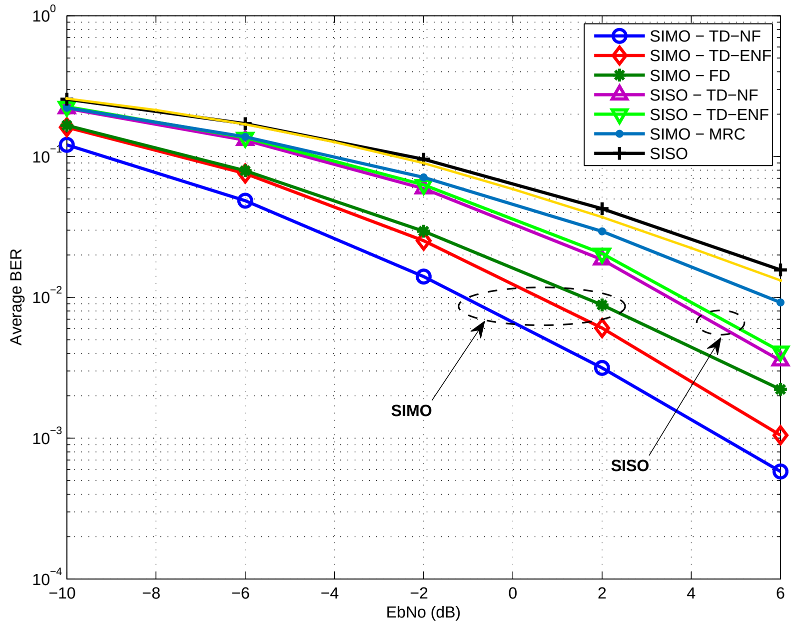

Figure 6.9: Uncoded average BER for different techniques assuming FFB-TI noise model.

6.3.3 Average BER Performance

The uncoded average BER performance is simulated for all proposed receivers in Fig. 6.9 where the FFB-TI noise model is used for all cases. As shown in Fig. 6.9, the SIMO TD-NF technique has a superior performance for all proposed techniques with more than 3 dB gain over the FD technique at an uncoded BER of 10^{-2} and 5 dB gain over the SISO TD-NF. The overall gain for the SIMO TD-NF technique over the SISO receiver without noise mitigation is 8 dB at an uncoded BER of 10^{-2}. The BER performance of the SIMO TD-ENF technique is worse than that of the SIMO TD-NF technique by 2 dB at an uncoded BER of 10^{-2}. The reason for this degradation is due to the limited performance of the finite impulse response (FIR) time-domain equalization in the SIMO TD-ENF technique. However, this SNR degradation comes as a price for the reduced-complexity design.

The coded average BER performance for all proposed receivers under the FFB noise model is shown in Fig. 6.10. The conclusions and performance differences for coded BER are

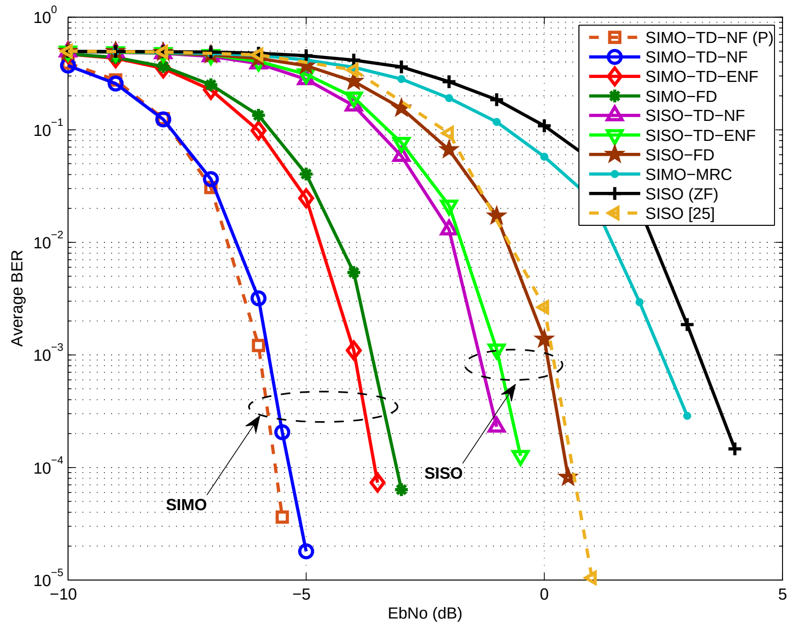

Figure 6.10: Coded average BER for different techniques assuming FFB-TI noise model.

almost the same as uncoded BER, where the SIMO TD-NF technique achieves a performance gain over all other techniques that is close to the corresponding gain in the uncoded BER case. An additional result shown in the coded BER curves is the performance of the FD noise mitigation technique for the SISO case. In this case, the estimated noise PSD per temporal region is used in the LLR calculations, which enhances the performance compared to the SISO receiver without noise filtering.

Since there is no previous work in the literature on the SIMO receivers under the cyclostationary noise, we show the performance of the following three cases as benchmarks

1. We show the performance of the conventional SIMO MRC combiner without noise filtering, i.e., assuming stationary noise. As shown in Fig. 6.10, the coded BER performance of the proposed SIMO TD-NF technique outperforms the conventional MRC receiver by more than 8 dB at a coded BER of 10^{-3}.

2. We include the SISO coded BER performance of the technique developed in (Shlezinger and Dabora, 2014) which is based on the cascaded FRESH filtering design. As shown in Fig. 6.10, our proposed SISO TD-NF outperforms the SISO technique developed in (Shlezinger and Dabora, 2014) by more than 1.5 dB at a coded BER of 10^{-3}. This performance gain comes as a result of two enhancements in our developed SISO TD-NF compared to the design in (Shlezinger and Dabora, 2014). The first is that our SISO algorithm uses a single stage that utilizes the cyclic frequencies of both the OFDM signal and the cyclostationary noise. More importantly, we optimize the FRESH filter parameters based on the cyclostationary noise parameters as will be discussed in the complexity analysis section. Moreover, the total number of taps in our proposed SISO FRESH filter design ($29 \times 40 = 1160$ taps) is much lower than the total number of taps used in the design of (Shlezinger and Dabora, 2014) which is $1600 \times 5 + 128 \times 5 = 8640$ taps. Note that our proposed SIMO TD-NF has the same total number of taps as in the SISO TD-NF.

3. The performance of the SIMO TD-NF where per-subchannel MMSE combining is used in the frequency domain assuming perfect knowledge of the per subchannel auto and cross-correlation functions of the residual noise (i.e., after FRESH filtering) for each temporal noise region. We refer to this receiver architecture in the coded BER results as SIMO TD-NF-P. Knowledge of the residual noise correlation matrix per subchannel is not possible unless training data is used. Instead, we calculate the average residual noise power for each receiver phase which corresponds to the TAMSE and apply a simple MRC combiner. As shown in Fig. 6.10, the BER performance of this simple MRC combiner after the TD-NF is very close to the per subchannel MMSE combiner TD-NF-p (the performance gap is around 0.3 dB only). The TAMSE can be calculated easily using (6.20) based on the estimated correlation matrix.

Table 6.3: Complexity comparison for the proposed techniques.

Technique	Initial Complexity (per $T_{av} = N_{av} T_{sampling}$)	Running Complexity (per $T_{sampling}$)
TD-NF	$\overline{\mathbf{R}}_{\mathbf{zz}}$ estimation $$\underbrace{\frac{(N_pKL)(N_pKL+1)}{2}}_{\left(\substack{\text{number of elements for}\\ \text{symmetric matrix}}\right)} \times \underbrace{2}_{\left(\substack{\text{number of multipliers}\\ \text{per element}}\right)} \times N_{av}$$ $\overline{\mathbf{r}}_{\mathbf{z}x_i}$ estimation $$\underbrace{N_pKL}_{\left(\substack{\text{number of elements}\\ \text{in the vector}}\right)} \times \underbrace{2}_{\left(\substack{\text{number of multipliers}\\ \text{per element}}\right)} \times N_{av}$$ $\overline{\mathbf{R}}_{\mathbf{zz}}$ inverse calculation $$\underbrace{\frac{(N_pKL)^3}{3}}_{\left(\substack{\text{based on cholesky}\\ \text{decomposition}}\right)}$$ $\hat{\mathbf{w}}_i$ generation $(N_pKL)^2$	Filtering $$N_p \times (N_pKL)$$ LLR calculation $$N_p \times \left(\frac{N_{ac}}{N_B}\right)$$
TD-ENF	$\overline{\mathbf{R}}_{\mathbf{zz}}$ estimation $$\underbrace{\frac{(N_pKL)(N_pKL+1)}{2}}_{\left(\substack{\text{number of elements for}\\ \text{symmetric matrix}}\right)} \times \underbrace{2}_{\left(\substack{\text{number of multipliers}\\ \text{per element}}\right)} \times N_{av}$$ $\overline{\mathbf{r}}_{\mathbf{z}d_i}$ estimation $$\underbrace{N_pKL}_{\left(\substack{\text{for multiplication by the channel, assuming prior}\\ \text{computation for OFDM correlation}}\right)}$$ $\overline{\mathbf{R}}_{\mathbf{zz}}$ inverse calculation $$\underbrace{\frac{(N_pKL)^3}{3}}_{\left(\substack{\text{based on cholesky}\\ \text{decomposition}}\right)}$$ $\hat{\mathbf{w}}$ generation $(N_pKL)^2$	Filtering $$(N_pKL)$$
FD	$\overline{\mathbf{R}}_{\mathbf{zz}}$ estimation $$\underbrace{\frac{(N_p)(N_p+1)}{2}}_{\left(\substack{\text{number of elements for}\\ \text{symmetric matrix per subchannel}}\right)} \times N_{ac} \times N_R \times N_{av}$$ $\overline{\mathbf{R}}_{\mathbf{zz}}$ inverse calculation $$\underbrace{\frac{(N_p)^3}{3}}_{\left(\substack{\text{based on cholesky}\\ \text{decomposition}}\right)} \times N_{ac} \times N_R$$	LLR calculation $$\underbrace{2}_{\left(\substack{\text{two calculations for}\\ \text{the binary PSK}}\right)} \times \left(N_p^2 + N_p\right) \times \left(\frac{N_{ac}}{N_B}\right)$$

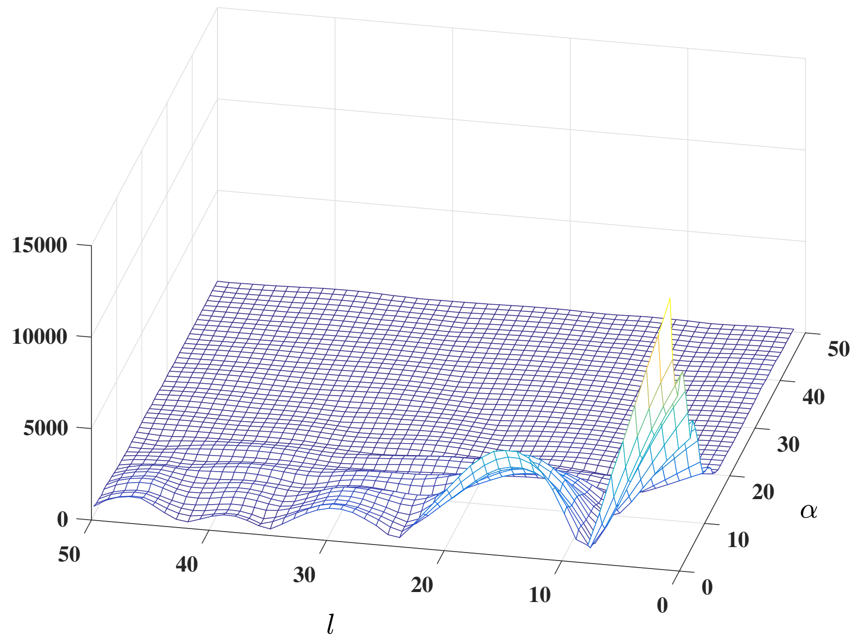

Figure 6.11: FFB-TI noise cyclic auto-correlation.

6.4 Complexity Analysis

In this section, we compare the complexities of the different proposed noise mitigation techniques in terms of the number of multiplications. The complexity of each technique can be categorized into initial and running complexities. Initial complexity includes the correlation matrices estimation in addition to the computations of the filter coefficients. The running complexity includes the filtering operations as well as equalization (or equivalently the LLR calculation). Table 6.3 shows the complexity comparison between the different techniques. As shown in Table 6.3, the SIMO TD-NF has the highest complexity among all proposed techniques in both the initial and running stages. The complexity of the SIMO TD-NF technique is totally controlled by K and L. As discussed earlier, the optimal value of K is a single complete cycle. However, for the NB-PLC noise's cyclic auto-correlation function, only few components contain most of the energy where the lower the component frequency is, the higher is its energy. Thus, the stationary component is the strongest component. This fact is demonstrated in Figs. 6.11 and 6.12 which show the cyclic auto-correlation function

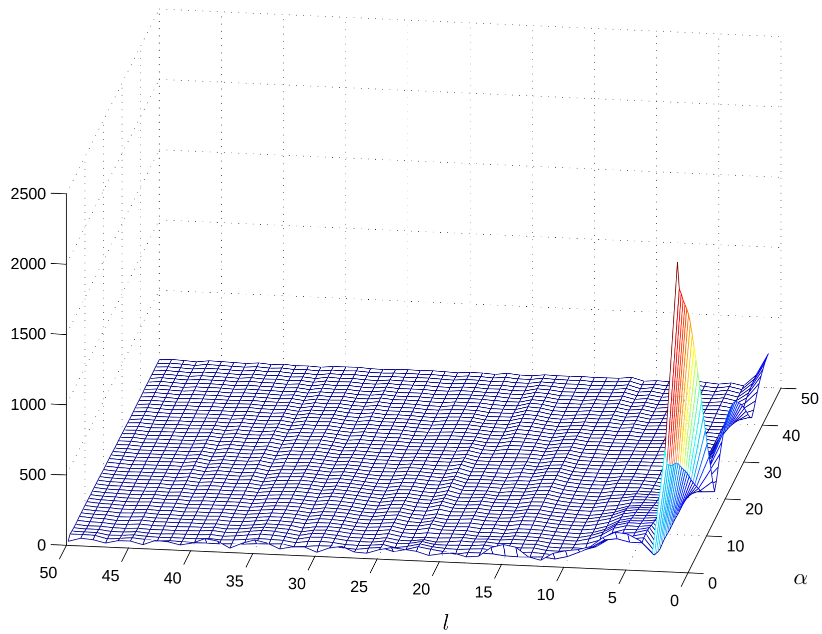

Figure 6.12: RB-LV14 noise cyclic auto-correlation.

for the FFB-TI and RB-LV14 noise models, respectively. On the other hand, the value of L is dictated by the maximum lag, denoted by ℓ_m, for which the cyclic auto-correlation function is non-zero over all cyclic frequencies. In general, the optimum number of coefficients is infinity. However, it is well-known that the auto-correlation function decays with lag ℓ_m and it can be shown from the cyclic auto-correlation functions in Figs. 6.11 and 6.12 that an approximated value for the maximum lag ℓ_m can be easily identified. It is clear that increasing K and/or L improves the performance. However, if the total number of coefficients of the FRESH filter ($L_{\text{tot}} = N_p K L$) is assumed to be fixed based on the overall allowable complexity level, the problem of selecting K and L can be viewed as an optimization problem. A fixed total number of filter coefficients means constant complexity even for different combinations of K and L since the auto-correlation matrix size is always $N_p KL \times N_p KL$. Assuming a fixed total number of coefficients for the FRESH filter, we may choose the combination of K and L using one of the following methods

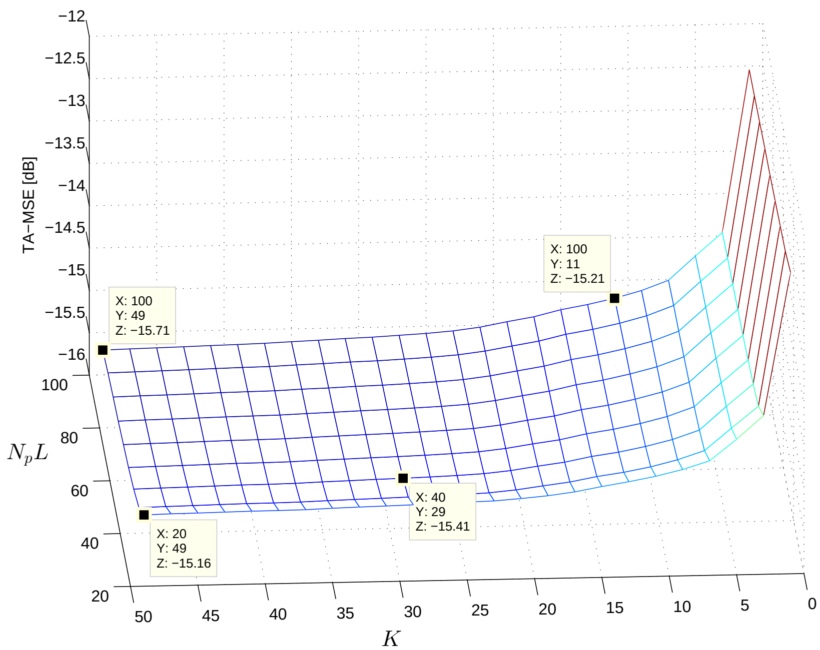

Figure 6.13: FFB-TI noise TAMSE versus both K and L for Phase B, SNR = 0 dB.

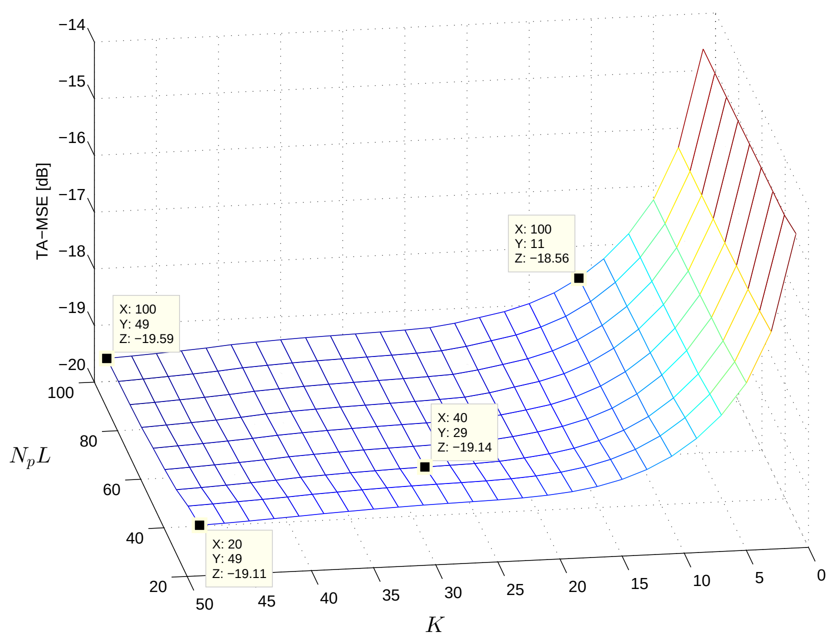

Figure 6.14: RB-LV14 noise TAMSE versus both K and L for Phase B, SNR = 0 dB.

1. **Assuming a constant number of coefficients per branch** $\ell(k) = L$. In this case, we first determine the maximum lag ℓ_m from the stationary component using a certain

threshold. We assume that the stationary component has the maximum lag ℓ_m which is a good assumption as shown in the cyclic auto-correlation function plots in Figs. 6.11 and 6.12. Then, we choose L as the closest integer value to ℓ_m that is a factor of L_{tot} and results in an odd number of branches K. Alternatively, we can calculate the average energy for each cyclic frequency and use some threshold to decide on the number of cyclic components to be included. Suppose that we decide to stop at the cyclic component k_m, then, choose K as the closest odd integer to k_m that is also a factor of L_{tot}. The resulting K and L from the previous methods are generally different.

Figs. 6.13 and 6.14 show the TAMSE vs both K and L for the FFB-TI and RB-LV14 noise models, respectively. Since the FFB-TI noise model has a relatively large correlation lag ℓ as shown in Fig. 6.11, choosing a large L is better than choosing a large K. On the other hand, since the RB-LV14 model has a relatively large number of cyclic frequencies as shown in Fig. 6.12, choosing a large K is better than choosing a large L. The TAMSE versus N_pKL is shown in Fig. 6.15.

2. **Assuming a variable number of coefficients per branch** $\ell(k)$. In this case, we first determine the maximum lag ℓ_m for the stationary component and choose it as $\ell(0)$. Then, compute the maximum lag ℓ_m for the first cyclic component and determine the number of coefficients per the first positive and negative components $\ell(1)$ and $\ell(-1)$ since they are symmetric. We continue to compute $\ell(k)$ for the other components until we reach the total number of coefficients, i.e., $L_{tot} = N_p \sum_k \ell(k)$. This method is expected to be better than the previous one since it results in more flexible choices but requires a higher complexity.

Interestingly, we observe from Fig. 6.16 that the energy of the cyclic frequency components of the OFDM signal is very small. We also arrive at the same conclusion through the TAMSE comparison with and without including the OFDM cyclic frequency components. As shown

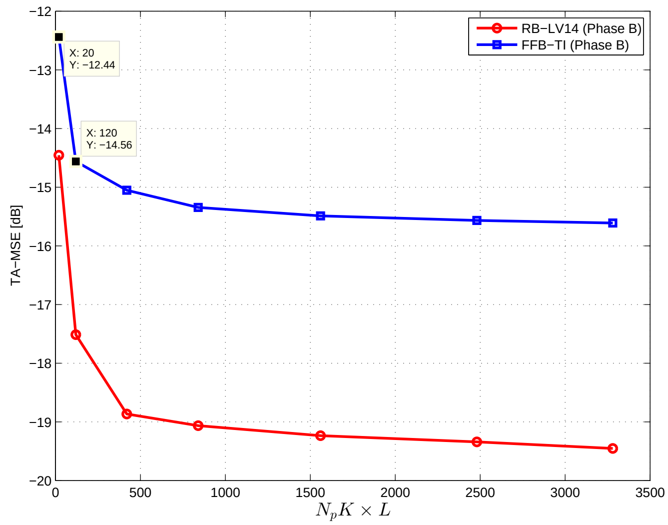

Figure 6.15: TAMSE versus N_pKL for the TD-NF technique.

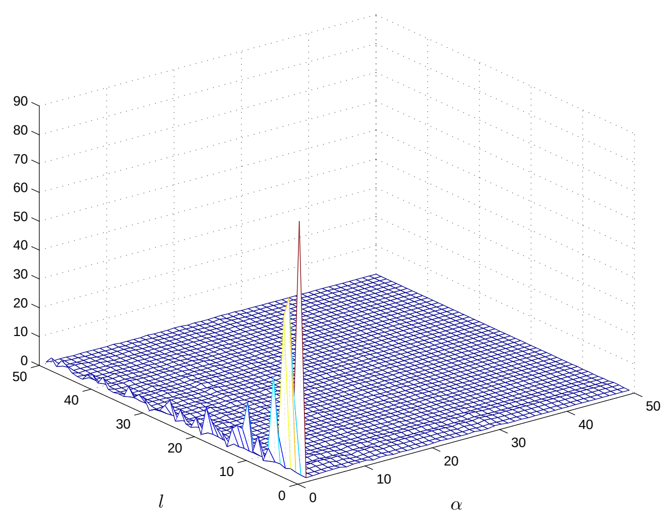

Figure 6.16: OFDM signal cyclic auto-correlation.

in Fig. 6.17, the TAMSE shows a very small enhancement (0.1 dB) when adding 18 OFDM cyclic frequency components. As a result, we may not use any OFDM cyclic frequency components in our FRESH filter design of the proposed receiver noise mitigation techniques and only the stationary component can be included which is common between the OFDM and noise signals.

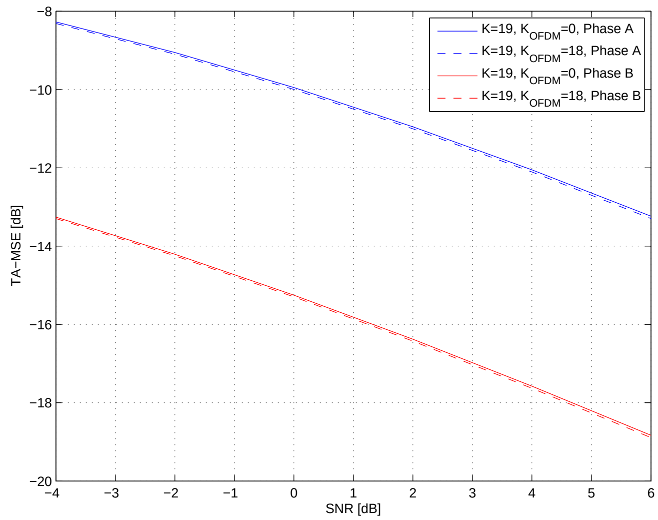

Figure 6.17: TAMSE of the SIMO TD-NF for the FFB-TI noise with/without including the OFDM cyclic frequencies.

CHAPTER 7

PROPOSED SPARSITY-BASED JOINT NBI AND IMPULSE NOISE MITIGATION IN HYBRID PLC-WIRELESS TRANSMISSIONS [1]

In this chapter, we develop NBI and IN mitigation techniques, based on the principles of compressive sensing (CS), that exploit the inherent (non-contiguous or contiguous) sparse structures of NBI and IN in the frequency and time domains, respectively (Mokhtar et al., 2015; Elgenedy et al., 2018). In addition, we investigate other features such as prior knowledge about the sparsity level at each receive antenna and powerline which helps to reduce implementation complexity or enhance the estimation performance. Moreover, we investigate the performance degradation assuming more realistic asynchronous NBI scenario and propose enhancement techniques for this case. Next, we show how to exploit the spatial correlations of the NBI and IN across the receive antennas and powerlines. To further improve the estimation performance, we propose a Bayesian linear minimum mean square error based approach for estimating both non-contiguous and contiguous NBI and IN based on their second-order statistics. Finally, we simulate the performance of the different proposed techniques, and we show the significant performance enhancement of the joint processing of our proposed NBI and IN sparsity-based mitigation techniques compared to separate processing of the wireless and powerline received signals.

Notation: For the rest of this chapter, $\mathbf{I}$ and $\mathbf{F}$ denote the identity and the unitary discrete Fourier transform (DFT) matrices, respectively, while subscripts denote their dimensions. Matrices/vectors in the frequency domain are denoted by $\mathbf{A}_X^{(u)}/\mathbf{a}_X^{(u)}$, where the subscript $X \in \{W, P\}$ denotes the communication system with W for wireless system and P for PLC system, while the superscript u denotes the u^{th} antenna/wire. The corresponding time domain matrices/vectors are denoted by $\bar{\mathbf{A}}_X^{(u)}/\bar{\mathbf{a}}_X^{(u)}$.

[1] © 2018 IEEE M. Elgenedy, M. M. Awadin, R. Hamila, W. U. Bajwa, A. S. Ibrahim and N. Al-Dhahir, "Sparsity-Based Joint NBI and Impulse Noise Mitigation in Hybrid PLC-Wireless Transmissions," in IEEE Access, vol. 6, pp. 30280-30295, 2018.

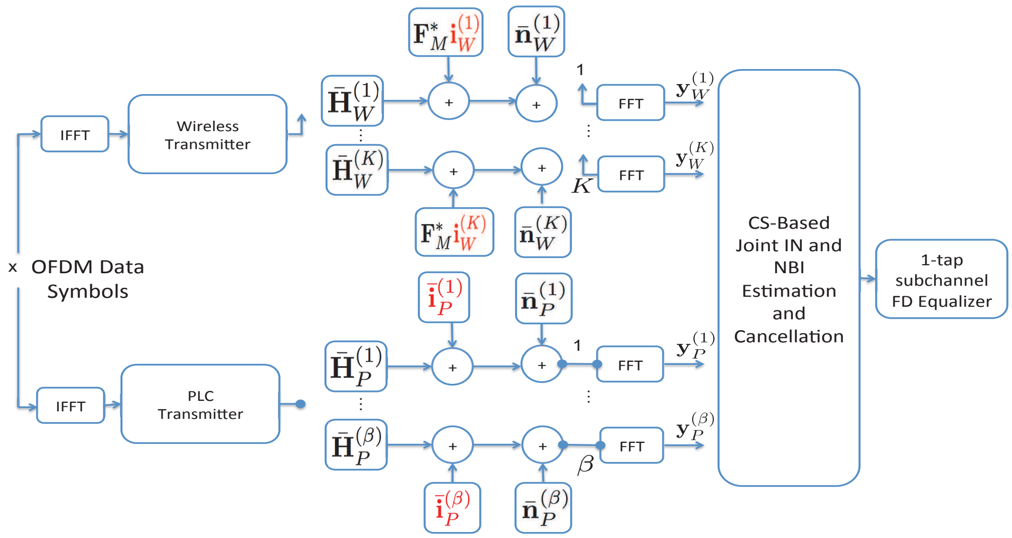

Figure 7.1: System model of the SIMO hybrid wireless/PLC system (red fonts indicate sparse vectors).

7.1 System Model

We assume single-input multiple-output (SIMO) OFDM simultaneous transmissions over wireless and PLC links (Lai and Messier, 2012) as shown in Fig. 7.1. The wireless link operates in the WLAN unlicensed frequency band and consists of a single-antenna transmitter and a K-antenna receiver. The PLC receiver can process up to $\beta \in \{1, 2, 3\}$ outputs over its 3 receive wires (phases). The NBI over the different wireless receive antennas is assumed to be uncorrelated. In addition, we assume that the PLC receive wires experience uncorrelated IN. Assuming uncorrelated NBI/IN over the different receive antennas/wires is a worst-case assumption since the spatial correlation between the wireless and/or PLC receive branches can be exploited to further enhance the NBI and IN mitigation performance, as will be discussed in Section 7.3.3. Given these assumptions, the received signals at the k^{th}, $k \in \{1, \ldots, K\}$, antenna and the j^{th}, $j \in \{1, \ldots, \beta\}$, wire are given by

$$\bar{\mathbf{y}}_W^{(k)} = \bar{\mathbf{H}}_W^{(k)} \bar{\mathbf{x}} + \bar{\mathbf{i}}_W^{(k)} + \bar{\mathbf{n}}_W^{(k)}, \tag{7.1}$$

$$\bar{\mathbf{y}}_P^{(j)} = \bar{\mathbf{H}}_P^{(j)} \bar{\mathbf{x}} + \bar{\mathbf{i}}_P^{(j)} + \bar{\mathbf{n}}_P^{(j)}, \tag{7.2}$$

Assuming M OFDM subcarriers per OFDM symbol, the $\bar{\mathbf{H}}_W^{(k)}$ and $\bar{\mathbf{H}}_P^{(j)}$ denote the $M \times M$ circulant channel matrices between the transmitter's antenna/wire and the $k^{\text{th}}/j^{\text{th}}$ receiver's antenna/wire of the wireless/PLC link. The first columns of these matrices are $\begin{bmatrix} \bar{\mathbf{h}}_W^{(k)T} & \mathbf{0}_{1\times M-L_W} \end{bmatrix}^T$ and $\begin{bmatrix} \bar{\mathbf{h}}_P^{(j)T} & \mathbf{0}_{1\times M-L_P} \end{bmatrix}^T$, where $\bar{\mathbf{h}}_W^{(k)}$ and $\bar{\mathbf{h}}_P^{(j)}$ are the wireless and PLC channel impulse response (CIR) vectors with L_W and L_P taps, respectively. The wireless CIR taps is assumed to be Gaussian distributed, while the magnitudes of the PLC CIR taps are assumed log-normal distributed (Guzelgoz et al., 2010). Furthermore, we assume perfect channel state information (CSI) at the wireless and PLC receivers. Using $\mathbf{x}$ for the $M \times 1$ OFDM data vector, the vector $\bar{\mathbf{x}}$ in (7.1) and (7.2) is defined as $\bar{\mathbf{x}} = \mathbf{F}_M^*\mathbf{x}$. Furthermore, $\bar{\mathbf{n}}_W^{(k)}$ and $\bar{\mathbf{n}}_P^{(j)}$ denote complex zero-mean circularly-symmetric AWGN vectors at the $k^{\text{th}}/j^{\text{th}}$ receiver's antenna/wire with variances σ_W^2 and σ_P^2, respectively. Finally, the NBI (sparse in the frequency domain) and the IN (sparse in the time domain) vectors at each antenna/wire are denoted by $\bar{\mathbf{i}}_W^{(k)}$ and $\bar{\mathbf{i}}_P^{(j)}$, respectively.

Applying the DFT to (7.1) and (7.2), we obtain

$$\underbrace{\mathbf{F}_M\bar{\mathbf{y}}_W^{(k)}}_{\triangleq \mathbf{y}_W^{(k)}} = \underbrace{\mathbf{F}_M\bar{\mathbf{H}}_W^{(k)}\mathbf{F}_M^*}_{\triangleq \Lambda_W^{(k)}}\mathbf{x} + \underbrace{\mathbf{F}_M\bar{\mathbf{i}}_W^{(k)}}_{\triangleq \mathbf{i}_W^{(k)}} + \underbrace{\mathbf{F}_M\bar{\mathbf{n}}_W^{(k)}}_{\triangleq \mathbf{n}_W^{(k)}}, \text{ and} \tag{7.3}$$

$$\underbrace{\mathbf{F}_M\bar{\mathbf{y}}_P^{(j)}}_{\triangleq \mathbf{y}_P^{(j)}} = \underbrace{\mathbf{F}_M\bar{\mathbf{H}}_P^{(j)}\mathbf{F}_M^*}_{\triangleq \Lambda_P^{(j)}}\mathbf{x} + \mathbf{F}_M\bar{\mathbf{i}}_P^{(j)} + \underbrace{\mathbf{F}_M\bar{\mathbf{n}}_P^{(j)}}_{\triangleq \mathbf{n}_P^{(j)}}, \tag{7.4}$$

where $\Lambda_W^{(k)}$ and $\Lambda_P^{(j)}$ are $M \times M$ diagonal matrices whose diagonal elements (collected in the vectors $\begin{bmatrix} h_{W,1}^{(k)} & \ldots & h_{W,M}^{(k)} \end{bmatrix}$ and $\begin{bmatrix} h_{P,1}^{(j)} & \ldots & h_{P,M}^{(j)} \end{bmatrix}$) are the channel frequency response (CFR) coefficients of the $k^{\text{th}}/j^{\text{th}}$ receiver's antenna/wire of the wireless/PLC output, respectively. The vector $\mathbf{i}_W^{(k)}$ denotes the frequency-domain (FD) NBI at the k^{th} antenna. In addition, the sparsity of NBI (in frequency) and IN (in time) implies that $\|\mathbf{i}_W^{(k)}\|_0 \triangleq \rho_W^{(k)} \ll M$ and $\|\bar{\mathbf{i}}_P^{(j)}\|_0 \triangleq \rho_P^{(j)} \ll M$.

Combining the received wireless and PLC signals in (7.3) and (7.4) for all $k \in \{1, \ldots, K\}$ and $j \in \{1, \ldots, \beta\}$ into a single column vector leads to the following model

$$\underbrace{\begin{bmatrix} \mathbf{y}_W^{(1)} \\ \vdots \\ \mathbf{y}_W^{(K)} \\ \mathbf{y}_P^{(1)} \\ \vdots \\ \mathbf{y}_P^{(\beta)} \end{bmatrix}}_{\triangleq \mathbf{y}} = \underbrace{\begin{bmatrix} \Lambda_W^{(1)} \\ \vdots \\ \Lambda_W^{(K)} \\ \Lambda_P^{(1)} \\ \vdots \\ \Lambda_P^{(\beta)} \end{bmatrix}}_{\triangleq \mathbf{G}} \mathbf{x} + \underbrace{\begin{bmatrix} \mathbf{i}_W^{(1)} \\ \vdots \\ \mathbf{i}_W^{(k)} \\ \mathbf{F}_M \bar{\mathbf{i}}_P^{(1)} \\ \vdots \\ \mathbf{F}_M \bar{\mathbf{i}}_P^{(\beta)} \end{bmatrix}}_{\triangleq \mathbf{i}} + \underbrace{\begin{bmatrix} \mathbf{n}_W^{(1)} \\ \vdots \\ \mathbf{n}_W^{(K)} \\ \mathbf{n}_P^{(1)} \\ \vdots \\ \mathbf{n}_P^{(\beta)} \end{bmatrix}}_{\triangleq \mathbf{n}}. \tag{7.5}$$

Here, we refer to the $M(K+\beta) \times 1$ vector $\mathbf{y}$ as the *measurement vector*, while we refer to the $M(K+\beta) \times M$ matrix $\mathbf{G}$ as the *channel matrix*. Note that $\mathbf{G}$ consists of the CFR matrices of the wireless and PLC links, i.e., $\mathbf{G} \triangleq \left[\mathbf{G}_W^H \;\; \mathbf{G}_P^H\right]^H$, where $\mathbf{G}_W$ and $\mathbf{G}_P$ denote the concatenated FD channel matrices for the wireless and PLC links, respectively. Finally, $\mathbf{i}$ denotes the $M(K+\beta) \times 1$ combined NBI and IN vectors, $\mathbf{n}$ is the equivalent $M(K+\beta) \times 1$ noise vector in frequency domain. Our main objective here is to use (7.5) to estimate the NBI and IN vectors.

In practice, the NBI and IN signals inherit several attractive features due to the nature of wireless and PLC links, respectively, that play an important role in mitigating their effects. Specifically, both NBI and IN can either be non-contiguous or contiguous, i.e., they can occupy either dispersed or consecutive frequency subcarriers and time samples, respectively. Moreover, NBI can be synchronous or asynchronous depending on the interference source. In the synchronous scenario, the NBI samples fall exactly on the desired signal's DFT grid while asynchronous NBI exhibits a carrier frequency offset with respect to the desired signal's carrier frequency. In this chapter, we mainly focus on the synchronous NBI and IN case. The asynchronous NBI is only discussed in Subsection 7.2.3. Consideration of asynchronous IN is beyond the scope of this chapter. In the next sections, we propose efficient algorithms to effectively exploit NBI and IN signal features.

7.2 Sparsity-Based Joint Estimation of Non-Contiguous NBI and IN

In this section, we investigate the use of sparse recovery algorithms for the mitigation of non-contiguous NBI and synchronous IN signals. Initially, we assume synchronous NBI, then we discuss the asynchronous NBI case in Subsection 7.2.3. To estimate NBI and IN vectors from $\mathbf{y}$, we first cancel the unknown term $\mathbf{Gx}$ in (7.5) by projecting $\mathbf{y}$ onto the left-null space of $\mathbf{G}$ using the projection matrix (Caire et al., 2008a; Gomaa and Al-Dhahir, 2011) $\mathbf{Q} = \mathbf{I}_{M(K+\beta)} - \mathbf{G}\mathbf{G}^{\dagger}$, where $\mathbf{G}^{\dagger}$ denotes the pseudoinverse of $\mathbf{G}$ given by $\left(\mathbf{G}^H\mathbf{G}\right)^{-1}\mathbf{G}^H$ for the case of a full column rank $\mathbf{G}$. Since $\mathbf{QG} = \mathbf{0}_{M(K+\beta)\times M}$, the projected received signal is given by

$$\mathbf{y}' \triangleq \mathbf{Qy} = \mathbf{Qi} + \mathbf{Qn}. \tag{7.6}$$

Let $\mathbf{i}_{\text{eqv}}$ represent the concatenation of the NBI vector in the frequency domain and IN vector in the time domain, i.e., $\mathbf{i}_{\text{eqv}} \triangleq \begin{bmatrix} \mathbf{i}_W^{(1)^T} & \dots & \mathbf{i}_W^{(K)^T} & \bar{\mathbf{i}}_P^{(1)^T} & \dots & \bar{\mathbf{i}}_P^{(\beta)^T} \end{bmatrix}^T$. Then, vector $\mathbf{i}$ can be written in terms of $\mathbf{i}_{\text{eqv}}$ as follows

$$\mathbf{i} = \underbrace{\begin{bmatrix} \mathbf{I}_{KM} & \mathbf{0}_{KM\times\beta M} \\ \mathbf{0}_{\beta M\times KM} & \mathbf{I}_{\beta}\otimes\mathbf{F}_M \end{bmatrix}}_{\triangleq\mathbf{A}} \mathbf{i}_{\text{eqv}}, \tag{7.7}$$

where $\otimes$ denotes the Kronecker product operation.

Now, (7.6) can be rewritten as follows

$$\mathbf{y}' \triangleq \mathbf{Q}_{\text{eqv}}\mathbf{i}_{\text{eqv}} + \mathbf{n}', \tag{7.8}$$

where the *measurement matrix* $\mathbf{Q}_{\text{eqv}}$ is defined in terms of $\mathbf{Q}$ as $\mathbf{Q}_{\text{eqv}} = \mathbf{QA}$, and $\mathbf{n}' \triangleq \mathbf{Qn}$. Now, we have reduced our joint NBI and IN estimation problem to the linear model in (7.8). While we can use conventional estimation techniques in this setting to estimate $\mathbf{i}_{\text{eqv}}$, we know from (Gomaa and Al-Dhahir, 2011; Caire et al., 2008a; Candes et al., 2006) that

Algorithm 1 OMP for Joint Estimation of Non-Contiguous NBI and IN

Inputs: Matrix $\mathbf{Q}_{\text{eqv}}$, vector $\mathbf{y}'$, and sparsity level S.

Initialization: Define set index $I_0 = \{\}$, set residual $\mathbf{r}_0 = \mathbf{y}'$, estimate $\hat{\mathbf{i}}_{\text{eqv}} = \mathbf{0}_{(K+\beta)M}$, and the iteration count $l = 1$.

The l^{th} iteration:

1. Calculate $\delta_i = \left|\mathbf{r}_{l-1}^H \mathbf{Q}_{\text{eqv}}(:, i)\right|$ for all $i \notin I_{l-1}$, where $\mathbf{Q}_{\text{eqv}}(:, i)$ denotes the column i in the matrix $\mathbf{Q}_{\text{eqv}}$.
2. Search for index of the next non-zero entry at the l^{th} iteration as $c_l = \underset{i}{\operatorname{argmax}}\ \delta_i$.
3. Update the non-zero entries indices as $I_l = I_{l-1} \cup\ \{c_l\}$.
4. Set $\hat{\mathbf{i}}_{\text{eqv}}(I_l) = \left(\mathbf{Q}_{\text{eqv}}(:, I_l)\right)^{\dagger} \mathbf{y}'$, where $\hat{\mathbf{i}}_{\text{eqv}}(I_l)$ denotes the entries of $\hat{\mathbf{i}}_{\text{eqv}}$ indexed by I_l.
5. Calculate the residual error term at the l^{th} iteration as $\mathbf{r}_l = \mathbf{y}' - \mathbf{Q}_{\text{eqv}}(:, I_l)\hat{\mathbf{i}}_{\text{eqv}}(I_l)$.
6. **If** $l = S$ then exit, **else** set $l = l + 1$ and go to Step 1.

exploiting the sparsity of $\mathbf{i}_{\text{eqv}}$ can further enhance the estimation performance. In particular, CS principles advocate for the estimation of sparse vectors by solving problems of the form (7.8) as follows

$$\hat{\mathbf{i}}_{\text{eqv}} \triangleq \underset{\mathbf{i} \in \mathbb{C}^{(K+\beta)M}}{\operatorname{argmin}} \|\mathbf{Q}_{\text{eqv}}\mathbf{i} - \mathbf{y}'\|_2^2 \ \text{ subject to } \ \|\mathbf{i}\|_0 \ = \ S, \tag{7.9}$$

where S is the number of non-zero elements of $\mathbf{i}_{\text{eqv}}$, defined as $S \triangleq \sum_{k=1}^{K} \rho_W^{(k)} + \sum_{j=1}^{\beta} \rho_P^{(j)}$.

Note that while (7.9) in its stated form has combinatorial complexity, there exist a number of greedy and optimization-based techniques in the CS literature that can be applied to efficiently solve this problem. In this chapter, we use a well-known greedy algorithm, named *orthogonal matching pursuit* (OMP) (Pati et al., 1993), because of its low computational complexity. OMP algorithm estimates $\hat{\mathbf{i}}_{\text{eqv}}$ iteratively by selecting S columns of $\mathbf{Q}_{\text{eqv}}$ that are most correlated with the observations $\mathbf{y}'$ and then solving a *restricted* least-squares (LS) problem using the selected columns. For completeness, we summarize its main steps in Algorithm 1 using the notation of this chapter.

Remark: The matrix $\mathbf{Q}_{\text{eqv}}$ has a closed-form expression since both $\mathbf{Q}$ and $\mathbf{G}$ have a special structure and can be decomposed into diagonal matrices. Specifically, after some algebraic manipulations, it follows that

$$\mathbf{Q} = \mathbf{I}_{M(K+\beta)} - \begin{bmatrix} \mathbf{G}_W \mathbf{G}_W^H & \mathbf{G}_W \mathbf{G}_P^H \\ \mathbf{G}_P \mathbf{G}_W^H & \mathbf{G}_P \mathbf{G}_P^H \end{bmatrix} \times \left(\mathbf{I}_{K+\beta} \otimes \Psi \right) \tag{7.10}$$

with the matrix Ψ defined as follows:

$$\begin{aligned} \Psi \triangleq \Big[& \Lambda_W^{(1)} \left(\Lambda_W^{(1)} \right)^H + \ldots + \Lambda_W^{(K)} \left(\Lambda_W^{(K)} \right)^H \\ & + \Lambda_P^{(1)} \left(\Lambda_P^{(1)} \right)^H + \ldots + \Lambda_P^{(\beta)} \left(\Lambda_P^{(\beta)} \right)^H \Big]^{-1}. \end{aligned} \tag{7.11}$$

Assuming perfect CSI, $\mathbf{Q}$ can be computed efficiently from (7.10) since it is much easier to compute the inverse of the diagonal matrix in (7.11), denoted by Ψ, instead of using the form $\mathbf{Q} = \mathbf{I}_{M(K+\beta)} - \mathbf{G}\mathbf{G}^{\dagger}$ which requires computation of the inverse of the general matrix $\left(\mathbf{G}^H \mathbf{G} \right)^{-1}$.

In the following, our proposed framework for joint estimation of non-contiguous NBI and IN is extended to include the following cases. First, in Subsection 7.2.1, we consider the general case of unequal sparsity levels of NBI and IN on different antennas/wires. Second, in Subsection 7.2.2, we exploit knowledge of the second order statistics of the NBI and IN to enhance the estimation quality. Finally, in Subsection 7.2.3, we investigate the case when the carrier frequency of the NBI signal is different than the desired signal's carrier frequency (asynchronous NBI), which leads to NBI leakage across the OFDM subcarriers.

7.2.1 Multi-Level OMP

In this subsection, we exploit knowledge of the, generally unequal, sparsity levels of the NBI and IN signals across antennas and wires, respectively.

In this case, the problem formulation in (7.9) can be rewritten as follows:

$$\hat{\mathbf{i}}_{\text{eqv}} \triangleq \underset{\mathbf{i}\in\mathbb{C}^{(K+\beta)M}}{\operatorname{argmin}} \|\mathbf{Q}_{\text{eqv}}\mathbf{i} - \mathbf{y}'\|_2^2$$
$$\text{subject to } \ \|\mathbf{T}_X^{(u)}\mathbf{i}\|_0 \ = \ \rho_X^{(u)}, \ \forall (X,u), \tag{7.12}$$

where $(X, u) \in \{(W, 1), ..., (W, K), (P, 1), ..., (P, \beta)\}$, $\mathbf{T}_X^{(u)}$ is a diagonal matrix of size $(K+\beta)M \times (K+\beta)M$ and its diagonal entries are all zeros except for M ones corresponding to the u^{th} receive antenna/wire. Hence, the operation $\|\mathbf{T}_X^{(u)}\mathbf{i}\|_0$ counts the number of non-zero entries in the NBI/IN vector at the u^{th} receive port.

To solve this problem, we present a modified version of the greedy OMP algorithm such that a multi-level sparsity constraint for each segment of vector $\mathbf{i}$ is satisfied. The modified multi-level OMP recovery algorithm aims to reduce computational complexity by reducing the search space based on the pre-defined different antennas'/wires' sparsity levels $\rho_X^{(u)}$. In other words, multi-level OMP aims to achieve the same performance as that of the greedy OMP at a much lower complexity. Specifically, we define the vector $z_X^{(u)}$ that counts the number of detected non-zero elements for each antenna/wire u for every iteration l. In each iteration l, we map the detected element index c_l to the corresponding antenna/wire u and update the vector $z_X^{(u)}$. Then, we compare the updated vector $z_X^{(u)}$ with the desired sparsity level $\rho_X^{(u)}$. Once the vector $z_X^{(u)}$ reaches the sparsity level for a specific antenna/wire u', i.e., $z_X^{(u')} = \rho_X^{(u')}$, we exclude all indices associated with the antenna/wire u' from the search space. The entire procedure for multi-level OMP is given in Algorithm 2.

Computational savings in multi-level OMP

We compare the total computational complexity of the multi-level OMP algorithm against the total computational complexity of the OMP algorithm in terms of the number of multiplications. As shown in Algorithm 1, for the OMP algorithm, a matrix/vector multiplication is required in Steps 1, 4 and 5. The first step of the OMP algorithm requires multiplying the

Algorithm 2 Multi-level OMP for Joint Estimation of Non-Contiguous NBI and IN

Inputs: Vector $\mathbf{y}'$, matrix $\mathbf{Q}_{\text{eqv}}$, multi-level sparsity constraints $\rho_X^{(u)}$, and overall sparsity S.
Initialization: Define set index $I_0 = \tilde{I}_0 = \{\}$, set residual $\mathbf{r}_0 = \mathbf{y}'$, estimate $\hat{\mathbf{i}}_{\text{eqv}} = \mathbf{0}_{(K+\beta)M}$, iteration count $l = 1$, and $z_X^{(u)} = 1$, $(X, u) \in \{(W, 1), ..., (W, K), (P, 1), ..., (P, \beta)\}$.
The l^{th} iteration:

1. Compute $\delta_i = \left|\mathbf{r}_{l-1}^H \mathbf{Q}_{\text{eqv}}(:, i)\right|$ for all $i \notin \tilde{I}_{l-1}$.
2. Search for index of the next non-zero entry at the l^{th} iteration as $c_l = \underset{i}{\operatorname{argmax}}\ \delta_i$.
3. **If** $c_l > MK$, **then** $X = P$ and $u = \left\lceil \frac{c_l - MK}{M} \right\rceil$, **else** $X = W$ and $u = \left\lceil \frac{c_l}{M} \right\rceil$.
4. For (X, u) calculated in the previous step, **if** $z_X^{(u)} > \rho_X^{(u)}$, **then** add all the column indices associated with the u^{th} receive port to the set $\tilde{I}_l$ if they do not exist already, i.e., $\tilde{I}_l = \tilde{I}_{l-1} \cup \psi$, where $\psi = \{(u-1)M + 1, ..., uM\}$ if $X = W$, and $\psi = \{((u-1)M + 1, ..., uM) + MK\}$ if $X = P$, and go to Step 1, **else** proceed to Step 5.
5. Update the non-zero elements indices as $I_l = I_{l-1} \cup \{c_l\}$ and $\tilde{I}_l = \tilde{I}_{l-1} \cup \{c_l\}$.
6. Set $\hat{\mathbf{i}}_{\text{eqv}}(I_l) = \left(\mathbf{Q}_{\text{eqv}}(:, I_l)\right)^{\dagger} \mathbf{y}'$, where $\hat{\mathbf{i}}_{\text{eqv}}(I_l)$ denotes the elements of $\hat{\mathbf{i}}_{\text{eqv}}$ indexed by I_l.
7. Calculate the residual error at the l^{th} iteration as $\mathbf{r}_l = \mathbf{y}' - \mathbf{Q}_{\text{eqv}}(:, I_l)\mathbf{i}_{\text{eqv}}(I_l)$ and set $z_X^{(u)} = z_X^{(u)} + 1$.
8. **If** $l = S$ then exit, **else** set $l = l + 1$ and go to Step 1.

---

vector $\mathbf{r}_{l-1}$ by the matrix $\mathbf{Q}_{\text{eqv}}(:, i)$, which is a subset of the matrix $\mathbf{Q}_{\text{eqv}}$ that includes all columns except the indices corresponding to the detected interference indices, i.e., $i \notin I_{l-1}$. To compute the LS estimate $\hat{\mathbf{i}}_{\text{eqv}}(I_l)$, Step 4 requires computation of the pseudo-inverse of $\mathbf{Q}_{\text{eqv}}(:, I_l)$ in addition to a matrix/vector multiplication, where $\mathbf{Q}_{\text{eqv}}(:, I_l)$ is a subset of the matrix $\mathbf{Q}_{\text{eqv}}$ that includes the columns corresponding only to the detected interference indices I_l. In Step 5, a matrix/vector multiplication between the estimated interference vector $\hat{\mathbf{i}}_{\text{eqv}}(I_l)$ and the matrix $\mathbf{Q}_{\text{eqv}}(:, I_l)$ is needed to compute the residual vector $\mathbf{r}_l$. Here, the computational complexity of Step 5 can be neglected since the vector $\hat{\mathbf{i}}_{\text{eqv}}(I_l)$ is a sparse vector with maximum sparsity level S. Moreover, in Step 4, $\mathbf{Q}_{\text{eqv}}(:, I_l)$ has a maximum dimension of $M(K + \beta) \times S$ in the last iteration. This means that, in the worst case, the LS estimation first requires inversion of a matrix of size $S \times S$ (which requires $S^3/3$ multiplications using Cholesky factorization) and then a matrix/vector multiplication requiring $M(K+\beta) \times S$ multiplications. Hence, under the assumption $S << M(K+\beta)$, the LS complexity is very small and can be neglected compared to the complexity of Step 1, which involves a matrix/vector multiplication requiring $M(K+\beta) \times M(K+\beta)$ multiplications. Similarly, for the multi-level OMP algorithm, the complexity is dominated by Step 1 under the assumption $S << M(K+\beta)$. Therefore, in the following computational complexity comparison, we focus only on the complexity of Step 1.

For simplicity, we assume the same sparsity level for all antennas and wires, i.e., $\rho_W^{(k)} = \rho_P^{(j)} = \rho$ for all $k \in \{1, ..., K\}$ and $j \in \{1, ..., \beta\}$. Now, let $N = M(K+\beta)$, then the total complexity of the OMP algorithm $\mathbb{C}_{OMP}$ can be expressed as follows:

$$\mathbb{C}_{OMP} = \sum_{i=0}^{S-1} N(N-i) = \sum_{m=1}^{K+\beta} \sum_{i=0}^{\rho-1} N(N-(m-1)\rho - i). \tag{7.13}$$

As discussed earlier, the computational savings for the multi-level OMP algorithm comes from the reduction of the search space (number of columns) in Step 1 with successive iterations. In particular, unlike the OMP algorithm, instead of eliminating one column every iteration, the multi-level OMP either eliminates one column or M columns in every iteration based on a condition on the number of detected NBI/IN subcarriers/samples at each antenna/wire. Since the complexity reduction in every iteration of the multi-level OMP is not deterministic, the complexity of the multi-level OMP is not fixed. Thus, we evaluate the best and worst case complexity for the multi-level OMP algorithm. For the best case complexity, the detection is performed for all NBI/IN indices associated with the first antenna/wire so that all columns corresponding to the first antenna/wire can be excluded from the remaining iterations, then the detection is performed for all NBI/IN indices associated with the following antenna/wire and so on. The complexity for the best case of the multi-level OMP algorithm $\mathbb{C}_{MOMP,b}$ can be evaluated as follows:

$$\mathbb{C}_{MOMP,b} = \sum_{m=1}^{K+\beta} \sum_{i=0}^{\rho-1} N(N-(m-1)M-i). \tag{7.14}$$

Comparing (7.13) and (7.14), it is clear that the best case complexity of the multi-level OMP algorithm is much smaller than the complexity of the OMP algorithm since $M >> \rho$. However, the worst case complexity of the multi-level OMP algorithm occurs when the column's exclusion is not possible until the last $(K+\beta)$ iterations where every antenna/wire has only one remaining NBI/IN index to be detected. Since the complexity saving in the worst case multi-level OMP algorithm (compared to OMP algorithm) is only in the last $(K+\beta)$ iterations, the worst case complexity of the multi-level OMP algorithm $\mathbb{C}_{MOMP,w}$ as a function of the complexity of the OMP algorithm $\mathbb{C}_{OMP}$ is given by the following expression:

$$\begin{aligned}\mathbb{C}_{MOMP,w} =& \mathbb{C}_{OMP} - \\ & \sum_{i=S-K-\beta+1}^{S-1} N(M-\rho)(i-S+K+\beta).\end{aligned} \tag{7.15}$$

Note that the term subtracted from the $\mathbb{C}_{OMP}$ in (7.15) is always positive. Hence, the worst case complexity of the multi-level OMP algorithm is always lower than the complexity of the OMP algorithm. In Section 7.4, we present numerical results for the computational complexity savings in the multi-level OMP compared to the OMP algorithm.

7.2.2 LMMSE Based OMP

In this subsection, we exploit knowledge of the second-order statistics of the NBI and IN signals, when they are available at the receiver, to further enhance the quality of their estimates. In particular, we propose replacing the LS estimator in Step 4 in Algorithm 1

(Step 6 in Algorithm 2) with the linear minimum mean square error (LMMSE) estimator based on the second-order statistics of NBI, IN and noise (Kay, 1993) as follows:

$$\hat{\mathbf{i}}_{\text{eqv}}(I_l) = \mathbb{E}\left[\mathbf{i}_{\text{eqv}}(I_l)\mathbf{y}'^H\right]\mathbb{E}\left[\mathbf{y}'\mathbf{y}'^H\right]^{-1}\mathbf{y}', \tag{7.16}$$

where $\mathbb{E}\left[\mathbf{i}_{\text{eqv}}(I_l)\mathbf{y}'^H\right] = \mathbf{R}_{\mathbf{i}_{\text{eqv}}}\mathbf{Q}^H_{\text{eqv}}(:, I_l)$, $\mathbb{E}\left[\mathbf{y}'\mathbf{y}'^H\right] = \left(\mathbf{Q}_{\text{eqv}}(:, I_l)\mathbf{R}_{\mathbf{i}_{\text{eqv}}}\mathbf{Q}^H_{\text{eqv}}(:, I_l) + \mathbf{R}_{\mathbf{n}'}\right)$, and $\mathbf{R}_{\mathbf{i}_{\text{eqv}}}$ and $\mathbf{R}_{\mathbf{n}'}$ are the covariance matrices for $\mathbf{i}_{\text{eqv}}$ and $\mathbf{n}'$ in (7.8), respectively. For simplicity, we assume that the non-zero entries of the NBI and IN vectors are independent and identically distributed (i.i.d.) zero-mean Gaussian random variables with variances $\mathcal{E}_W$ and $\mathcal{E}_P$, respectively. In addition, we assume i.i.d. zero-mean Gaussian noise for both the wireless and PLC links with variances σ^2_W and σ^2_P, respectively.

To evaluate (7.16), we need to compute $\mathbf{R}_{\mathbf{i}_{\text{eqv}}}$ and $\mathbf{R}_{\mathbf{n}'}$. First, we derive an expression for $\mathbf{R}_{\mathbf{i}_{\text{eqv}}}$. Since both NBI and IN are assumed independent over different antennas/wires, $\mathbf{R}_{\mathbf{i}_{\text{eqv}}}$ is a block diagonal matrix and can be written as follows:

$$\mathbf{R}_{\mathbf{i}_{\text{eqv}}} = \text{diag}\left[\mathbf{R}^{(1)}_{\mathbf{i}_{\text{eqv}},W}, \cdots, \mathbf{R}^{(K)}_{\mathbf{i}_{\text{eqv}},W}, \mathbf{R}^{(1)}_{\mathbf{i}_{\text{eqv}},P}, \cdots, \mathbf{R}^{(\beta)}_{\mathbf{i}_{\text{eqv}},P}\right], \tag{7.17}$$

where each submatrix $\mathbf{R}^{(u)}_{\mathbf{i}_{\text{eqv}},X}$ can be evaluated as follows:

$$\begin{aligned}\mathbf{R}^{(u)}_{\mathbf{i}_{\text{eqv}},X} &= \mathbb{E}\left[\mathbf{i}^{(u)}_{\text{eqv},X}\mathbf{i}^{(u)^H}_{\text{eqv},X}\right] \\ &= \sum_{\omega^u_X \in \mathfrak{U}^u_X} \mathbb{E}\left[\mathbf{i}^{(u)}_{\text{eqv},X}\mathbf{i}^{(u)^H}_{\text{eqv},X}|\omega^u_X\right] p(\omega^u_X).\end{aligned} \tag{7.18}$$

Here, $\mathbf{i}^{(u)}_{\text{eqv},X} = \mathbf{i}^{(k)}_W$ when $X = W$, and $\mathbf{i}^{(u)}_{\text{eqv},X} = \bar{\mathbf{i}}^{(j)}_P$ when $X = P$. The summation in (7.18) is taken over the set of all possible sparsity profiles, denoted by $\mathfrak{U}^u_X$, while $p(\omega^u_X)$ is the probability that the ω^u_X sparsity profile is activated and it is assumed to be a uniform distribution[2], i.e.,

$$p(\omega_X^u) = \frac{1}{\binom{M}{\rho_X^{(u)}}}. \tag{7.19}$$

It is then straightforward to show that

$$\mathbf{R}_{\mathbf{i}_{\text{eqv}},X}^{(u)} = \mathcal{E}_X \frac{\binom{M-1}{\rho_X^{(u)}-1}}{\binom{M}{\rho_X^{(u)}}} \mathbf{I}_M = \mathcal{E}_X \frac{\rho_X^{(u)}}{M} \mathbf{I}_M. \tag{7.20}$$

Next, we evaluate the covariance matrix of the equivalent noise in (7.8), which is given by

$$\mathbf{R}_{\mathbf{n}'} = \mathbb{E}\left[\mathbf{n}'\mathbf{n}'^H\right] = \mathbf{Q}\mathbf{R}_{\mathbf{nn}}\mathbf{Q}^H, \tag{7.21}$$

where $\mathbf{R}_{\mathbf{nn}} = \text{diag}\,[\sigma_W^2 \mathbf{I}_{KM}, \sigma_P^2 \mathbf{I}_{\beta M}]$.

7.2.3 Joint Processing with Asynchronous NBI

In practice, the carrier frequency of the NBI signal can deviate from that of the desired signal which causes NBI energy leakage across the OFDM subcarriers, therefore, the sparsity level of the NBI is reduced. To improve the robustness of sparsity-based NBI recovery against carrier frequency offset (CFO), we apply time-domain windowing to reduce the DFT side lobes and enhance the sparsity level of the NBI signal. After applying the time-domain windowing to the wireless received signal and performing the DFT of (7.1), we get

$$\underbrace{\mathbf{F}_M \Phi \bar{\mathbf{y}}_W^{(k)}}_{\triangleq \check{\mathbf{y}}_W^{(k)}} = \underbrace{\mathbf{F}_M \Phi \bar{\mathbf{H}}_W^{(k)} \mathbf{F}_M^*}_{\triangleq \check{\Lambda}_W^{(k)}} \mathbf{x} + \underbrace{\mathbf{F}_M \Phi \mathbf{D}_W^{(k)} \bar{\mathbf{i}}_W^{(k)}}_{\triangleq \check{\mathbf{i}}_W^{(k)}} + \underbrace{\mathbf{F}_M \Phi \bar{\mathbf{n}}_W^{(k)}}_{\triangleq \check{\mathbf{n}}_W^{(k)}}, \tag{7.22}$$

[2]Note that the assumptions on the NBI and IN statistical distributions are only required in this Subsection and Subsection 7.3.2 to evaluate the covariance matrices. However, all other algorithms proposed in this chapter are independent of NBI and IN statistical distributions assumptions.

where the matrix $\mathbf{D}_W^{(k)} \triangleq \text{diag}\left[1,\ \exp\left(i\frac{2\pi\alpha^{(k)}}{M}\right),\ \cdots,\ \exp\left(i\frac{2\pi\alpha^{(k)}(M-1)}{M}\right)\right]$ with $\alpha^{(k)}$ denoting the CFO between the NBI signal and the wireless received signal normalized to the OFDM subcarrier spacing. The CFO $\alpha^{(k)}$ is assumed to be uniformly-distributed in the range $[-0.5,\ 0.5]$, and i.i.d. across different antennas. The windowing matrix Φ is an $M \times M$ diagonal matrix where the diagonal elements are the window coefficients. Moreover, the matrix $\check{\Lambda}_W^{(k)}$ denotes the new $M \times M$ effective channel matrix after applying the windowing operation. Here, $\check{\mathbf{i}}_W^{(k)}$ denotes the FD NBI vector at the k^{th} receive antenna. The concatenated received wireless and PLC vector, denoted by $\check{\mathbf{y}}$, is given by

$$\check{\mathbf{y}} \triangleq \check{\mathbf{G}}\mathbf{x} + \check{\mathbf{i}} + \check{\mathbf{n}}, \tag{7.23}$$

where the *modified channel matrix* $\check{\mathbf{G}}$ is the same as $\mathbf{G}$ defined in (7.5) with $\Lambda_W^{(k)}$ replaced with $\check{\Lambda}_W^{(k)}$. In addition, the vector $\check{\mathbf{i}}$, which represents the combined NBI and IN vectors, is the same as $\mathbf{i}$ defined in (7.5) but $\mathbf{i}_W^{(k)}$ is replaced with $\check{\mathbf{i}}_W^{(k)}$. Similar to (7.8), we project $\check{\mathbf{y}}$ onto the left-null space of $\check{\mathbf{G}}$ using the projection matrix $\check{\mathbf{Q}} = \mathbf{I}_{M(K+\beta)} - \check{\mathbf{G}}\check{\mathbf{G}}^{\dagger}$. The projected received signal $\check{\mathbf{y}}'$ is given by

$$\check{\mathbf{y}}' \triangleq \check{\mathbf{Q}}\underbrace{\mathbf{A}\check{\mathbf{i}}_{\text{eqv}}}_{\triangleq \check{\mathbf{i}}} + \check{\mathbf{Q}}\check{\mathbf{n}} = \check{\mathbf{Q}}_{\text{eqv}}\check{\mathbf{i}}_{\text{eqv}} + \check{\mathbf{n}}' \tag{7.24}$$

where, $\check{\mathbf{i}}_{\text{eqv}} \triangleq \begin{bmatrix} \check{\mathbf{i}}_W^{(1)^T} & \ldots & \check{\mathbf{i}}_W^{(K)^T} & \bar{\mathbf{i}}_P^{(1)^T} & \ldots & \bar{\mathbf{i}}_P^{(\beta)^T} \end{bmatrix}^T$, $\check{\mathbf{n}}' \triangleq \check{\mathbf{Q}}\check{\mathbf{n}}$, and the *modified measurement matrix* $\check{\mathbf{Q}}_{\text{eqv}} \triangleq \check{\mathbf{Q}}\mathbf{A}$, where $\mathbf{A}$ is defined in (7.7).

Although the windowing operation enhances sparsity, we found that the OMP algorithm was not effective due to the power leakage caused by the CFO. Therefore, we instead estimate $\check{\mathbf{i}}_{\text{eqv}}$ by solving the following convex optimization problem using convex optimization techniques:

$$\hat{\mathbf{i}}_{\text{eqv}} \triangleq \underset{\mathbf{i} \in \mathbb{C}^{(K+\beta)M}}{\text{argmin}} \|\mathbf{i}\|_1 \text{ subject to}$$

$$\|\check{\mathbf{Q}}_{\text{eqv}}\mathbf{i} - \check{\mathbf{y}}'\|_2^2 \leq \epsilon_1 \quad \text{and} \quad \|\check{\mathbf{y}} - \mathbf{A}\mathbf{i}\|_2^2 \leq \epsilon_2,$$

where ϵ_1 and ϵ_2 are set such that $\epsilon_1 \leq \|\check{\mathbf{n}}'\|_2^2$ and $\epsilon_2 \leq \|\check{\mathbf{G}}\mathbf{x} + \check{\mathbf{n}}\|_2^2$ with high probability. Note that, in contrast to (7.9), the sparsity level of NBI is unknown due to the power leakage. The constraint in OMP on the sparsity level $\|\mathbf{i}\|_0 = S$ is effectively replaced here by the absolute squared error, $\|\check{\mathbf{Q}}_{\text{eqv}}\mathbf{i} - \check{\mathbf{y}}'\|_2^2 \leq \epsilon_1$. In addition, to further improve the $\check{\mathbf{i}}_{\text{eqv}}$ estimate, we have introduced an additional constraint on the received signal $\check{\mathbf{y}}$ (before nulling the information signal) based on (7.23), $\|\check{\mathbf{y}} - \mathbf{A}\mathbf{i}\|_2^2 \leq \epsilon_2$. The estimated $\hat{\mathbf{i}}_{\text{eqv}}$ can now be used to find the support (non-zero indices) of $\check{\mathbf{i}}_{\text{eqv}}$. In particular, we compare the power of each element j of the vector $\hat{\mathbf{i}}_{\text{eqv}}$, determined by $\left|\hat{\mathbf{i}}_{\text{eqv}[j]}\right|^2$, with the average noise power per element, determined by $\frac{\max\{\epsilon_1, \epsilon_2\}}{(K+\beta)M}$, to estimate the support vector I as follows:

$$I = \left\{ j : \ \left|\hat{\mathbf{i}}_{\text{eqv}}[j]\right|^2 > \frac{\max\{\epsilon_1, \epsilon_2\}}{(K+\beta)M} \right\}. \tag{7.25}$$

7.3 Sparsity-Based Joint Estimation of Contiguous NBI and IN

In this section, we propose a sparse recovery framework for estimating contiguous NBI and IN signals. In this case, both NBI and IN are modeled as block sparse vectors with few non-zero blocks, each block of a size d_X elements and $X \in \{W, P\}$. Here, the blocks' boundaries are assumed to be known and each non-zero block can only start at one of the following indices $\{1,\ d_X+1,\ 2d_X+1, ...,\ (\zeta_X - 1)d_X + 1\}$, where $\zeta_X = \frac{M}{d_X}$, $X \in \{W, P\}$. In addition, we make the assumption that the number of subcarriers per OFDM symbol, denoted M, is an integer multiple of the block size[3] d_X. Hence, $\mathbf{i}_W^{(k)}$ and $\bar{\mathbf{i}}_P^{(j)}$ can be decomposed into ζ_W and ζ_P blocks denoted by $\mathbf{i}_{W,b_W}^{(k)}$ and $\bar{\mathbf{i}}_{P,b_P}^{(j)}$, respectively, where $b_W \in \{1 \cdots \zeta_W\}$ and $b_P \in \{1 \cdots \zeta_P\}$, and can be written as follows:

[3] When M is not an integer multiple of the block size d_X, the last few elements that form an incomplete block will not be considered as a block and, hence, will not be detected. In this case, $\zeta_X = \lfloor \frac{M}{d_X} \rfloor$, while everything else in the proposed framework still holds.

$$\mathbf{i}_W^{(k)} = \Big[\underbrace{i_W^{(k)}[1]\ \cdots\ i_W^{(k)}[d_W]}_{\left(\mathbf{i}_{W,1}^{(k)}\right)^T}\ \cdots\ \underbrace{i_W^{(k)}[M-d_W+1]\ \cdots\ i_W^{(k)}[M]}_{\left(\mathbf{i}_{W,\zeta_W}^{(k)}\right)^T}\Big]^T, \tag{7.26}$$

$$\bar{\mathbf{i}}_P^{(j)} = \Big[\underbrace{\bar{i}_P^{(j)}[1]\ \cdots\ \bar{i}_P^{(j)}[d_P]}_{\left(\bar{\mathbf{i}}_{P,1}^{(j)}\right)^T}\ \cdots\ \underbrace{\bar{i}_P^{(j)}[M-d_P+1]\ \cdots\ \bar{i}_P^{(j)}[M]}_{\left(\bar{\mathbf{i}}_{P,\zeta_P}^{(j)}\right)^T}\Big]^T. \tag{7.27}$$

In particular, $\mathbf{i}_W^{(k)}$ and $\bar{\mathbf{i}}_P^{(j)}$ are block-sparse vectors and $\rho_{W,B}^{(k)} \triangleq \sum_{b_W=1}^{\zeta_W} \mathbf{1}\left\{\|\mathbf{i}_{W,b_W}^{(k)}\|_2\right\}$ and $\rho_{P,B}^{(j)} \triangleq \sum_{b_P=1}^{\zeta_P} \mathbf{1}\left\{\|\bar{\mathbf{i}}_{P,b_P}^{(j)}\|_2\right\}$ count the number of non-zero blocks in $\mathbf{i}_W^{(k)}$ and $\bar{\mathbf{i}}_P^{(j)}$, respectively. The indicator function $\mathbf{1}\{.\}$ is equal to 1 for a non-zero argument and is 0 otherwise. For $d_W = d_P = 1$, $\rho_{W,B}^{(k)}$ and $\rho_{P,B}^{(j)}$ count the number of non-zero elements in $\mathbf{i}_W^{(k)}$ and $\bar{\mathbf{i}}_P^{(j)}$, respectively.

Following the same procedure in (7.6) through (7.8), the problem of contiguous NBI and IN recovery can be reduced to the estimation of a block sparse vector $\mathbf{i}_{\text{eqv}}$ with S_B non-zero entries, where $S_B \triangleq \sum_{k=1}^{K} \rho_{W,B}^{(k)} + \sum_{j=1}^{\beta} \rho_{P,B}^{(j)}$. Exploiting this block-sparse structure, we can estimate $\mathbf{i}_{\text{eqv}}$ from (7.8) by solving the following optimization problem (Eldar et al., 2010):

$$\hat{\mathbf{i}}_{\text{eqv}} \triangleq \underset{\mathbf{i}\in\mathbb{C}^{(K+\beta)M}}{\operatorname{argmin}} \sum_{l=1}^{M(\frac{K}{d_W}+\frac{\beta}{d_P})} \|\mathbf{i}_l\|_2, \text{ subject to } \|\mathbf{Q}_{\text{eqv}}\mathbf{i} - \mathbf{y}'\|_2^2 \leqslant \epsilon,$$

where $\mathbf{i}_l$ denotes the block number l in the vector $\mathbf{i}$.

As an alternative, several greedy algorithms from the CS literature can be applied to solve this problem efficiently. One example is the *block orthogonal matching pursuit* (BOMP) algorithm (Eldar et al., 2010), which is an extension of the traditional OMP algorithm (Pati et al., 1993). BOMP constructs the blocks of $\mathbf{i}_{\text{eqv}}$ iteratively by determining the sub-block of the measurement matrix $\mathbf{Q}_{\text{eqv}}$ that is most correlated with the measurements in (7.8) followed by solving the LS problem using the selected sub-blocks. These sub-blocks are constructed from the column vectors of $\mathbf{Q}_{\text{eqv}}$ with a size of $M(K+\beta) \times d$ each, where $d = \min\{d_W,\ d_P\}$, and $\mathbf{Q}_{\text{eqv}}$ is defined as follows:

$$\mathbf{Q}_{\text{eqv}} = \tag{7.28}$$

Algorithm 3 BOMP for Joint Estimation of Contiguous NBI and IN

Inputs: Matrix $\mathbf{Q}_{\text{eqv}}$, vector $\mathbf{y}'$, and block sparsity level S_B.

Initialization: Define set index $I_0 = \{\}$, set residual $\mathbf{r}_0 = \mathbf{y}'$, estimate $\hat{\mathbf{i}}_{\text{eqv}} = \mathbf{0}_{(K+\beta)M\times 1}$, and iteration count $l = 1$.

The l^{th} iteration:

1. Calculate $\delta_i = \| \left(\mathbf{Q}_{\text{eqv},i}\right)^H \mathbf{r}_{l-1}\|_2$ for all $i \notin I_{l-1}$.
2. Select index of the next non-zero block at the l^{th} iteration as $c_l = \underset{i}{\operatorname{argmax}}\ \delta_i$.
3. Update the non-zero blocks indices as $I_l = I_{l-1} \cup \{c_l\}$.
4. Solve the following optimization problem to find $\hat{\mathbf{i}}_{\text{eqv},l}(j)$ for $j \in I_l$:
$$\min_{\{\mathrm{i}(j)\}\in I_l} \left\| \mathbf{y}' - \sum_{j\in I_l} \mathbf{Q}_{\text{eqv},j}\mathbf{i}(j) \right\|_2 . \tag{7.29}$$
5. Calculate the residual error term in the l^{th} iteration as
$$\mathbf{r}_l = \mathbf{y}' - \sum_{j\in I_l} \mathbf{Q}_{\text{eqv},j}\hat{\mathbf{i}}_{\text{eqv},l}(j). \tag{7.30}$$
6. **If** $l = S_B$ then exit, **else** set $l = l + 1$ and go to Step 1.

$$\big[\underbrace{\mathbf{q}_{\text{eqv}}[1]\ \cdots\ \mathbf{q}_{\text{eqv}}[d]}_{\mathbf{Q}_{\text{eqv},1}}\ \cdots\ \underbrace{\mathbf{q}_{\text{eqv}}[M(K+\beta)-d+1]\ \cdots\ \mathbf{q}_{\text{eqv}}[M(K+\beta)]}_{\mathbf{Q}_{\text{eqv},\frac{M(K+\beta)}{d}}}\big],$$

where $\mathbf{q}_{\text{eqv}}[b]$ denotes the b^{th} column of $\mathbf{Q}_{\text{eqv}}$. For completeness, we summarize the BOMP algorithm main steps in Algorithm 3 using the notation of this chapter.

Note that in case of the size of the non-zero blocks d in the vector $\mathbf{i}_{\text{eqv}}$ is known but the boundaries of those blocks are not known, the BOMP performance will be significantly degraded because the modified measurement matrix $\mathbf{Q}_{\text{eqv}}$ cannot be partitioned into sub-matrices that are aligned perfectly with the blocks of $\mathbf{i}_{\text{eqv}}$. This challenge is investigated in the next section.

Next, for our proposed joint estimation of contiguous NBI and IN algorithm, we investigate the following extensions[4]. First, in Subsection 7.3.1, we consider the general problem of unknown NBI and IN bursts' boundaries. Second, in Subsection 7.3.2, we exploit knowledge of the second order statistics of NBI and IN to enhance their estimation for the contiguous NBI and IN sparse recovery problem. Finally, in Subsection 7.3.3, we exploit the high spatial correlation of the NBI and IN signals across different antennas/wires to convert a generally non-contiguous sparse recovery problem to a multi-level contiguous sparse recovery problem.

7.3.1 Joint Estimation of NBI-IN with Unknown Bursts' Boundaries

In this subsection, we relax our assumption of the *known blocks boundaries* and extend the recovery algorithm to cover the general case of *unknown bursts' boundaries*, i.e., the non-zero bursts of $\mathbf{i}_{\text{eqv}}$ may not align with the predefined sub-matrices of $\mathbf{Q}_{\text{eqv}}$ in (7.28). Instead, only the number of non-zero entries, denoted by S, and the number of bursts, denoted by $\mathcal{C}$, are assumed to be known.

In (Cevher et al., 2009), a new CS recovery algorithm, called the $(S, \mathcal{C})$ algorithm, was introduced. The $(S, \mathcal{C})$ algorithm exploits the bursts' sparse structure without any prior knowledge of the bursts' boundaries, i.e., only knowledge of S and $\mathcal{C}$ is needed. The $(S, \mathcal{C})$ algorithm builds on the matching pursuit (CoSaMP) algorithm (Needell and Tropp, 2009) with modified pruning based on dynamic programming principles. For completeness, we summarize the key steps of the $(S, \mathcal{C})$ algorithm in Algorithm 4 using the notation of this chapter.

The main idea behind the pruning algorithm in (Cevher et al., 2009) is to use dynamic programming principles to construct the bursts iteratively. In each pruning iteration, either new entries are added to the constructed bursts, or those bursts are split into more bursts

[4]We do not discuss the asynchronous case for the contiguous NBI and IN recovery problem since it is similar to the non-contiguous NBI and IN recovery problem.

Algorithm 4 $(S,\mathcal{C})$ Algorithm for Joint Estimation of Contiguous NBI and IN with Unknown Bursts' Boundaries

Inputs: Matrix $\mathbf{Q}_{\text{eqv}}$, vector $\mathbf{y}'$, number of non-zero entries S, burst sparsity level $\mathcal{C}$ and the normalized difference between the estimated vector in two consecutive iterations, denoted by μ, where μ quantifies the performance-complexity trade-off (smaller μ results in better estimates with more iterations).

Initialization: Set residual $\mathbf{r}_0 = \mathbf{y}'$, estimate $\hat{\mathbf{i}}_{\text{eqv},0} = \mathbf{0}_{(K+\beta)M\times 1}$, and iteration count $l = 1$.

The l^{th} iteration:

1. Update the residual as $\mathbf{r}_l = \mathbf{y}' - \mathbf{Q}_{\text{eqv}}\hat{\mathbf{i}}_{\text{eqv},l-1}$.
2. Calculate $\mathbf{e} = \mathbf{Q}_{\text{eqv}}^H \mathbf{r}_l$.
3. Prune $\mathbf{e}$ using $|\mathbf{e}|$ to calculate the best $2S$ indices set $\mathbf{\Omega}$ for $2\mathcal{C}$ bursts based on the pruning algorithm in (Cevher et al., 2009).
4. Form set $T = \mathbf{\Omega} \cup \text{supp}\left(\hat{\mathbf{i}}_{\text{eqv},l-1}\right)$, where $\text{supp}\left(\mathbf{x}\right)$ denotes indices of the non-zero entries of $\mathbf{x}$.
5. Define the vector $\mathbf{b} = \mathbf{0}_{(K+\beta)M\times 1}$ and estimate the elements in the set T by applying the LS estimator as follows: $\mathbf{b}(T) = \mathbf{Q}_{\text{eqv}}(:,T)^{\dagger}\mathbf{y}'$, where $\mathbf{Q}_{\text{eqv}}(:,T)$ is formed from the $\mathbf{Q}_{\text{eqv}}$ columns indexed by T.
6. Prune the vector $\mathbf{b}$ using the absolute values $|\mathbf{b}|$ to calculate the best S non-zero entries in $\mathcal{C}$ bursts and compute $\hat{\mathbf{i}}_{\text{eqv},l}$.
7. The stopping criterion will depend on the convergence of the estimated $\hat{\mathbf{i}}_{\text{eqv},l}$. **If** $\frac{\|\hat{\mathbf{i}}_{\text{eqv},l} - \hat{\mathbf{i}}_{\text{eqv},l-1}\|}{\|\hat{\mathbf{i}}_{\text{eqv},l}\|} \leq \mu$, **then** exit, **else** set $l = l + 1$ and go to Step 1.

until all of the S non-zero elements in the $\mathcal{C}$ bursts are calculated. The reader is referred to (Cevher et al., 2009) for more details.

7.3.2 LMMSE Based BOMP

Similar to Subsection 7.2.2, replacing LS with LMMSE in BOMP entails computing the covariance matrices of $\mathbf{i}_{\text{eqv}}$ and $\mathbf{n}'$. The noise covariance matrix $\mathbf{R}_{\mathbf{n}'}$ can be evaluated exactly as in (7.21). However, we need to derive the covariance matrix of $\mathbf{i}_{\text{eqv}}$, denoted $\tilde{\mathbf{R}}_{\mathbf{i}_{\text{eqv}}}$, and capture the sparsity profile of the contiguous NBI and IN vectors. Similar to Subsection

7.2.2, since the NBI and IN vectors are assumed to be independent from each other and independent across the antennas/wires, the covariance matrix $\tilde{\mathbf{R}}_{\mathbf{i}_{\text{eqv}}}$ is a block diagonal matrix of submarices $\tilde{\mathbf{R}}^{(u)}_{\mathbf{i}_{\text{eqv}},X}$ as in (7.17). In addition, each submatrix $\tilde{\mathbf{R}}^{(u)}_{\mathbf{i}_{\text{eqv}},X}$ can be expressed as in (7.18). However, evaluation of the expression in (7.18) will be different here since the sparsity profile set for the block sparse NBI and IN, denoted by $\tilde{\mathfrak{U}_X}$, includes only the block sparse profiles which is different than the sparsity profile set of the non-contiguous sparse NBI and IN assumed in Subsection 7.2.2. In particular, assume that the NBI/IN blocks are of width $d_X,\ X \in \{W, P\}$, and assume d_X to be an odd number. The center of the block c is selected uniformly at random from all valid indices of the OFDM symbols which are given by the set $\{\frac{d_X-1}{2}+1, \frac{d_X-1}{2}+2, \cdots, M-\frac{d_X-1}{2}\}$. Note that indices less than $\frac{d_X-1}{2}+1$ and greater than $M-\frac{d_X-1}{2}$ are not valid indices for the center of block c since they can not construct a complete block. The probability density function (PDF) of activating the $\tilde{\omega_X}$ block in an OFDM symbol with M subcarriers can be defined by characterizing the PDF of the center of block which can be written as follows:

$$p(\tilde{\omega}_{c,X}) = \begin{cases} \frac{1}{\tilde{N}}, & \frac{d_X-1}{2} < c \leq M - \frac{d_X-1}{2}, \\ 0, & \text{otherwise}, \end{cases} \tag{7.31}$$

where c is the center index of the selected $\tilde{\omega}$ block and $\tilde{N} = M - d_X + 1$. Hence, each submatrix $\tilde{\mathbf{R}}^{(u)}_{\mathbf{i}_{\text{eqv}},X}$ can be evaluated as follows:

$$\tilde{\mathbf{R}}^{(u)}_{\mathbf{i}_{\text{eqv}},X} = \mathcal{E}_X \times \begin{cases} \frac{m}{\tilde{N}}, & 1 \leq m < d_X, \\ \frac{d_X}{\tilde{N}}, & d_X \leq m \leq M - d_X + 1, \\ \frac{N-d_X+1}{\tilde{N}}, & M - d_X + 1 < m \leq M. \end{cases} \tag{7.32}$$

7.3.3 Multi-Level BOMP

Here, we exploit the NBI and IN spatial correlation across the receive ports (either antennas or wires for the wireless or PLC systems, respectively) to convert the non-contiguous NBI and IN estimation problem to a block sparse recovery problem to enhance the estimation performance and/or reduce the complexity. In practice, the NBI tends to affect the same subcarriers over different receive antennas while the IN tends to occur at the same time samples on different receive wires. Thus, the NBI and IN signals share the same support indices over different antennas and wires, respectively.

In other words, although the problem formulation was originally non-contiguous (non-block sparse) NBI and IN recovery, we can convert it to a block sparse NBI and IN recovery problem by stacking the per subcarrier/time-sample received signal over the different antennas/wires. As a result, the non-block sparse NBI (in the frequency domain) will be converted to *block sparse* NBI with a block size equal to the number of antennas K. Similarly, the non-block sparse IN (in the time domain) will be converted to *block sparse* IN with a block size equal to the number of wires β. Moreover, we assume that NBI and IN affect the same subcarrier/samples indices over different antennas/wires which results in the same sparsity level for all antennas, i.e., $\rho_W^{(k)} = \rho_W$ for all $k \in \{1, ..., K\}$, and the same sparsity level for all wires, i.e., $\rho_P^{(j)} = \rho_P$ for all $j \in \{1, ..., \beta\}$. Hence, the problem can be considered as a *multi-level* block sparse recovery problem with only two block sizes K and β (since K and β are generally unequal), unlike the multi-level OMP recovery problem in Subsection 7.2.1 which assumed different sparsity levels for the different antennas/wires.

To reap the benefits of this spatial correlation in SIMO hybrid powerline-wireless transmission, we extend the conventional BOMP algorithm in (Eldar et al., 2010) to support multiple block sparsity levels as described in the sequel.

Mathematically, in contrast to concatenating the FD received signals of the wireless and PLC links as shown in (7.5), here, we stack the FD wireless received signal on top of the TD

PLC received signal as follows:

$$\underbrace{\begin{bmatrix} \mathbf{y}_W^{(1)} \\ \vdots \\ \mathbf{y}_W^{(K)} \\ \bar{\mathbf{y}}_P^{(1)} \\ \vdots \\ \bar{\mathbf{y}}_P^{(\beta)} \end{bmatrix}}_{\triangleq \tilde{\mathbf{y}}} = \underbrace{\begin{bmatrix} \Lambda_W^{(1)} \\ \vdots \\ \Lambda_W^{(K)} \\ \bar{\mathbf{H}}_P^{(1)} \mathbf{F}_M^H \\ \vdots \\ \bar{\mathbf{H}}_P^{(\beta)} \mathbf{F}_M^H \end{bmatrix}}_{\triangleq \tilde{\mathbf{G}}} \mathbf{x} + \underbrace{\begin{bmatrix} \mathbf{i}_W^{(1)} \\ \vdots \\ \mathbf{i}_W^{(k)} \\ \bar{\mathbf{i}}_P^{(1)} \\ \vdots \\ \bar{\mathbf{i}}_P^{(\beta)} \end{bmatrix}}_{\triangleq \tilde{\mathbf{i}}} + \underbrace{\begin{bmatrix} \mathbf{n}_W^{(1)} \\ \vdots \\ \mathbf{n}_W^{(K)} \\ \bar{\mathbf{n}}_P^{(1)} \\ \vdots \\ \bar{\mathbf{n}}_P^{(\beta)} \end{bmatrix}}_{\triangleq \tilde{\mathbf{n}}} . \tag{7.33}$$

Using the hybrid frequency-time domain structure in (7.33), the received signal samples can be permuted such that the NBI and IN vectors at particular subcarriers and time samples from different antennas and wires form blocks of size K and β, respectively. This can not be accomplished in the pure frequency-domain structure in (7.5) because of the DFT matrix multiplying the IN vector. In particular, the received signal samples are permuted as follows:

$$\underbrace{\begin{bmatrix} y_W^{(1)}[1] \\ \vdots \\ y_W^{(K)}[1] \\ \vdots \\ y_W^{(1)}[M] \\ \vdots \\ y_W^{(K)}[M] \\ \bar{y}_P^{(1)}[1] \\ \vdots \\ \bar{y}_P^{(\beta)}[1] \\ \vdots \\ \bar{y}_P^{(1)}[M] \\ \vdots \\ \bar{y}_P^{(\beta)}[M] \end{bmatrix}}_{\triangleq \tilde{\mathbf{r}}} = \underbrace{\begin{bmatrix} \mathbf{S}_W & \mathbf{0}_{\beta M \times \beta M} \\ \mathbf{0}_{KM \times KM} & \mathbf{S}_P \end{bmatrix}}_{\triangleq \mathbf{S}} \underbrace{\begin{bmatrix} y_W^{(1)}[1] \\ \vdots \\ y_W^{(1)}[M] \\ \vdots \\ y_W^{(K)}[1] \\ \vdots \\ y_W^{(K)}[M] \\ \bar{y}_P^{(1)}[1] \\ \vdots \\ \bar{y}_P^{(1)}[M] \\ \vdots \\ \bar{y}_P^{(\beta)}[1] \\ \vdots \\ \bar{y}_P^{(\beta)}[M] \end{bmatrix}}_{\triangleq \tilde{\mathbf{y}}}, \tag{7.34}$$

where $\mathbf{S}_W$ and $\mathbf{S}_P$ are permutation matrices. Note that in (7.34), the elements of vector $\tilde{\mathbf{r}}$ are arranged such that for each subcarrier, we stack the received samples of all antennas/wires together. In contrast, the elements of vector $\tilde{\mathbf{y}}$ are arranged such that for each antenna/wire, we stack all subcarriers together. From (7.33) and (7.34), we can write

$$\tilde{\mathbf{r}} = \mathbf{S}\tilde{\mathbf{y}} \triangleq \mathbf{S}\tilde{\mathbf{G}}\mathbf{x} + \mathbf{S}\tilde{\mathbf{i}} + \mathbf{S}\tilde{\mathbf{n}}. \tag{7.35}$$

Similar to (7.6), we null the desired signal by projecting $\tilde{\mathbf{r}}$ on to the left null space of $\mathbf{G}_{\text{eqv}} = \mathbf{S}\tilde{\mathbf{G}}$ to get

$$\mathbf{r}' \triangleq \tilde{\mathbf{Q}}_{\text{eqv}}\tilde{\mathbf{r}} = \tilde{\mathbf{Q}}_{\text{eqv}}\mathbf{S}\tilde{\mathbf{i}} + \tilde{\mathbf{n}}', \tag{7.36}$$

where $\tilde{\mathbf{Q}}_{\text{eqv}} = \mathbf{I}_{M(K+\beta)} - \mathbf{G}_{\text{eqv}}\mathbf{G}_{\text{eqv}}^{\dagger}$ and $\tilde{\mathbf{n}}' \triangleq \tilde{\mathbf{Q}}_{\text{eqv}}\mathbf{S}\tilde{\mathbf{n}}$.

Let $\tilde{\mathbf{i}}_{\text{eqv}} \triangleq \mathbf{S}\tilde{\mathbf{i}}$ denote the permuted version of the $\tilde{\mathbf{i}}$ vector. Since $\tilde{\mathbf{i}}_{\text{eqv}}$ is a block sparse vector, this reduces the problem of estimating $\tilde{\mathbf{i}}_{\text{eqv}}$ to a conventional block-sparse recovery problem with the main difference being that the sizes of the blocks are known but *not* equal. Consequently, we modify the conventional BOMP algorithm presented in (Eldar et al., 2010) by dividing the measurement matrix $\tilde{\mathbf{Q}}_{\text{eqv}}$ into two submatrices to accommodate different block sizes as follows:

$$\tilde{\mathbf{Q}}_{\text{eqv}} = \left[\tilde{\mathbf{Q}}^{(W)}_{\text{eqv},1},\ \cdots,\ \tilde{\mathbf{Q}}^{(W)}_{\text{eqv},M},\ \tilde{\mathbf{Q}}^{(P)}_{\text{eqv},1},\ \cdots,\ \tilde{\mathbf{Q}}^{(P)}_{\text{eqv},M}\right],$$

where $\tilde{\mathbf{Q}}^{(W)}_{\text{eqv},i}$ and $\tilde{\mathbf{Q}}^{(P)}_{\text{eqv},i}$, $i \in \{1,\ \cdots,\ M\}$ are submatrices that consist of K and β columns, respectively. Our proposed multi-level BOMP is summarized in Algorithm 5.

Note that the complexity reduction in the multi-level BOMP algorithm is mainly due to converting the noncontiguous sparse problem (which can be solved using OMP algorithm) into a block sparse problem (which can be solved using BOMP algorithm). It is well known that BOMP algorithm complexity is much less than the OMP algorithm complexity. However, the multi-level block sizes in the multi-level BOMP algorithm are mainly to account for the general case where the number of antennas is different than the number of wires (i.e., $K \neq \beta$), not for complexity reduction.

7.4 Numerical Results

In this section, we investigate the performance of our proposed sparsity-based algorithms for joint NBI and IN mitigation in SIMO hybrid PLC-wireless links. Unless stated otherwise, we assume that $K = 3, \beta = 3$, $M = 64$, and our comparison is with respect to the benchmark of sparsity-based separate wireless and PLC receive signal processing. We assume wireless channel with a uniform power delay profile, $L_W = 8$, CIR taps are zero-mean

Algorithm 5 Multi-level BOMP for Joint Estimation of NBI and IN

Initialization: Define index set $\tilde{I}_0^{(W)} = I_0^{(W)} = \{\}$ and $\tilde{I}_0^{(P)} = I_0^{(P)} = \{\}$, set residual $\mathbf{r}_0 = \mathbf{r}'$, $\hat{\tilde{\mathbf{i}}}_{\text{eqv}} = \mathbf{0}_{(K+\beta)M}$, iteration count $l = 1$, and set $z_X = 0$ where $X \in \{W, P\}$.

The l^{th} iteration:

1. Compute $\delta_i^{(W)} = \|\mathbf{r}_{l-1}^H \tilde{\mathbf{Q}}_{\text{eqv},i}^{(W)}\|_2 / \|\tilde{\mathbf{Q}}_{\text{eqv},i}^{(W)}\|$ and $\delta_j^{(P)} = \|\mathbf{r}_{l-1}^H \tilde{\mathbf{Q}}_{\text{eqv},j}^{(P)}\|_2 / \|\tilde{\mathbf{Q}}_{\text{eqv},j}^{(P)}\|$ $\forall\ i \notin I_{l-1}^{(W)}$ and $j \notin I_{l-1}^{(P)}$.
2. Find the index $c_W = \underset{i}{\text{argmax}}\ \delta_i^{(W)}$ and the index $c_P = \underset{j}{\text{argmax}}\ \delta_j^{(P)}$. **If** $\delta_{c_W}^{(W)} > \delta_{c_P}^{(P)}$, **then** $c_l = c_W$ and $X = W$, **else** $c_l = c_P$ and $X = P$. Update $z_X = z_X + 1$.
3. **If** $z_X > \rho_X$, **then** set $I_l^{(X)} = \{1, \ \cdots, \ M\}$ and go to Step 1, **else** proceed to the next step.
4. Update the indices of non-zero blocks as $I_l^{(X)} = I_{l-1}^{(X)} \cup \{c_l\}$ and $\tilde{I}_l^{(X)} = \tilde{I}_{l-1}^{(X)} \cup \{c_l\}$.
5. Construct the row block matrix $\tilde{\mathbf{Q}}_l$ from $\tilde{\mathbf{Q}}_{\text{eqv},i}^{(W)}$ and $\tilde{\mathbf{Q}}_{\text{eqv},j}^{(P)}$ indexed by $i \in \tilde{I}_l^{(W)}$ and $j \in \tilde{I}_l^{(P)}$, respectively. Compute $\hat{\tilde{\mathbf{i}}}_{\text{eqv}}(\Omega_l) = \left(\tilde{\mathbf{Q}}_l\right)^{\dagger} \mathbf{r}'$, where $\hat{\tilde{\mathbf{i}}}_{\text{eqv}}(\Omega_l)$ denotes the elements of $\hat{\tilde{\mathbf{i}}}_{\text{eqv}}$ that are indexed by Ω_l defined as $\{(i-1)K + 1, \ \cdots, \ iK : i \in \tilde{I}_l^{(W)}\} \cup \{(j-1)\beta + 1 + KM, \ \cdots, \ j\beta + KM : j \in \tilde{I}_l^{(P)}\}$.
6. Calculate the residual error term at the l^{th} iteration as $\mathbf{r}_l = \mathbf{r}' - \tilde{\mathbf{Q}}_l \hat{\tilde{\mathbf{i}}}_{\text{eqv}}(\Omega_l)$ and set $z_X = z_X + 1$.
7. **If** $z_W > \rho_W$ and $z_P > \rho_P$, **then** exit, **else** go to Step 1.

complex Gaussian, and normalized powers; i.e., $\mathbb{E}\big[|\bar{\mathbf{h}}_W^{(k)H} \bar{\mathbf{h}}_W^{(k)}|^2\big] = 1, \ k \in \{1, 2, 3\}$. Moreover, we assume synchronous NBI where each NBI signal has a fixed width of 3 contiguous subcarriers, i.e., $\rho_W^{(k)} = \rho_{W,B}^{(k)} = 3, \ \forall \ k \in \{1, 2, 3\}$, and whose values are i.i.d. zero-mean complex Gaussian with fixed NBI-to-background Gaussian noise (NBI-GN) ratio, defined as $\frac{\mathbb{E}\left[\mathbf{i}_W^{(k)H} \mathbf{i}_W^{(k)}\right]}{\sigma_W^2} = \frac{\mathcal{E}_W}{\sigma_W^2}, \ \forall \ k \in \{1, 2, 3\}$. This scenario is similar to a Bluetooth signal (with 1 MHz bandwidth) interfering with an IEEE 802.11n WLAN signal (with 20 MHz bandwidth) (Perahia and Stacey, 2013), and is important in practice due to the coexistence of Bluetooth and WLAN signals in the 2.4 GHz unlicensed frequency band.

Furthermore, we assume synchronous IN which spreads over 3 contiguous time samples[5], i.e., $\rho_P^{(j)} = \rho_{P,B}^{(j)} = 3, \ \forall\ j \in \{1,2,3\}$. Moreover, we assume a fixed IN-to-background Gaussian noise (IN-GN) ratio, defined as $\frac{\mathbb{E}\left[\bar{\mathbf{i}}_P^{(j)H}\bar{\mathbf{i}}_P^{(j)}\right]}{\sigma_P^2} = \frac{\mathcal{E}_P}{\sigma_P^2}, \ j \in \{1,2,3\}$. In addition, we assume that each PLC CIR consists of two equal-power taps, i.e., $L_p = 2$, having uniformly-distributed phases and lognormal distributed magnitudes with standard deviations of 0.6 (Galli, 2011a; Guzelgoz et al., 2010). Once again, we assume unit-power channels; i.e., $\mathbb{E}\left[|\bar{\mathbf{h}}_P^{(j)H}\bar{\mathbf{h}}_P^{(j)}|^2\right] = 1, \ \forall\ j \in \{1,2,3\}$. Finally, for simplicity, we assume that both the PLC and wireless links have the same signal to noise ratio (SNR), i.e., $\frac{\mathbb{E}\left[\mathbf{x}^H\mathbf{x}\right]}{\sigma_W^2} = \frac{\mathbb{E}\left[\mathbf{x}^H\mathbf{x}\right]}{\sigma_P^2}$, although they could be different in practice.

In Fig. 7.2, we compare the bit error rate (BER) of four scenarios to quantify the performance gain of joint over separate processing in the presence of non-contiguous NBI and IN. In the first scenario, the NBI and IN signals are treated as noise and maximum ratio combining (MRC) is used to combine the received wireless and PLC signals. The second scenario corresponds to separate processing where the receiver of each link individually estimates and cancels the non-contiguous NBI and IN followed by MRC to combine both signals. Since it is shown in (Gomaa and Al-Dhahir, 2011; Caire et al., 2008a) that sparsity-based techniques outperform traditional NBI and IN mitigation techniques, the second scenario corresponds to sparsity-based individual NBI and IN estimation. Fig. 7.2 demonstrates that the NBI/IN signals cannot be completely canceled in the second scenario and the residual NBI/IN signals result in an error floor. The third scenario represents the case of NBI and IN mitigation using our proposed method which can eliminate the error floor of (Gomaa and Al-Dhahir, 2011; Caire et al., 2008a). More specifically, our proposed method approaches the performance of the fourth scenario that corresponds to NBI-free and IN-free links. Next, we quantify the performance gains of joint processing over separate processing in Fig. 7.3.

[5]Note that since the contiguous NBI/IN is a special case of non-contiguous NBI/IN, we can test the performance of the proposed non-contiguous sparse recovery techniques on the assumed contiguous NBI/IN, i.e., non contiguous NBI/IN techniques will not exploit the fact that NBI and IN are contiguous.

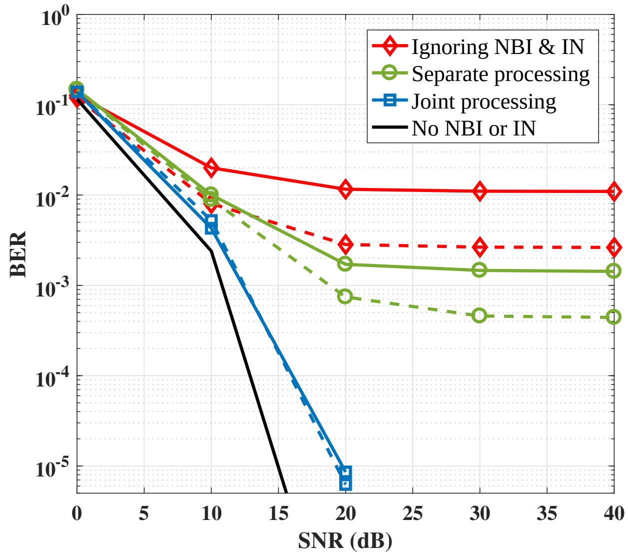

Figure 7.2: BER performance for non-contiguous NBI and IN with $R = 4$ bits/sec/Hz with solid and dashed lines for S-NBI and S-IN ratios equal to -10 dB and -5 dB, respectively.

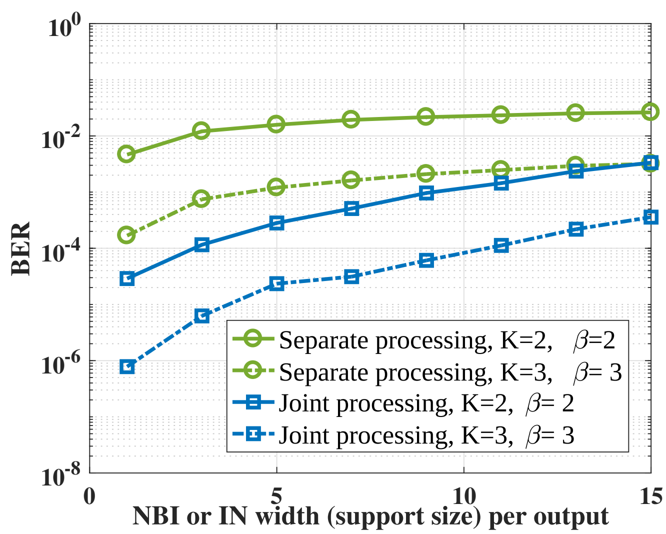

Figure 7.3: BER performance for non-contiguous NBI and IN with S-NBI and S-IN equal to -5 dB while SNR=20 dB, and $R = 4$ bits/sec/Hz.

This figure shows the BER as a function of the NBI and IN widths per receive signal port, which we are assume to be the same at each antenna/wire. Increasing the NBI and/or IN widths results in a higher BER since the sparsity is reduced. However, joint processing still outperforms separate processing significantly in this reduced-sparsity setting.

In Fig. 7.4, we investigate the performance of the multi-level OMP algorithm presented in Subsection 7.2.1 to exploit apriori knowledge of the sparsity level at each receive antenna and wire. It is clear that multi-level OMP achieves the same performance as OMP with much lower complexity by reducing the search space as discussed in Subsection 7.2.1. In Fig. 7.5, we plot the computational complexity saving ratio of the multi-level OMP algorithm relative to the OMP complexity as a function the ratio ρ/M. The complexity ratio for the best and worst cases of the multi-level OMP algorithm are defined as $\frac{\mathbb{C}_{MOMP,b}-\mathbb{C}_{OMP}}{\mathbb{C}_{OMP}} \times 100$ and $\frac{\mathbb{C}_{MOMP,w}-\mathbb{C}_{OMP}}{\mathbb{C}_{OMP}} \times 100$. The quantities $\mathbb{C}_{OMP}$, $\mathbb{C}_{MOMP,b}$ and $\mathbb{C}_{MOMP,w}$ are computed using (7.13), (7.14) and (7.15), respectively. As shown in Fig. 7.5, for very small values of ρ/M, the worst and best cases achieve the same complexity reduction of close to 50%. In practice, this ratio ρ/M is expected to be small (less than 0.1) as shown in Fig. 7.6. For the parameters' default settings given in this section ($\rho = 3$, $M = 64$ and $K+\beta = 6$), the best case complexity reduction is 40% while the worst-case complexity reduction is 15%. Moreover, in Fig. 7.6, we show the complexity reduction calculated based on simulation of the multi-level OMP over the SNR range of (0 : 40 dB). As shown in Fig. 7.6, the complexity reduction based on simulations is bounded by the best and worst cases' curves computed based on our derived mathematical expressions. Furthermore, we can see that the complexity is slightly reduced with increasing $K + \beta$.

In Fig. 7.7, we examine the effect of Hamming windowing under asynchronous NBI[6] with CFO that is uniformly-distributed as defined in Subsection 7.1. In addition, assuming that the NBI and IN bursts have the same width of 3, we set NBI-GN=IN-GN, and we use the proposed algorithm in Section 7.2.3. As illustrated in this figure, the weaker the desired signal is, the higher is the performance gain due to windowing since the NBI effect becomes more pronounced. Furthermore, the BER simulations show up to 3 dB SNR gain at BER = 5×10^{-4} due to time-domain windowing.

[6]Note that all simulation results assume synchronous NBI and IN except Fig. 7.7 which assumes asynchronous NBI.

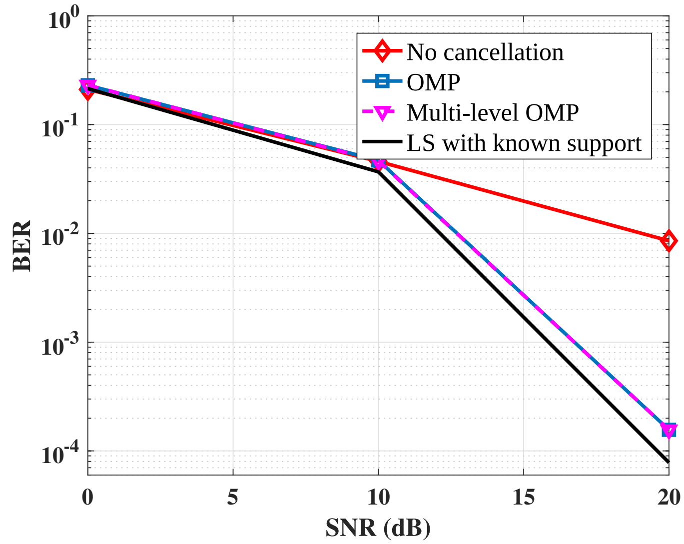

Figure 7.4: BER performance versus SNR for $R = 6$ bits/sec/Hz and NBI-S=IN-S=3 dB using the modified multi-level OMP recovery algorithm for 3 antennas and 3 wires hybrid wireless-PLC system.

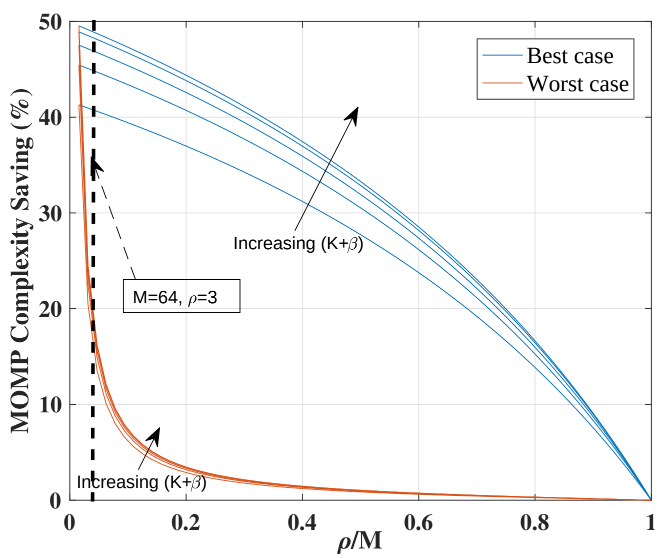

Figure 7.5: Computational savings in multi-level OMP relative to OMP as a function of the ratio ρ/M.

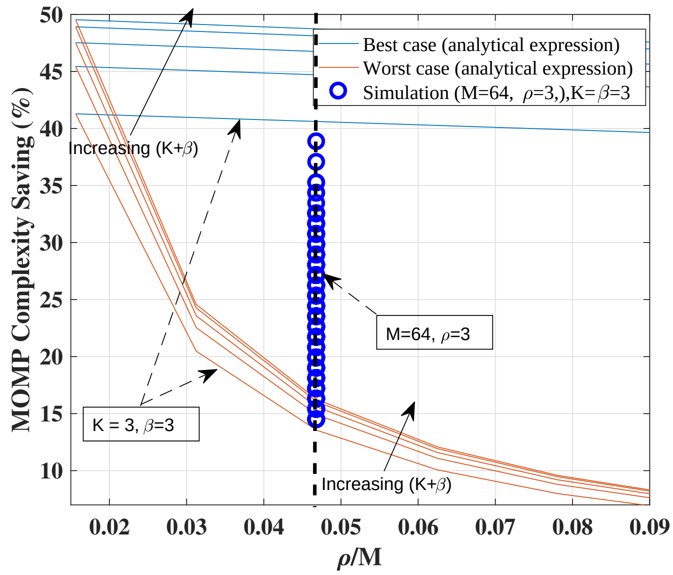

Figure 7.6: A zoomed view of computational savings in multi-level OMP relative to OMP as a function of the ratio ρ/M.

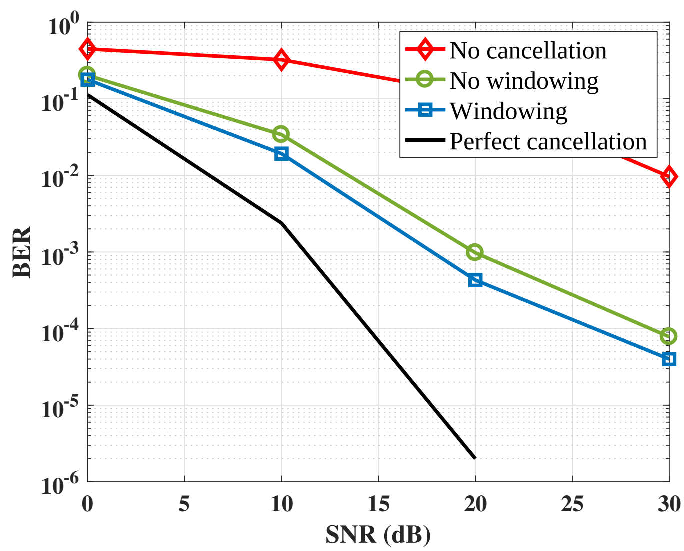

Figure 7.7: BER performance versus SNR for $R = 4$ bits/sec/Hz and NBI-GN=IN-GN=40 dB using the CS recovery algorithm in Section 7.2.3.

To study the performance of the block-sparse recovery algorithms, we set the number of PLC and wireless receive ports to $K = \beta = 1$ to isolate any performance gain due to the processing of multiple receive signals. In Fig. 7.8, we use the performance metric of *average error vector magnitude* (AEVM), which we define as $\eta \triangleq \frac{\sum_{u=1}^{U} \|\mathbf{i}_{\mathrm{eqv}} - \hat{\mathbf{i}}_{\mathrm{eqv}}\|_2^2}{\sum_{u=1}^{U} \|\mathbf{i}_{\mathrm{eqv}}\|_2^2}$ with U denoting the number of channel realizations ($U = 5000$ in these experiments). Note that a smaller value of η indicates better estimation performance. As a performance lower bound, we show the (ideal) LS performance assuming that the locations of the non-zero elements in the sparse IN and NBI vectors are perfectly known. We assume that the NBI and IN bursts have the same width of 5 and can occur anywhere within the OFDM symbol, i.e., we do not know the locations of the burst boundaries. For BOMP, we have a mismatch between the bursts' boundaries and the predefined sub-matrices of $\mathbf{Q}_{\mathrm{eqv}}$ in (7.28). As Fig. 7.8 shows, the BOMP performance is significantly degraded when compared with the performance of the OMP and $(S, \mathcal{C})$ algorithms and this degradation increases as the IN-GN level increases. Moreover, the $(S, \mathcal{C})$ algorithm outperforms the traditional OMP algorithm over the entire IN-GN range. At high IN-GN levels, the performance gap between the $(S, \mathcal{C})$ and the traditional OMP algorithm diminishes because the higher power levels of the NBI and IN signals (relative to the thermal noise power level) enable accurate sparse recovery using both algorithms without the need for exploiting the bursty nature of the NBI and IN signals. Furthermore, the performances of both algorithms approach the ideal LS lower bound.

To further quantify the performance gain realized by exploiting the block-sparse structure, Fig. 7.9 compares the BERs of the aforementioned joint NBI/IN estimation algorithms. The $(S, \mathcal{C})$ algorithm achieves more than 2 dB and 5 dB SNR gain at BER=10^{-4} over the traditional OMP and BOMP algorithms, respectively. In addition, as SNR increases, the $(S, \mathcal{C})$ algorithm's performance approaches the LS performance assuming perfect knowledge of NBI and IN locations. Fig. 7.10 shows the BER performance for the case of a more generic scenario where the NBI and IN bursts have different widths of 3 and 5, respectively. Here,

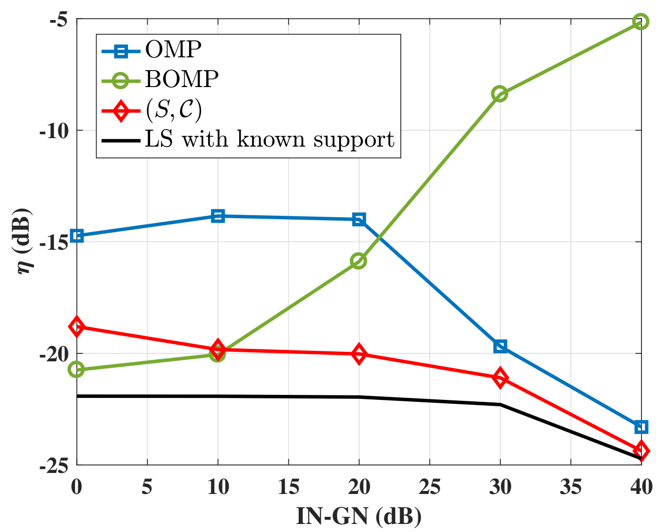

Figure 7.8: AEVM versus IN-GN with NBI-GN=40dB for SISO systems. Here, NBI and IN bursts are assumed to be of width 5.

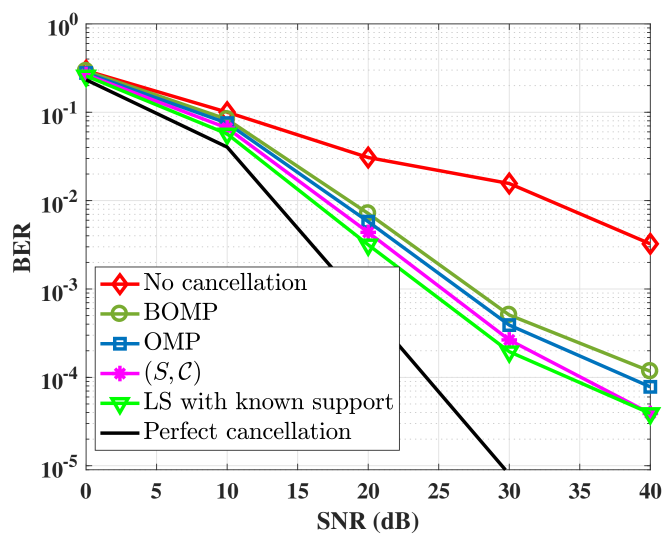

Figure 7.9: BER performance versus SNR for $R = 4$ bits/sec/Hz, NBI-GN=40 dB and IN-GN=20 dB. Both NBI and IN have the same width of 5.

the performance gain of the $(S, \mathcal{C})$ algorithm over the BOMP algorithm is higher compared to the equal-width scenario in Fig. 7.9. For example, at BER $=10^{-3}$, an SNR gain of 5 dB is achieved for different-width NBI and IN bursts while only a gain of 2.5 dB is achieved when the NBI and IN bursts have the same width.

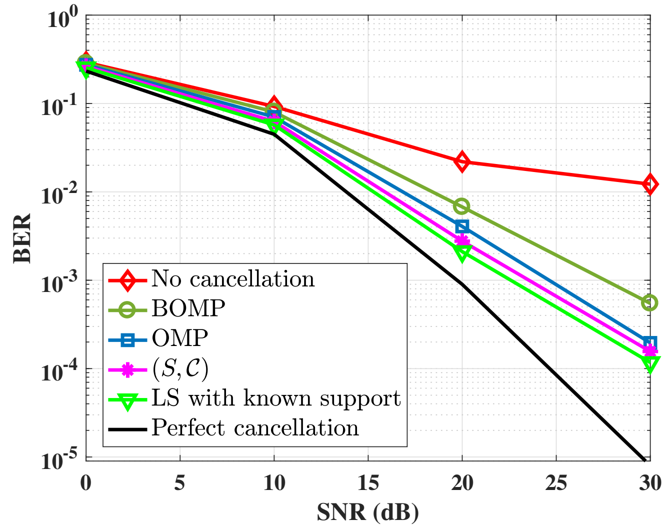

Figure 7.10: BER performance versus SNR for $R = 4$ bits/sec/Hz, NBI-GN=40 dB and IN-GN=20 dB, with NBI and IN widths of 3 and 5, respectively.

In Fig. 7.11, we plot the BER versus SNR for a fixed signal-to-NBI (S-NBI) and signal-to-IN (S-IN) ratios, defined as $\frac{\mathbb{E}\left[\mathbf{x}^H\mathbf{x}\right]}{\mathbb{E}\left[\mathbf{i}_W^{(k)H}\mathbf{i}_W^{(k)}\right]}$ and $\frac{\mathbb{E}\left[\mathbf{x}^H\mathbf{x}\right]}{\mathbb{E}\left[\mathbf{i}_P^{(j)H}\mathbf{i}_P^{(j)}\right]}$ $\forall\ k, j \in \{1, 2, 3\}$, respectively, equal to -3 dB. In this figure, we exploit the fact that NBI and IN share the same support set over different antennas and wires, respectively, for the case of 3 antennas and 2 wires. It is evident that the proposed multi-level BOMP algorithm in Subsection 7.3.3 results in significant performance gain to the extent that it approaches the LS with known support indices.

In Fig. 7.12, we show η for both joint (our proposed approach) and separate processing for different non-contiguous NBI-GN and IN-GN levels. We make the following two conclusions based on this figure. First, the higher the NBI-GN and IN-GN levels are, the better the estimation performance of both joint and separate processing will be. Second, our proposed joint processing always results in better performance than separate processing.

Finally, in Fig. 7.13, we examine the effect of replacing LS with LMMSE on the performance of the OMP algorithm. We plot BER for a 3-antenna and 3-wire system versus the NBI-GN and IN-GN levels that are assumed to be equal. For weak NBI and IN, we observe

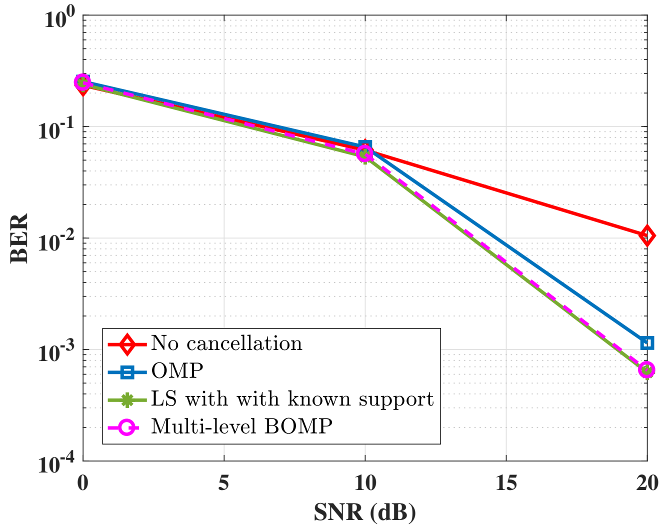

Figure 7.11: BER versus SNR for $R = 6$ bits/sec/Hz, S-IN=S-NBI=-3 dB and $K = 3$ and $\beta = 2$.

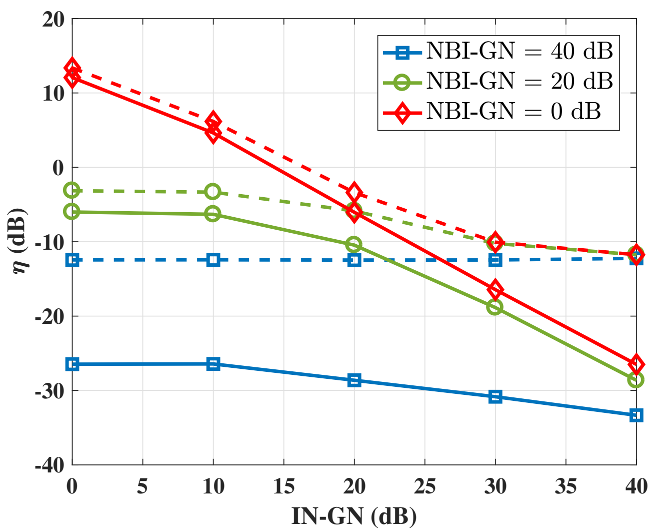

Figure 7.12: AEVM for non-contiguous NBI and IN with joint (solid lines) and separate (dashed lines) processing for different NBI-GN and IN-GN levels.

significant performance improvement over OMP and LS due to apriori knowledge about the NBI and IN statistics.

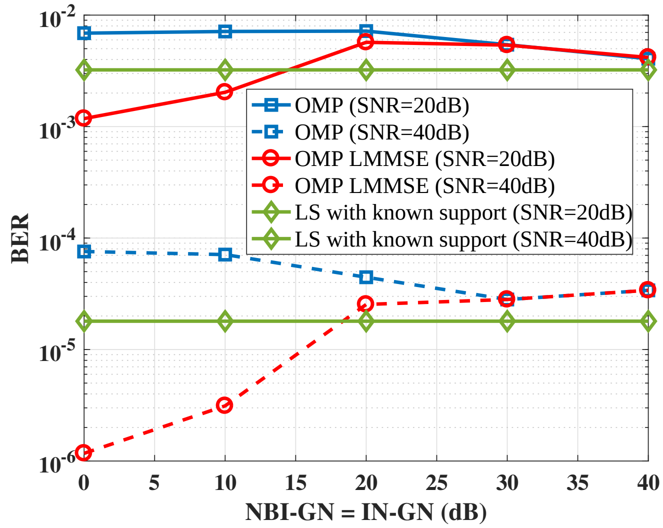

Figure 7.13: BER versus NBI and IN power for $R = 4$ bits/s/Hz.

CHAPTER 8

PROPOSED MIMO-OFDM NB-PLC DESIGNS IN UNDERGROUND MEDIUM-VOLTAGE NETWORKS [1]

The scope of this chapter is to investigate the applicability of MIMO NB-PLC designs to MV UG cable networks (Elgenedy et al., 2019). To the best of the authors' knowledge, MIMO-OFDM transmission has not been investigated for NB-PLC MV UG networks. Unlike wireless transmission, possible MIMO configurations in PLC systems are limited by the maximum number of physically available ports. In particular, a MV three-phase UG power-line system consists of three MV single-core cables, each made up of conductor and sheath, resulting in a total of 6 ports. Since every two ports form an independent link, we have three different SISO links, namely, conductor-conductor, conductor-sheath and sheath-sheath. In addition, since the maximum number of ports available is 6, the largest MIMO configuration supported is 5×6 because the sixth transmit port will be fully dependent on the other ports. In this work, we examined the largest configuration (MIMO 5×6) and also examined different smaller MIMO configurations to study the performance-complexity trade-off.

8.1 UG MIMO-MV NB-PLC Channel Modeling

To analyze PLC systems, proper models for the characterization of the noise and the UG cables are required for physical layer (PHY) simulations and data-rate calculations. The proposed approaches are described in detail in the next sub-sections.

8.1.1 MV UG Cable Channel Modeling

A typical MV three-phase cable arrangement is examined, which consists of three MV single-core cables, each made up of conductor and sheath as shown in Fig. 8.1. The per-unit-length

[1] © 2019 IEEE M. Elgenedy, T. Papadopoulos, S. Galli, A. Chrysochos, G. Papagiannis, N. Al-Dhahir, MIMO-OFDM NB-PLC Designs in Underground Medium-Voltage Networks, in IEEE Systems Journal, 2019.

(pul) parameters of the examined arrangement are calculated according to (Ametani, 1980). Assuming that the NB-PLC channel is time-invariant[2], the PLC signal in the frequency-domain (FD) is simulated using nodal analysis, considering long multi-conductor lines (Papadopoulos et al., 2013).

The transfer function matrix $\boldsymbol{T}$ relating the signal voltages at the sending (S) and receiving (R) ends of the cable system at a frequency f is described by the relation

$$V_R = \boldsymbol{T} V_S = \begin{bmatrix} T_{11} & \cdots & T_{1m} \\ \vdots & \ddots & \vdots \\ T_{n1} & \cdots & T_{nm} \end{bmatrix} V_S, \tag{8.1}$$

where $m \leq 5$, $n \leq 6$, and $T_{ij}(1 \leq i \leq n, 1 \leq j \leq m)$ is the complex channel frequency response (CFR) from the j^{th} transmitting node to the i^{th} receiving node. The voltage vectors V_S and V_R include all measured voltages at S and R, respectively. The CFR coefficients for both $i = j$ and $i \neq j$ are the direct- and cross-channel gains, respectively. Four configurations of PLC signal injection are examined, giving rise to the following four $m \times n$ MIMO configurations as shown in Fig. 8.2:

1. MIMO (3x3): the signal is injected into each of the cable conductors #1, #2 and #3 in Fig. 8.1, while the return path is via the corresponding sheath of each cable.

2. MIMO (2x3): the signal is injected between the conductors of cable #1 and #2, as well as #2 and #3 in Fig. 8.1. The received signals are measured between cable conductors #1 and #2, #2 and #3, #1 and #3 at end R.

3. MIMO (4x6): the total number of inputs is increased to 4, since the signal is injected between the conductors and between the sheaths of cables #1 and #2, as well as #2

[2] PLC channel in MV networks is mainly characterized by the line length, transmitter impedance and receiver termination, which can be practically considered almost constant for a specific network configuration (Papadopoulos et al., 2013; ITU-T G.9901, 2017).

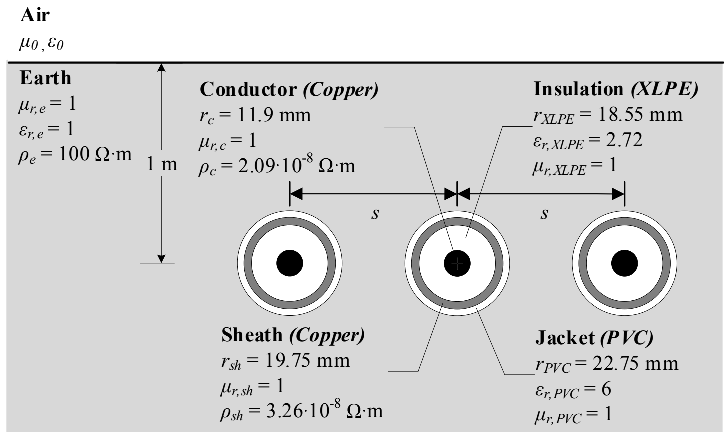

Figure 8.1: Cable arrangement with geometric and electromagnetic properties.

and #3 in Fig. 8.1. The number of outputs is 6, since the received signals are measured between all cable conductors and sheaths at end R.

4. MIMO (5x6): the signal is injected with reference to cable sheath #3 and all remaining conductors and sheaths, thus the number of inputs is 5. The number of outputs is 6 as in the MIMO (4x6) case.

All configurations are considered single-bonded. The grounding resistances in the MIMO (3x3) and MIMO (2x3) configurations are 1 Ohm. In the MIMO (4x6) and (5x6) cases, since the cable sheaths are used as additional channel paths, carrier-wave (CW) traps using ferrite ring chokes were considered to reduce EMI. For consistency, the inductance of the CW traps is taken equal to 3.18 mH, resulting in 1 Ohm impedance at 50 Hz. In all cases, $\boldsymbol{T}$ is calculated in the frequency range from 1 kHz to 500 kHz and in a column-wise fashion by applying the superposition theorem to all voltage sources. Voltages at the ports of interest are calculated for each source independently while all other sources are replaced by short-circuits. Next, all obtained voltages are summed coherently. Thus, each column T_j of the matrix $\boldsymbol{T}$ is calculated individually and represents the response of the system to the j^{th} source (Chrysochos et al., 2016b).

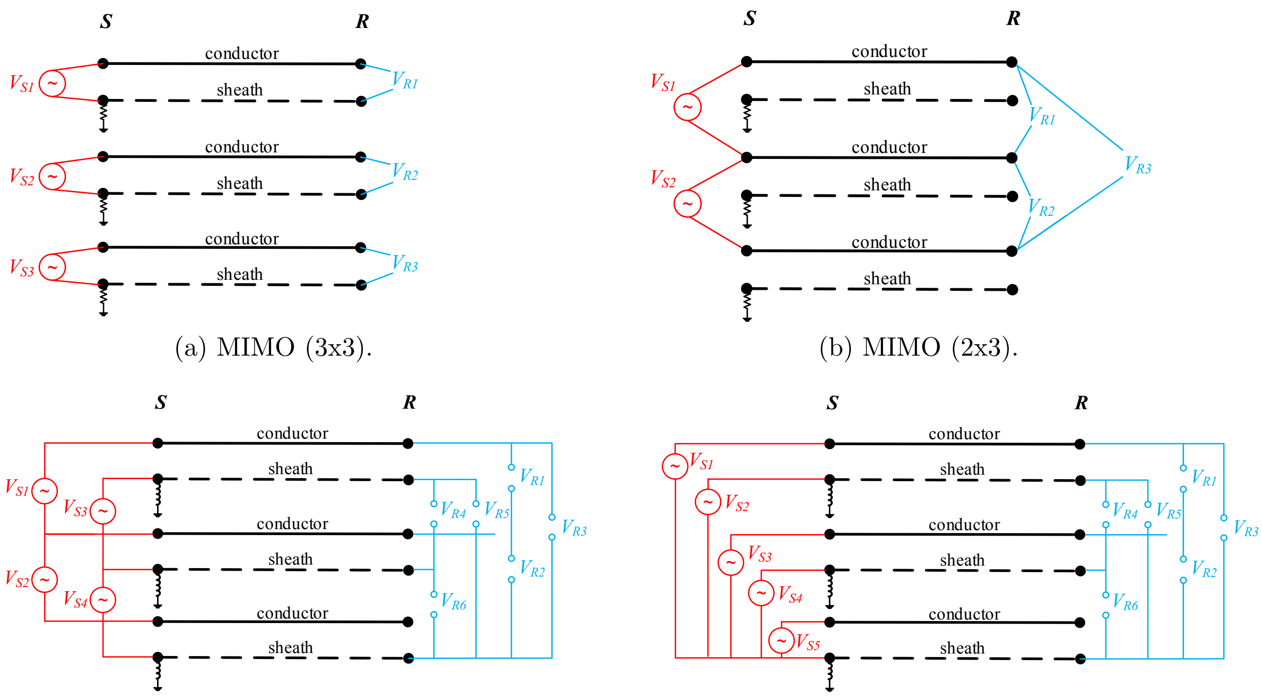

(a) MIMO (3x3).

(b) MIMO (2x3).

(c) MIMO (4x6).

(d) MIMO (5x6).

Figure 8.2: MIMO signal injection configurations.

8.1.2 Noise PSD

In MV NB-PLC networks, according to the origin, intensity, spectrum occupancy, and time duration, the following noise categories are considered: (a) background noise, (b) narrow-band noise, (c) periodic impulsive noise asynchronous to the mains frequency, (d) periodic impulsive noise synchronous to the mains frequency, and (e) asynchronous impulsive noise (IEEE P1901.2, 2013). Although the last two types of noise present significant fluctuations over short periods of time and location, only the first three are included in our data rate analysis. This is justified by their origination from non-steady state operating conditions and the fact that they can be readily tackled by proper countermeasures. The first three types of noise can be considered stationary over long periods of time and thus their PSD can be modeled with certain functions of frequency, i.e., exponential functions. In particular, the colored background noise mainly results from the summation of harmonics of the mains

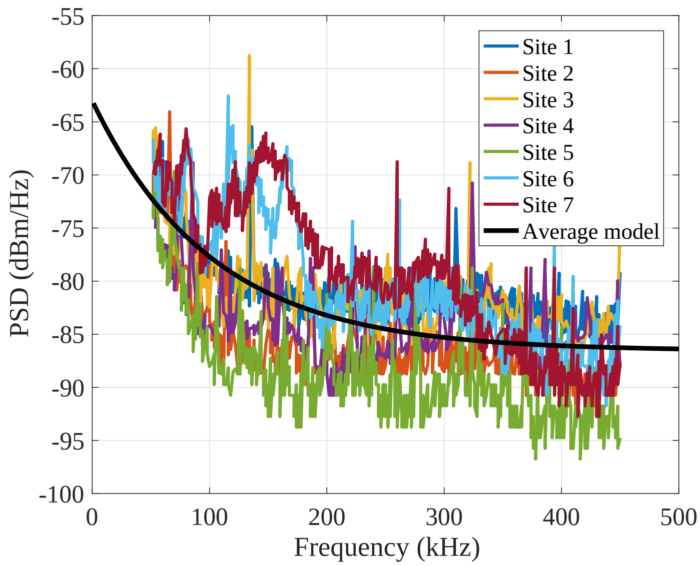

Figure 8.3: Spectral densities from different sites and resulting average model.

cycle and different low-power noise sources present in the system, and is usually characterized with a PSD which is decreasing with frequency (IEEE P1901.2, 2013). Therefore, as indicated in the IEEE 1901.2 standard (IEEE P1901.2, 2013), the noise PSD is high in the lower frequency range (usually up to 100 kHz) and then decays with frequency with the exception of the narrow band interferers. Hence, noise measurements in the frequency range of 50 kHz – 450 kHz for the different MV sites reported in Appendix D of the IEEE 1901.2 standard (IEEE P1901.2, 2013, Subsection D.3.1.2.2) (summarized in Fig. D-29) are used to develop an average colored noise model with decaying PSD level over frequency, as shown in Fig. 8.3. The proposed PSD model which is described by an exponential function is given by (8.2), revealing that MV networks are rather hostile for PLC applications and especially for frequencies lower than 200 kHz.

$$PSD_{noise} = 23.54e^{(-0.009766f)} - 86.56 \text{ dBm/Hz}. \tag{8.2}$$

8.2 MIMO-OFDM Communication Model

In MIMO-OFDM transmission, the CFR is decoupled into N orthogonal frequency sub-channels, where N is the OFDM symbol size. Hence, the received signal is only coupled across space for each frequency sub-channel. In particular, at sub-channel k, the spatial signal model can be written as follows

$$Z_k = \boldsymbol{H}_k S_k + W_k; \quad k = 1, \ldots, N \tag{8.3}$$

where Z_k is the $N_R \times 1$ phase-to-phase received signal vector, S_k is the $N_T \times 1$ transmitted signal vector, $\boldsymbol{H}_k$ is the $N_R \times N_T$ MIMO CFR matrix of the MV line at the k^{th} sub-channel, and W_k is the per sub-channel zero-mean Gaussian independent and identically distributed (i.i.d.) $N_R \times 1$ noise vector with noise variance $\sigma^2_{w,k}$. Assuming that the equivalent MIMO CFR matrix is available at both the receiver (using a training signal) and the transmitter (through a reliable feedback channel from the receiver), next we describe signal processing techniques that enhance the achievable data rate.

8.2.1 Spatial Channel Diagonalization

The equivalent channel matrix $\boldsymbol{H}_k$ can be factorized using the singular value decomposition (SVD) as follows

$$\boldsymbol{H}_k = \boldsymbol{M}_k \boldsymbol{\Lambda}_k \boldsymbol{U}_k^H; \quad k = 1, \ldots, N \tag{8.4}$$

where $\boldsymbol{M}_k$ and $\boldsymbol{U}_k$ are $N_R \times N_R$ and $N_T \times N_T$ unitary matrices, respectively, while $\boldsymbol{\Lambda}_k$ is a $N_R \times N_T$ diagonal matrix with non-negative real numbers on its diagonal. It can be shown from (Ginis and Cioffi, 2002) that the MIMO channel throughput is maximized by spatial decoupling of the two transmitted information streams using (8.4). At the transmitter, the original information vector $\tilde{S}_k$ is precoded by $\boldsymbol{U}_k$ resulting in the transmitted signal

$S_k = \boldsymbol{U}_k \tilde{S}_k$, while at the receiver, the vector Z_k is equalized by $\boldsymbol{M}_k^H$, resulting in the following filtered signal vector $\tilde{Z}_k$

$$\tilde{Z}_k \triangleq \boldsymbol{M}_k^H Z_k = \boldsymbol{M}_k^H \boldsymbol{H}_k S_k + \boldsymbol{M}_k^H W_k. \tag{8.5}$$

Substituting from (8.4) into (8.5) yields

$$\tilde{Z}_k = \boldsymbol{\Lambda}_k \tilde{S}_k + \grave{W}_k; \quad k = 1, \ldots, N \tag{8.6}$$

where $\grave{W}_k = \boldsymbol{M}_k^H W_k$. Hence, (8.5) can be rewritten as follows

$$\tilde{Z}_k = \begin{bmatrix} \lambda_{k,1} & \cdots & 0 \\ \vdots & \ddots & 0 \\ 0 & \cdots & \lambda_{k,N_T} \\ 0 & 0 & 0 \end{bmatrix} \begin{bmatrix} \tilde{s}_{k,1} \\ \vdots \\ \tilde{s}_{k,N_T} \end{bmatrix} + \begin{bmatrix} \tilde{w}_{k,1} \\ \vdots \\ \tilde{w}_{k,N_R} \end{bmatrix} \tag{8.7}$$

Therefore, the $N_R \times N_T$ cross-coupled MIMO channel matrix at each frequency sub-channel has been decomposed into N_T spatially-decoupled scalar channels. Note that since the channel in the MV PLC networks is considered a time-invariant system, the channel transfer function estimation and SVD calculations can be performed once at the beginning of the transmission and then fed back to the transmitter.

8.2.2 Bit Loading Optimization

Our objective is to maximize the achievable data rate over all OFDM frequency sub-channels subject to a given transmit PSD mask. This objective is achieved by adaptive OFDM bit loading over both frequency sub-channels and spatial streams. Assuming SISO transmission and using the gap approximation (Cover and Thomas, 1991), the bit loading at the k^{th} OFDM sub-channel is

$$b_k = log_2(1 + \frac{\mathsf{SNR_k}}{\Gamma}), \tag{8.8}$$

where $\mathsf{SNR_k}$ is the signal-to-noise ratio (SNR) at the k^{th} OFDM sub-channel. The quantity Γ is called the SNR gap since the number of bits required to achieve a certain probability of error P_e is less than the theoretical capacity $C = log_2(1 + \mathsf{SNR_k})$ which assumes error-free transmission. Hence, bit loading using the gap approximation is based on the capacity of a channel with $\mathsf{SNR_k}$ reduced by a factor of Γ. The SNR gap for any coded quadrature amplitude modulation (QAM) scheme is given by (Cioffi, a)

$$\Gamma = \frac{\gamma_m}{3\gamma_c}[Q^{-1}(P_e/4)]^2, \tag{8.9}$$

where $Q(x) = 1/\sqrt{2\pi}\int_x^\infty e^{(-u^2/2)}du$, γ_c is the coding gain, γ_m is the desired system margin. In this chapter, a target error rate P_e of 10^{-7} is assumed to ensure reliable data transmission. Hence, from (8.9), the SNR gap in dB is

$$\Gamma_{dB} = 9.8 + \gamma_m - \gamma_c. \tag{8.10}$$

The transmit energy allocation can also be optimized across space to maximize the data rate using the well-known water-filling algorithm (Cover and Thomas, 1991) and (Cioffi, a). The energy per sub-channel, denoted by E_k, is constrained by the transmitter PSD mask $\bar{E}$. The spatial energy allocation optimization problem of the MIMO decoupled N_T streams is formulated as follows

$$\max_{E_{k,i}} \sum_{k=1}^{N}\sum_{i=1}^{N_T} log_2\left(1 + \frac{\lambda_{k,i}^2 E_{k,i}}{\sigma_{w,k}^2\Gamma}\right) \quad s.t. \quad \sum_{i=1}^{N_T} E_{k,i} = \bar{E}. \tag{8.11}$$

To generate a water-filling energy allocation that yields an integer number of bits, we implement the following algorithm based on the incremental energy concept defined in (Cioffi, b) for joint energy allocation and bit loading. As described in Algorithm 6, for each sub-channel k, we compute the additional energy required to add one bit for spatial stream i, denoted by $\Delta E_{k,i}$. Then, we find the information stream $\hat{i}$ that requires the minimum energy. If $\Delta E_{k,\hat{i}}$ is less than the total energy budget $E_{current}$ (initially set equal to $\bar{E}$), we increase the number of bits for stream $\hat{i}$ by one bit then update the energy budget according to $E_{current} = E_{current} - \Delta E_{k,\hat{i}}$. We repeat this procedure until $\Delta E_{k,\hat{i}}$ becomes greater than the updated energy budget $E_{current}$. Finally, the data rate R is

$$R = \sum_{k=1}^{N} \sum_{i=1}^{N_T} b_{k,i} \Delta f, \tag{8.12}$$

where Δf is the OFDM sub-channel width.

8.3 Reduced-Complexity Per Sub-Channel Spatial Precoder/Detector Designs

In this section, we show how to exploit the special structure of the MIMO channel matrix to reduce the complexity of spatial precoding and detection at each frequency sub-channel.

8.3.1 MIMO (3x3)

We observed that the channel matrix $\boldsymbol{H}_k$ of the MIMO (3x3) case is strongly row-wise diagonally dominant, which means that $|h_k(i,i)| > \sum_{(i \neq j)} |h_k(i,j)|$, where $h_k(i,j)$ refers to the i^{th} row and j^{th} column in the channel matrix $\boldsymbol{H}_k$. Hence, we propose using the diagonalizing precoder design in (Cendrillon et al., 2007) that eliminates the need for the receiver spatial decoder matrix based on the left singular vectors of the channel matrix (c.f. (8.4)). This in turn, reduces the number of operations at the receiver side. The diagonalizing spatial precoder matrix per sub-channel k, denoted by $\boldsymbol{P}_k$, is given by

Algorithm 6 Joint Energy Allocation and Bit loading.

Input:Γ,$\overline{E}$, $\{\lambda_{k,i}\}$, $\{{\sigma_{w,k}}^2\}$,$\forall k\in\{1,\ldots,N\}$,$i\in\{1,\ldots,N_T\}$

1. **for** $k \le N$
2. $E_{current} = \bar{E}$
3. **while** $E_{current} > 0$
4. $\Delta E_{k,i} = \left(\frac{{\sigma_{w,k}}^2\Gamma}{{\lambda_{k,i}}^2}\right) 2^{b_{k,i}}, \quad \forall i \in \{1,\ldots,N_T\}$
5. $\hat{i} = argmin_i(\Delta E_{k,i})$
6. **if** $E_{current} > \Delta E_{k,\hat{i}}$
7. $E_{current} = E_{current} - \Delta E_{k,\hat{i}}$
8. $b_{k,\hat{i}} = b_{k,\hat{i}} + 1$
9. **end if**
10. **end while**
11. **end for**
12. **return** $b_{k,i}$

$$\boldsymbol{P}_k \triangleq \beta_k^{-1}\boldsymbol{H}_k^{-1} diag\left\{h_k(1,1),\ldots,h_k(N_T,N_T)\right\}, \tag{8.13}$$

where $diag\{\alpha_1,...,\alpha_N\}$ denotes a diagonal matrix with elements $\alpha_1,...,\alpha_N$ on the main diagonal. The scaling factor β_k ensures a normalized precoder so that the transmit PSD constraint is still satisfied, and is given by

$$\beta_k \triangleq \max_n \left\|[\boldsymbol{H}_k^{-1} diag\left\{h_k(1,1),\ldots,h_k(N_T,N_T)\right\}]_{row\,n}\right\|. \tag{8.14}$$

The achievable data rate using the diagonalizing precoder is given by

$$\hat{R} = \sum_{k=1}^{N}\sum_{i=1}^{N_T}\left\lfloor log_2\left(1+\frac{E_{k,i}|h_k(i,i)|^2}{\beta^2\sigma_{w,k}^2\Gamma}\right)\right\rfloor \Delta f. \tag{8.15}$$

We apply the floor operator ($\lfloor\,\rfloor$) in (8.15) to ensure that an integer number of bits is transmitted on every sub-channel to calculate more practical data rate projections. As proved in (Cendrillon et al., 2007), since $\boldsymbol{H}_k$ is strongly row-wise diagonally dominant, the scalar β_k is very close to 1, and hence, the diagonalizing precoder performs near-optimal channel matrix diagonalization. The assigned energy-level $E_{k,i}$ is computed using the bit loading algorithm defined in Algorithm 6 by replacing $\lambda_{k,i}^2$ with $|h_k(i,i)|^2$. In addition, we observed that the diagonal elements of the channel matrix $\boldsymbol{H}_k$ are very close to each other. Hence, we can assign an equal input energy level of $\bar{E}/3$ for each data stream without the need to run the bit loading algorithm resulting in the following data rate estimate

$$\hat{R} = \sum_{k=1}^{N} \sum_{i=1}^{N_T} \left\lfloor log_2 \left(1 + \frac{\bar{E}|h_k(i,i)|^2}{3\beta^2 \sigma_{w,k}^2 \Gamma} \right) \right\rfloor \Delta f. \tag{8.16}$$

In the numerical results section, we quantify the data rate loss due to the different approximations.

8.3.2 MIMO (2x3)

The MIMO (2x3) channel matrix has the following special structure

$$\boldsymbol{H}_k = \begin{bmatrix} a_k & b_k \\ b_k & a_k \\ c_k & c_k \end{bmatrix}. \tag{8.17}$$

When performing the SVD for $\boldsymbol{H}_k$, it can be shown that the matrix of the right-singular vectors $\boldsymbol{U}_k$ is always a 2x2 Hadamard matrix which is independent of the actual values of a_k,b_k and c_k, and is given by

$$\boldsymbol{U}_k = \frac{1}{\sqrt{2}} \begin{bmatrix} 1 & 1 \\ 1 & -1 \end{bmatrix}. \tag{8.18}$$

The main benefit of exploiting this structure is that the precoding operation with the Hadamard matrix (contains only +1 or -1) will not require any multiplication operations, i.e., only addition and subtraction operations are required, which significantly reduces the implementation complexity.

8.3.3 MIMO (4x6)

The MIMO (4x6) channel matrix has also a special structure that can be viewed as four 3x2 matrices with the same structure as the 2x3 matrix in (8.17). In particular, the channel matrix can be *approximated*[3] by the following structure

$$\hat{\boldsymbol{H}}_k = \begin{bmatrix} a_k & b_k & a_k & b_k \\ b_k & a_k & b_k & a_k \\ c_k & c_k & -c_k & -c_k \\ x_k & y_k & x_k & y_k \\ y_k & x_k & y_k & x_k \\ z_k & z_k & -z_k & -z_k \end{bmatrix}. \tag{8.19}$$

It can be shown that the matrix of the right-singular vectors $\hat{\boldsymbol{U}}_k$ of the approximated channel matrix $\hat{\boldsymbol{H}}_k$ in (8.19) is always a Hadamard matrix which we propose to use for transmit spatial precoding since it is constant (i.e., not channel-dependent) and involves only additions/subtractions operations as shown below

[3]Note that the channel matrix structure in (8.19) is approximate while the channel matrix structure in (8.17) is exact. Therefore, for the MIMO 2×3 case, there is no performance degradation when using the Hadamard precoder. However, for the MIMO 4×6 case, the spatial streams are not fully decoupled (i.e., there is residual interference between them) when using the Hadamard precoder approximation, and the performance is slightly degraded compared to the case when the exact optimal precoder is used.

$$\hat{\boldsymbol{U}}_k = \frac{1}{2}\begin{bmatrix} -1 & -1 & 1 & 1 \\ -1 & 1 & -1 & 1 \\ 1 & -1 & -1 & 1 \\ 1 & 1 & 1 & 1 \end{bmatrix}. \tag{8.20}$$

The received signal in this case is given by

$$Z_k = \boldsymbol{H}_k \hat{\boldsymbol{U}}_k \tilde{S}_k + W_k = \underbrace{\boldsymbol{M}_k \boldsymbol{\Lambda}_k \boldsymbol{U}_k^H \hat{\boldsymbol{U}}_k}_{\boldsymbol{G}_k} \tilde{S}_k + W_k \tag{8.21}$$

To detect the original transmitted signal, the received signal Z_k is multiplied by the zero-forcing matrix equalizer filter $\boldsymbol{G}_k^{-1} = \hat{\boldsymbol{U}}_k \boldsymbol{U}_k \boldsymbol{\Lambda}_k^{-1} \boldsymbol{M}_k^H$, resulting in the vector $\tilde{Z}_k$

$$\tilde{Z}_k = \tilde{S}_k + \boldsymbol{G}_k^{-1} W_k. \tag{8.22}$$

Let $\boldsymbol{\Upsilon}_k^H = \boldsymbol{G}_k^{-1}(\boldsymbol{G}_k^{-1})^H = \hat{\boldsymbol{U}}_k \boldsymbol{U}_k \boldsymbol{\Lambda}_k^{-2} \boldsymbol{U}_k \hat{\boldsymbol{U}}_k$, the resulting data rate can be evaluated as follows

$$\hat{R} = \sum_{k=1}^{N} \sum_{i=1}^{N_T} \left\lfloor log_2 \left(1 + \frac{E_{k,i}}{\sigma_{w,k}^2 \Gamma \Psi_k(i,i)} \right) \right\rfloor \Delta f, \tag{8.23}$$

where $\Psi_k(i,i)$ refers to the i^{th} diagonal element of the matrix $\boldsymbol{\Upsilon}_k$. The assigned energy $E_{k,i}$ is computed using the bit loading algorithm described in Algorithm 6 by replacing $\lambda_{k,i}^2$ with $1/\Psi_k(i,i)$.

8.4 Reducing the Number of Receiver Phases

In this section, we study the effect of reducing the number of processed outputs to be always equal to the number of inputs $N_R = N_T$ while minimizing the effect of this reduction on the achievable data rate. There is a total of $\begin{pmatrix} N_R \\ N_T \end{pmatrix}$ possible output port combinations and we choose the one that achieves the highest data rate. As an example, assume that we reduce the number of processed outputs for MIMO (4x6) from 6 to 4 outputs. The number of possible selected output port combinations is $\begin{pmatrix} 6 \\ 4 \end{pmatrix} = 15$. The best combination is generally dependent on the channel transfer function which varies from one sub-channel to another. In addition, the optimal way for choosing the best combination is to maximize the final calculated data rate for each combination which is too complex especially if the selection is done per sub-channel. A simpler approach is to choose the best combination based on the maximum multi-channel SNR (Cioffi, b) which is defined for a set of parallel channels (N_R) as follows

$$\mathsf{SNR_{mc}} \triangleq \left[\left(\prod_{n=1}^{N_R} \left[1 + \frac{\mathsf{SNR_n}}{\Gamma} \right] \right)^{\frac{1}{N_R}} - 1 \right] \Gamma. \tag{8.24}$$

The multi-channel SNR is a single SNR measure that characterizes the set of OFDM sub-channels by an equivalent single AWGN channel that achieves the same data rate. When the term $\{\mathsf{SNR_n}\}/\Gamma$ is $\gg 1$, the multi-channel SNR reduces to the geometric mean of the $\mathsf{SNR_n}$, i.e.,

$$\mathsf{SNR_{mc}} \triangleq \left(\prod_{n=1}^{N_R} \mathsf{SNR_n} \right)^{\frac{1}{N_R}}. \tag{8.25}$$

Another simplification is to assume that the same outputs are selected for all frequency sub-channels. Interestingly, as it will be shown in the numerical results sections, some configurations for the receive phases achieve almost the same performance as maximizing the data rate per sub-channel based on the maximum data rate.

8.5 Simulation Results

In this section, we quantify the achievable data rates for the different SISO/MIMO configurations. The achievable data rates are evaluated assuming the new wide FCC band (union of FCC low and FCC high) specified in the ITU-T G.9903 (ITU-T G.9903, 2017) and IEEE 1901.2 (IEEE P1901.2, 2013) standards with the systems parameters listed in Table 8.1. As specified in G.9903 (ITU-T G.9903, 2017) (Table 8-2), the coupling loss is assumed to be 3 dB. Thus, we include a total of 6 dB coupling loss (for both the transmitter and receiver). In addition, considering convolutional coding with rate 1/2 and a constraint length of 7, as specified in the IEEE 1901.2 standard (IEEE P1901.2, 2013), the resulting coding gain (using soft-decision Viterbi decoding) is 5.8 dB as indicated in (Proakis, 2008, Table 8.6-2). Therefore, we assume the value of γ_c to be 6 dB for simplicity. Moreover, we assume a 6 dB system margin γ_m to account for any unexpected sources of noise and interference and other modeling inaccuracies. However, since γ_m is a design parameter, it can be changed for either more optimistic or pessimistic data rate projections. Hence, the gap Γ (in dB) is modified from (8.10) to be

$$\Gamma_{dB} = 9.8 + \gamma_m - \gamma_c + 6 = 15.8 \quad \text{dB}. \tag{8.26}$$

For NB-PLC, the transmitted signal constraints are often given in terms of conducted emissions. According to the international standard ITU-T Recommendation G.9901 (ITU-T G.9901, 2017), the following maximum transmit voltages are specified for ITU-T Recommendations G.9902 (ITU-T G.9902, 2012), G.9903 (ITU-T G.9903, 2017), and G.9904[4] (ITU-T G.9904, 2012):

- 134 dBµV, for frequencies in the band 3-148.5 kHz – same as specified in (CENELEC EN 50065-1, 2011).
- 137 dBµV, for frequencies in the band 148.5-535 kHz.

[4] These voltage limits must be met when the transceiver is loaded with the Line Impedance Stabilization network (LISN), often called the Artificial Mains Network, as specified in Clause 4.4 (IEC CISPR 16-1-2, 2014).

Table 8.1: System parameters.

Frequency band	37.5-487.5 kHz (BW = 450 kHz)
Number of FFT points	256
Sampling frequency (f_s)	1.2 MHz
Sub-channel width (Δf)	4.6875 kHz
Number of used sub-channels	97

Assuming a 50 Ohm resistor, these voltage limits correspond to PSD limits of -24.43 and -25.86 dBm/Hz, respectively. In the simulation results, we set a constant PSD limit of -26 dBm/Hz over all frequencies. In practice, one could even afford to increase the above transmit PSD limits when operating on UG MV cables since, being buried cables, their interference onto wireless services is much smaller than interference from aerial power lines. Furthermore, UG MV cables are also often shielded, as in our examined arrangement. For all results, the cable length varies from 0.1 km up to 4 km. In addition, source and termination impedances of the cable conductors are set equal to the cable conductor characteristic impedance calculated at 200 kHz ($\sim$ 16 Ω). Similarly, source and termination impedances of the cable sheaths are set to the cable sheath characteristic impedance calculated at 200 kHz ($\sim$ 5.2 Ω). The 200 kHz frequency is selected as the middle point of the examined channel bandwidth which is a slightly imperfect choice for other frequency sub-channels and may cause a minor standing waves behavior.

8.5.1 SISO/MIMO – Configurations

Fig. 8.4 shows the data rates for the different SISO/MIMO configurations. It is clear from Fig. 8.4 that the SISO conductor-sheath configuration achieves the highest data rate compared to the other two SISO configurations (conductor-conductor and sheath-sheath). This is mainly attributed to the fact that the SISO conductor-sheath injection is solely characterized by the signal propagation between each conductor and sheath, resulting in low signal attenuation. The other two SISO configurations are described by the corresponding propagation between the cable conductors and sheaths, respectively, which, however, involve the imperfect earth thus leading to slightly higher overall attenuation (Papadopoulos et al., 2013).

Moreover, we notice a significant improvement in the data rates for the MIMO cases over the SISO case even for long line lengths (4 km). For example, the data rate for MIMO (5x6) configuration at line length 4 km is 16 Mbps compared to 5.5 Mbps for the SISO (conductor-sheath) configuration (i.e., a three-fold increase). In addition, we notice a big gap between the data rates achieved by MIMO (3x3) versus MIMO (2x3) configurations although there is only one additional transmit phase for the MIMO (3x3) configuration. This is because the MIMO (3x3) configuration uses only the conductor-sheath configuration (which is the most efficient SISO configuration) for each of the three phases unlike the MIMO (2x3) configuration which is based on the conductor-conductor signal injection for all phases. Finally, due to the slightly imperfect matching for the source and termination impedances (which causes a minor standing waves behavior), it is not always guaranteed that small increases in the line lengths (which implies small increases in the channel attenuation) will cause a noticeable data rate loss. For example, for the MIMO 4×6 case, the data rate achieved at 0.1 km line length is slightly lower than the data rate achieved at 0.25 km line length.

8.5.2 Effect of the Transmit PSD Level

In Fig. 8.5, we compare the achievable data rates for the SISO and MIMO cases assuming two different transmit PSD levels

1. PSD = -26 dBm/Hz, based on the latest version of G.9901 (ITU-T G.9901, 2017) for NB-PLC, as discussed earlier in this section.

2. PSD = -55 dBm/Hz, based on BB-PLC standards (ITU-T G.9963, 2015; IEEE P1901TM/D3.00, 2010).

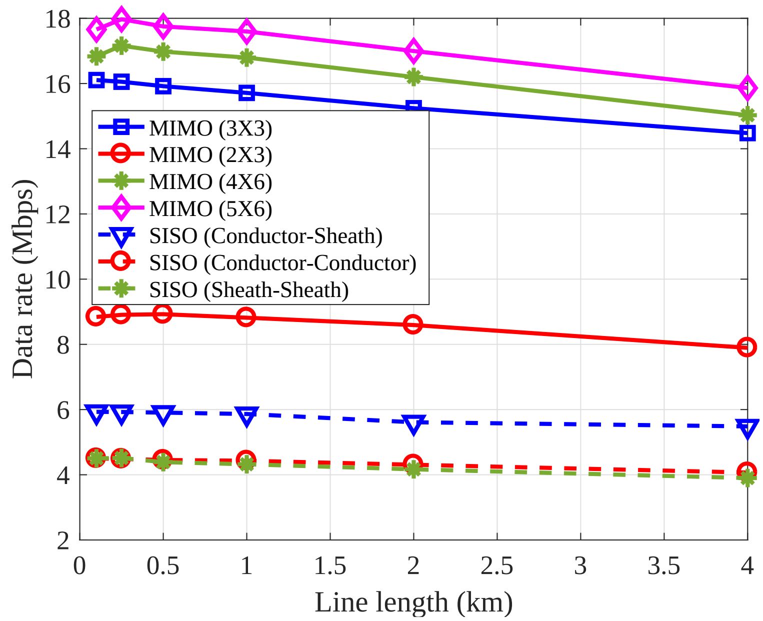

Figure 8.4: The data rates for the different MIMO configurations vs line length.

As shown in Fig. 8.5, the achievable data rate for MIMO (4x6) is increased by a factor of 5 assuming the -26 dBm/Hz PSD level compared to the -55 dBm/Hz PSD level. Moreover, the SISO (conductor-sheath) configuration shows a data rate increase by a factor of 3 with the -26 dBm/Hz PSD level compared to the -55 dBm/Hz PSD level.

8.5.3 Effect of the Channel Delay Spread

In this subsection, we discuss the effect of channel impulse response characteristics for all proposed configurations. In particular, we evaluate the channel delay spread for the different configurations and investigate their CP requirements. In addition, we study the effect of the CP length on the transmission efficiency and evaluate the net data rate with the CP overhead. We calculate the channel root mean square delay spread (RMS-DS) of the CIR as follows (Galli, 2011b)

$$\sigma = \acute{T}_s \sqrt{\mu^{(2)} - (\mu)^2}. \tag{8.27}$$

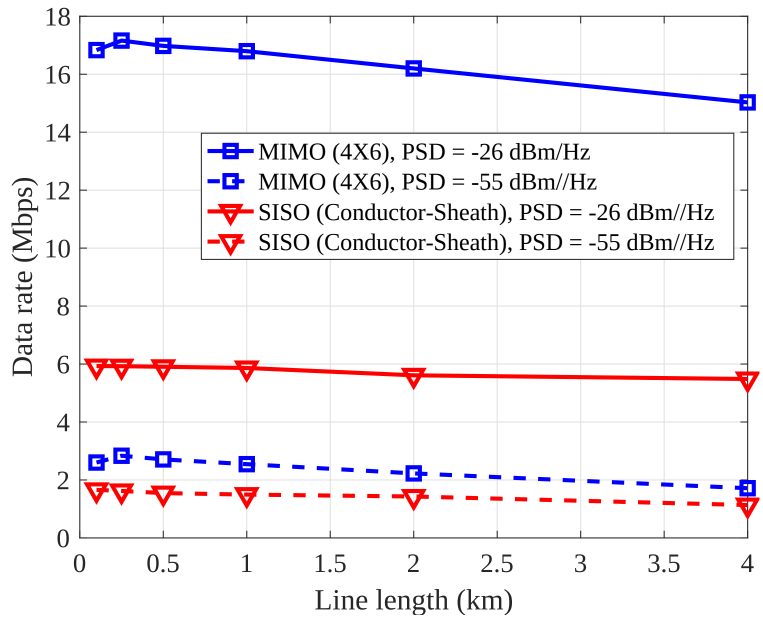

Figure 8.5: The effect of the PSD level on the achieved data rates for MIMO (4x6) and SISO (conductor-sheath).

The parameters μ and $\mu^{(2)}$ are defined as:

$$\mu = \frac{\sum_{i=0}^{L-1} i|h_i|^2}{\sum_{i=0}^{L-1} |h_i|^2}, \qquad \mu^{(2)} = \frac{\sum_{i=0}^{L-1} i^2|h_i|^2}{\sum_{i=0}^{L-1} |h_i|^2}, \tag{8.28}$$

where $h_i \triangleq h(t = i\acute{T}_s)$, $i \in \{0, 1, 2, \ldots, L\}$, is the sampled CIR at $\acute{f}_s = 1/\acute{T}_s$ and the CIR memory is $L - 1$. In this analysis, we use an oversampling factor of 4 (i.e., $\acute{f}_s = 4f_s = 4 \times 1200 \quad$ kHz) to ensure accurate results especially for shorter line lengths where the propagation delay is very small. Moreover, the non-zero CIR taps are determined such that they contain at least 95 % of the CIR power. Table II summarizes the RMS-DS results for the SISO conductor-sheath configuration for the different line lengths where we can see a slight increase in the RMS-DS when increasing the line length up to 4 km line length. In Table 8.2, we also include the estimated channel propagation delay based on the CIR peak delay and compare it to the channel mean group delay for verification. As shown in Table 8.2, both values are almost equal since the phase of the channel is almost linear.

Although choosing the CP length to be longer than the CIR length completely cancels the inter symbol interference (ISI), this choice does not necessarily maximize the achievable data rates. The CP length optimization represents a fundamental design trade-off where a long CP results in a data rate loss due to the CP overhead, while a short CP results in a data rate loss due to the ISI. In this analysis, we choose the CP length to be larger than 4 times the estimated RMS-DS (Galli et al., 2008).

According to Table 8.2, 5 samples should be enough for the CP length for the conductor-sheath configuration with up to 4 km line length. In addition, we calculate the estimated RMS-DS for the two other SISO configurations and they have almost the same RMS-DS as of the SISO conductor-sheath configuration. Based on that, the CP length could be as long as 5 samples for all configurations up to 4 km line length. Thus, the estimated CP length for all configurations for the UG MV cables would be compliant with the ITU-T G.9903 (ITU-T G.9903, 2017) and IEEE 1901.2 (IEEE P1901.2, 2013) standards where the CP length is specified to be 30 samples assuming a sampling frequency $f_s = 1200$ kHz, i.e., an overhead of $30/256 \times 100 \sim 12\%$. A value of 30 samples was adopted for the CP in the standards is due to the fact that LV networks have substantial multipath because of mismatched impedances and bridged taps. However, UG topologies have a point-to-point topology, hence, standards for MV UG scenarios should accommodate options for smaller CPs to ensure a higher transmission efficiency. In Fig. 8.6, we calculate the net data rate for all SISO/MIMO configurations by considering a 30 samples CP length overhead which results in a $\sim 12\%$ data rate loss for all cases compared to the data rates computed in Fig. 8.4.

8.5.4 Effect of Bit Caps

The transmit PSD level for UG NB-PLC (-26 dBm/Hz) yields high SNR levels for some of the sub-channels. Without any bit cap, i.e., without limiting the maximum number of bits

Table 8.2: SISO Conductor-Sheath CIR RMS-DS, Delay Spread, Group Delay and Propagation Delay at different line lengths.

Cable length (km)	RMS-DS (μs)	CIR duration (μs)	Propagation Delay (μs)	Mean Group Delay (μs)
0.1	0.97	6.46	0.833	0.551
1	0.99	6.67	5.833	5.544
2	1.0	6.87	11.25	11.082
4	1.0	6.87	22.5	22.164

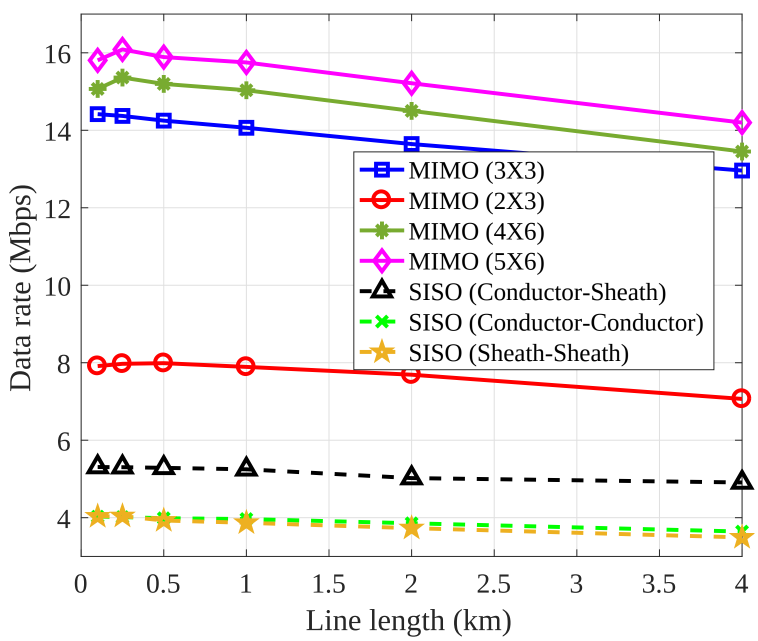

Figure 8.6: The net data rates for the different SISO/MIMO configurations vs line length, CP length = 30 samples.

per QAM symbol, some of the sub-channels can support up to 15 bits. Fig. 8.7 shows the bit loading profile for the MIMO (4x6) case with 500 m line length. In practical NB-PLC systems which are characterized by low complexity and low SNR, the maximum spectral efficiency is typically limited to 4 bits/sec/Hz, e.g. the 16-QAM mode specified in the ITU-T G.9903 (ITU-T G.9903, 2017) and IEEE 1901.2 (IEEE P1901.2, 2013) standards. In Fig. 8.8, we show the net data rates with bit caps of 4 and 10 bits per sub-channel. However,

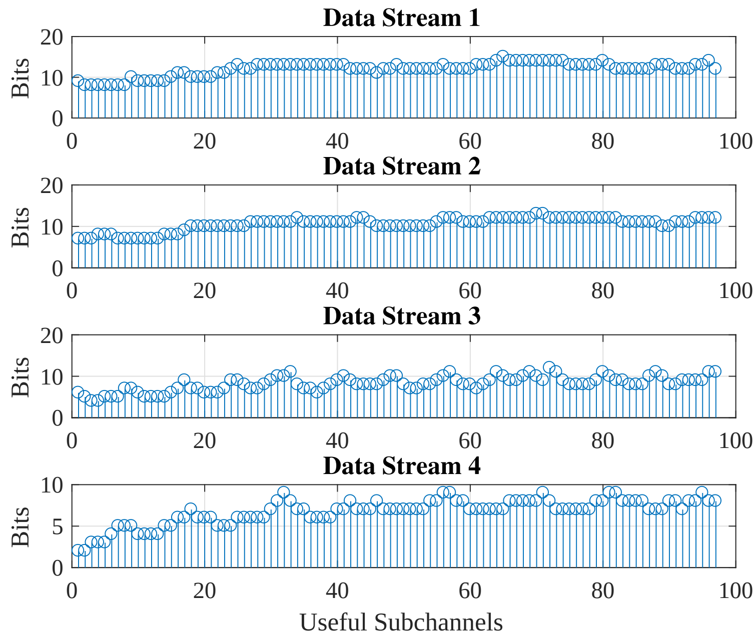

Figure 8.7: The bit loading profile for MIMO (4x6) at 500 m line length.

we also point out that this low complexity constraint argument holds mostly for LV smart meters whereas modems used for backhauling over MV may very well allow for spectral efficiencies of 10-12 bits per sub-channel. As Fig. 8.8 shows, higher bit capping limits are indeed justified especially for short-to-medium distances.

8.5.5 Effect of Reduced Complexity Spatial Precoder/Detector Designs

Fig. 8.9 shows that the achievable data rate for MIMO (3x3) with the diagonalizing precoder is almost the same as that of the optimal precoder/decoder which performs exact channel matrix diagonalization. Although the channel gains experienced by the three data streams are almost the same, assigning an equal input energy level of $\bar{E}/3$ for every stream is not optimal since it does not guarantee an integer number of bits. As shown in Fig. 8.9, the resulting data rate loss is about 4% compared to the case of running the bit loading algorithm, which represents a practical performance-complexity trade-off. In Fig. 8.10, the data rate

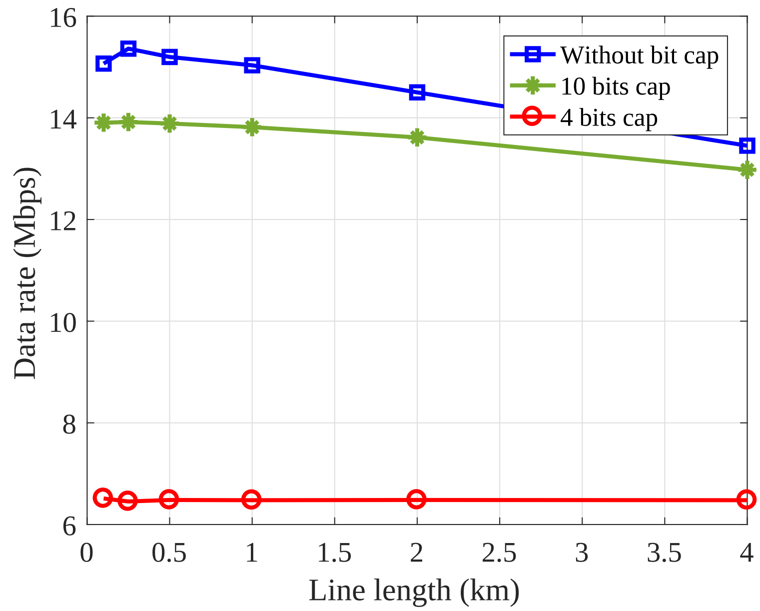

Figure 8.8: The net data rate for MIMO (4x6) for bit caps of 4 and 10 bits per sub-channel, CP overhead is included, CP = 30 samples.

loss due to the near-optimal Hadamard spatial precoding matrix is only 3% for line lengths less than 1 km and 1.5% for line lengths longer than 1 km.

In Table 8.3, we compare the transceiver implementation complexities of the different proposed MIMO configurations in terms of the required number of multiplications per OFDM sub-channel. In addition, we quantify the computational savings of the reduced-complexity spatial precoder/detector designs. The complexity can be categorized into initial and running complexities. In particular, initial complexity includes channel estimation and SVD operations (including channel feedback to the transmitter). The running complexity includes transmitter precoding and receiver detector (including channel equalization) operations. However, since the channel in the MV networks can be considered as a time-invariant system, channel estimation and SVD are calculated once and stored. Hence, initial computational complexity and feedback overhead can be ignored. Considering the exact precoder/detector design, the running complexity at the transmitter side is determined by the operation of multiplying the original information vector $\tilde{S}_k$ with the precoding matrix $\boldsymbol{U}_k$

Table 8.3: Transceiver complexity for the different MIMO configurations in terms of required number of multiplications per sub-channel for the full complexity versus reduced-complexity designs.

	Full Complexity		Reduced Complexity	
	TX	RX	TX	RX
SISO	0	1	-	-
MIMO 3×3	9	9+3=12	9	0
MIMO 2×3	4	9+3=12	0	9+3=12
MIMO 4×6	16	36+6=42	0	36
MIMO 5×6	25	36+6=42	-	-

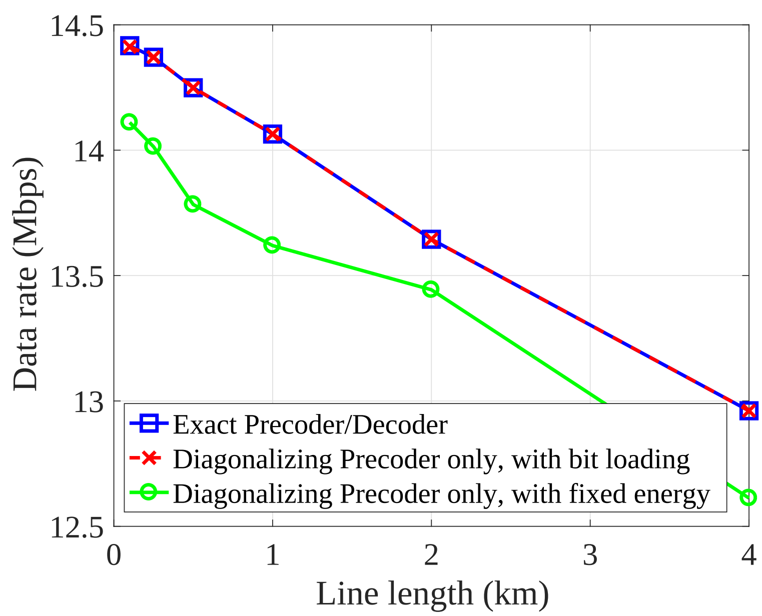

Figure 8.9: The data rates for MIMO (3x3) versus the line length for diagonalizing precoder with optimum or flat energy allocation.

which requires N_T^2 multiplications. At the receiver side, the complexity is mainly determined by the operation of multiplying the detector matrix $\boldsymbol{M}_k^H$ with the received data vector Z_k which requires N_R^2 multiplications. Additional N_T multipliers are required at the receiver side to perform channel equalization (i.e., scaling by the reciprocal of $\lambda_{k,i}$).

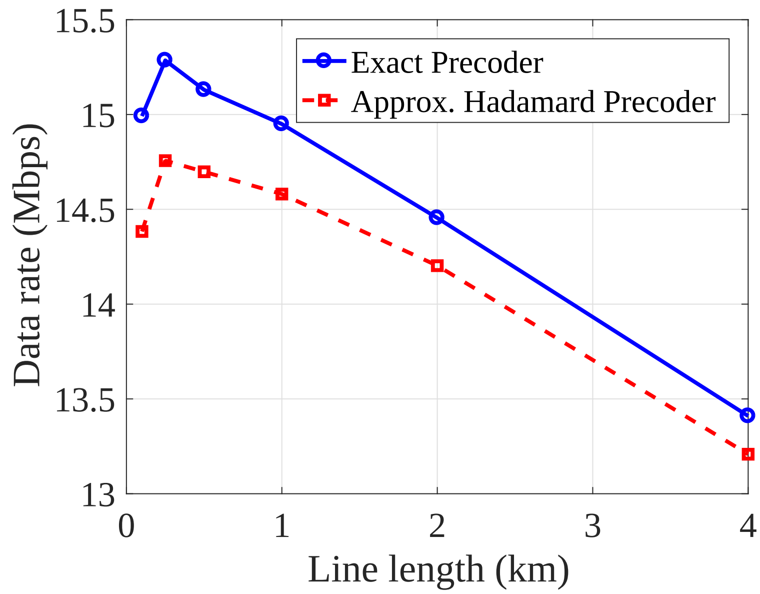

Figure 8.10: The data rates for MIMO (4x6) versus the line length for the exact versus approximated Hadamard precoder.

8.5.6 Effect of Reducing the Number of Output Phases

As shown in Fig. 8.11, the data rate loss due to reducing the number of receive phases by maximizing the data rate (optimal approach) is 10%. Moreover, using the geometric SNR metric in (Cioffi, b) is a very good approximation. In addition, assuming the same outputs for all frequency sub-channels, all MIMO configurations with 2-conductors/2-sheathes at the receiver side achieve the highest data rate which is very close to maximizing the data rate per sub-channel and a little better than maximizing the geometric SNR. In addition, the achievable data rate for the MIMO configurations with 3-conductors/one-sheath is very close to the MIMO configurations with 2-conductors/2-sheathes. However, there is a noticeable data rate loss (more than 10%) for the MIMO configurations with 1-conductor/3-sheaths at the receiver side when compared to 2-conductors/2-sheaths or 3-conductors/1-sheath configurations. Again, these results are consistent with the data rate results in Fig. 8.4 which show that the conductor-sheath SISO configuration achieves the highest data rate.

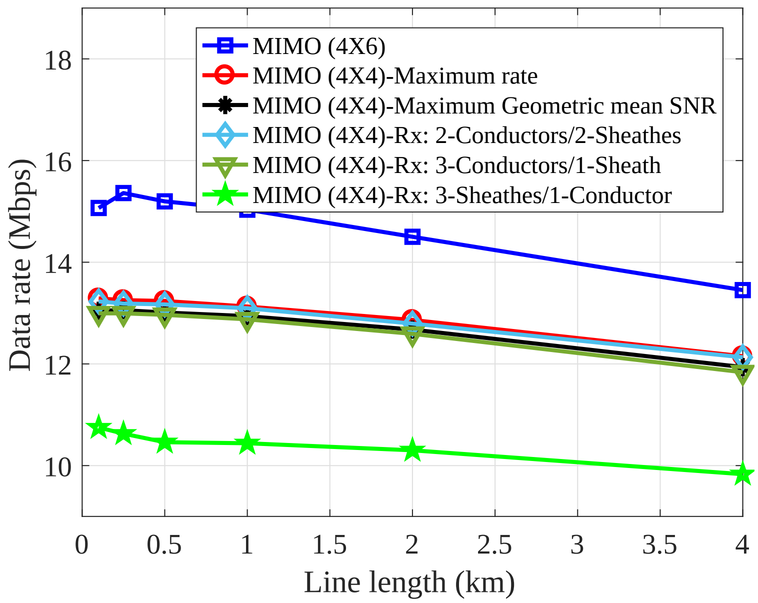

Figure 8.11: Data rate for MIMO (4x6) for different selections of $N_R = 4$.

CHAPTER 9

CONCLUSION AND FUTURE RESEARCH

In this dissertation, we proposed different techniques to enhance the transmission data rate and/or reliability of PLC in LV/MV smart grids. Specifically, we investigated cyclostationary noise mitigation in LV NB-PLC, NBI/IN mitigation in hybrid BB-PLC and unlicensed wireless, and increased data-rates in the MV UG NB-PLC MIMO-OFDM systems. For the proposed techniques, we exploited mainly the spatial domain to enhance the reliability of transmission (SIMO for LV NB-PLC and BB-PLC) or to increase the data rate (MIMO-OFDM for MV UG PLC). In addition, to better mitigate the impulsive noise, we exploited the temporal domain features including the noise cyclostationary and sparsity.

First, for the NB-PLC, we proposed the following three techniques to mitigate the cyclostationary noise: (1) erasure decoding, (2) temporal-region-based noise cancellation, and (3) FRESH-filtering-based noise cancellation. In addition, to ensure realistic performance projections, we developed novel methods to generate the cyclostationary noise for single and multiple phases NB-PLC based on FRESH filtering where the filter coefficients are extracted based on field measurements.

For the erasure decoding noise based mitigation, we investigated different techniques to mark erasures to the decoders. In particular, the cyclostationarity of the noise allows us to estimate its PSD which can be used to enhance the erasure decoding for both the Viterbi and RS decoders. Simulation results showed about $0.5 - 1$ dB gain at BER of 10^{-5} from erasure decoding for the RS decoder. Moreover, the noise's high spatial correlation provides us with an estimate of the instantaneous noise samples which can be used to mark erasures for both RS and Viterbi decoders. Simulation results showed a considerable SNR gain (up to 3 dB at BER of 10^{-5}) for typical PLC spatial correlation factors.

The proposed SIMO LMMSE temporal-region-based mitigation technique exploits the cyclostationarity of the noise to estimate its PSD and cross-correlation per frequency sub-channel over multiple stationary noise temporal regions. Simulation results showed that the proposed SIMO receiver achieves close to 7 dB gain at a coded BER of 10^{-4} over a SISO receiver and a 6 dB gain at coded BER of 10^{-4} over a conventional SIMO MRC receiver designed assuming stationary noise. The proposed temporal-region-based technique enjoys very low complexity compared to algorithms proposed in the literature.

The SIMO FRESH filtering exploits the cyclic auto-correlation of both the NB-PLC noise and the OFDM information signal in addition to the cyclic cross-correlation of the received signal across the receive phases. Furthermore, the FRESH filtering technique utilizes the cyclic components of both the cyclostationary noise and the OFDM signal in a single stage, which is shown analytically to be optimal for this problem. In particular, we proposed two TD LMMSE estimation techniques for SIMO NB-PLC cyclostationary noise mitigation based on FRESH filtering, namely the TD-NF and the TD-ENF techniques. The TD-ENF technique enjoys a lower complexity than the TD-NF technique, but it requires CIR estimation to design the FRESH filters. On the other hand, the TD-NF technique does not require the CIR estimate to design the FRESH filters but instead requires estimates of the cyclic auto-correlation and cross-correlation functions of the NB-PLC noise during a silence period prior to the transmissions. Hence, we concluded that the TD-NF technique is more suitable for the differential modulation case since it does not require CSI knowledge and the TD-ENF technique is more suitable for the coherent modulation case since it has a much lower complexity than the TD-NF technique. Simulation results showed that the coded BER performance of the proposed SIMO TD-NF technique outperforms the conventional MRC receiver by more than 8 dB at a coded BER of 10^{-3}.

Second, we investigated the diversity gain of simultaneous transmission in the BB-PLC and unlicensed wireless, namely, hybrid PLC-wireless system. In particular, we proposed a new framework to model and jointly estimate and mitigate non-contiguous and contiguous NBI and IN in SIMO hybrid PLC-wireless transmissions by exploiting their sparsity in the frequency and time domains, respectively. In addition, we exploited prior knowledge of the generally unequal sparsity levels at different antennas and wires and developed a multi-level OMP algorithm to further reduce the complexity of the sparse recovery algorithm. For contiguous NBI and IN, the presented joint NBI and IN mitigation framework exploits their inherent block sparsity with or without knowledge of the bursts boundaries. Moreover, we exploited the spatial correlation across the receive antennas and across the three-phase powerlines to convert the non-contiguous NBI and IN problem to a block sparse NBI and IN problem, after which we proposed a multi-level BOMP algorithm that can efficiently exploit the new block-sparse structure. For both contiguous and non-contiguous NBI and IN with known second-order statistics, we quantified the performance gains of LMMSE-based sparse recovery algorithms over the conventional LS-based recovery of joint NBI and IN with known support indices. Simulations demonstrated the superiority of the joint PLC-wireless processing approach over PLC-only or wireless-only processing approaches.

Third, to enhance the data-rate of the NB-PLC transmission over MV UG networks, we proposed different MIMO-OFDM configurations. After optimizing the bit loading across the spatial data streams for all frequency sub-channels, the achievable data rates are evaluated for all proposed MIMO configurations and are shown to be significantly increased (up to three times higher) when compared to SISO configurations. The achievable data rates are evaluated for different line lengths and are shown to be high even for long line lengths (up to 4 km). In addition, we calculated the channel RMS-DS for the different transmission phases and verified the adequacy of the current CP-length specifications in the IEEE 1901.2 standard for MV UG powerline networks. Moreover, we demonstrated the effect of practical design limitations on the achievable data rate loss by considering the CP overhead and bit caps. Furthermore, we proposed efficient methods to reduce the design complexity while minimizing the data rate loss.

Finally, we investigated the complexity for most of the proposed algorithms and suggested different approaches for optimizing the design parameters, which reduce the design complexity appreciably with a negligible performance loss.

9.1 Future Research

We propose the following ideas for future work

- For the cyclostationary noise modeling problem,
  - A parameterized model with a few number of parameters will be useful for system analysis.
  - Machine learning based modeling is a promising approach.
- For the NB-PLC cyclostationary noise mitigation problem,
  - Investigating the erasure decoding with an iterative decoding.
  - Investigating the adaptive FRESH filtering for low complexity design.
  - Investigating the sparse FRESH filtering for low complexity design.
  - Investigating other transmitter based precoding techniques to mitigate the cyclostationary noise.
- For the hybrid PLC-wireless system,
  - Examining the performance of the proposed techniques under more realistic channel and noise models.
  - Exploring practical scenarios including the required changes for PLC and wireless standards.

  - Exploring the challenges in the serially connected PLC-wireless system, for relaying as an example.

- For the MIMO-OFDM in the UG MV PLC problem,

  - It will be interesting to investigate additional data rate gains that can be achieved using OFDM with index modulation (Basar et al., 2013; Wen et al., 2017) and spatial modulation (Li et al., 2017) techniques for MIMO-OFDM NB-PLC systems.

APPENDIX

PRELIMINARIES

Cyclostationary Signals

Consider a real-valued discrete-time process $\{x(n), n \in \mathbb{Z}\}$. If both the expected value $\mathbb{E}\{x(n)\}$ and the auto-correlation function $r_{xx}(n+l, l) = \mathbb{E}\{x(n+\ell)x(n)\} = r_{xx}(n; l)$, $l \in \mathbb{Z}$ of $x(n)$ are periodic with some integer period P such that $\mathbb{E}\{x(n)\} = \mathbb{E}\{x(n+P)\}$ and $r_{xx}(n;\ell) = r_{xx}(n+P;\ell)$, the process $x(n)$ is said to be a wide-sense second-order cyclostationary process (referred to henceforth as cyclostationary) (Gardner et al., 2006). Since $r_{xx}(n;\ell)$ is periodic in n for each $l \in \mathbb{Z}$, it has a Fourier series expansion whose coefficients are referred to as the cyclic auto-correlation function. Hence, the Fourier series pair is given by

$$r_{xx}(n;l) = \mathbb{E}\{x(n+\ell)x(n)\} \sim \sum_{\alpha \in \mathcal{A}_{xx}} r_{xx}^{\alpha}(l) e^{j2\pi\alpha n}, \tag{A.1a}$$

$$r_{xx}^{\alpha}(l) = \frac{1}{P} \sum_{n=0}^{P-1} r_{xx}(n;l) e^{-j2\pi\alpha n}, \tag{A.1b}$$

where $\alpha \in \mathcal{A}_{xx} = \{0, 1/P, \ldots, (P-1)/P\}$, are the cyclic frequencies and the symbol $\sim$ is used in (A.1a) since the Fourier series does not converge in general to the given function.

Furthermore, a more general class of cyclostationary processes is obtained if the auto-correlation function $r_{xx}(n;\ell)$ is almost periodic in n for each $l \in \mathbb{Z}$, which is referred to as an *almost cyclostationary (ACS)* process. A function is said to be almost periodic if it can be approximated by a uniformly convergent trigonometric polynomial where the approximation error is bounded for a certain number of approximation terms and does not depend on the function's argument (Corduneanu, 1989). Almost periodic functions occur frequently as a result of sampling a continuous-time periodic function and the functional dependence on two or more purely periodic functions with incommensurate continuous-time periodicities, which is the case of interest in this dissertation. For a more general and rigorous definition of almost periodic functions, please refer to (Corduneanu, 1989). The auto-correlation function $r_{xx}(n;\ell)$, being an almost periodic function, can be expressed in terms of its generalized Fourier series coefficients as follows

$$r_{xx}(n;l) = \mathbb{E}\{x(n+\ell)x(n)\} \sim \sum_{\alpha \in \mathcal{A}_{xx}} r_{xx}^{\alpha}(l)e^{j2\pi\alpha n}, \tag{A.2a}$$

$$r_{xx}^{\alpha}(l) = \lim_{P\to\infty} \frac{1}{P}\sum_{n=0}^{P-1} r_{xx}(n;l)e^{-j2\pi\alpha n}, \tag{A.2b}$$

where $\mathcal{A}_{xx} = \{\alpha \in \mathbb{R} : r_{xx}^{\alpha}(l) \neq 0\}$ is a countable set and the limit in (A.2b) is proven to exist if $r_{xx}(n;l)$ is an almost periodic function (Corduneanu, 1989, Theorem. 1.12). In the case when $r_{xx}(n;l)$ has more than one periodicity, α ranges over all integer multiples of all fundamental frequencies of interest, for example $1/P_1$, $1/P_2, \cdots$.

Let $x(n)$ and $y(n)$, $n \in \mathbb{Z}$ be two real-valued discrete-time ACS processes with a second-order cross-correlation function

$$r_{xy}(n;l) = \mathbb{E}\{x(n+\ell)y(n)\} \sim \sum_{\alpha \in \mathcal{A}_{xy}} r_{xy}^{\alpha}(l)e^{j2\pi\alpha n}, \tag{A.3a}$$

$$r_{xy}^{\alpha}(l) = \lim_{P\to\infty} \frac{1}{P}\sum_{n=0}^{P-1} r_{xy}(n;l)e^{-j2\pi\alpha n}, \tag{A.3b}$$

where $\mathcal{A}_{xy} = \{\alpha \in \mathbb{R} : r_{xy}^{\alpha}(l) \neq 0\}$ is a countable set. If the set $\mathcal{A}_{xy}$ contains at least one nonzero element, then $x(n)$ and $y(n)$ are said to be jointly ACS.

Two main representations are commonly used to analyze the cyclostationary signals as described in (Gardner, 1986) and (Giannakis, 1998): Decimated Components and Subband Components. In the Decimated Components representation, the cyclostationary process $x[n]$ with a period P is represented as P different stationary processes $x_i[n] = x[nP+i]$, $i = 0, \ldots, P-1$. In other words, for each time sample, we have a different stationary process. Auto- and cross-correlations for the $x_i[n]$ processes can be computed through the cyclic auto-correlation function of $x[n]$. In the Subband Components representation, the cyclostationary process $x[n]$ with a period P is represented as a superposition of P stationary NB subprocesses, where $x[n] = \sum_{m=0}^{P-1} \bar{x}_m[n]\, \mathrm{e}^{-j2\pi mn/P}$. Similarly, the auto- and cross-correlation functions for $\bar{x}_m[n]$ can be computed from the cyclic auto-correlation function of $x[n]$.

Estimation of Cyclostationary Correlation Functions

The cyclostationary correlation functions defined in (A.1b), (A.2b), and (A.3b) involve ideal ensemble averages which require reliable estimation. In practice, for stationary processes, the time-averaged correlation converges to the ensemble-averaged result if the averaging length is long enough. For cyclostationary processes, the time-variant correlations are expressed in terms of a set of time-invariant cyclic correlations. Each time-invariant cyclic correlation can be viewed as a valid correlation function for a stationary process (Giannakis, 1998). Hence, the cyclic correlations and, accordingly, the time-variant ACS correlations can be estimated using the formulas

$$r_{xx}^{\alpha}(l) = \frac{1}{N}\sum_{n=0}^{N-1} x(n+\ell)x(n)e^{-j2\pi\alpha n}, \tag{A.4a}$$

$$r_{xx}(n;l) \sim \sum_{\alpha\in\mathcal{A}_{xx}} r_{xx}^{\alpha}(l)e^{j2\pi\alpha n}. \tag{A.4b}$$

Frequency-Shift (FRESH) Filtering

The cyclostationary counterpart of linear time-invariant (LTI) filtering is the FRESH filtering. For example, linear periodic time variant (LPTV) filtering can be equivalently implemented in the form of FRESH filtering(Gardner, 1993) as we describe next. Let $h[n,m]$ denote the impulse response of an LPTV filter. The output signal $y[n]$ corresponding to input $x[n]$ is given by

$$y[n] = \sum_{m=-\infty}^{\infty} g[n,m]x[m]. \tag{A.5}$$

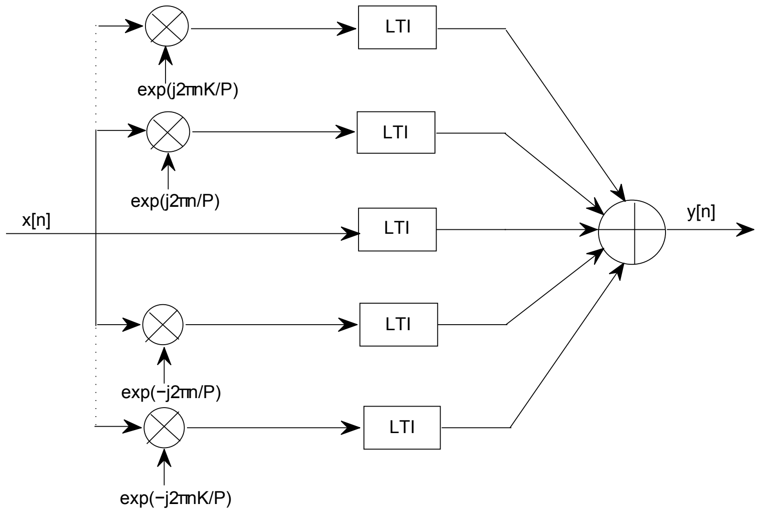

Figure A.1: FRESH filtering block diagram.

The impulse response $g[n,m]$ is defined as $g[n,m] = \sum_{k=0}^{P-1} g^{\alpha_k}[n-m]\mathrm{e}^{j2\pi\alpha_k m}$, where P is the cyclic period of the LPTV filter $g[n,m]$, $g^{\alpha_k}[n-m]$ is the k-th Fourier series coefficient of $h[n,m]$, and $\alpha_k = \frac{k}{P}$ is the k-th cyclic frequency. The relationship between the input $x[n]$ and the output $y[n]$ of the LPTV filter can therefore be written as

$$y[n] = \sum_{k=0}^{P-1} \sum_{m=-\infty}^{\infty} g^{\alpha_k}[n-m]x_k[m] \tag{A.6}$$

where $x_k[n] = x[n]\mathrm{e}^{j2\pi\alpha_k n}$. We observe from (A.6) that the LPTV system performs LTI filtering of frequency-shifted versions of $x[n]$. Therefore, the FRESH filters can be modeled as an LTI filter-bank applied to the frequency-shifted versions of the input signal (Ojeda and Grajal, 2011). Fig. A.1 shows a block diagram of FRESH filtering.

Cyclostationarity of the OFDM Signal

Due to the presence of a cyclic prefix, the transmitted OFDM signal is a cyclostationary random process with auto-correlation function derived in (Heath and Giannakis, 1999) to be given by

$$r_{xx}(nN_B + p; l) = \sigma_s^2 N_{SC}\Bigg[\delta(l) + \delta(l - N_{SC})$$

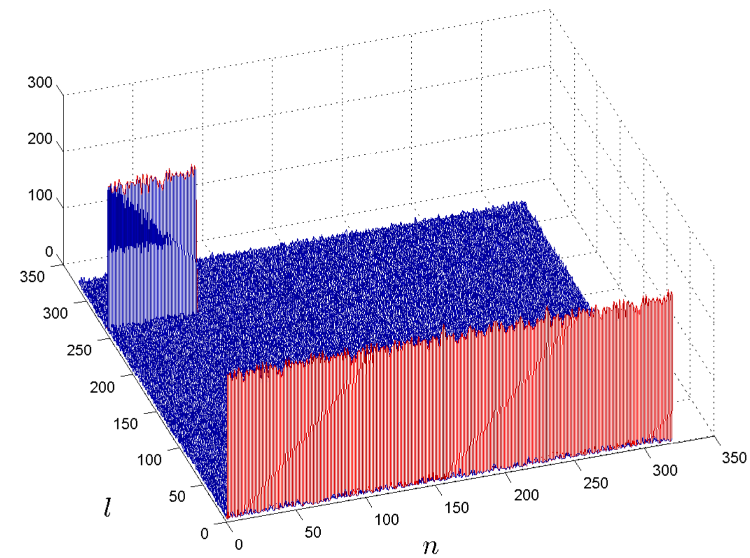

(a) General OFDM auto-correlation function.

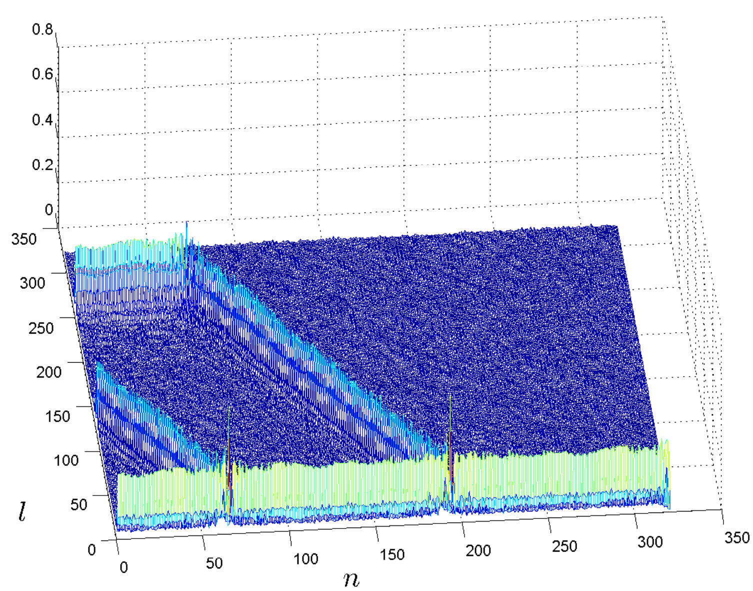

(b) Symmetric OFDM auto-correlation function.

Figure A.2: OFDM auto-correlation function with $N_{SC} = 256$ and $N_{CP} = 64$

$$\times \sum_{r=0}^{N_B-N_{SC}-1} \delta(p-r) + \delta(l+N_{SC})$$
$$\times \sum_{r=N_{SC}}^{N_B-1} \delta(p-r) \Bigg] \tag{A.7}$$

Since the auto-correlation is a function of p and not of n, the OFDM signal is a cyclostationary random process with a period of N_B.The cyclic auto-correlation function for a generic OFDM signal is shown in Fig. A.2a. However, in our case of NB-PLC baseband transmission and binary phase shift keying (BPSK) modulation, the data is real and symmetric in the frequency domain which also leads to a symmetry in the time domain. This symmetry affects the cyclic auto-correlation function of the OFDM signal as shown in Fig. A.2b.

REFERENCES

Ametani, A. (1980, May). A general formulation of impedance and admittance of cables. *IEEE Transactions on Power Apparatus and Systems PAS-99*(3), 902–910.

Anatory, J., N. Theethayi, and R. Thottappillil (2009, Oct). Performance of underground cables that use OFDM systems for broadband power-line communications. *IEEE Transactions on Power Delivery 24*(4), 1889–1897.

Ancillotti, E., R. Bruno, and M. Conti (2013). The role of communication systems in Smart Grids: Architectures, technical solutions and research challenges. *Computer Communications 36*(17), 1665–1697.

Banwell, T. and S. Galli (2005). A novel approach to the modeling of the indoor power line channel part i: circuit analysis and companion model. *IEEE Transactions on power delivery 20*(2), 655–663.

Basar, E., U. Aygolu, E. Panayirci, and H. V. Poor (2013, Nov). Orthogonal frequency division multiplexing with index modulation. *IEEE Transactions on Signal Processing 61*(22), 5536–5549.

Berger, L. T., A. Schwager, P. Pagani, and D. Schneider (2014). *MIMO power line communications: narrow and broadband standards, EMC, and advanced processing.* CRC Press.

Bert, L. D., P. Caldera, D. Schwingshackl, and A. M. Tonello (2011, April). On noise modeling for power line communications. In *2011 IEEE International Symposium on Power Line Communications and Its Applications*, pp. 283–288.

Blackard, K. L., T. S. Rappaport, and C. W. Bostian (1993, Sep.). Measurements and models of radio frequency impulsive noise for indoor wireless communications. *IEEE Journal on Selected Areas in Communications 11*(7), 991–1001.

Caire, G., T. Al-Naffouri, and A. Narayanan (2008a, July). Impulse Noise Cancellation in OFDM: An Application of Compressed Sensing. In *Proc. IEEE Intl. Symp. Information Theory (ISIT)*, pp. 1293–1297.

Caire, G., T. Y. Al-Naffouri, and A. K. Narayanan (2008b). Impulse noise cancellation in OFDM: an application of compressed sensing. In *Proc. 2008 IEEE International Symposium on Information Theory (ISIT)*, pp. 1293–1297.

Candes, E., J. Romberg, and T. Tao (2006, Mar). Stable Signal Recovery from Incomplete and Inaccurate Measurements. *Comm. Pure App. Math. 59*(9), 1207–1223.

Cataliotti, A., A. Daidone, and G. Tine (2008, Oct). Power line communication in medium voltage systems: Characterization of MV cables. *IEEE Transactions on Power Delivery 23*(4), 1896–1902.

Cendrillon, R., G. Ginis, E. V. den Bogaert, and M. Moonen (2007, May). A near-optimal linear crosstalk precoder for downstream VDSL. *IEEE Transactions on Communications 55*(5), 860–863.

CENELEC EN 50065-1 (2011). Signalling on low-voltage electrical installations in the frequency range 3 kHz to 148,5 kHz - Part 1: General requirements, frequency bands and electromagnetic disturbances.

Cevher, V., P. Indyk, C. Hegde, and R. G. Baraniuk (2009, May). Recovery of Clustered Sparse Signals from Compressive Measurements . In *Proc. Int. Conf. Sampling Theory Applicat. (SAMPTA)*.

Chan, M. H. L. and R. W. Donaldson (1989, Aug). Amplitude, width, and interarrival distributions for noise impulses on intrabuilding power line communication networks. *IEEE Transactions on Electromagnetic Compatibility 31*(3), 320–323.

Chrysochos, A. I., T. A. Papadopoulos, A. ElSamadouny, G. K. Papagiannis, and N. Al-Dhahir (2016a). Optimized MIMO-OFDM design for narrowband-PLC applications in medium-voltage smart distribution grids. *Electric Power Systems Research 140*, 253–262.

Chrysochos, A. I., T. A. Papadopoulos, A. ElSamadouny, G. K. Papagiannis, and N. Al-Dhahir (2016b). Optimized MIMO-OFDM design for narrowband-PLC applications in medium-voltage smart distribution grids. *Electric Power Systems Research 140*, 253 – 262.

Chrysochos, A. I., T. A. Papadopoulos, G. K. Papagiannis, A. ElSamadouny, and N. Al-Dhahir (2015, Nov). MIMO-OFDM narrowband-PLC transmission through distribution transformers: Modeling and achievable data rates. In *IEEE International Conference on Smart Grid Communications (SmartGridComm)*, pp. 109–114.

Cioffi, J. *A multicarrier primer, Amati Communications Corporation and Stanford University, USA*.

Cioffi, J. *Multi-channel Modulation, Stanford University, USA*.

Corduneanu, C. (1989). *Almost periodic functions*. Chelsea Pub Co.

Cover, T. and J. Thomas (1991). *Elements of information theory*. Wiley.

Diggavi, S. N., N. Al-Dhahir, A. Stamoulis, and A. R. Calderbank (2004, Feb). Great expectations: the value of spatial diversity in wireless networks. *Proceedings of the IEEE 92*(2), 219–270.

Eldar, Y., P. Kuppinger, and H. Bolcskei (2010, June). Block-Sparse Signals: Uncertainty Relations and Efficient Recovery. *IEEE Transactions on Signal Processing 58*(6), 3042–3054.

Elgenedy, M., M. M. Awadin, R. Hamila, W. U. Bajwa, A. S. Ibrahim, and N. Al-Dhahir (2018). Sparsity-based joint nbi and impulse noise mitigation in hybrid plc-wireless transmissions. *IEEE Access 6*, 30280–30295.

Elgenedy, M., T. Papadopoulos, S. Galli, A. Chrysochos, G. Papagiannis, and N. Al-Dhahir (2019). MIMO-OFDM NB-PLC designs in underground medium-voltage networks. *IEEE Systems Journal 6*, 30280–30295.

Elgenedy, M., M. Sayed, and N. Al-Dhahir (2016, Dec). A frequency-shift-filtering approach to cyclostationary noise modeling in mimo nb-plc. In *2016 IEEE Global Conference on Signal and Information Processing (GlobalSIP)*, pp. 881–885.

Elgenedy, M., M. Sayed, N. Al-Dhahir, and R. C. Chabaan (2018a). Cyclostationary noise mitigation for simo powerline communications. *IEEE Access 6*, 5460–5484.

Elgenedy, M., M. Sayed, N. Al-Dhahir, and R. C. Chabaan (2018b, May). Temporal-region-based cyclostationary noise mitigation for simo powerline communications. In *2018 IEEE International Conference on Communications (ICC)*, pp. 1–6.

Elgenedy, M., M. Sayed, A. El Shafie, I. H. Kim, and N. Al-Dhahir (2016, Dec.). Cyclostationary Noise Modeling Based on Frequency-Shift Filtering in NB-PLC. In *Proc. IEEE Globecom*, Washington, DC, pp. 1–6.

Elgenedy, M., M. Sayed, M. Mokhtar, M. Abdallah, and N. Al-Dhahir (2015, Nov.). Interference mitigation techniques for narrowband powerline smart grid communications. In *Proc. IEEE SmartGridComm*, Miami, FL, pp. 368–373.

Ferreira, H., L. Lampe, J. Newbury, and T. Swart (2010). *Power Line Communications: Theory and Applications for Narrowband and Broadband Communications over Power Lines*. John Wiley & Sons.

Ferreira, H. C., T. G. Swart, J. Newbury, and L. Lampe (2010). Power line communications: theory and applications for narrowband and broadband communications over power lines.

Galli, S. (2011a, May). A Novel Approach to the Statistical Modeling of Wireline Channels. *IEEE Trans. Commun.*, 1332–1345.

Galli, S. (2011b). A novel approach to the statistical modeling of wireline channels. *IEEE Transactions on Communications 59*(5), 1332–1345.

Galli, S. and T. Banwell (2005). A novel approach to the modeling of the indoor power line channel-part ii: transfer function and its properties. *IEEE Transactions on Power Delivery 20*(3), 1869–1878.

Galli, S., H. Koga, and N. Kodama (2008, April). Advanced signal processing for PLCs: Wavelet-OFDM. In *2008 IEEE International Symposium on Power Line Communications and Its Applications*, pp. 187–192.

Galli, S., A. Scaglione, and Z. Wang (2011). For the grid and through the grid: The role of power line communications in the smart grid. *Proceedings of the IEEE 99*(6), 998–1027.

Gardner, W. A. (1986). Introduction to random processes: with applications to signals and systems.

Gardner, W. A. (1993). Cyclic Wiener filtering: theory and method. *IEEE Transactions on Communications 41*(1), 151–163.

Gardner, W. A., A. Napolitano, and L. Paura (2006). Cyclostationarity: Half a century of research. *Signal processing 86*(4), 639–697.

Giannakis, G. B. (1998). Cyclostationary signal analysis. *Digital Signal Processing Handbook*, 17–1.

Ginis, G. and J. M. Cioffi (2002, Jun). Vectored transmission for digital subscriber line systems. *IEEE Journal on Selected Areas in Communications 20*(5), 1085–1104.

Gomaa, A. and N. Al-Dhahir (2011, June). A Sparsity-Aware Approach for NBI Estimation in MIMO-OFDM. *IEEE Trans. Wireless Comm.*, 1854–1862.

Gungor, V. C., D. Sahin, T. Kocak, S. Ergut, C. Buccella, C. Cecati, and G. P. Hancke (2011). Smart grid technologies: communication technologies and standards. *IEEE Transactions on Industrial informatics 7*(4), 529–539.

Guzelgoz, S., H. Celebi, and H. Arslan (2010, Aug.). Analysis of a Multi-Channel Receiver: Wireless and PLC Reception. In *Proc. EUSIPCO*, pp. 1106–1110.

Hao, L. and J. Guo (2007, March). A MIMO-OFDM scheme over coupled multi-conductor power-line communication channel. In *IEEE International Symposium on Power Line Communications and Its Applications*, pp. 198–203.

Hashmat, R., P. Pagani, T. Chonavel, and A. Zeddam (2012a, March). Analysis and modeling of background noise for inhome MIMO PLC channels. In *Power Line Communications and Its Applications (ISPLC), 2012 16th IEEE International Symposium on*, pp. 316–321.

Hashmat, R., P. Pagani, T. Chonavel, and A. Zeddam (2012b, Oct). A time-domain model of background noise for in-home MIMO PLC networks. *IEEE Transactions on Power Delivery 27*(4), 2082–2089.

Hashmat, R., P. Pagani, A. Zeddam, and T. Chonavel (2010, March). MIMO communications for inhome PLC networks: Measurements and results up to 100 MHz. In *ISPLC2010*, pp. 120–124.

Heath, R. W. and G. B. Giannakis (1999, Mar). Exploiting input cyclostationarity for blind channel identification in OFDM systems. *IEEE Transactions on Signal Processing 47*(3), 848–856.

IEC CISPR 16-1-2 (2014). Specification for radio disturbance and immunity measuring apparatus and methods - Part 1-2: Radio disturbance and immunity measuring apparatus - Coupling devices for conducted disturbance measurements.

IEEE 802.11ah (2016). IEEE standard for information technology–telecommunications and information exchange between systems - local and metropolitan area networks–specific requirements - part 11: Wireless lan medium access control (MAC) and physical layer (PHY) specifications amendment 2: Sub 1 GHz license exempt operation.

IEEE 802.15.4g (2012). IEEE standard for local and metropolitan area networks–part 15.4: Low-rate wireless personal area networks (LR-WPANs) amendment 3: Physical layer (phy) specifications for low-data-rate, wireless, smart metering utility networks.

IEEE P1901.2 (2013). Ieee Standard for Low Frequency (less than 500 kHz) Narrow Band Power Line Communications for Smart Grid Applications.

IEEE P1901TM/D3.00 (2010). Broadband over power lines PHY/MAC working group of the IEEE Communications Society - Draft standard for broadband over power line networks: Medium access control and physical layer specifications.

ITU-T G.9901 (2017). Recommendation for Narrowband orthogonal frequency division multiplexing power line communication transceivers for G3-PLC networks - power spectral density specification.

ITU-T G.9902 (2012). Recommendation for Narrowband orthogonal frequency division multiplexing power line communication transceivers for ITU-T G.hnem networks.

ITU-T G.9903 (2017). Recommendation for Narrowband orthogonal frequency division multiplexing power line communication transceivers for G3-PLC networks.

ITU-T G.9904 (2012). Recommendation for Narrowband orthogonal frequency division multiplexing power line communication transceivers for PRIME networks.

ITU-T G.9963 (2015). Recommendation for Unified high-speed wireline-based home networking transceivers - Multiple input/multiple output specification.

Katayama, M., T. Yamazato, and H. Okada (2006). A mathematical model of noise in narrowband power line communication systems. *IEEE Journal on Selected Areas in Communications 24*(7), 1267–1276.

Kay, S. M. (1993). *Fundamentals Of Statistical Signal Processing: Estimation Theory*. Prentice Hall.

Kim, I. H., B. Varadarajan, and A. Dabak (2010). Performance analysis and enhancements of narrowband OFDM powerline communication systems. In *Proc. IEEE SmartGridComm*, pp. 362–367.

Lai, S. and G. Messier (2012, Dec). Using the Wireless and PLC Channels for Diversity. *IEEE Trans. Commun.*, 3865–3875.

Lai, S. W., N. Shabehpour, G. G. Messier, and L. Lampe (2014, Dec). Performance of Wireless/Power Line Media Diversity in the Office Environment. In *Proc. IEEE Global Communications Conference*, pp. 2972–2976.

Lampe, L. (2011a). Bursty impulse noise detection by compressed sensing. In *Proc. 2011 IEEE International Symposium on Power Line Communications and Its Applications (ISPLC)*, pp. 29–34.

Lampe, L. (2011b, April). Bursty Impulse Noise Detection by Compressed Sensing. In *IEEE International Symposium on Power Line Communications and Its Applications (ISPLC), 2011*, pp. 29–34.

Lampe, L. (2016). *Power Line Communications: Principles, Standards and Applications from Multimedia to Smart Grid*. John Wiley & Sons.

Lazaropoulos, A. G. (2013). Broadband over power lines systems convergence: Multiple-input multiple-output communications analysis of overhead and underground low-voltage and medium-voltage BPL networks. *ISRN Power Engineering 2013*(2).

Lee, J. H. and Y. H. Kim (2014, June). Diversity relaying for parallel use of power-line and wireless communication networks. *IEEE Transactions on Power Delivery 29*(3), 1301–1310.

Li, J., M. Wen, X. Cheng, Y. Yan, S. Song, and M. H. Lee (2017, Feb). Generalized precoding-aided quadrature spatial modulation. *IEEE Transactions on Vehicular Technology 66*(2), 1881–1886.

Li, T., W. H. Mow, and M. Siu (2008). Joint erasure marking and Viterbi decoding algorithm for unknown impulsive noise channels. *IEEE Transactions on Wireless Communications 7*(9), 3407–3416.

Lin, J., M. Nassar, and B. L. Evans (2013). Impulsive noise mitigation in powerline communications using sparse Bayesian learning. *IEEE Journal on Selected Areas in Communications 31*(7), 1172–1183.

Lin, J., T. Pande, I. H. Kim, A. Batra, and B. L. Evans (2015). Time-frequency modulation diversity to combat periodic impulsive noise in narrowband powerline communications. *IEEE Transactions on Communications 63*(5), 1837–1849.

Liu, C., K. Chau, D. Wu, and S. Gao (2013). Opportunities and challenges of Vehicle-to-Home, Vehicle-to-Vehicle, and Vehicle-to-Grid technologies. *Proceedings of the IEEE 101*(11), 2409–2427.

Liu, S., F. Yang, W. Ding, J. Song, and Z. Han (2016). Impulsive noise cancellation for MIMO-OFDM PLC systems: A structured compressed sensing perspective. In *IEEE Global Communications Conference (GLOBECOM)*, pp. 1–6.

Lopes, J. A. P., F. J. Soares, and P. M. R. Almeida (2011). Integration of electric vehicles in the electric power system. *Proceedings of the IEEE 99*(1), 168–183.

Ma, Y. H., P. L. So, and E. Gunawan (2005, April). Performance analysis of ofdm systems for broadband power line communications under impulsive noise and multipath effects. *IEEE Transactions on Power Delivery 20*(2), 674–682.

Mahadevan, A., J. Pons, and P. Duvaut (2008). Performance and design of an impulse noise detector for OFDM systems with Reed-Solomon erasure-decoding. In *Proc. IEEE Global Telecommunications Conference (GLOBECOM)*, pp. 1–6.

Meng, H., Y. L. Guan, and S. Chen (2005, April). Modeling and analysis of noise effects on broadband power-line communications. *IEEE Transactions on Power Delivery 20*(2), 630–637.

Mokhtar, M., W. U. Bajwa, M. Elgenedy, and N. Al-Dhahir (2015, Nov.). Exploiting Block Sparsity for Joint Mitigation of Asynchronous NBI and IN in Hybrid Powerline-Wireless Communications. In *Proc. IEEE International Conference on Smart Grid Communications (SmartGridComm)*, pp. 362–367.

Nassar, M., A. Dabak, I. H. Kim, T. Pande, and B. L. Evans (2012, Mar.). Cyclostationary noise modeling in narrowband powerline communication for smart grid applications. In *Proc. IEEE ICASSP*, Kyoto, Japan, pp. 3089–3092.

Nassar, M., K. Gulati, Y. Mortazavi, and B. L. Evans (2011, Dec). Statistical modeling of asynchronous impulsive noise in powerline communication networks. In *2011 IEEE Global Telecommunications Conference - GLOBECOM 2011*, pp. 1–6.

Nassar, M., K. Gulati, A. K. Sujeeth, N. Aghasadeghi, B. L. Evans, and K. R. Tinsley (2008, March). Mitigating near-field interference in laptop embedded wireless transceivers. In *2008 IEEE International Conference on Acoustics, Speech and Signal Processing*, pp. 1405–1408.

Nassar, M., J. Lin, Y. Mortazavi, A. Dabak, I. H. Kim, and B. L. Evans (2012, Sep.). Local utility power line communications in the 3500 khz band: Channel impairments, noise, and standards. *IEEE Signal Processing Magazine 29*(5), 116–127.

Nassar, M., P. Schniter, and B. L. Evans (2013). A factor graph approach to joint OFDM channel estimation and decoding in impulsive noise environments. *arXiv preprint arXiv:1306.1851*.

Needell, D. and J. Tropp (2009, May). CoSaMP: Iteative Signal Recovery from Incomplete and Inaccurate Samples. *Appl. Computat. Harmon. Anal. 26*(3), 301–321.

Ojeda, O. A. Y. and J. Grajal (2011). *Adaptive-FRESH filtering.* INTECH Open Access Publisher.

Oksman, V. and J. Zhang (2011, December). G.HNEM: The New ITU-T Standard on Narrowband PLC Technology. *IEEE Comm. Mag.*, 36–44.

Papadopoulos, T. A., A. I. Chrysochos, A. ElSamadouny, N. Al-Dhahir, and G. K. Papagiannis (2017). MIMO-OFDM narrowband-PLC in distribution systems: Impact of power transformers on achievable data rates. *Electric Power Systems Research 151*, 251–265.

Papadopoulos, T. A., A. I. Chrysochos, and G. K. Papagiannis (2013). Narrowband power line communication: Medium voltage cable modeling and laboratory experimental results. *Electric Power Systems Research 102*, 50 – 60.

Papadopoulos, T. A., C. G. Kaloudas, A. I. Chrysochos, and G. K. Papagiannis (2013, April). Application of narrowband power-line communication in medium-voltage smart distribution grids. *IEEE Transactions on Power Delivery 28*(2), 981–988.

Pati, Y., R. Rezaiifar, and P. Krishnaprasad (1993). Orthogonal Matching Pursuit: Recursive Function Approximation with Applications to Wavelet Decomposition. In *Proc. Asilomar Conf. Sig., Syst. and Comp.*, pp. 40–44.

Perahia, E. and R. Stacey (2013). *Next Generation Wireless LANs.* Cambridge University Press.

Pitt III, G. and L. Swanson (1985). Erasure information for a Reed-Solomon decoder. *TDA Progress Report 42 83*, 39–44.

Pollara, F. (1987). Erasure declaring Viterbi decoders. In *The Telecommunications and Data Acquisition Report.*

Prakash, P. (2013, Sep.). Data concentrators: The core of energy and data management. *http://www.ti.com/lit/wp/spry248/spry248.pdf*.

Proakis, J. G. (2008). *Digital communications* (5th ed. ed.). New York, NY, USA: McGraw-Hill.

Reed, I. S. and G. Solomon (1960). Polynomial codes over certain finite fields. *Journal of the Society for Industrial & Applied Mathematics 8*(2), 300–304.

Saaifan, K. A. and W. Henkel (2017, Nov). Measurements and modeling of impulse noise at the 2.4 ghz wireless LAN band. In *2017 IEEE Global Conference on Signal and Information Processing (GlobalSIP)*, pp. 86–90.

Sacuto, F., F. Labeau, and B. L. Agba (2014, March). Wide band time-correlated model for wireless communications under impulsive noise within power substation. *IEEE Transactions on Wireless Communications 13*(3), 1449–1461.

Sayed, M. and N. Al-Dhahir (2014). Narrowband-PLC/wireless diversity for smart grid communications. In *Proc. IEEE GLOBECOM*, Austin, TX, pp. 2966–2971.

Sayed, M. and N. Al-Dhahir (2016, Dec). Differential modulation diversity combining for hybrid narrowband-powerline/wireless smart grid communications. In *Proc. IEEE Global Conference on Signal and Information Processing (GlobalSIP)*, pp. 876–880.

Sayed, M., I.-H. Kim, T. Pande, A. Batra, and N. Al-Dhahir (2015). Proposed frame and preamble structure for MIMO narrowband power line communications. In *Proc. IEEE ISPLC*, Austin, TX, pp. 65–70.

Sayed, M., G. Sebaali, B. L. Evans, and N. Al-Dhahir (2015, Nov). Efficient diversity technique for hybrid narrowband-powerline/wireless smart grid communications. In *2015 IEEE International Conference on Smart Grid Communications (SmartGridComm)*, pp. 1–6.

Sayed, M., A. E. Shafie, M. Elgenedy, R. C. Chabaan, and N. Al-Dhahir (2017, June). Enhancing the reliability of two-way vehicle-to-grid communications. In *2017 IEEE Intelligent Vehicles Symposium (IV)*, pp. 1922–1927.

Sayed, M., T. A. Tsiftsis, and N. Al-Dhahir (2017, July). On the diversity of hybrid narrowband-plc/wireless communications for smart grids. *IEEE Transactions on Wireless Communications 16*(7), 4344–4360.

Schwager, A., D. Schneider, W. Baschlin, A. Dilly, and J. Speidel (2011, April). MIMO PLC: Theory, measurements and system setup. In *IEEE International Symposium on Power Line Communications and Its Applications*, pp. 48–53.

Sebaali, G. and B. L. Evans (2015, March). Design tradeoffs in joint powerline and wireless transmission for smart grid communications. In *Proc. IEEE International Symposium on Power Line Communications and Its Applications (ISPLC)*, pp. 83–88.

Shlezinger, N. and R. Dabora (2014). Frequency-shift filtering for OFDM signal recovery in narrowband power line communications. *IEEE Transactions on Communications 62*(4), 1283–1295.

Tian, J., H. Guo, H. Hu, and H. H. Chen (2011). Frequency-shift filtering for OFDM systems and its performance analysis. *IEEE Systems Journal 5*(3), 314–320.

Toumpakaris, D., J. M. Cioffi, and D. Gardan (2004). Reduced-delay protection of DSL systems against nonstationary disturbances. *IEEE Transactions on Communications 52*(11), 1927–1938.

Tse, D. and P. Viswanath (2005). *Fundamentals of wireless communication.* Cambridge university press.

Viterbi, A. (1982). A robust ratio-threshold technique to mitigate tone and partial band jamming in coded MFSK systems. *1*, 22–4.

Wen, M., E. Basar, Q. Li, B. Zheng, and M. Zhang (2017, Sept). Multiple-mode orthogonal frequency division multiplexing with index modulation. *IEEE Transactions on Communications 65*(9), 3892–3906.

Zimmermann, M. and K. Dostert (2002). A multipath model for the powerline channel. *IEEE Transactions on Communications 50*(4), 553–559.

BIOGRAPHICAL SKETCH

Mahmoud Elgenedy received his BSc and MSc degrees in electrical engineering in 2005 and 2010, respectively, from Cairo University, Cairo, Egypt. He is currently working toward his PhD degree in electrical engineering from The University of Texas at Dallas, Richardson, TX, USA. From 2005 to 2007, he worked on the design of Bluetooth V2+EDR chip at SySDSoft, Cairo, Egypt. From 2008 to 2010, he worked on developing military communications standards at MTSE, Cairo, Egypt. From 2010 to 2014, he worked on the development of the LTE-UE, DVB-T2, DVB-C, and ZigBee at Wasiela, Cairo, Egypt. During his PhD studies, he joined Broadcom Corp., Qualcomm Corp., and TI Kilby labs as Intern Engineer where he participated in the design and implementation of the DOCSIS 3.1, C-V2X (LTE UE R14,15), and SERDES, respectively.

CURRICULUM VITAE

Mahmoud Elgenedy

Personal Data

Date of Birth: 11 March 1984
Email: melgenedy@gmail.com, mahmoud.elgenedy@utdallas.edu

Summary

Through my professional work for more than thirteen years in industrial research and development in the area of signal processing and digital communication, I gained a significant practical experience in hardware oriented algorithm design from theory to implementation. Specifically, I have more than **9+ years of industry experience** in startup companies in Egypt in the area of PHY layer design and implementation. During this period, I participated in the system design and fixed point implementation of the PHY Layer of various digital communications standards including Cellular (LTE UE R8,9), Digital Video Broadcasting (DVB-T2, DVB-C), WLAN (IEEE 802.11a), PAN (Bluetooth V2+EDR, Zigbee IEEE802.15), Military (HF Mil-Std-110B, TADIL-A). Moreover, I participated in the development of machine learning algorithms for different image and speech processing applications. During my PhD, I had three internships in **Broadcom, Qualcomm, and TI Kilby labs** where I participated in the design and implementation of the DOCSIS 3.1, C-V2X (LTE UE R14,15), and SERDES, repectively. My PhD research is in the area of impulsive noise and interference mitigation in powerline communications (IEEE 1901.1 and 1901.2 standards). I received the B.Sc. and M.Sc. degrees in electrical engineering from Cairo University, Egypt, in 2005 and 2010, respectively. I am currently in my fifth year toward pursuing the Ph.D. degree in electrical engineering with The University of Texas at Dallas, Richardson, TX, USA.
Objective: seeking a challenging opportunity as a system design engineer in a creative environment to help innovating, contributing, and creating the future.

Key Skills

- Ability to develop mathematical models and applying signal processing techniques to simulate physical problems.
- Solid background in digital communications, basic mathematical and signal processing tools including fundamentals (linear algebra, probability theory, stochastic processes), signals and systems, signal estimation and detection, machine learning, compressed sensing.
- Fixed point analysis and implementation for the signal processing algorithms considering different target hardware platforms including for example ASIC and DSP implementation.

- Software programing and implementation tools: algorithms simulation (C/C++, MATLAB), embedded implementation for algorithms (C/C++ and assembly for DSP scalar/vector processors), scripting (Linux shell, python, Perl), machine learning (Tensorflow, MATLAB), project management tools (Microsoft project, JIRA project tracking), source control (SVN, CVS).

- Entrepreneurship: helped 4 startup companies in Egypt in different areas, co-founded one startup company, initiated business plan competition in Cairo University, and participated in many events related to entrepreneurship in Egypt and US.

- Leadership and management skills: managed a team of 10-15 systems engineers working in 2-3 different projects for four years to develop PHY-layer standards. Leading responsibilities include planning, breakdown, assign, follow up and review for all tasks.

- Teaching skills: I used to work as a teaching assistant in UT DALLAS for more than 4 years. I helped as a TA in the following courses: signals and systems, communications systems, linear algebra, probability theory, detection and estimation, advanced mathematics, digital design lab, signal processing lab.

Industrial Work Experience

Kilby Labs, Texas Instruments, Inc., Dallas, Texas www.ti.com
Communication System Design Engineer, Internship ***May 2018-August 2018*** Research and development for the equalization and synchronization of the Serializer/Deserializer **(SerDes)**

- System design for the single carrier decision feedback equalizer (investigated MMSE adaptive LMS versus non-adaptive designs).

- System design for the phase frequency detector and time tracking circuits (including the development of a digital PLL and convergence verification).

- Fixed point and design simplification to meet the strict implementation requirements (novel structures for the equalizer to be patented).

Qualcomm Technologies, Inc., Boxborough, Massachusetts www.qualcomm.com
Firmware Design Engineer, Internship ***May 2017-August 2017***
Developing Firmware routines for the Cellular Vehicle to Everything **(C-V2X)**

- Floating and fixed point design for the LTE Sidelink receiver (R14, 15 new modifications) using Octave and C.

- Firmware implementation for the developed fixed point algorithms on the Hexagon vector processor (Q6 SILVER).

- Verification for the developed Firmware routines vs Octave/C.

Broadcom, Irvine, California www.broadcom.com
Communication System Design Engineer, Internship ***May 2015-August 2015***
Development and testing for the new standardized (Gigabit) Data Over Cable Service Interface modem **(DOCSIS 3.1)**

- Study the coexistence for the new OFDM based DOCSIS 3.1 system with the legacy single carrier system (Exclusion bands effect).
- Performance evaluation for the phase noise estimation/compensation and time/frequency tracking loops within the overall system.
- Worked on the C++ integrated model (Floating and fixed).
- Developed Python scripts for performance evaluation and verification.

Varkon Semiconductors, Cairo, Egypt www.wasiela.com/
System Design Team Leader ***May 2010-July 2014***
Leading responsibilities include breakdown, assign, follow up and review for all tasks. Participated specifically in the following:

1. **LTE (Rel-8) UE PHY-Layer Floating and Fixed Point Design (2.5-years)**
   - Downlink Cell Search (PSS, SSS and CP type detection) and initial acquisition (time and frequency synchronization). (Novel contributions)
   - Downlink receiver channel estimation. (Novel contributions)
   - Downlink receiver sampling/carrier frequency tracking. (Novel contributions)
   - DC offset estimation/cancellation. (Jointly studied with the carrier frequency offset)
   - UE Link Adaptation Measurements (CQI, Noise variance estimation).
   - UE Handover Measurements. (Novel contributions)
   - Uplink physical channels transmitter fixed point. (PUSCH, PUCCH and PRACH)
   - Fixed point design for DFT/FFT/IFFT with dynamic scaling. (Novel contributions)
   - Design for the Multistage Upsampling/Dowbsampling and ACI filters.
   - Helped in the verification on (Agilent PXB/SystemVue) and (Anritsu 8430).
2. **DVB-T2 PHY-Layer Floating and Fixed Point Design (1-year)**
   - P1 detection algorithm (Symbol and frame synchronization).
   - Frequency offset initial acquisition and tracking.
   - Sampling frequency error estimation and tracking.
   - Verification with third party testers. (Verification/Validation from ETSI).
3. **ZigBee IEEE 802.15.4 OQPSK PHY-Layer Floating and Fixed Point Design (3-months)**
   - Investigation for the Coherent VS Non-Coherent receiver design.
   - Basic Coherent receiver design and implementation.
   - Preamble detection, Initial timing, frequency offset estimation and time tracking.
4. **DVB-C PHY-Layer Floating and Fixed Point Design (6-months)**

- Blind symbol rate estimation SRE floating and fixed point. (Novel algorithm)
- Multi-rate filter design. (accepting input variable rate and convert it to a fixed rate)
- System integration with the SRE and verification with third party tester.

Modern Technology MTSE, Cairo, Egypt www.mtse.com.eg
System Design Engineer ***May 2007 April 2010***

1. **HF MIL-STD-188-110B App.C Floating Point Design (2-years)**
   - Single carrier equalization symbol/fractional spaced (MMSE-DFE, Kalman-DFE, SC-Frequency domain equalization, Least square channel estimation, Iterative and turbo structures).
   - Error correction coding/decoding (Tail-biting Viterbi decoder).
2. **IEEE 802.11a WLAN PHY layer Floating/Fixed Point Design and DSP implementation (6 months)**
   - Initial acquisition and time/frequency tracking.
   - Implementation of the fixed point on TMS320C6416T.
3. Basic simulation for the TADIL-A (Multi-tone MIL-STD).
4. Participated in the design of channel sensing for VUHF radios on TMS320C6416T (Spectrum analysis and nonlinearity test).
5. Automatic Electricity-Meter reading recognition using machine learning techniques

The Engineering Company for Development RDI, Cairo, Egypt www.rdi-eg.com
Speech researcher engineer (4 months) ***September 2007 - December 2007***
Development of machine learning techniques (based on Hidden Markov Models (HMM)) to image and speech processing applications. In particular, I applied the HMM techniques (using HTK-tool) to the following applications,

- "Hafss product" Enhancements (Software to afford an effective assistance in the self learning of spoken Arabic language and learn Tajweed of the glorious Quran).
- Arabic optical character recognition (AOCR).

SySDSoft (Acquired by Intel Mobile Communications), Cairo, Egypt
System Design Engineer ***October 2005 - April 2007***

1. **Bluetooth version 2+EDR Floating and Fixed Point Design**
   - Basic Tx-Rx for GFSK and DPSK fixed point design (two different designs for different customers).
   - Blind frequency offset estimation for the GFSK. (Novel algorithm)
   - Early-late gate for sampling clock error estimation and correction.
2. Worked on the WUSB MAC layer (test plans design and test execution).

Publications

1. M. Elgenedy, M. Sayed, N. Al-Dhahir and R. C. Chabaan, "Cyclostationary Noise Mitigation for SIMO Powerline Communications," in IEEE Access, vol. 6, pp. 5460-5484, 2018.
2. M. Elgenedy, M. M. Awadin, R. Hamila, W. U. Bajwa, A. S. Ibrahim and N. Al-Dhahir, "Sparsity-Based Joint NBI and Impulse Noise Mitigation in Hybrid PLC-Wireless Transmissions," in IEEE Access, vol. 6, pp. 30280-30295, 2018.
3. M. Elgenedy, T. A. Papadopoulos, S. Galli, A. I. Chrysochos, G. K. Papagiannis, N. Al-Dhahir, "MIMO-OFDM NB-PLC Designs in Underground Medium-Voltage Networks," submitted to IEEE Systems journal.
4. J. Sung, M. Sayed, M. Elgenedy, B. L. Evans, N. Al-Dhahir, I. H. Kim, K. Waheed, "Hybrid Powerline/Wireless Diversity for Smart Grid Communications: Design Challenges and Real-time Implementation," to be submitted to IEEE Communications Magazine.
5. S. Moaveninejad, A. Kumar, M. Elgenedy, M. Magarini, N. Al-Dhahir, and A. M. Tonello, Gaussian-Middleton Classification of Cyclostationary Correlated Noise in Hybrid MIMO-OFDM WiNPLC, in Proc. of IEEE International Conference on Communications (ICC 2019).
6. M. Elgenedy, M. Sayed, N. Al-Dhahir and R. C. Chabaan, "Temporal-Region-Based Cyclostationary Noise Mitigation for SIMO Powerline Communications," 2018 IEEE International Conference on Communications (ICC), Kansas City, MO, USA, 2018, pp. 1-6.
7. M. Elgenedy, M. Sayed, A. El Shafie, I. H. Kim and N. Al-Dhahir, "Cyclostationary Noise Modeling Based on Frequency-Shift Filtering in NB-PLC," 2016 IEEE Global Communications Conference (GLOBECOM), Washington, DC, 2016, pp. 1-6.
8. M. Elgenedy, M. Sayed and N. Al-Dhahir, "A frequency-shift-filtering approach to cyclostationary noise modeling in MIMO NB-PLC," 2016 IEEE Global Conference on Signal and Information Processing (GlobalSIP), Washington DC, DC, USA, 2016, pp. 881-885.
9. M. Sayed, A. El Shafie, M. Elgenedy, R. Chabaan, N. Al-Dhahir, "Enhancing the Reliability of Two-Way Vehicle-To-Grid Communications," 2017 IEEE Intelligent Vehicles Symposium, Crown Plaza, Redondo Beach, CA, USA.
10. M. Elgenedy, M. Sayed, M. Mokhtar, M. Abdallah and N. Al-Dhahir, "Interference Mitigation Techniques for Narrowband Powerline Smart Grid Communications," *in Proc. of IEEE SmartGridComm,* Miami, Florida, November 2015.
11. M. Mokhtar, W. Bajwa, M. Elgenedy and N. Al-Dhahir, "Exploiting Block Sparsity for Joint Mitigation of Asynchronous NBI and IN in Hybrid Powerline-Wireless Communications," *in Proc. of IEEE SmartGridComm,* Miami, Florida, November 2015.
12. M. Elgenedy, A. Elezabi, "Blind Symbol Rate Estimation using Autocorrelation and Zero Crossing Detection," *in Proc. of IEEE International Conference on Communications (ICC2013),* Budapest, Hungary, June 2013.

13. M. Elgenedy, E., and M. Nafie, "Iterative MMSE-DFE Equalizer for the High Data Rates HF Waveforms in the HF Channel," *in Proc. of the 47th Asilomar Conference on Signals, Systems and Computers,* Pacific Grove, Calif., Nov. 2013.

14. M. Elgenedy, E. Sourour, and M. Fikri, "Iterative Bi-directional Kalman-DFE equalizer for the high data rate HF waveforms in the HF channel," *in Proc. of IEEE 1st International Conference on Communications, Signal Processing, and their Applications (ICCSPA2013),* Sharjah, Feb. 2013.

Patents

Shalash, Ahmed F., Khairy, Mohamed, Elgenedy, Mahmoud Abdel-Moneim. 2008. Demodulator of digital GFSK receiving system and method thereof. T.W. Patent 200835250, filed Feb. 15, 2007, and issued Aug. 16, 2008. Source : Taiwan Patent Search - No. 200835250. , espacenet database - No. 096105844.

Education

The University of Texas at Dallas, Dallas, Tx
P.hD. in Electrical Engineering, ***August 2014 - Current***
(GPA: 4)
Advisor: Prof. Naofal Al-Dhahir.
Research: Impulsive noise mitigation for narrowband/broadband powerline communications

Cairo University, Egypt
M.Sc. in Electrical Engineering, ***Sept. 2005 - December 2010***

Cairo University, Egypt
B.Sc. in Electronics and Communications Engineering, ***Sept. 2000 - June 2005***

Honors and Awards

- Recipient of the Jan Van der Ziel prestigious Graduate Fellowship at UT Dallas for the 2018-2019 academic year.
- Recipient of the Louis Beecherl, Jr. prestigious Graduate Fellowship at UT Dallas for the 2017-2018 academic year.
- Teaching assistantship at UT Dallas for five years.
- Best use of visualization award in U-HACK MED 2018 at UTSW, "TEAM 8: DIFFERENTIATION OF METASTATIC POTENTIAL IN MELANOMA CELLS". https://www.u-hackmed.org/outcomes

Volunteering and Social Organizations

- Co-founder of the UTD TA/RA association (Activities started April 2017).
- Co-founder of the Club of Electronics and Communications Engineering (CECE) at Cairo University.
- Member of Graduate Student Assembly (GSA) at UT Dallas (Initiated Spring 2018 and officially announced summer 2018).
- Councilor at Egypt Scholars Association.
- Member at the Institute of Electrical and Electronics Engineers (IEEE Communications Society, IEEE Power and Energy Society, IEEE SmartGrids Society).